AN INVESTIGATION INTO THE EFFECTS OF SHAPE AND STRUCTURE ON THE ANTIBACTERIAL EFFICACY OF METAL NANOPARTICLES

Alanod Alshareef

MSc in Micro Electronics and Nano Technology

BSc in Biology

A thesis submitted to De Montfort University
in partial fulfilment of the requirements for the
degree of Doctor of Philosophy (PhD)

Emerging Technologies Research Centre

De Montfort University, Leicester, UK

July 2019

Acknowledgements

I would like to express my gratitude to my supervisors, Dr Richard Cross, Dr Katie Laird and Professor Shashi Paul. Their advice and encouragement has made this thesis possible.

I would like to thanks Mr. Paul Taylor, senior technician at EMTERC for ordering equipment and assistance. Special thanks go to all EMTERC members and students for their advice and for all the nice moments, we shared together especially Krishna, Zahraa, Hanaa and Mariam.

My appreciation goes to all the microbiology team, Jasira Patel, Richard Smith, Karen Stones, and Abdul Razaaq; for their help. My grateful goes to Rachel Armitage, Leone and Liz O'Brien for all their assistance with the SEM. In addition, thankful goes to Mr Zahoor Ul-Haq and Blenda for accessing chemistry lab and their help when needed.

My gratitude goes to my dad, god bless his soul. I am very thankful to my mum and family for their love and support throughout all years. Special thanks go to my husband, Ahmad Bahar, for his unfailing love and encouragement. A huge thanks goes to my kids (Malik, Leen and Ali), for their unconditional love and kindness. Finally, I am grateful to Saudi culture bureau for the financial support of my studentship.

Abstract

Increasing numbers of microbial organisms are becoming resistant to antibiotics, demonstrating a need for new, effective antibacterial agents. Metal nanoparticles (NPs) such as silver (AgNPs), copper (CuNPs) and gold (AuNPs) exhibit antimicrobial properties against bacteria, including *Escherichia coli* and *Enterococcus faecium*. *E. coli* O157:H7, which is known to be virulent and infectious, causing bowel discomfort, diarrhoea, nausea or vomiting. Enterococci frequently causes gastrointestinal infections, urinary tract infections, hepatobiliary sepsis, endocarditis as well as hospital-acquired infections, e.g. nosocomial bacteraemia and surgical wound infection. As regards *E. coli*, NHS trusts in England reported 38,132 cases of bacteraemia between 1 April 2015 and 31 March 2016 (NHS, 2017). There was an overall increase in the incidence of bacteraemia caused by *Enterococcus spp* between 2010 and 2017, from 9.9 to 13.1 per 100,000 of the population in England respectively. The antibacterial activity of metal nanoparticles has been investigated extensively due to their high surface area-to-volume ratio and the generation of reactive oxygen species. Metal nanoparticles have potential as alternatives to current antimicrobials used in the hospital environment to combat Healthcare Associated Infections (HCAIs).

Nanoparticles were synthesised using the chemical reduction method, where the size and shape were controlled via the precursor or reduction agent, reaction time, temperature and the molar ration between the precursor and reduction agent. Nanoparticles were characterised using ultra-violet/visible spectroscopy (UV-Vis), scanning electron microscopy (SEM), energy-dispersive spectroscopy (EDX), X-ray diffraction (XRD) and transmission electron microscopy (TEM). Minimum inhibitory concentration (MIC) was used to assess the antimicrobial efficacy of metal NPs. The antimicrobial activity was then determined using growth inhibition kinetics by 96 well plate reader and viable counts. Visualisation of the interaction between metal NPs and bacteria were assessed using SEM.

Different shapes of metal NPs were obtained *in vitro* such as spherical shape NPs (AgNS, AuNS and CuNS), octahedron (AgNOct and AuNOct) and cube shapes (CuNC). All produced NPs are crystalline in nature, confirmed by selected area electron diffraction. The MICs of AgNOct against *E. coli* were the lowest at 10µg/ml, followed by MICs of CuNC and AuNOct of 15 and 50µg/ml respectively. The MICs of spherical shape (AuNS) against *E. faecium* and *E. coli* were the highest at 250 and 230 µg/ml respectively. Significant ($p \leq 0.05$) reductions of $\geq 8 \log_{(10)}$ CFU/mL and $\geq 5 \log_{(10)}$ CFU/mL were observed for *E. coli* and *E. faecium* respectively treated with AgNOct. While treatment of CuNC resulted in significant ($p \leq 0.05$) reductions of 7.92 $\log_{(10)}$ CFU/mL and 3.5 $\log_{(10)}$ CFU/mL against *E. coli* and *E. faecium* respectively. Reduction data for spherically shaped NPs (AuNS and CuNS), the lowest inhibition, were reduced by ≥ 1.9 $\log_{(10)}$ CFU/mL against *E. faecium*. Damage to the bacteria cell wall was observed under SEM after treatment with NPs, while the cellular integrity was lost following exposure to AgNOct, AuNOct and CuNC for 24 hours.

The antimicrobial efficacy of NPs have been shown to be shape dependent against *E. coli* and *E. faecium*. Truncated octahedral AgNOct, AuNOct and cubic shape CuNC exhibited greater antibacterial activity when compared with spherical shape NPs (AgNS, AuNS and CuNS). AgNOct has the greatest antibacterial activity against *E. coli* and *E. faecium* compared with AuNOct and CuNC, being bactericidal against *E.coli* and bacteriostatic against *E. faecium*. The difference in shape resulted in differences in efficacy, which could possibly be due to the higher surface area and variations in active facets and surface energies. This higher reactivity may ultimately cause more rapid cell death. Among these metals (silver, gold and copper), silver nanoparticles show strong antibacterial activity against *E. coli* and *E. faecium.* It is suggested that this is caused by the generation of reactive oxygen species (ROS) at the cell wall affecting metabolic processes by damaging DNA reproduction.

List of Contents

List of Acronyms

AgNP….....Silver nanoparticle

AgNOct……... ……..……Truncated octahedral silver nanoparticles

AgNS……..…….……..…Spherical silver nanoparticles

AMCSD……..….American Mineralogist Crystal Structure Database

ATP…….…… adenosine triphosphate

AuNP……...…….Gold nanoparticle

AuNOct…….…….. Truncated octahedral gold nanoparticles

AuNS……..…..….. Spherical gold nanoparticles

B. subtilis…….. *Bacillus subtilis*

CFU…….……..…..Colony forming unit

CuNP….....Copper nanoparticle

CuNC……..…….Cubic copper nanoparticles

CuNS……. Spherical copper nanoparticles

E. coli…….……..…. *Escherichia coli*

E. faecium…….. *Enterococcus faecium*

EDX……..……..…… Energy-dispersive X-ray spectroscopy

HRTEM…….……High resolution Transmission Electron Microscopy

ICDD…….……... International Centre for Diffraction Data

MIC…….Minimum inhibitory concentration

NP……..……Nanoparticle

OD……..……Optical density

P. aeruginosa…….. *Pseudomonas aeruginosa*

ROS…….…..…… Reactive oxygen species

SAED……...….Selected area electron diffraction

SEM……..…Scanning Electron Microscopy

S. aureus…….…. *Staphylococcus aureus*

TEM……..Transmission Electron Microscopy

UV-Vis……..…….Ultraviolet–visible spectroscopy

XRD……X-ray diffraction

Chapter 1.

Introduction

1. Introduction

Nanotechnology is a field that focuses on materials or devices with dimensions ranging from 1-100nm in one dimension (Bazargan *et al*., 2016). Nanoparticles are utilised in the fields of diagnostics, high-sensitivity bio-molecular detection, therapeutics, antimicrobials, micro-electronics and catalysis (Ghorbani *et al*., 2011).

Many physical parameters help to determine the properties of metal nanoparticles including their shape, size, structure and composition. These can be modulated to help tailor the properties for a particular application. For instance, in surface-enhanced Raman scattering and localized surface plasmon resonance, both experimental and computational studies indicate that the structure and shape of Ag or Au nanoparticles play crucial roles in influencing the position, number and intensity of localized surface plasmon resonance (LSPR) modes and polarization dependence, or a spectral region for effective molecular detection by surface-enhanced Raman Scattering (SERS) (Ghorbani *et al*., 2011). For catalytic reactions, the properties of metals can be enhanced by means of size reduction (Khodashenas & Ghorbani, 2015). For example, NPs of copper were used extensively as catalysts during research in the 1, 3-Dipolar Cycloaddition of the terminal Azides and Alkynes (Chandra & Kumar, 2016). NPs materials have properties which are distinct from bulk material properties and as such they are used as magnetic, electronic, pharmaceutical, material application, cosmetic and catalytic reactions (Chandra & Kumar, 2016). Many different nanoparticle morphologies have been produced for a variety of materials, these include but are not limited to: sphere, cuboctahedron, cube, tetrahedron, octahedron, decahedron, right bipyramid, triangular, icosahedron, circular profile, hexagonal, square, pentagonal, rectangular, rod or wire among others (Wiest *et al*., 2015).

There are a number of methods by which NPs can be prepared including biological, physical and chemical approaches. The physical approach involves evaporation, condensation and finally laser oblation as the most crucial method. The advantage of physical over chemical methods is the absence of contamination solvent and uniform distribution of nanoparticles. The chemical approach is the most extensively employed method for silver nanoparticle chemical reduction by way of inorganic and organic reducing agents like elemental hydrogen, which reduces silver precursor forming metallic silver then follows agglomeration to form oligomer clusters. The clusters later form silver particles as a colloidal (Bai &Tian, 2013). The biological approach uses organisms ranging from prokaryotic cells of bacteria to eukaryotic fungi and even large plants (Mittal, Chisti & Banerjee, 2013; Ingale & Chaudhari, 2013). The biological approach is useful for well characterised and stable nanoparticles and it is the most eco-friendly in comparison to all other synthesis methods. However, it is a time consuming method which takes several hours to produce the nanoparticles (Kulkarni & Muddapur, 2014). There are many reasons to choose the chemical reduction method, such as fast reaction time, simple process, as well as the economical and high-yield production

(Iravani *et al*., 2014). Scientists have in the recent past introduced a non-traditional method for tackling resistant strains of bacteria which pose a life-threating challenge. Moreover, nanomaterial has demonstrated toxic impact towards strains of bacteria, as such it is of use in applications such as antibacterial, biomedical gene delivery, drugs and the engineering of tissues. They can also serve as vessels for nanomaterial introduction in the field of medicine (Khodashenas, Ghorbani, 2015).

Metal NPs such as silver, gold and copper are attracting more attention due to their antibacterial activity against various diseases and environmental application (Acharya *et al*., 2018). A previous report described that silver-based products are highly toxic to different microorganisms, which include 16 species of bacteria (Prabhu & Poulose., 2012). Numerous reports have demonstrated that the size of the NPs affects their antibacterial activity. For example, 5nm of AgNPs exhibit greater antibacterial activity when compared to 15 nm and 55 nm particles in Gram-positive and Gram-negative bacteria (Xiong *et al*., 2017; Raza *et al*., 2016; Jo *et al*., 2015). However, there is very little work in the literature investigating to what degree NP shape might affect the level of antibacterial activity, for instance rod shaped AgNPs exhibit strong antibacterial activity against Gram-positive bacteria such as *Bacillus subtilis* and *Staphylococcus aureus* and Gram-negative bacteria such as *E. coli*, *Klebsiella pneumonia* and *P. aeruginosa* when compared with spherical shape nanoparticles (Acharya, 2018). A previous report suggests that the shape effect on the antibacterial activity of AgNPs is attributable to surface area and facet reactivity. Moreover, AgNPs with larger effective contact areas and higher reactive facets exhibit stronger antibacterial activity (Rojas *et al*., 2015).

The World Health Organisation (WHO) illustrates that HCAIs as infections that develop in patients after 48 hours of hospitalisation or when they reside at a healthcare facility, excluding the infection have been existing or incubating when the patient was admitted. Infections developing in a period four weeks after discharge are also defined as a HCAI (World Health Organisation, 2002). HCAIs have become a developing problem in the last few years related to an increase in patient stays in hospital, morbidity, mortality and medical costs (Hensley & Monson, 2015). The high costs affiliated with HCAIs and the shortage of disinfectants commonly used against resistant bacterial species, requires further research into novel antimicrobials which can be utilised as disinfectants. Disinfectant targeted bacteria are a common cause of outbreaks and HCAIs (Rutala & Weber, 2016). While there has been significant investigation into the antibacterial effect of NPs on bacteria, many researches have concentrated on the efficacy of the NPs size. However, the efficacy of NPs shape is not well known. This study aims to fill this gap in the knowledge and conduct a comparative study of shape dependent metal NPs efficacy on both the treatment and

prevention of *E. coli* and *E. faecium* to establish whether metal NPs could be an alternative option to the current antimicrobials that have become ineffective against resistant bacteria.

1.1 Aims and objectives

- The main aim is to synthesise NPs with controlled shape and size of different metals such as silver, gold and copper and investigate their antimicrobial effects. To achieve this, a number of objectives need to be met:
- To optimise fabrication conditions to control the NPs size and tailor NPs shape.
- To assesses the efficacy of the metal NPs as antimicrobial agents against both a Gram positive *(Enterococcus faecium*) and a Gram-negative (*Escherichia coli*) organism with reference to their shape and size.

1.2 Organisation of thesis

This thesis is divided into nine chapters describing the crystallisation process, methodology, characterisation and results of this work. Following this chapter, which gives an overview, the thesis is organised as follows:

Chapter 2. Gives an introduction into the crystallisation process, followed by a review of the crystal structure, unit cell and miller indices.

Chapter 3. Describes the fabrication methods of the nanoparticles.

Chapter 4. Illustrates the antibacterial activity of the NPs, followed by a review of *E. coli* and *E. faecium*. Subsequently, the application of the antibacterial activity of NPs is also illustrated.

Chapter 5. Describes characterisation methods of the devices used in this work.

Chapter 6. Describes experimental methods employed in the research for the fabrication of the NPs and presents the results of the synthesis of crystalline NPs and it characterisation.

Chapter 7. Illustrates the shape controlling synthesis methods of NPs obtained by optimising the experimental parameters such as temperature, reaction time and molar ratio of the capping agent with the precursor.

Chapter 8. Interprets the antibacterial studies of the NPs and establishes the minimum inhibitory concentration (MIC) and the colony-forming unit (CFU). This is followed by visualisation of the interaction between NPs and bacteria using SEM.

Chapter 9. Conclusion of the work and suggestions for future research in the area are given.

1.3 Important findings of the research

This section highlights the most important results and findings from the research.

Six different shapes of metal NPs were obtained *in vitro* by way of a chemical reduction method were characterised using UV-VIS spectroscopy, SEM, EDX, XRD and TEM, to confirm the presence of NPs and identify the morphology, elemental analysis, crystalline nature and lastly TEM to obtain SAED for assignation of the crystalline nature and HRTEM for elucidation of the d-spacing of the lattice fringes.

For the first time, comparative studies of the efficacy of different shaped metal nanoparticles as antibacterial agents against *E. coli* and *E. faecium* were conducted. The MIC of AgNOct against *E. coli* was the lowest 10µg/ml, followed by MICs of CuNC and AuNOct 15 and 50µg/ml respectively. The MIC of AgNOct against *E. faecium* was higher than the MICs against *E. coli* 55µg/ml, followed by the MIC of CuNC and AuNOct 90 and 100µg/ml respectively. The MICs of AuNS against *E. faecium* and *E. coli* are the highest 250 and 230 µg/ml respectively. The differences in MICs inhibition concentration dependent on the shape of nanoparticles due to different crystal structure and orientation may reveal different antibacterial activity. It was suggested that the truncated octahedron silver (AgNOct) having plane (111) has higher electron density than spherical silver (AgNS). Similarly, the intensities of the (111) plane was higher in copper nanocube (CuNC) and truncated octahedron gold (AuNOct) than spherical shaped NPs (AuNS) and (CuNS).

Moreover, significant ($p \leq 0.05$) reductions of ≥ 8 $\log_{(10)}$ CFU/mL were observed for *E. coli* treatment with AgNOct. It can be concluded that the AgNOct had greatest antimicrobial activity followed by CuNC and AuNOct. However, the reductions of the spherical shaped NPs (AuNS and CuNS) was the lowest; only ≥ 1.9 $\log_{(10)}$ CFU/mL against *E. faecium*. Damage to the cell wall of the *E. coli* and *E. faecium* after 24h treatment with AgNOct was observed in the SEM imaging. The results from this study suggests that AgNOct, CuNC and AuNOct could be a potential alternative to antibiotics for treatment in the future as antimicrobial agents utilised against *E.coli and E. faecium*.

1.4 -Peer Reviewed Publications and Conference Presentations

Peer Reviewed Published Work

1- Alshareef, A., Laird, K. and Cross, R.B.M., 2017. Chemical Synthesis of Copper Nanospheres and Nanocubes and Their Antibacterial Activity Against Escherichia coli and Enterococcus sp. *Acta metallurgica sinica (english letters)*, *30*(1), pp.29-35. (Impact factor 1.29)

2- Alshareef, A., Laird, K. and Cross, R.B.M., 2017. Shape-dependent antibacterial activity of silver nanoparticles on Escherichia coli and Enterococcus faecium bacterium. *Applied Surface Science*, *424*, pp.310-315. (Impact factor 3.38)

Conference Presentations

1-"Chemical synthesis of copper nanospheres and nanocubes and their antibacterial activity against E.coli and Enterococcus sp" A. Alshareef, K. Laird, R.B.M. Cross, 5th International advances in applied physics & materials science congress and exhibition, APMAS 16-19 April 2015, Oludeniz Turkey.

2- "Investigation of nanoparticles for antibacterial application", A. Alshareef, K. Laird, R.B.M. Cross, 7th Saudi conference, SSC2014, 1st-2nd of February 2014, Edinburgh, United Kingdom

3- Shape-dependent antibacterial activity of silver nanoparticles on Escherichia coli and Enterococcus faecium bacterium, A. Alshareef, K. Laird, R.B.M. Cross, 11th International Conference On Physics Of Advanced Materials,ICPAM-11, 8-14 September 2016, Cluj- Napoca, Romania.

Papers in preparation

1- "Hexagonal prism of silver nano particles: a novel shape derived from single seeds", Alanod Alshareef, K Nama Manjunatha, R. B. M. Cross.

2- "Visualization of interaction between inorganic nanoparticles and bacteria", Alanod Alshareef, Katie Laird, R. B. M. Cross.

Chapter 2.

Crystallization process and structure

2.1.1 Nucleation: The Birth of a New Phase

Nucleation involves the first phase of the crystallization process. Most studies lack experimental tools for capturing, monitoring and identifying the nuclei which is a tiny cluster comprising of very few ions and atoms formed in the earliest stages of nanoparticle synthesis (Xia *et al*., 2015). It is also next to impossible to directly observe nuclei formation in real space since when a crystal is successfully visible with an electron microscope, it has grown past the first stage of nucleation. For example, high resolution Transmission Electron Microscope (HRTEM) has a resolution below 0.5Å at magnifications over 50 million times (Erni *et al*., 2009). The nucleation process can be followed in a liquid or vapor phases using scanning probe microscopy (Karpov *et al*., 2015). A physical tip and solid substrate involvement however, lead to additional features including steps, kinks and other defects that might serve as the site of nucleation or a tip for atom interactions. This is because, laser beam imaging usually have interference with the procedures being under the study this lead to the alteration of the results or outcome, therefore we employ the use of situ liquid to comprehend the difference in the electrode position and the beam induced which lead to growth of crystallites of gold and the nucleation (Karpov *et al*., 2012). The synthesis of a nanoparticle involves a precursor compound being erduced or decomposed to produce a zero-valent atom which is a building block of a nanocrystal. However, it is still unclear how nanoparticles and nuclei evolve from a precursor (Xia *et al*., 2015). In the decomposition process, the nucleation process followed LaMer and colleagues` proposed route (Figure 2-1).

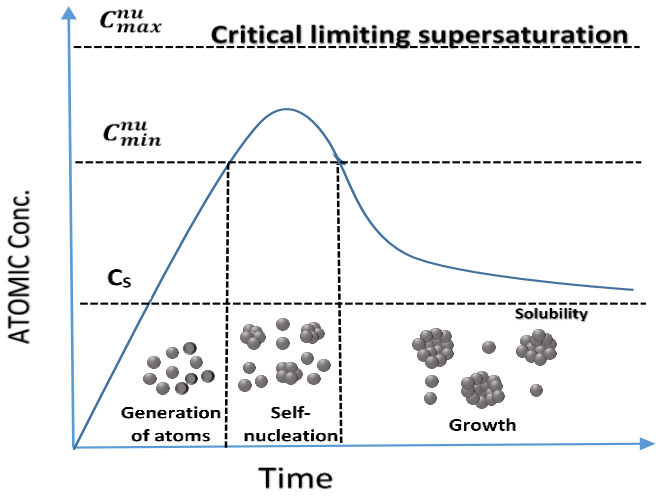

Figure 2-1: Atomic concentration and time depicting process and growth Source.

This process is based on a broad study of solution-stage synthesis of the mono-disperse (Xia *et al*., 2015) or metal nanoparticle synthesis, their concentration rises steadily when the precursor undergoes

decomposition caused by sonication or heat. The atoms begin to aggregate into small collections of nuclei once the atoms reach super-saturation points through self or homogeneous nucleation (Xia *et al*., 2015). The nuclei grow steadily as the concentration of the atoms in the solution drops. In an event that the atoms goes below the minimum super-saturation, nucleation events will cease immediately (Xia *et al*., 2009). A continued supply of atoms through ongoing precursor decomposition leads to the nuclei growing into nanoparticles of large size until equilibrium state is arrived at between the atoms in the solution and the atoms on the Nano crystal's surface (Bai & Tian, 2013).

However, it is also unclear whether the precursor compound will be reduced to zero-valent atoms that aggregate to nuclei and then undergo growth to nanoparticles; or the unreduced species start forming nuclei before the reduction process (Bai & Tian, 2013). One way to investigate is by utilising first-principles simulations of molecular dynamics, which is the technique of studying the pattern of the atomic evolution degree of freedom through solving numerically the motion equations of Newton (Bai & Tian, 2013). Repeated simulations leads to the extractions of models for the right dynamic procedures. It has been indicated that the precursor compound can directly be transformed into nuclei that then adds to other growing nanocrystals or nuclei without undergoing the zero-valent state (Bai & Tian, 2013). For instance, studies indicate that Pt^{II}-Pt^{I} dimer stabilized by Cl can be generated directly from $PtCl_2$ $(H_2O)_2$ complexes via an introduction of one electron (Bai & Tian, 2013).

Most of the methods for producing nanocrystals use a salt precursor that is dissolved in a solvent (Bai & Tian, 2013). A previous study on aqueous $AgNO_3$ solutions indicate that it is not always the case (metal ions can be complex as large units and their presence determine the outcomes of the reactions (Bai & Tian, 2013). Mass spectrometry studies indicate high abundance of trimetric Ag collections within aqueous solutions that are prepared from powders of commercially available $AgNO_3$ (Chandra & Kumar, 2016).

It is important to fully characterize the solutions and regents used for nanoparticles syntheses. For the characterization process, the solution species that are present under different conditions are vital to understanding the reason for the shape of the nanocrystals.

The nuclei size greatly affect the rate of growth and nucleation and also the sizes of the nanoparticles, since the final sizes of the nanoparticle increases with the increase with critical value of the nuclei. In conclusive account of their likely or explicit roles (Bai & Tian, 2013). Electrospray mass spectrometry has been used in the past to provide information about the small clusters of nuclei present in the precursor solution. Furthermore, it can be used for discerning the larger collections formed during nucleation process (Brügger, 2014). However, the drawback of mass spectrometry is that it only depicts the cluster size (Chandra, and Kumar, 2016). To establish the geometric shape and internal structure, they are used in electrospray photoelectron spectroscopy accompanied by an accurate ab initio estimations. Also,

collision-induced dissociation of clusters together with mass spectrometry can be used to offer structural information. Furthermore, both emission spectroscopic and absorption can be employed for situ characterization of certain element for instance, emission spectroscopy makes the valuable and new method of spectroscopy which is applicable in situ sample heat treatment.

2.1.2 Evolution from Nuclei to seeds

Once the cluster grows beyond a critical mass, any structural fluctuations are energetically costly, hence the bond on the cluster forming a well-defined structure. This point is known as the formation of a seed (Xia *et al*., 2013). A seed plays a critical position since it bridges the nuclei and the nanocrystal. Seeds structures include a singly-twinned, single crystal or multiple-twinned (Chandra & Kumar, 2016). These structures can sometimes coexist within a synthesis. Through tight control of the seed population with varying internal structures, it is possible to obtain one nanoparticle shape. The population of different seed structure is usually influenced by the statistical thermodynamics of free energies of the several species together with the kinetic effects in relation to the production of metal atoms to nuclei (Chandra & Kumar, 2016).

When the reaction goes through thermodynamic control, the highest portion of the stable product is generated. To estimate the most stable products, the generation of a single-particle seeds can be used in the Wulff`s theorem that tries to minimize the system`s total interfacial free energy (γ) in a given volume. The interfacial free energy includes the energy needed to produce a unit area of a new surface (Xia *et al*., 2015).

$$\gamma = \left(\frac{\delta G}{\delta A}\right) \boldsymbol{n_i}, T, P \text{.....(2.1)}$$

G represents the free energy and A represents the surface area.

In a newly formed seed, the symmetry of the crystal has been broken since bonds are missing at the surface. Hence, atoms at the surface are absorbed towards the interior. To ensure the atoms maintain their original position, a pull force is required to restore them. The formula for an ideal surface can be given using a simple model.

$$\gamma = \frac{1}{2} \boldsymbol{N_b \varepsilon P_a} \text{.....(2.2)}$$

Wulff`s model (Xia *et al*., 2015). This implies that the single-crystal seeds should take tetrahedral or octahedral structures to maximize their {111} expression facets and minimize the total surface energy. However, the tetrahedral and octahedral shapes have bigger surface areas than a cube of similar volume.

Therefore, single-crystal seeds should exist in Wulff polyhedrons or (truncated octahedrons) that are enclosed within a mix of facets of {100} and {111}. These shapes take spherical profiles and hence smallest surface areas to minimize total interfacial free energy are possible (Chandra & Kumar, 2016), such seed shapes have been seen experimentally in a number of nanocrystals (metals) syntheses (Chandra & Kumar, 2016).

In kinetic control, the objective is to control the seed population comprising of different numbers of twin defects through the variation of the decomposition or the reduction rate of the precursor (Xia *et al*., 2015). In the case where the multiply-twinned seeds are relatively small and the extra strain energy as a result of twinning is compensated for maximizing the surface coverage through {111} facets and hence the achievement of the lowest total free energy (Xia *et al*., 2013). However, in theoretical analysis, the {111} facets` low surface energy cannot remedy the excessive strain energy when rapid expansion of the seeds occurs. This will lead to the conversion of the multiply-twinned seeds to single-crystals. Therefore, the multiply-twinned seed requires to be confined within relatively small sizes to increase their yield (Xia *et al*., 2009). This condition is usually accomplished experimentally through maintaining the rates of addition and atomic generation low. This allows for the prevailing of multiple-twinned seeds over the single-crystals since the slow generation keeps the small sizes for an extended period. Under similar conditions of kinetics, the single-twinned seeds can appear in low quantities (Chandra & Kumar, 2016).

Oxidation etching is another process that can be used in manipulating the distribution of twinned and single-crystal seeds through oxidization of zero-valent metal atoms into ion (Chandra & Kumar, 2016). Most syntheses are undertaken in the air in the presence of oxygen. The presence of a ligand for metal ion in the solution used leads to the combination of oxygen atoms and ligand to form a powerful etchant for the seeds and the nuclei (Xia *et al*., 2013). The defect zones within the twinned seeds have higher energy as compared to single-crystal regions and therefore are more prone to an oxidative surrounding their atoms interact with the etchant then oxidized and dissolved to the solution. Conversely, the single-crystal seeds are resistant to oxidative etching since they do not have twin boundary defects. Therefore, by taking advantage of oxidative etching selectivity, different types of seeds within the reaction solution can be regulated controllably (Xia *et al*., 2009). For instance, a polyol is an organic compound which has several groups of hydroxyl. It is a molecule which has over two hydroxyl groups. In the Ag polyol synthesis, all twinned seeds can be eliminated through the addition of a trace of Cl to the reaction resulting in the manifestation of single-crystal seeds. Less corrosive anions such as Br can replace Cl making it possible for the selectivity to do away with only the multiply twinned seeds to leave behind a mixture of singly twinned seeds and single-crystal. The use of oxidative etching has been certified for several noble metals including silver and gold. For these metals, ligand and O_2 are required to undertake oxidative etching. In

most cases, the presence of tiny amounts of ionic impurities or metal precursors in the chemical reagents can lead to oxidative etching and have a profound effect on the population of different kinds of seeds (Xia *et al*., 2009).

2.1.3 Evolution from seeds to nanocrystals

Once a seed has been generated, it grows in size due to the addition of metal atoms. However, observing particle growth on the atomic level can be difficult or even impossible, especially when growth occurs in a solution (Langille *et al*., 2012). Studies of chemical deposition indicate that when adding atoms to the surface, the added atoms diffuse around till they come across a site where they can be fused. The growth of a crystal is regulated by the competition between an increase in surface energy that favors dissolution and a decrease in bulk energy that favors growth. Hence, dynamic interplay of dissolution and growth dictates the evolution of seeds to nanocrystals (Xia *et al*., 2009). Using electron microscopy, it is possible to resolve shapes and the internal structures of nanocrystals for instance, the cells of animals are colorless and tiny but through the discovery of the internal features of these cells was influenced by improvement of diverse strains which provided enough contrasts which make those internal features visible. Seeds generated at different phases of a synthesis. Consequently, one-to-one correspondence between the preliminary seed and the final nanoparticles has been discovered for several noble metals. Nanoparticle grows homogeneously to larger ones. The two steps are conducted completely by polyol process in one-pot, which account for the slower and controllable rate of reaction for reduction of polyol in comparison to general reduction of chemical by use of hydrazine (Chandra & Kumar, 2016).

Since this type of study above has been performed only for restricted sets of samples, it is hard to perfectly reveal details of a growth process. Generally, from single-crystal seeds, cubes, cuboctahedrons or octahedrons will be generated depending on the growth rates along the {100} and {111} directions. If uniaxial growth is prompted, the cubic and cuboctahedral seeds grow into rectangular bars or octagonal rods respective (Bai & Tian, 2013). Single-twinned seeds, right bipyramids that are enclosed by the [100] facets and nanocrystals comprising of two right tetrahedrons that have a symmetrically placed base-to-base are generated (Wang *et al*., 2013). However, these seeds might evolve into nanobeams when a uniaxial growing process is instigate (Bai & Tian, 2013). Multiply-twinned seeds produces decahedrons, icosahedrons and nanowires (pentagonal nanorods) dependent on whether {100} planes within the side surface become stable or not. Seeds with stacking faults usually grow into thin plates with the bottom and top faces that are {111} facets while the side surfaces are enclosed with a mixture of {111} and {100}

facets. These seeds become thin plated with a hexagonal cross-section due to the six-fold symmetry (Bai & Tian, 2013). With the continuing growth, final products sometimes take triangular shapes through the elimination of the {111} facets occurring at the side surfaces. In other cases, the final product takes up a shape that is very dissimilar from the common generic shapes due to defect structures, presence of exotic seeds, crystal overgrowth and surface capping effects (Xia *et al*., 2015). The figure below depicts evolution from seeds to nanocrystals (Figure 2-2).

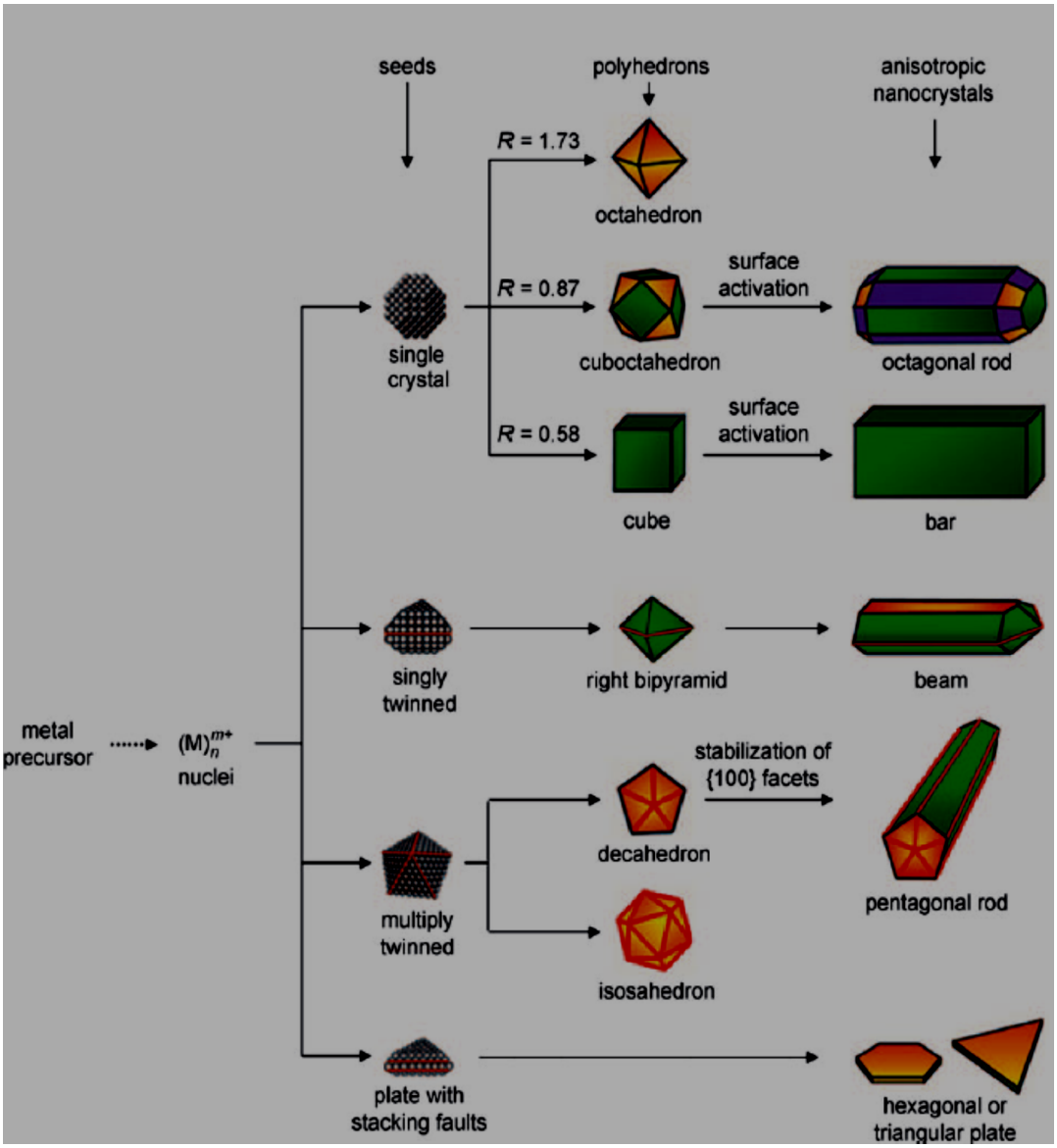

Figure 2- 2: Seeds and shapes of the nanocrystals. From single-crystal seeds, cubes, cuboctahedrons or octahedrons will be generated depending on the growth rates along the {100} and {111} directions. If uniaxial growth is prompted, the cubic and cuboctahedral seeds grow into rectangular bars or octagonal rods respective (Xia *et al*., 2009).

One technique that forces a final nanocrystal to take up another shape than those shown in the figure above is via the introduction of the capping agent (Bai & Tian, 2013). Different catalysis literatures have documented that the chemisorption of molecular or atomic species from the gas stage to metal nanocrystal can lead to drastic morphological modifications. For instance (Harris, 1986), indicated that quasi-spherical Pt nanoparticles evolved into nanotubes when exposed to H_2 gas that is contaminated with traces of H_2S. Some scholars propose that {100} facets are formed preferentially over the {111} facets in an environment. In a solution environment, surface capping/ chemisorption process can have an intense effect on the shape gained by a nanoparticle (Bai & Tian, 2013). In general, the binding affinity of a chemisorption agent varies from one particle facet to another and such preferential capping hinders the growth of a particular facet hence providing a way for regulating the surface areas of various facets (Harris, 1986). The capping agents can include byproducts that are generated during synthesis (Wang *et al*., 2013). For instance, the decomposition of metal carbonyl compounds produces carbon monoxide (CO), that can bind strongly to various metal surfaces inhibiting metal addition, due to a dead zone - a regime with low super- saturation whereby crystal growth ceases (Xia *et al*., 2009).

Xia *et al*., (2009) indicate that stacking faults and twin defects can be used in accomplishing anisotropic shapes by breaking the cubic symmetry. Since FCC metals are comprised of cubic crystal structures, no intrinsic driving pressure can force them to grow to one-dimensional or two-dimensional nanoparticles since 1-D and 2-D are only obtained when cubic symmetry of its lattice is broken-down (Harris, 1986). Stacking faults or twin defects are incorporated into the nanoparticles that lead to anisotropic growth either via reaction confinement within micelles assembled from surfactants or via preferential adsorption on a specific crystal facets such as citrate on {111} or PVP on {100}. Stacking typically takes place within close-packed lattices that comprise of atomic planes that are hexagonally packed with six fold symmetry (Oliver *et al*., 2015).

The presence of a mixture of different facets within the surface of a crystal leads to shape evolution. In relation to the growth of nanoparticles, pre-formed nanocrystals with facets that are well-defined can be added to a synthesis to serve as the primary site for the nucleation process. When crystal growth occurs, if the added metal atoms remain with the unchanged structure like that of the seed, this process is known as epitaxial. Epitaxial process is achieved when the seed has identical chemical properties as the growth atoms (Oliver *et al*., 2015).

2.2.1 Crystal structure

Crystal structure refers to the atomic arrangement of crystal. The periodicity in the arrangement of atoms, ions, and molecules in different directions (Kakani, 2006). The crystal structure is assumed to comprise of

points in space referred to as lattice points. The lattice points form the space-lattice or the crystal lattice. Crystals are solids which have a regular periodic arrangement of their particles bounded by strong metallic bonds and arranged in an orderly manner to each other (Figure 2-3). "Crystals are symmetrical about various elements such as planes, points or lines. Symmetry is important especially while classifying and describing the behavior of crystal structure (Askeland & Phulé, 2006; Kakani, 2006).

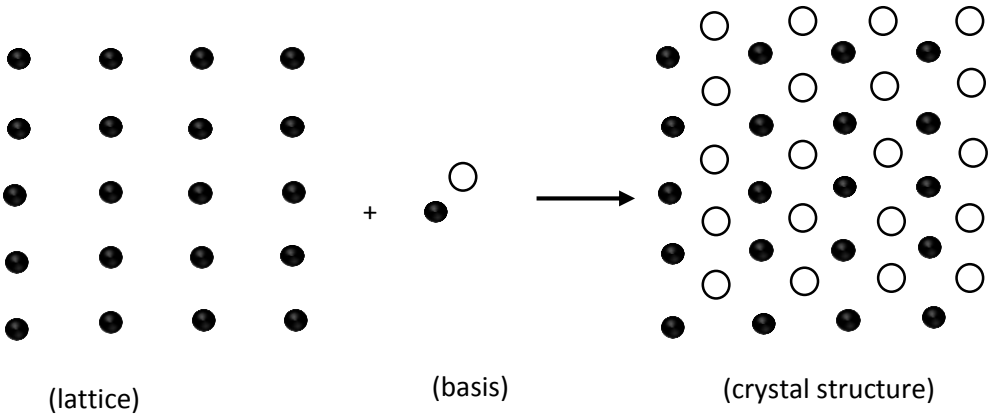

Figure 2-3: Crystal structure generation from lattice and basis.

2.2.2 Polycrystalline materials

Polycrystalline solids are comprising of many single grain or crystallites where every grain are thought to be single crystals in which the atomic structures has long order of range. While there is no relationship between the solid isotropic polycrystalline therefore there is no periodicity in the polycrystalline solids. While the amorphous have no long range of order at all. Then a large number of unit cells are grouped together they form a macroscopic crystal (Chawla, 2012). The figure below shows the basic structure of a unit cell of the 3-dimensional crystal lattice. The unit cell comprises of intercepts a, b and c along three directions as shown in Figure 2-4 (Kakani, 2006).

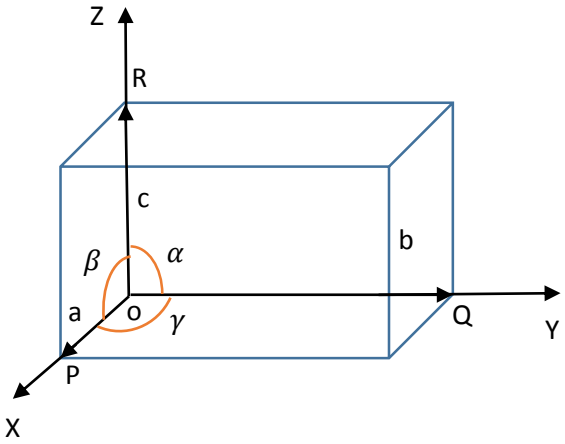

Figure 2-4: Lattice parameter of the unit cell.

The unit cell can be described by vectors a, b and c. The length of each side is a (2r) where r represents the radius of the atom at the lattice points, this distance is referred to as the space constant. An important property of the unit cell is the nearest distance between the centers of these atoms distance specifically because it is held up tightly than the other areas by the nuclei force.

There are various forms of lattices for unit cell this includes simple cubic (SC), body-centered cubic (BCC) and face-centered cubic (FCC). The total volume of unit cell VC is defined by product of its edges length.

$$Vc = a \times b \times c$$

The Atomic Packing Factor (APF) of a unit cell is defined by the equations shown below (Askeland & Phulé, 2006; Kakani, 2006).

$$\text{APF} = \frac{Total\ number\ of\ atoms \times Volume\ of\ one\ atom}{Volume\ of\ the\ unit\ cell} = \frac{v}{V}$$

A schematic diagram of Miller indice notation examples for crystallography planes for instance, (111), (100) and (110) (Figure 2-5).

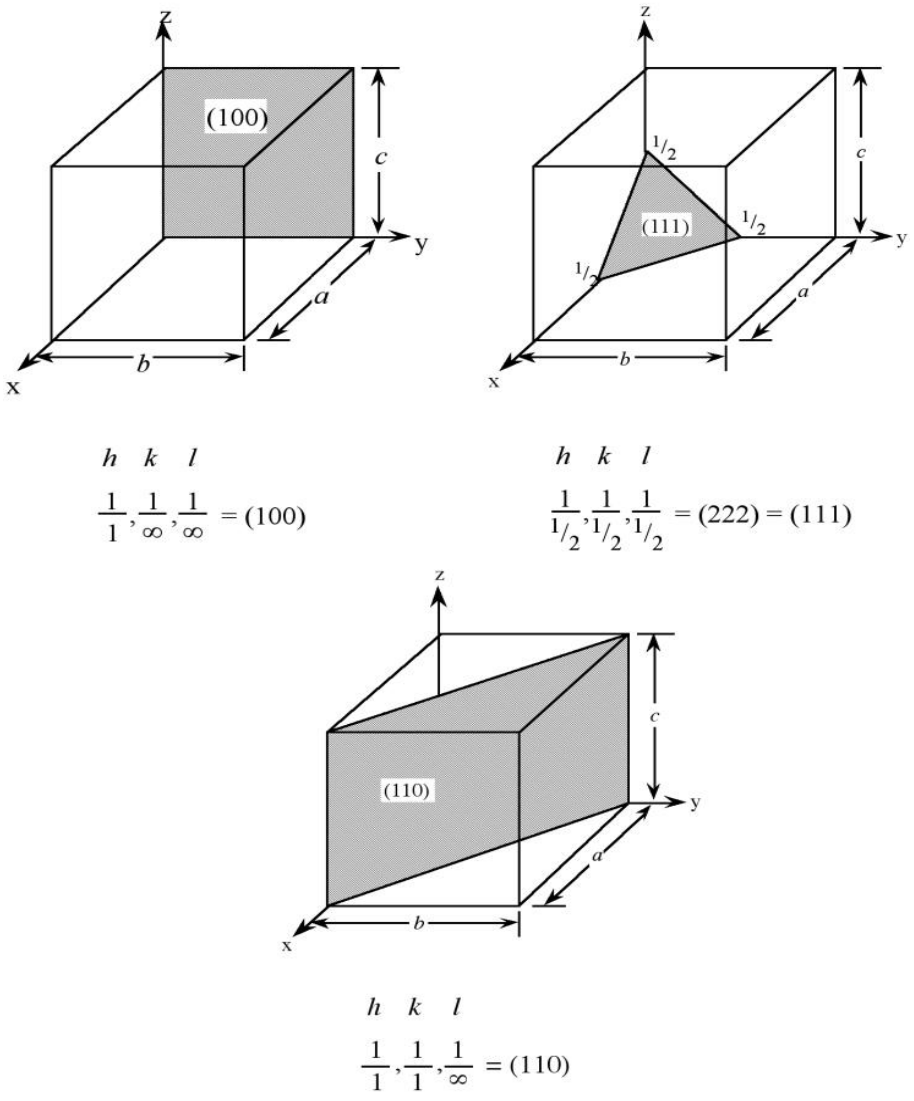

Figure 2-5: Examples of Miller indices notation for crystal planes. source: (sirajuddeen, 2011)

Simple cubic structures (SC)

For a SC cell, the total number of atoms in all the corners $= \frac{1}{8} \times 8 = 1$ atom

A simple cubic cell has a radius of a = 2r

$$Volume\ of\ cubic\ cell = a^3 = (2r)^3$$

Therefore, the Atomic packing factor is the ratio between unit cells and the volume basic atoms to the unit cell volume. Atomic packing factors is dependent on the atom radius and the chemical bond characterization and can be expressed as: $APF = \frac{1 \times \frac{4}{3}\pi r^3}{(2r)^3} = \frac{\pi}{6} = 0.52 = 52\%$

Body-centered cubic structures (BCC)

A BCC unit cell system has atoms on the eight corners shared and one atom at the center of the cell as shown in the figure 2-6.

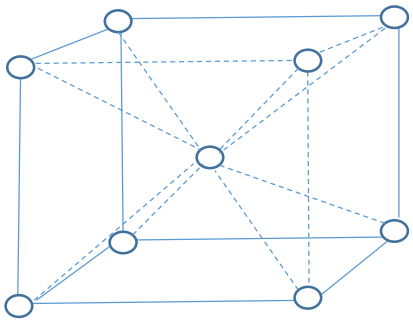

Figure 2-5*:* BBC structure.

A BCC structure has a lattice constant of 9. Lattice constant is the physical dimension of the unit cells in the crystal lattice. Lattice is usually three dimensional which is a, b, and c. lattice parameters are group of lattice constants. The lattice constant is the measure of compatibility of the materials with other materials structurally. Lattice constant of 9 indicate the strength of the compatibility of the material. BCC metals are stronger but less ductile, they include iron (Küry *et al*. 2017). Metals that possess this form of structure include sodium, lithium, chromium, potassium, alpha-iron, vanadium, and tungsten. Such metals are usually hard and less malleable compared to closed packed metals such as gold due to their higher lattice constants which makes them more compactible. BCC crystal structures do not allow atoms to be closely packed together as FCC crystal structures. When metals are deformed, the plane of atoms slips over each other which are difficult due to the structural compatibility of the BCC structures (NDT Resource Center, 2016).

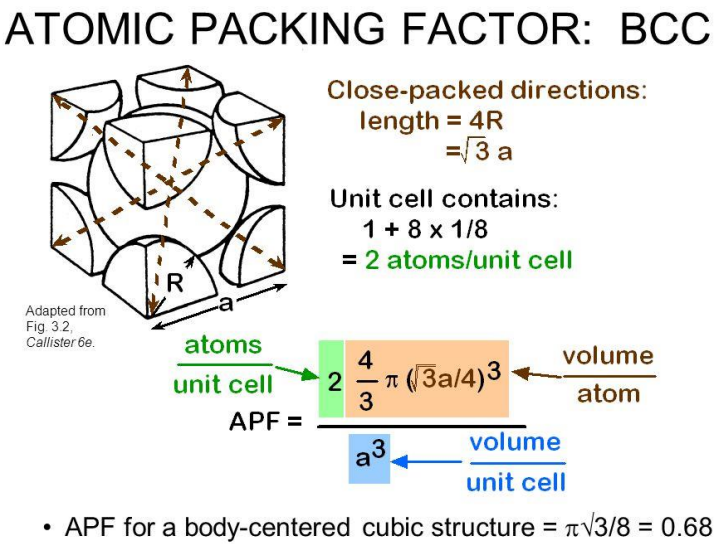

Figure 2-7*:* Atomic Packing Factor. source: (sirajuddeen, 2011)

The share of each cube is equivalent to an eighth of every corner atom. Therefore,

$$Total\ number\ of\ atoms = \frac{1}{8} \times 8 = 1\ atom$$

Total atoms in BCC structure = 1 + 1 = 2 atoms

$$Body\ diagonal^2 = total\ squares\ for\ all\ the\ \ three\ sides$$

$$(4r)^2 = a^2 + a^2 + a^2$$

$$a = \sqrt{\frac{16r^2}{3}}$$

$$= \frac{4r}{\sqrt{3}}$$

Total volume = $2 \times \frac{4r}{\sqrt{3}} \pi r^3$

$$r = \frac{a\sqrt{3}}{4}$$

Thus, the volume of the unit cell can be computed as;

$$a^3 = \left(\frac{4r}{\sqrt{3}}\right)^3$$

$$\text{APF} = \frac{\mathbf{2} \times \frac{\mathbf{4}}{\mathbf{3}} \boldsymbol{\pi}\, \boldsymbol{r^3}}{(\mathbf{4}\, \boldsymbol{r}/\sqrt{\mathbf{3}})^{\mathbf{3}}} = \frac{\sqrt{\mathbf{3}}}{\mathbf{8}}\, \boldsymbol{\pi} = \mathbf{0.68}$$

Face-centered cubic structure

A face-centered cubic structure (FCC) where the atoms are located at the eight corners of the unit cell and at the centre of each face as shown in figure 2-8. The main difference between face-centred cubic structure (FCC) and BCC is that the coordination number for FCC is 12, whereas the coordination number for BCC is 8. A face-centred cubic structure (FCC) also commonly refers to cubic close packed (ccp) and hexagonal close-packed (hcp) based on their symmetry.

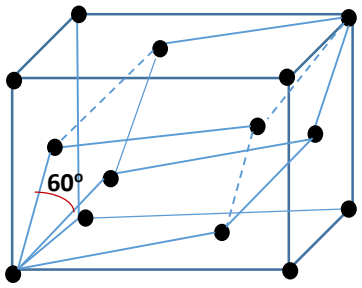

Figure 2-8*:* Face-centered cubic structure.

This form of lattice structure is more common compared to BCC structures because they are pack close together, than they do in the bcc structures. Some common metals with this type as a structure include copper, aluminum, silver, and gold. Other includes α-Fe, ϒ-iron, and β-Co. Metals with FCC structures have four times the number of atoms in a unit cell which implies that FCC structures are more densely packed compared to BCC structures (Mishin et. al, 2001; Lennon & Ramesh, 2004). Every face atom in FCC structure is divided by two cells thus, a single face of FCC unit comprises of ½ atom (Kleitz et.al, 2003).

$$\mathbf{APF} = \frac{6 \times \frac{4}{3}\pi r^3}{(3\sqrt{3}/2 \times (2r)^2\sqrt{2/3}) \times 4r} = \frac{\pi}{\sqrt{18}} = \mathbf{0.74}$$

The atomic packing factor is 74%. Atoms forms one layer nest themselves in empty spaces between the atoms of the adjacent layers. There is no other unit cell structure that possesses such a high number of close packed planes and directions. The arrangement of these atoms impacts significantly on the mechanical properties of metals. For example metals with FCC, structures are critically deformed. The coordination number is the number of the sphere which are in contact with the other two sphere in the arrangement of the lattice constant points surrounded by given number of sphere, in BCC or FCC metal structure is 12 which results in higher APF (Sanders & Gibson, 2003). The atomic backing factor of FCC (0.74) is higher than the atomic backing factor of BCC (0.68) and SC (0.52) respectively. The importance to measuring the

atomic backing factor to understand many properties of materials for instance, metals with a high atomic packing factor will have a higher "workability" (malleability or ductility).

2.3.1 Miller Indices

The crystal lattice is composed of an aggregate of a set of parallel and equidistant planes which passes through the lattice point (Küry *et al*., 2017). The crystal planes play a key role especially in determining hardening reactions and plastic deformation among other properties and behavior of metals (Rice et. al, 1997). Miller indices are defined as the reciprocal of the intercept made by the planes in the crystallographic axes when reduced to the smallest numbers."Miller indices define planar or directional orientation within a crystal lattice (Abbaschian & Reed-Hill, 2008; Tian et. al, 2010). It may refer to a specific crystal face, set of faces, a direction or set of directions. Miller developed a method to assign parallel planes in a lattice crystal by three numbers h, k, and 1 (William, Smith and Hashemi, 2011; Chien ET. al, 2005).

There are four key steps of evaluating Miller indices. Firstly, the coordinates of the intercepts that have been made by the planes along the crystallographic axes is determined. For example, in Figure 2-9 the length of the plane along x-direction is 2a, along the y-direction is 3b and along the z-direction is c (Kakani, 2006).

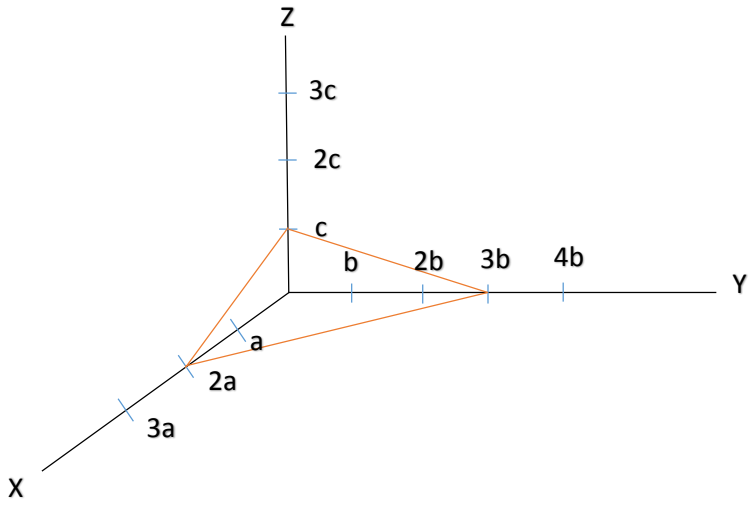

Figure 2-9: Intercepts of lattice planes on three crystallographic axes.

The above intercepts are expressed as lattice parameters along the axes or as multiple of unit-cell dimensions which results to x= 2a/a, y= 3b/b and z = c/c with intercepts 2, 3 and 1 respectively. Taking

the reciprocals of the intercepts in the x, y and z directions results to 1/2, 1/3 and 1, the reciprocals are reduced to the smallest sets of integral numbers h: k: l, which represents the Miller indices.

$$\frac{1}{2}:\frac{1}{3}:\frac{1}{1}=3:2:6$$

It is specified by a bar at the top of the corresponding index as shown in the Figure 2-10.

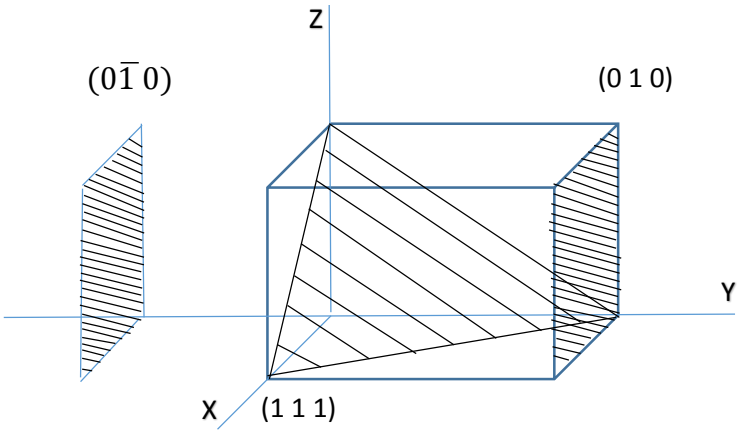

Figure 2-10*:* Miller indices of (111) plane.

2.3.2 Miller indices for crystal structure direction

Miller indices of various sides of a unit cell of a cubic lattice plane are of the same form which is collectively represented as familiar planes or equivalent planes. Some key generalities may be derived from the Miller indices. Firstly, a 0 indicate a parallel axis to the plane. Secondly, a smaller number describes axis which is closer to being parallel to the plane while a large number implies that the axis is almost perpendicular. Lastly, the orientation of the plane remains the same when the Miller indices are divided or multiplied by a constant (Baker & Cohen, 2004). Crystallographic or lattice direction is defined as a line which joins two-points of the lattice structure (Küry *et al*., 2017). Based on the same notations, the direction of a line in the crystallographic plane is described based on unit vectors (Shackelford & Muralidhara, 2005). Miller indices for lattice directions are vector components of the direction.

Millar Indices of crystal planes have various important features. Firstly, all equidistant parallel planes have equal Miller indices. Secondly, Miller indices of two planes that have the same ratio are said to be parallel to each other. In essence, all equally spaced planes with a given orientation have same index number. Thirdly, the direction of space is represented by square brackets [xyz]. Fourthly, the inter-planar spacing or distances between planes are represented by a number of parts of the body diagonal of a unit cell (Küry *et al*., 2017). Notes that one of the key features of Miller indices for the cubic crystal is that a plane that is parallel to any one of the coordinate axes has intercept at infinity. Thus, Miller index for such

axis is zero. The author also argues that a plane passing through the origin is defined in terms of parallel planes that have non-zero intercepts. (Küry *et al*., 2017).

2.4 Crystallographic planes and directions

Crystallographic based on the same notations discussed above, the direction of a line in the crystallographic plane is described based on unit vectors. According to Giacovazzo (2002), crystals are anisotropic thus they can be specified in a simple directions or planes under which the physical properties were observed. Crystals have directions and lattice planes that are highly concentrated with atoms. Two lattice points in a crystal lattice define a row.

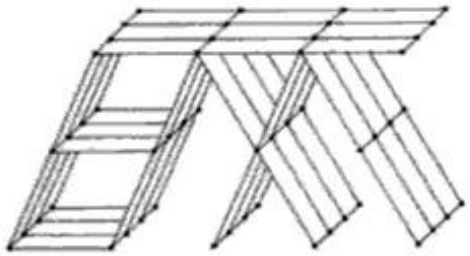

Figure 2- 61*:* Lattice planes and rows. Source: Giacovazzo (2002, p.8)

A lattice row defines a crystallographic direction. Choosing a unit cell, two crystal lattice vectors $Q_{nu,\ nv,\ nw}$ and $Q_{u,v,w}$ with u, v, w and n as integers defines two distinct lattice points which have the same direction. This characteristic is deployed to characterise directions. For example, directions that are related to vector $Q_{9,\ 3,\ 6}$ or $Q_{6,\ 2,\ 4}$ can be defined by vector $Q_{3,\ 1,\ 2}$. The direction is indicated by the symbol [3, 1, and 2]. The figure below shows a bidirectional unit vector $Q_{2,\ 1}$ and $Q_{4,\ 2}$.

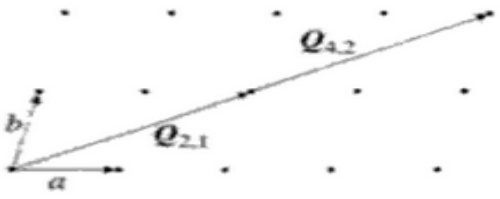

Figure 2- 72*:* Bidirectional unit vector. Source: Giacovazzo (2002, p.8)

To specify the direction of straight line which joins lattice points in a crystal lattice, any lattice point on the line can be chosen as origin and the vector joining this to any other lattice point can be defined as follows:

$$\vec{r} = \acute{n_1}\vec{a} + \acute{n_2}\vec{b} + \acute{n_3}\vec{c}$$

The direction of the line is defined by a set of integers n_1', n_2', n_3'. If these integers' numbers have common factors, they are removed and the direction is denoted by [n_1, n2, n3]. This line denotes all the lines that are parallel to the line. Figure 2-13 shows three different directions in a cubic lattice, the direction [111] is represented by a line passing through the origin O and the point P. The direction [100] is the line passing through the origin O and the point Q. The point Q is at a distance 1, 0, 0 from x, y and z-axes. Similarly, the direction [101] is the line passing through origin O to a point R where point R is at a unit cell distance 1,0,1 from x, y and z axes (Giacovazzo, 2002)."

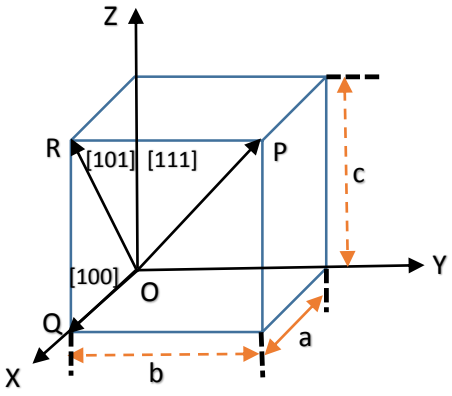

Figure 2- 83*:* Crystal direction of cubic lattice.

While specifying crystal directions, the axes of the crystal axes are assumed to be the base directions. The directions [444], [333] or [222] are identical to the direction [111]. The lowest integer's combinations is deployed to specify the directions (Küry *et al*., 2017). Besides this, there are other directions that are not parallel to each other and are equivalent to each other through rotation symmetry. The equivalent directions of [100] are [010], [001], [-100], [0-10] and [00-1]. All the six directions are grouped together in the symbol <100> whereby the bracket represents the whole family (Giacovazzo, 2002)."Crystal planes and directions impact on behaviours of metals such as hardening, deformation among others (Küry *et al*., 2017).

Chapter 3.

Synthesis of Nanoparticles

Introduction

Metal nanoparticles have been shown to exhibit strong antibacterial activity against both Gram-positive bacteria and Gram-negative bacteria including antibiotic resistant strains (Slavin *et al*., 2017). Since ancient times, AgNPs had been used as antibacterial agents (Van Dong *et al*., 2012). Many reports demonstrated that the size and the shape of the AgNPs exhibit their antibacterial activity (Acharya *et al*., 2018). However, there is very little work in the literature to investigate Au and Cu nanoparticles shape might affect the level of antibacterial activity (Lee *et al*., 2007; Ruparelia *et al*., 2008). Therefore, in this study Ag, Au and Cu nanoparticles has been selected due to their antibacterial activity (Slavin *et al*., 2017).

Metal nanoparticles have been fabricated through different methods such as chemical method e.g. (chemical reduction, photochemical, electrochemical or pyrolysis) (Dang *et al*., 2011; Remita *et al*., 2007; Ghorbani *et al*., 2011), biological method e.g. (using plant extract, bacteria, yeast or fungi) (Mittal *et al*., 2013; Ingale *et al*., 2013; Mourato *et al*., 2011) and physical method (Panigrahi, 2013). Among these methods, chemical reduction method is the most preferred because synthesis process is simple, fast reaction time, low cost and in high-yield production. The size and the shape of the nanoparticles can by determined by optimizing the experimental parameters such as temperature, reaction time and molar ratio of the capping agent with the precursor (Dang *et al*., 2011) .

In chemical reduction methods, the reducing agent is a chemical solution such as sodium citrate, N, N-dimethyformamide polyols, NaBH4 and N2H4, whereas in biological methods, collection of enzymes especially nitrate reductase. Spray pyrolysis methods are carried out in operating conditions of high temperature and pressure; electrochemical methods are based on electrolysis of solution.

3.1 Chemical method

3.1.1 Chemical reduction

The chemical reduction synthesis method was most extensively used to synthesis silver (Khatoon et al. 2011), gold (Jiang *et al*., 2011) and copper (Dang *et al*., 2011) because is found to be the most versatile for metal NPs (Khanna *et al*., 2007). The chemical reduction approach has been applied in preparing stable colloidal dispersions in organic solvents or water. The reducing agents used include NaBH4, N,N-dimethyformamide, polyols, Sodium citrate and N_2H_2. In preventing the aggregation of Ag nanoparticles, it requires to stabilize by using a capping agents like polyvinyl pyrrolidone, sodium dodecyl sulphate and tri-sodium citrate (Ghorbani *et al*., 2011). Some chemical reduction reactions might be undertaken at room temperature, but others need elevated temperatures to enhance the reaction rates (Ghorbani *et al*., 2011). The thermal methods like reduction of silver ion by hydrazine or dextrose (reduction agents) and the

Tollen`s reduction that employs m-hydroxy banzaldehide are from the chemical reduction methods (Ghorbani *et al*., 2011). The nanoparticle morphologies largely depend on the temperatures adopted in the synthesis process (Ghorbani *et al*., 2011). For instance, Sarkar *et al*., (2007) were able to synthesize both 3-D and 2-D Ag nano-structures with globular and disk morphology by undertaking a simple silver-mirror reaction in the presence of anionic surfactants. Experiments using tri-sodium citrate as the initial surfactant/reducing agent (sodium formaldehyde sulphoxylate to silver nitrate) have been undertaken hence establishing a large-scale approach for preparing silver nanopowder, the desired temperature (between 50 and 100 °C) is required to obtains particle that are less than the size of 50 nm (Ghorbani *et al*., 2011).

Salzemman *et al*., (2004) used micro-emulsion technique to fabricate copper nanoparticles of size 3-13 nm. In developing a flower-like silver nanoarchitecture with size 20 nm at room temperature, ascorbic acid was utilized as the reducing agent and citric acid played a key role in the nano-structure formation. Janardhanan *et al* (2009) synthesized silver nanoparticles using an aqueous chemical method with organic base but without any external capping agents. Silver nanocrystals of 40 and 80 nm can be formed through oxidation of glucose to gluconic acid by amine in the presence of gluconic acid caps and silver nitrate. Also, silver nanoparticles have been synthesized through the polyol process with the help of super-critical carbon dioxide and silver nitrate that is utilized as the base material while polyvinyl pyrrolidone is used as the stabilizer for the silver clusters and the reducing agent/solvent is ethylene glycol. In this experiment, polyvinyl protected the nanosize silver particles from aggregation and promoted the process of nucleation (Ghorbani *et al*., 2011). Shape and size control in a chemical reduction method have the advantages of it simple process, fast reaction time, economical and in high-yield production (Iravani *et al*. 2014).

3.1.2 Photochemical method (irradiation)

Photochemical method has also been used in synthesizing nanoparticles (Ghorbani *et al*., 2011). The system is usually excited by radiation, hence producing an active reducing agent like electrons, radicals and excited compounds. For instance, laser irradiation of aqueous solution comprising of a surfactant and Ag salt can fabricate silver nanoparticles of well-defined size and shape distribution (Ghorbani *et al*., 2011; Sharma *et al*. 2009). Laser irradiation requires no reducing agent by using UV light instead of chemical materials. Silver nanoparticles have been synthesized from ethylene glycol H_2O mixtures without using a stabilizer. The researchers used pulse radiolysis technique to generate nanocrystals by silver perchlorate. Remita *et al*., (2007) demonstrated that X-ray irradiation of metal salt solutions (aqueous) in the presence of a stabilizer causes the synthesis of metal nanocrystals similar to γ-ray irradiation. The generated nano-objects usually appear spherical with a radius of approximately 14 nm. Reduction of silver ions has also been achieved by the use of UV light in place of the chemical materials. Silver nanoparticles were produced

in a natural rubber matrix through photo-reduction of film cast from latex (natural rubber) comprising of silver salt and their size ranged between 4 and 10 nm. Synthesis approaches that use microwave irradiation have been undertaken and this technique is known to offer faster heating rate than other conventional heating methods that use convection or conduction. Yanagida, Komameni and Liu (2009) reported the utilization of fixed frequency microwave in synthesizing silver and platinum nanoparticles. However, the disadvantage in this method, high cost of the equipment's (Iravani *et al*. 2014).

3.1.3 Pyrolysis

Another chemical method used in synthesizing nanoparticles includes spray pyrolysis (Zhang *et al* 2009). Nanosilver powder of 100 nm size was fabricated through spray pyrolysis using silver nitrate solution, 0.32 MP a flux of carrier gas, furnace set up at a temperature of 720°C and 336 ml h^{-1} flux of silver nitrate solution. In another study, nanosilver powder was fabricated from MgO/Ag composite powder through spray pyrolysis (Ghorbani *et al*., 2011). The impacts of molar ratio, furnace temperature, concentration of the mixed solution, the flux of the carrier gas on the particle sizes and morphology of silver powder were studied. A suitable quantity of commercial reagent $Mg(NO_3)_2$ and $AgNo_3$ were dissolved into water (deionized) forming an aqueous solution of 40% mass percentage and molar ratio of $Mg(NO_3)_2$ and $AgNo_3$ of ratio 8:2. This solution was then mixed up and fed to the nozzle of a solution feed rate 500 mL h–1, hot air of 790°C and carrier gas flux of 0.30 MPa (Ghorbani *et al*., 2011). To remove MgO template from MgO/Ag composite, ammonium chloride solution was used. $Mg(No_3)_2$ from spray pyrolysis was then used in inhibiting nano-Ag growth. The drawback of this method is condensation growth that causes agglomeration of the particles (Schubert, 2012).

3.1.4 Electrochemical method (electrolysis)

Electrolysis process has been used in the past for reducing metal ions. However, some literatures indicate that the method can be employed in synthesizing metal nanoparticles, especially for silver (Ghorbani *et al*., 2011). For instance, silver nanospheres of approximate size 11 nm have been grown at room temperature in large scale by the reduction of silver nitrate in a solution of polyol using electrolysis approach in the presence of KNO3 and PVP. In this experiment, a 6 mm diameter rotating disk (Ti electrode) was utilized as the cathode and Pt plate of 2 cm diameter as the anode resulting in the formation of electro-deposited Ag nanocrystals. The disadvantage in this method, the reaction time is slow that takes several hours to synthesis NPs (Lim *et al*. 2006)

3.2 Biological method

Biological synthesis of nanoparticles has been studied by many scholars due to the belief that it is ecofriendly method (Ingale & Chaudhari, 2013). Natural sources of synthesizing nanoparticles through biological method include yeast, bacteria, fungi and plants (Kulkarni & Muddapur, 2014). Furthermore, multicultural and unicellular organisms can synthesize extra cellular and intracellular inorganic nanoparticles. The section below summarizes some of the studies and literature about biological method of synthesizing nanoparticles. The drawback of this method is not easy to achieve a high-yield of NPs by using biological synthesis (Iravani *et al*. 2014).

3.2.1 Plant nanoparticles synthesize

Synthesis of nanoparticles here employs a single step of biosynthesis process and tender a superior approach for synthesizing nanoparticles since the protocol involving plants is free from toxicants and the natural capping agents are supplied by the plants. According to Mittal, Chisti and Banerjee (2013), biomolecules from plant extracts can be utilized to reduce and to produce nanoparticles through a single-step green synthesis. This process is indicated to be quite rapid and can be undertaken under room pressure and temperature and can also be scaled up. Furthermore, synthesis facilitated by plants is usually biodegradable. The reducing agents include water soluble plant metabolites such as phenolic, alkaloids, coenzymes and terpenoids (Mittal, Chisti & Banerjee, 2013). Gold and silver nanoparticles have received a considerable focus when it comes to plant-based syntheses. Extracts coming from a diverse range of plants have been used to make these nanoparticles for example using ginger and lemon extract (Singh et al. 2011; Dhulappanavar et al. 2011). Moreover, live plants can be utilized for the synthesis. Plant extract for synthesizing nanocrystals is especially useful for generating nanoparticles free of contaminants or toxic substances used for therapeutic field. In medicine, nanoparticles are applied in making antimicrobial agents such as bandages. Applications targeted for clinical diagnostics and drug delivery are being developed (Mittal, Chisti & Banerjee, 2013). One of the big drawback of bio-synthesized is the long reaction time for instance 48h is required to synthesis AgNPs from leaf extract of Cassia auriculata was demonstrated (Udayasoorian *et al*. 2011).

3.2.2 Nanoparticle Synthesis using bacteria

Bacillus species have been demonstrated to synthesize nanoparticles. Ingale and Chaudhari (2013) indicate that bacteria have the ability of decreasing silver and fabricating extracellularly consistently circulated nanocrystals that range from 10 to 20 nm. Slawson *et al*., (2004) indicates that the silver generating bacteria which is isolated from silver mines demonstrates the accumulation of silver nanoparticles in the periplasmic space of the *Pseudomonas stutzeri* AG259. Bacteria have also been used

in synthesizing gold nanoparticles. Sharma *et al*., (2012) reported that the entire cells of a novel strain of the *Marinobacter Pelagius* can be used for the formation of stable and monodisperse gold nanoparticles. Prasad *et al*., (2007) used Lactobacillus strains in synthesizing titanium nanoparticles. Silver nanoparticles have also been synthesized of approximately 50 nm using supernatant *Bacillus licheniformis* whereby silver nitrate was added. The obtained silver nanoparticles were highly stable and the time required for the entire reaction to complete included 24 hours. However, studies have deduced that the use of microorganisms on nanoparticle synthesis can be slow (Kulkarni & Muddapur, 2014).

3.2.3 Fungi

The use of fungi for nanoparticles synthesis is relatively a recent addition to the list of existing biological methods. The fungi biological generation of nanoparticles has increased drastically due to reduced toxicity, comparatively economic, effortless method of synthesis, higher bioaccumulation and simple biomass handling and processing (Ingale & Chaudhari, 2013). The extracellular biosynthesis of silver nanocrystals from *Aspergillus niger,* Aspergillus oryzae and Fusarium solani are reported to generate silver nanoparticles (Gade *et al*., 2008; Binupriya *et al*., 2010; Ingle *et al*., 2009). *Pleurotus sajor caju* has been used also in synthesizing nanoparticles extracellularly (Nithya & Ragunathan, 2009). Furthermore, spherical nanoparticles are synthesized by using *Trichoderma viride* (Thakkar, Mhatre & Parikh, 2010). The prologue of silver ions to *Fusarium oxysporum* allows for the synthesis of stable nanoparticles of silver hydrosols (Ahmad *et al*., 2003). Additionally, *Phoma glomerata* has been indicated to generate a silver nanoparticle that is more efficient as compared to *Pseudomonas aeruginosa* (*P. aeruginosa*), *S. aureus* and *E. coli* when assessed (Birla *et al*., 2009). Silver nanoparticles have been synthesized using fungus *Verticillium*. It included the exposure of a biomass of fungal to an aqueous solution of Ag+ resulting in the intracellular reduction of metal ions and the synthesis of silver nanoparticles of a dimension 25 nm.

According to Balaji *et al*., (2009), extracellular biosynthesis of AgNPs is determined using *Caldosporium cladosporioides*. AgNPs of dimensions 10 to 100 nm were generated and measured by TEM images (Balaji *et al*., 2009). Also, vitro biosynthesis of nanoparticles of silver was accomplished using silver nitrate as a substrate on *Penicillium fellutanum* that was isolated from the coastal mangrove sediment. It was discovered in this study that nanoparticles biosynthesis is maximum when culture filtrate is treated with 1.0mmol L-1 silver nitrate and maintained at 0.3% sodium chloride and a PH of 6.0 while being incubated at a temperature of 5°C for 24 hours (Kathiresan *et al*., 2009). Furthermore, Filamentous fungi are good candidates for the synthesis of metal nanocrystals. On the other hand, fungi synthesis is longer time reaction compared to the chemical reduction method (Ghorbani *et al*., 2011).

3.2.4 Yeast nanoparticle synthesis

Kowshik *et al*., (2003) described extracellular synthesis of AgNPs in large amounts using a straightforward downstream process. Kowshik and colleagues were involved in isolating silver tolerant yeast strain (MKY3) by injecting them with aqueous silver nitrate. It was discovered that the formation of silver nanoparticles of 2-5 nm takes place under forced ecological conditions. Dameron *et al*., (2009) reported the production of cadmium nanoparticles using *Schizosacharomyce pombe* and *Candida glabrata*. Mourato *et al*., (2011) also investigated the biosynthesis of gold and silver nanoparticles using extremophilic yeast strain that was isolated from acid mine drainage.

3.3 Physical methods

In physical approaches, nanoparticles are synthesised generally by evaporation-condensation that can be undertaken using a tube furnace at atmospheric pressure. The vaporization process can be divided into chemical and physical technique depending whether a reaction is present. When the resultant nanocrystals comprise of similar composition with the target materials, they can be synthesised through physical vapor condensation (Panigrahi, 2013). On the other hand, nanoparticles that have a varying composition to that one of the target materials can be prepared through chemical vapor condensation. The source materials are placed within a boat located at the center of the furnace and it is then vaporized into a carrier gas. The nanoparticles of different materials like Au, Ag, Fullerene (molecule of carbon of sixty or more atoms) and PBS have been created through the evaporation/condensation method. However, different scholars indicate that the generation of nanoparticles through the tube furnace can lead to various drawbacks since the tube furnace occupies a huge space, requires more time in achieving thermal stability and consumes large amount of energy while it raises the environmental temperature in the surrounding environment. A typical furnace needs energy consumption ranging to several kilowatts and the preheating time can go up to many tens of minutes so as to attain a stable temperature of operation. Jung *et al*., (2006) demonstrated that nanoparticles of silver can be generated through a small ceramic heater using a local heating source. The evaporated vapor usually cools at an appropriate rate since the gradient of the temperatures within a heated surface is very steep as compared to tube furnace. This allows for the production of small nanocrystals in a high concentration. This evaporation/condensation method can be employed for generating nanoparticles for inhalation long-term experiments where toxicity studies are being undertaken and calibration devices for nanocrystal measurement apparatus (Jung *et al*., 2006).

Laser ablation has been used in synthesizing nanoparticles using bulk metallic materials in a solution. The features of the metal particles generated and the efficiency of ablation is dependent on several parameters (the duration of the laser pulse, the laser fluence, laser wavelength of the encroaching target of the metal, effective liquid medium and ablation time). Laser fluence is one of the critical parameters and the ejection

of particles from a target needs a minimum fluence power. The mean size of nanoparticles has been indicated to increase as the laser fluence increase and they are smallest when near laser breakdown threshold. Another factor that influences the efficiency and particles produced includes the lesser number (time spent on laser vaporization). Laser shots determine the morphology and concentration of the metal particles ejected in liquid. Longer times subjection to laser beams leads to increase of metal particle concentration, however, it can saturate as it absorbs light in the colloid highly concentrated metal particles. Furthermore, nanocrystals can change in shape and size depending on their interaction with the laser light that passes through. Surfactant coating terminates the production of nanoparticles by the laser ablation process. When the surfactant concentration is high, the formed nanoparticles are smaller in size than in a low concentration surfactant. One of the benefits of using laser ablation in the preparation of metal colloids as compared to other conventional techniques is that chemical reagents are absent in the solution used. Therefore, laser ablation leads to the production of pure colloids that can be more useful (Panigrahi, 2013). The disadvantage of the physical method is high costs of equipment and consumes a huge amount of energy (Iravani *et al*. 2014).

Using different method of nanoparticles synthesis produced different crystal structure or directions may reveal different chemical, physical and antibacterial properties. For instance, the (111), (100) and (110) surfaces of the face centered cubic (fcc) metal have different surface atom densities, chemical reactivity and electronics structure (Zhou *et al*. 2011; Lee *et al*. 2007). Also, It has been argued previously that the antibacterial activity of silver is greater when high atomic density facets are present such as the {111} plane (Figure 3-1) represents miller index of (111) plane.

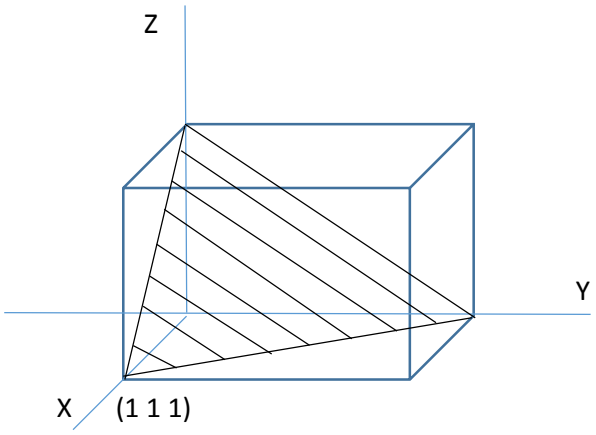

Figure 3-1: Miller indices of (111) planes

Chapter 4.

Bacterial-Nanoparticle Interactions

4.1 Antibacterial activity of metal nanoparticles

The antimicrobial applications of nanosized material from metals in a wide range of consumer goods have attracted attention owing to their distinct macroscopic characteristics (Mühling *et al.*, 2009; Ahmed, Imdad and Ashraf, 2012). Especially, metallic nanomaterials (such as gold, copper, and silver) exhibit favorable physicochemical characteristics resulting in significant levels of antibacterial activity (Vimbela *et al*., 2017). There is increasing antimicrobial application of gold nanoparticles (AuNPs), copper nanoparticles (CuNPs) and silver nanoparticles (AgNPs) in disinfectants with the view of reducing the risk of microbial common cause of outbreaks and HCAIs (Ahmed *et al.,* 2012; Mukherji *et al*., 2012; Vimbela *et al*., 2017). However, the antimicrobial activity of silver ions and silver-based compounds is extensively documented as the most effective agents against bacteria, viruses, and other eukaryotes (Ahmed *et al.,* 2012; Mukherji *et al.,* 2012). The exact mechanisms through which AgNPs confer antibacterial activity are not well known. However, it is widely documented that AgNPs exhibit antibacterial activity through bacterial inactivation and growth inhibition (Zhou *et al*., 2012). A previous study by Durán *et al.,* (2016) has demonstrated that *E. coli* treated with silver nitrate solution ($AgNO_3$) had their cytoplasmic membranes detached from the cell wall. Electron microscopy and X-ray microanalysis revealed that Ag^{2+} induced condensation of the deoxyribonucleic acid (DNA) molecules in the nucleus, thereby losing its replication ability. Furthermore, traces of Ag^{2+} were detected in the electron-dense granules and cytoplasm deposited within *E. coli* cells, detected by X-ray microanalysis. The observed morphological disruptions induced by Ag^{2+} strongly points to the antimicrobial activity of silver and silver-based compounds (Durán *et al*., 2016). Therefore, it is suggested that the mechanism of action of AgNPs is quiet similar to that of silver Ag^{2+} though speculative (Durán *et al*., 2016). However, a recent report that demonstrated the ability of *K. pneumonia* to resist Ag ions with the presence of operons for resistance against Ag and Cu ions indicated that the toxicity may not due to the silver or copper ions but mainly depend on NPs (Acharya *et al*., 2017). The inhibition of the bacteria is due to physical mutilation by the NPs as a result of direct interaction of NPs with bacteria cell.

It has been demonstrated in a previous study that surgical masks coated with AgNPs have antimicrobial activity against the Gram-negative *E. coli.* This strongly suggesting that AgNPs used as surface coatings on personal protective equipment and clothing is likely to minimize risk of transmission of the infectious bacteria including *E. coli* and *Enterococcus* (Perelshtein *et al*., 2016).Similarly, in an earlier study (Pal *et al.,* 2007), Luria–Bertani (LB) growth medium were applied on solid and liquid agar systems and then supplemented with different concentrations of AgNPs (0-50µg mL^{-1}). The agar systems were then inoculated with 5 $Log_{(10)}$ of *E. coli* and incubated at 37 ˚C for 24 hours. Scanning and transmission electron microscopy (SEM and TEM) were used to examine the bactericidal activity of AgNPs, where it was observed that the cell walls of *E. coli* cells were damaged characterised by numerous perforations.

Importantly, the numbers of observed *E. coli* colonies were reduced with increasing concentrations of AgNPs ranging from 10-100 μg/mL, suggesting a dose-response relationship in the antibacterial activity of AgNPs. A 100% inhibitory effect of AgNPs was observed at concentration of 50–60 μg/mL (Sondi and Salopek-Sondi, 2004). Similar findings were observed in recent studies where AgNPs exhibited 90-100% inhibition of *E. coli* at a minimum inhibitory concentration (MIC) of 100μg/mL (Pal *et al.,* 2007; Wang *et al.,* 2012).

Although gold, silver and copper NPs have exhibit strong putative antibacterial activity (Zhou *et al.,* 2012; Wani, Ahmad and Manzoor, 2013). In a recent study, antibacterial activity of AgNPs and AuNPs were compared with respect to the survival of *E. coli* (ATCC 35218) cells in aqueous suspensions. It was demonstrated that AgNPs treatments, completely inactivated *E. coli* cells with a 5-$Log_{(10)}$ reductions (Dror-Ehre *et al.,* 2009). The antibacterial activity of AgNPs treatment exhibited a dose-response relationship as demonstrated previously by Sondi and Salopek-Sondi (2004). However, AuNPs did not exhibit any inactivation ability against *E. coli* cells (Dror-Ehre *et al.,* 2009). Similarly, a previous study demonstrated that treatment of 10^5-10^6 CFU/ml of *S. aureus* and *E. coli* with 0.2 ppm Ag^{2+} solution resulted in a more than 5-$Log_{(10)}$ CFU/mL reductions of these bacteria after 90 minutes, which also exhibited a dose-response relationship (Jung *et al.,* 2008).

Furthermore, it was recently demonstrated that *E. coli* and *S. aureus* are highly sensitive to the antimicrobial activity of AgNPs as compared to CuNPs (Ruparelia *et al.,* 2008; Mukherji *et al.,* 2012). Energy-dispersive X-ray spectral analysis of AgNPs and CuNPs has revealed that CuNPs have oxide layers, which putatively degrade the antimicrobial power of CuNPs (Ruparelia *et al.,* 2008). This explains why CuNPs have lower antimicrobial activity as compared to AgNPs, and suggests that the antibacterial activity of NPs primarily vary depending on the metal and the oxidisability NPs (Dror-Ehre *et al.,* 2009; Ruparelia *et al.,* 2008; Van Dong *et al.,* 2012).

It is demonstrated that the size of NPs effect their antibacterial activity. For instance, AgNPs of 5nm exhibit higher antibacterial activity when compared to 15nm and 55nm particles in Gram-positive and Gram-negative bacteria (Z. Lu, Rong *et al.,* 2013) owing to their high surface area to volume ratio (Dror-Ehre *et al.,* 2009; Van Dong *et al.,* 2012). This suggests that the degree of antimicrobial activity of various metal NPs such as AuNPs, CuNPs and AgNPs is not uniform as there are additional multifaceted dimensional factors in play. Furthermore, it is extensively documented that the antimicrobial activity of NPs is dependent on various nanoshapes, implying that not all nanoshapes of NPs have desirable antimicrobial activities (Pal *et al.,* 2007; Van Dong *et al.,* 2012). This warrants careful determination of NP shapes with optimal antibacterial activity. Recent studies for instance, have demonstrated that AgNPs

exhibit antibacterial activity in a shape-dependent manner (Pal *et al.* 2007; Van Dong *et al.* 2012). To elucidate this claim, the Gram-negative *E. coli* cells were subjected to the triangular AgNPs with a {111} lattice plane as the basal plane, spherical AgNPs, rod-shaped AgNPs and Ag^{2+}(in form of $AgNO_3$). The truncated triangular AgNPs with a {111} lattice plane exhibited strong antibacterial activity against *E. coli* as compared to the other nanospheres and nanorods (Pal *et al.* 2007). For instance, triangular AgNPs exhibit *E.coli* inhibition at 1 μg however, 12.5 and 50 to 100 μg of spherical and rod NPs was required respectively (Sadeghi *et al.*, 2012).

These findings are consistent with those from a previous work by Van Dong *et al.* (2012) where sharp-edged triangular silver nanoprisms with sharp vertexes exhibited enhanced antibacterial activity against *E. coli* as compared to the spherical AgNPs. The zone of inhibition of triangular nanoprisms was 1.3cm higher than the inhibition of spherical AgNPs 0.5cm (Van Dong *et al.*, 2012). These strongly support that the effectiveness of NPs as antibacterial agents is multifaceted with respect to the nature of the mental element, nanosizes and nanoshapes of the prepared NPs.

While AgNPs with the putative {111} lattice shapes confers enhanced antimicrobial activity, it is also evident that the shape choice of AgNPs determine different range of nanosizes (Van Dong *et al.*, 2012) for example, it was possible to obtain spherical AgNPs with nanosizes of 4, 21 and 40 nm on average, while nanosizes of AgNPs with {111} lattice planes were obtained only in a range sizes of 25-400 nm. Therefore, establishing the order or criteria for prioritising dimensional metrics of NPs is likely to guide optimization of antimicrobial activity of NPs. For instance, selection of sharp-edged triangular nanoprisms with the smallest possible nanosizes gives high surface area to volume ratio, which is likely to confer optimised antibacterial activity of NPs. It is clearly evident that shapes of NPs have significant influence on the antimicrobial activity of the prepared NPs. Therefore, the first priority of developing effective NPs is shape of {111} lattice followed by the smallest possible NP nanosizes.

The attractiveness of AgNPs nanoparticles as antimicrobial agents is influenced by prevent development of resistance to metals in the naturally existing infectious bacteria (Singh *et al*., 2013). Mühling *et al.*, (2009) demonstrated that releasing AgNPs into estuarine (marine) water does not indirectly induce antibiotic resistance among the existing bacteria in sediments. A 50 days exposure was carried out to examine the effects of AgNPs on the antibiotic resistance of bacteria in sediments from an estuary in southwest England, sediment samples were plated after the exposure time in the presence of bacteria resistant to eight altered antibiotics. The study shows no increase in antibiotic resistance between the bacterial populations in the sediment even in the presence of AgNPs. This strongly suggests that the use of AgNPs in water treatment is less likely to induce antibiotic resistance in the existing microbial population.

Synergistic effect of AgNPs with antibiotic such as (cephalexin) against *E. coli* shows enhancement of the antibacterial activity of the antibiotic, the minimum inhibitory concentration decreasing from 300µg to 200 µg when using AgNPs and cephalexin conjugated AgNPs (Singh *et al*., 2012).

However, potential health and environmental risks associated with these emerging nanomaterials in consumer goods are not well delineated (Kim *et al.,* 2011). However, a recent study has suggested that human exposure to NPs can not only induce inflammatory responses and oxidative stress but also impair epithelial barrier functions, thereby increasing vulnerability to pulmonary infections (Kim *et al.,* 2011).

4.2 *Escherichia coli* as a Model Organism for Studying Bacterial-Nanoparticle Interactions

Escherichia coli inhabit human intestines, they are rod-shaped filamentous bacterium with an average length, width and volume ranges of between 1.6-3.1 µm, 0.7–1.1 µm and 0.5–4 μm^3, respectively as shown in Figure 4.1 (Volkmer & Heinemann, 2011). There are several types of *E. coli* strains, which form part of the normal microflora of animal and human intestines, and are therefore harmless. However, there are few strains of *E. coli* known to be virulent and infectious, causing bowel discomforts especially travellers and bloody diarrhea including nausea or vomiting (Muniesa *et al.,* 2012). The most infectious *E. coli* serotype is *E. coli O157:H7,* which causes bloody diarrhea and severe abdominal cramps. The Shiga-like toxin excreted by *E. coli O157:H7* affects renal endothelial cells, thereby causing haemolytic uremic syndrome (HUS) (Muniesa *et al.,* 2012). HUS is characterised by morphological impairment of renal vascular systems, thereby causing clogging of blood cells in kidney nephrons, thrombocytopenia (deficiency of blood platelets) causing renal tissue bleeding, which subsequently result in renal impairment and kidney failure (Loirat and Frémeaux-Bacchi, 2011; Muniesa *et al.,* 2012; Hammerl *et al.,* 2012).

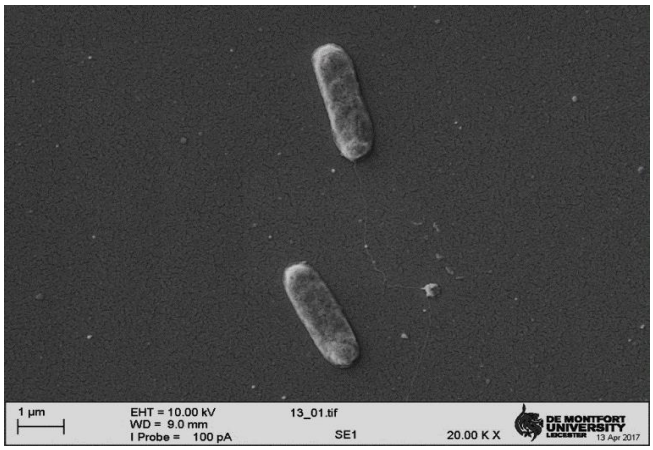

Figure 4- 1: Scanning electron microscope image of rod-shaped *Escherichia coli*, with an average length, width and volume ranges of between 1.6-3.1 µm, 0.7–1.1 µm and 0.5–4 μm^3 respectively.

It also causes urinary tract infections and bacteraemia. In August 2009, an outbreak of *E. coli O157* occurred among visitors to Godstone animal farm in Surrey. Public Health England established that the outbreak of *E. coli* infections were due to visits to the open animal farm (HPA, 2013). In this regard, intestines of farm animals especially sheep, cows and swine harbour high bacterial reservoir including *E. coli O157:H7* (Callaway *et al.*, 2013). A recent report of NHS trusts in England of *E. coli* bacteraemia shows 38,132 cases reported between 1 April 2015 and 31 March 2016 (NHS, 2017). This strongly points to the significance of *E. coli* infections in the UK and calls for improved screening for these infectious pathogens in food, water, and open animal farms (HPA, 2017).

4.3 *Enterococcus faecium* as a Model Organism for Studying Bacterial-Nanoparticle Interactions

Enterococci are Gram-positive, oxidase- and catalase-negative, non-spore-forming, lactic acid bacteria (facultative anaerobe) with cell sizes of up to 1.0 µm (Figure 4-2). Enterococci can occur as single cocci or in chains (streptococci), but frequently occur as diplococci (Naser *et al.* 2005; Fisher & Phillips, 2009). They thrive well at wide range of temperature (5-50 ^{o}C); where their optimum, maximum, and minimum growth temperatures are 42.7, 6.5, and 47.8 ^{o}C, respectively under aerobic conditions. They also thrive well in a wide range of pH conditions (4.6–9.9), with optimal pH of 7.5 (Fisher & Phillips, 2009). Being non-food lactic acid bacteria, *Enterococci* produce a wide range of bacteriocins (enterocins), where some are toxic to humans. Like *E. coli*, *Enterococci* are ubiquitous in animal and human gastrointestinal tracts. *E. faecalis* and *E. faecium* are the most prevalent *Enterococcus* species, where *E. faecalis* accounts for over 90% of clinical isolates (Macovei & Zurek, 2006; Palmer, Kos and Gilmore, 2010). Clinical isolates of *Enterococcus* species have the highest virulence followed closely by food isolates and then starter probiotic strains. Their virulence is influenced by their respective profiles of hydrolytic enzymes (Ribeiro & Oliveira, 2011).

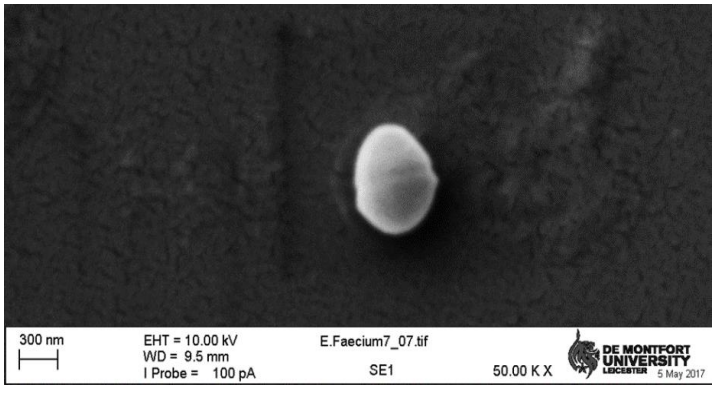

Figure 4- 2*: Enterococcus faecium* is diplococcus bacteria. Gram-positive, oxidase- and catalase-negative, non-spore-forming, lactic acid bacteria with cell sizes of up to 1.0 µm.

In terms of food safety, *Enterococci* pose a high risk in ready-to-eat (RTE) food products especially RTE dairy and meat food products, including raw produce (Macovei & Zurek, 2006). *Enterococci* often cause gastrointestinal infections, urinary tract infections, hepatobiliary sepsis, endocarditis, hospital acquired infections especially nosocomial bacteremia and surgical wound infection. Therefore, *Enterococci* are frequently implicated in nosocomial infections (Murray, 1990; Fisher & Phillips, 2009; Palmer *et al.,* 2010).

Although there is a wide range of antibiotics for treatment of *Enterococci* infections, treatment of *E. faecalis* presents a significant challenge owing to its phenotypic resistance against antibiotic treatments involving common antibiotics especially tetracycline, penicillin, streptomycin, erythromycin, rifampin, fluoroquinolones, ciprofloxacin, and kanamycin (Palmer *et al.*, 2010). Importantly, the bacterium is highly resistant to two glycopeptide-based antibiotics (vancomycin and teicoplanin) licensed in the UK (Fisher and Phillips, 2009). This has resulted in a significant decline in the number effective antibiotics against human infections involving *E. faecalis* (Macovei & Zurek, 2006). 42% of *Enterococcus spp* were reported in UK, *E. faecalis* identified as the most frequently *Enterococcus spp* in 2016 (n=3,177/7,501) followed by *E. faecium* was the second most frequently identified *Enterococcus spp* (33%; n=2,871/7,501) (HPA, 2017). In addition, it has been observed that *E. faecalis* is capable of transferring its genetic elements of antibiotic resistance horizontally to other infectious bacterial species occurring in the human body (Macovei & Zurek, 2006; Palmer *et al.,* 2010). This further increases the risk of antibiotic resistance in other infectious bacteria occurring in the human body.

There are various methods for screening *E. coli* and *Enterococci* in food and drinking water, which include but not limited to the conventional biochemical screening, Vitek Immunodiagnostic Assay System (VIDAST), and-Real-time PCR Screening (Petersen, Bisgaard & Christensen, 2010; Burns *et al.,* 2011; Temelli, Eyigor & Anar, 2012). The conventional biochemical screening can be timely due to it involving lengthy biochemical reactions to test for the presence of these bacteria in colonies cultured from suspicious food and water samples (Burns *et al.,* 2011). On the other hand, VIDAST and Real-time PCR Screening methods offer rapid screening for various serotypes of *E. coli* including *Enterococcus* in food and water samples (Petersen, Bisgaard & Christensen, 2010; Burns *et al.*, 2011; Temelli, Eyigor & Anar, 2012).

The ubiquitous, virulence, and antibiotic resistance nature of *E. coli* and *Enterococci* necessitates effective infection control of these microorganisms. There is increasing evidence of antimicrobial activity of metallic nanoparticles against a wide range of bacteria species including infectious strains of *E. coli* and *Enterococci*. Metal nanoparticles well known for their highly potent antibacterial effect, include silver (Ag), gold (Au), copper (Cu), copper oxide (CuO), iron oxide (Fe3O4), titanium oxide (TiO2) and zinc oxide

(ZnO). Most metal nanoparticles exhibit bactericidal activities due to reactive oxygen species (ROS) generation although some are effective through their physical structure and metal ion release. *E. coli*, as a representative of Gram-negative bacteria, Ag nanoparticles were shown to cause "pits" in the cell wall by increasing the membrane permeability and inactivating the respiratory chain (Beyth & Houri-Haddad, 2015).

The two different cell wall types can be identified in the laboratory by a variance stain known as the Gram stain, Gram-negative bacteria will stain pink whereas Gram-positive bacteria will stain purple, schematic comparison of structure of Gram-positive and Gram-negative cell walls is shown in Figure 4-3 (Atanasova, 2010). Gram-positive cell walls consist of one layer of lipid plasma membrane and a thick peptidoglycan layer connected with lipoteichoic and teichoic acids, while Gram-negative bacteria have an outer and an inner cell membrane and only a thin layer of peptidoglycan in the periplasmic space between the outer and inner membrane. The outer membrane of Gram-negative bacteria contains lipopolysaccharide (Atanasova, 2010).

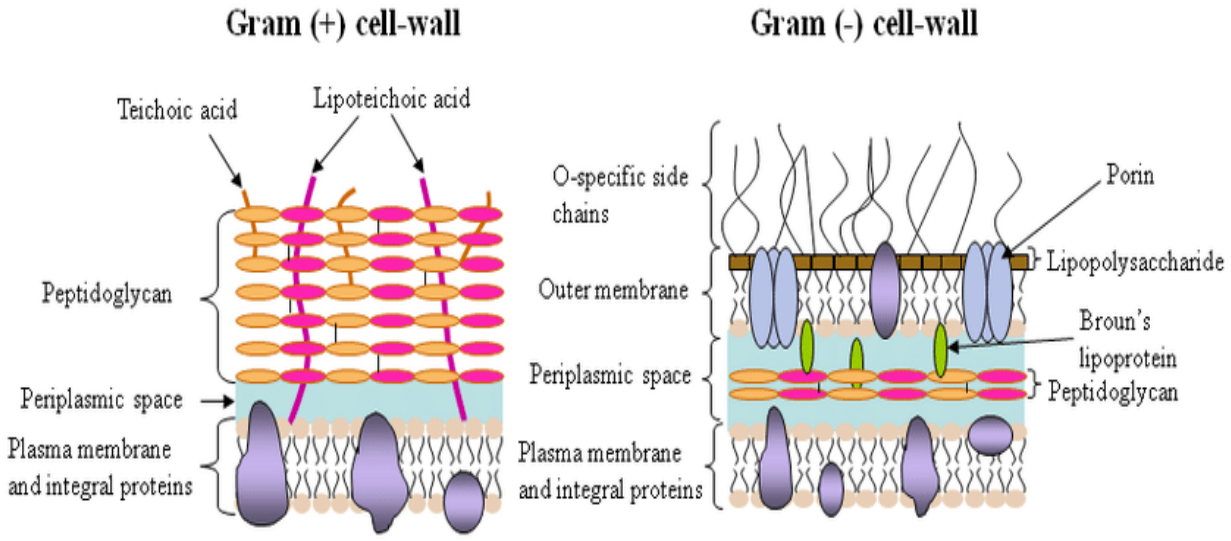

Figure 4-3: Schematic structure of Gram-positive and Gram-negative cell walls. Gram-positive cell walls consist of one layer of lipid plasma membrane and a thick peptidoglycan layer connected with lipoteichoic and teichoic acids, while Gram-negative bacteria have an outer and an inner cell membrane and only a thin layer of peptidoglycan in the periplasmic space between the outer and inner membrane. The outer membrane of Gram-negative bacteria contains lipopolysaccharide layer lining in it (Atanasova, 2010).

4.4 Antibacterial Applications of Nanoparticles

4.4.1 Wound Dressing

There is an increase in the application of silver wound dressings. Noteworthy is that these antibacterial products are available commercially (Jeeva *et al*., 2014). For example, silver or copper disposition technology aids in the development of antibacterial agents. Wound dressings are designed either to afford a constant source of silver ions for delivery into the wound up to seven days to maximize bacterial inhibition, or Ag^{+}ion were deposited to the dressing material and utilize their antibacterial activity on discharge being drawn out of the wound by the result of the dressing (Wilkinson *et al*., 2011). A concentration of 1 μg/ml of Ag^{+} is assumed to be attainable in wound exudate exposed to other Ag-treated dressing. A previous report suggests that 1ppm silver is sufficient to obtain bactericidal action. AgNPs-based dressing, Acticoat™ Flex 3, has been applied to a 3D fibroblast cell culture in to real burn patient and *in vitro*, the result show that AgNPs significant reduce mitochondrial activity, whereas cellular staining methods demonstrate that nuclear integrity is retained, with no signs of cell death (Rigo *et al*., 2013).

4.4.2 Coated Textile Fabrics

Textile taken through antimicrobial treatment performs several functions apart from being active against microorganisms. For instance, the textile is suitable for purposes such as textile processing to improve durability in laundering, hot pressing, and dry-cleaning processes (Lee *et al*., 2014). An example of such antibacterial agents is Zn-CuO nanoparticles has been used for coated textile fabrics were shown strong antibacterial activities at the end of the process even after 65 cycles washed in hospital washing machines (75 or 92 °C) (Perelshtein *et al*., 2016).

4.4.3 Coated Medical Devices

Antibacterial substances are common in the coating of medical devices to prevent infestation by bacteria. In particular, the coating of the device is achievable using either copper or silver. The coating such as the silver coating in most devices aids in the prevention of diseases (Ouyang *et al*., 2013). The use of silver nanoparticles on the exterior of the medical devices can preclude bacterial adhesion and a consequent biofilm development. Coated textiles can also serve as medical devices because they have undergone processing to improve their performance in disease prevention especially when the antibacterial coating encounters a pathogen (Perelshtein *et al*., 2013). An example of such antibacterial agents is titanium nanotube loaded with AgNPs were inhibit the growth of *Pseudomonas aeruginosa, E. coli* and *S. aureus* when used for implants. Also, AgNPs coated catheters have shown a strong antibacterial activity against *E. coli* even After 30 days of soaking in high water flow (De Giglio *et al*., 2013; Pollini *et al*., 2011).

4.4.4 Drug Delivery

Nanoparticles are mostly applied as antibacterial drug carriers, nano-based formulations of different antibacterial drugs have been revealed to improve either antibacterial activates or pharmacokinetics by reaching sustained release directly at the infection site. An example of such antibacterial agents is ciprofloxacin from polyvinyl alcohol based iron oxide nanoparticles were inhibited *E. coli* growth for the purpose of drug delivery alongside with antibacterial activity (Cover *et al*., 2012; Bajpai *et al*., 2011).

4.4.5 Water Disinfection

Titanium dioxide NPs is used for water disinfection because it is stable in water, non-toxic by ingestion and low cost. The efficiency of TiO_2 have demonstrated potential of TiO_2 for drinking water disinfection. In the recent year, it was revealed that doping TiO_2 with silver NPs strongly improved photocatalytic bacterial inactivation by UV-activated TiO_2. It can be used either as a suspension in a slurry UV reactor, a membrane filter or a thin film coated on a reactor surface (Li *et al*., 2008).

4.4.6 Food Preservation

To prevent the development of detrimental microorganisms in the diet, one can add antimicrobials into the product formulation either coated on the surface or fused into the wrapping material (Velmurugan *et al*., 2014). The author further added that the incorporation antimicrobials into the wrapping material enable them to offer an immediate short-term decrease of bacterial populations. However, the antimicrobial films can maintain a prolonged activity.

The increasing demand for expand fresh food shelf life along with the need of protection against foodborne diseases enhanced the development of antibacterial food packaging. Through the most effective methods, the combination of (organic-inorganic) packaging such as polymers loaded metal nanoparticles proved to be highly effective. AgNPs have anti-fungi, anti-yeasts, anti-viral and antibacterial activity and can be combined with both edible and non-degradable polymers for effective food packaging. Food containers coated with AgNPs are an inventive concept in effective food packaging to increase the food shelf life and the quality upkeep. The fresh food shelf life such as, dairies products, meat and fruit are significantly raised by biocide effects against *E. coli*, *Pseudomonas spp*, *S. aureus*, *L. monocytogens* and *Salmonella* (Carbone *et al*., 2016).

Chapter 5.

Nanoparticles characterisation methods

5. Characterisation methods of nanoparticles

In this study, all nanoparticles were characterised using ultraviolet/visible spectroscopy (UV-Vis), scanning electron microscopy (SEM), energy-dispersive X-ray (EDX) spectroscopy, X- ray diffraction (XRD) and transmission electron microscopy (TEM), to confirm the presence of NPs and identify the morphology, elemental analysis, crystalline nature and lastly TEM to obtain selected area electron diffraction (SAED) data for assignation of the crystalline nature and high resolution transmission microscopy (HRTEM) for elucidation of the d-spacing of the lattice fringes. The absorbance of the colloidal solution (1mg of powder NPs was dissolved in 4ml of DI water) was recorded using a UV-visible spectrophotometer (Evolution 300 UV-VIS) in the wavelength range 300nm to 1000nm. SEM and EDX investigations were undertaken on NPs dispersed onto silicon substrates using a LEO S430; and the NPs of both types were deposited onto glass substrates for examination via XRD (Bruker D8 Advance diffractometer). TEM samples were prepared by deposited the NPs onto copper grid.

5.1 UV-Visible Spectroscopy

This is a characterisation technique used to obtained information about the absorbance, transmittance and reflectance spectra with respect to the wavelength of a material by using ultraviolet and visible light from electromagnetic radiation. In this technique, extinction in terms of scattering and absorption can also be obtained when light travels through a biomolecules that consists of nanoparticles. The unique optical properties possess by nanoparticles can be related to a localised surface plasmon resonance which is the collection of electrons oscillating in the conduction band of the nanoparticles (copper, gold or silver) in resonance with a particular wavelength of the light incident on the sample (Shang & Gao. 2014) .

In view of this, ultra-violet visible spectroscopy is a useful tool for the identification, characterisation and studying of nanoparticles in a sample. In Figure 5-1, a beam of light from ultraviolet-visible light source is been separated by diffraction grating or prism into their respective wavelengths (Hafdallah, 2007). Every one of monochromatic beam of light is then split into a two equal intensity by a half-mirrored device. One of the beam passes through a cuvette (transparent) containing the sample to be measure while the other beam passing through a reference cuvette that consist of de-ionised water.

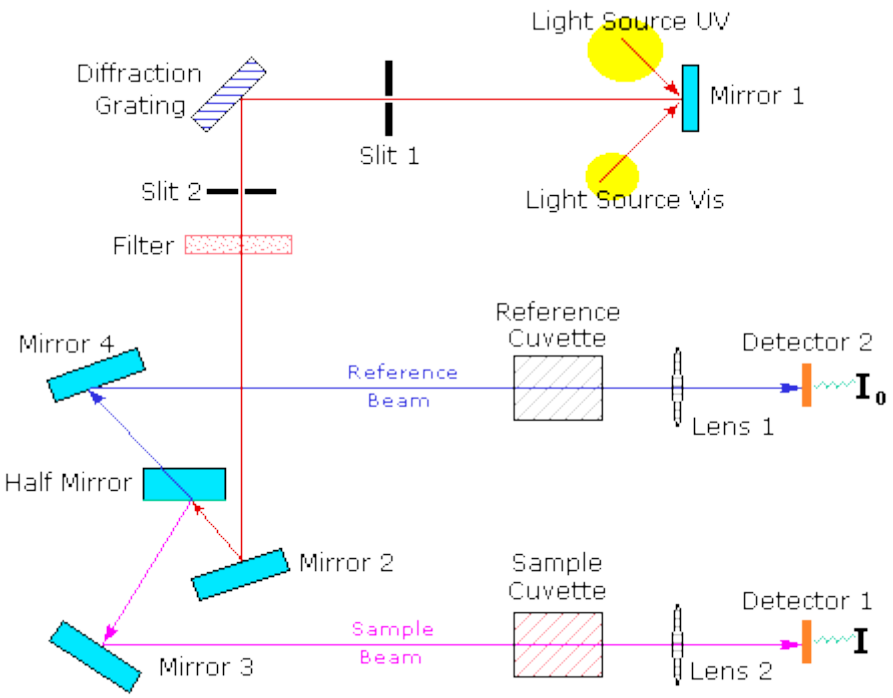

Figure 5-1: Schematic diagram of spectrophotometer (Hafdallah, 2007).

This intensity of light (I), when light beams passes through the sample or material, compare to the intensity of light passing through the reference sample (I_o) by electronic detector in the spectrophotometer and recorded in term of transmittance as expressed in equation 5.1. 1

$$T\ (\%) = \frac{I}{I_o} \ldots\ldots\ldots\ldots\ldots\ldots\ldots\ldots\ldots\ldots\ldots \ 5.1.1$$

Where T is the transmittance expressed in percentage.

The relationship between absorbance and transmittance can be expressed as:

$$A = -\log T \ldots\ldots\ldots\ldots\ldots\ldots\ldots\ldots\ldots\ldots\ 5.1.2$$

Solution with metallic nanoparticles such as gold, silver, titanium interacts strongly with light form ultra-violet visible region at particular or specific wavelength. A unique extinction (absorption and scattering) peaks on several spectra exists, which can be used to determine the concentration of nanoparticle by using Beer-Lambert law as expressed in equation 5.1.3 (Cytodiagnostics, 2018).

$$A = \varepsilon bc \ldots\ldots\ldots\ldots\ldots\ldots\ldots\ldots\ 5.1.3$$

Where A = absorbance, ε = molar extinction coefficient ($M^{-1}cm^{-1}$), b = path length of the solution sample (cm), c =concentration of nanoparticles in solution sample (M).

Surface Plasmon Resonance

SPR is the starting point of various standard instruments for the measurement of adsorption of materials onto the planar metallic surface (Au and Ag) or surface of metal nanoparticles and serves as the basic principle behind various colour-based biosensor applications (Pranveer, 2014).

The principle of surface plasmons can be best described by Kretschmann configuration as shown in Figure 5-2. Where a metal thin film (like gold or silver) placed at the interface of two dielectric media, in which the refractive index of medium 1 (prism) is greater than the refractive index of medium 2 (air or solution) ($\eta_1 > \eta_2$). In this technique, a plane parallel polarised light incident from medium 1 to the medium 2, in which the total internal reflection occurred in medium 1 (i.e. the angle of incidence (θ)is greater than the critical angle (θ_c)). At medium 2, evanescent waves formed with the total internal reflection condition, these waves is increased, travelled through the gold film and exist in the second medium. The magnitude of these waves is expressed in equation 5.1.4 (Shang & Gao. 2014; Pranveer, 2014).

$$k_{evan.||} = \frac{2\pi}{\lambda}\eta_1 \sin(\theta) \text{..... Equation 5.1.4}$$

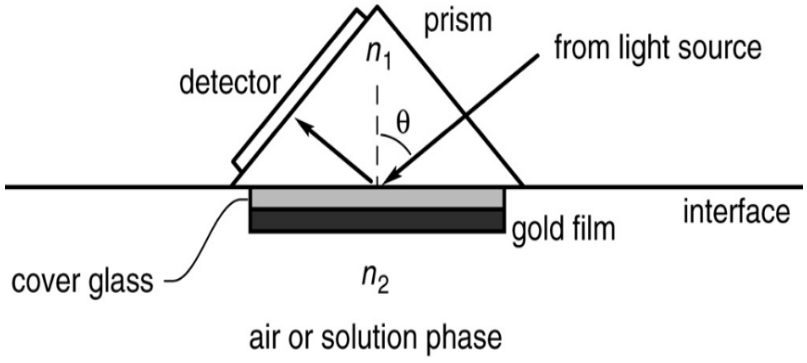

Figure 5-2: Schematic diagram of Surface Plasmon Resonance (Shang & Gao, 2014).

Where $k_{evan.||}$ is the component of the evanescent waves vector parallel to the interface, θ is the angle of incidence, λ is the wavelength of the incident light and η_1 is the refractive index of the glass prism. The wave propagation confined at the gold thin film – dielectric interface are quantized with wave vector magnitude of the surface plasmon. This is in relation to the dielectric constant of both the medium 2 and the gold thin film. If the media is non – absorbing, the dielectric constant (ε) is the same as the square of the refractive index ($\varepsilon = \eta_2^2$). The wave vector of the surface plasmon is given in the equation 5.1.5.

$$k_{sp} = \frac{2\pi}{\lambda}\sqrt{\frac{\eta_2^2\eta_g^2}{\eta_2^2+\eta_g^2}}$$ .....Equation 5.1.5

When the intensity of the light (reflected) decrease, decays in the excited surface plasmon is experienced and photons or phonons is also being converted leads to the phenomenon called surface plasmon resonance. The equality of equation 5.1.4 and 5.1.5 leads to the expression of equation 5.1.6 and θ_{SPR} is the angle required for the resonance (Shang and Gao, 2014).

$$\theta_{SPR} = \sin^{-1}\left(\frac{2\pi}{\lambda}\sqrt{\frac{\eta_2^2\eta_g^2}{\eta_2^2+\eta_g^2}}\right)$$ .....Equation 5.1.6

The adsorption and desorption on the gold thin film surface changes with respect to the refractive index of medium 2 near the gold thin film – dielectric interface as the resonance angles also change.

Localised surface plasmon resonance

It has been established that the frequency of beam of light incident on a material matching the natural frequency of the valence or outer electrons oscillate against the restoring force of positive nuclei. In a solution that consists of metallic nanoparticles such as gold and silver, SPR is referred to as Localised surface plasmon resonance (LSPR). The change in size, shape and composition of nanoparticles makes the light response to change or tuned from ultraviolet through visible to near infra-red regions of electromagnetic spectrum as shown in Figure 5-3 (Nanocomposix, 2018).

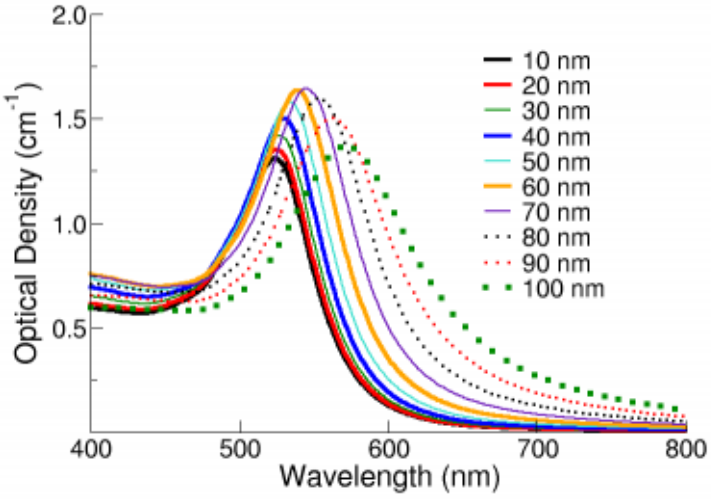

Figure 5-3: Extinction spectra of gold nanoparticles with diffrent diameters (10-100) at mass concentrations of 0.05mg/ml (Nanocomposix, 2018).

A solution with smaller nanoparticles or nanospheres absorb more light and have peak close to 520nm while larger nanoparticles display an increase in scattering as the peaks widen significantly and have red shift on the wavelengths.

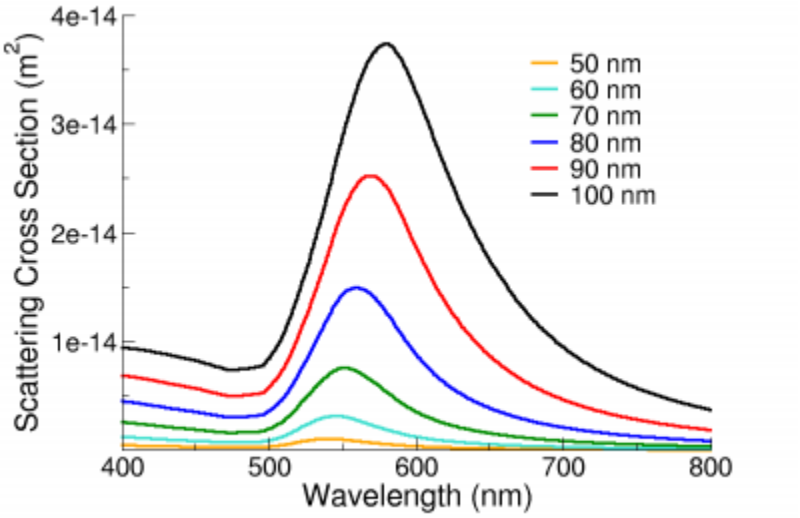

Figure 5-4: Scattering spectra of various diameter nanoparticles (Nanocomposix, 2018).

The larger nanoparticles scatter huge light incident on the solution due to larger optical cross sections and the ratio of scattering total extinction (albedo) also increases with nanoparticles size as shown in Figure 5-4 (Nanocomposix, 2018).

In this work, Thermo Scientific Evolution 300 UV-Vis double beam spectrophotometer shown in Figure 5-5 was used. The de-ionzed water was used to obtained background spectrum, solution samples are scanned and spectra data collected in reference to wavelengths at room temperature (300 K) respectively.

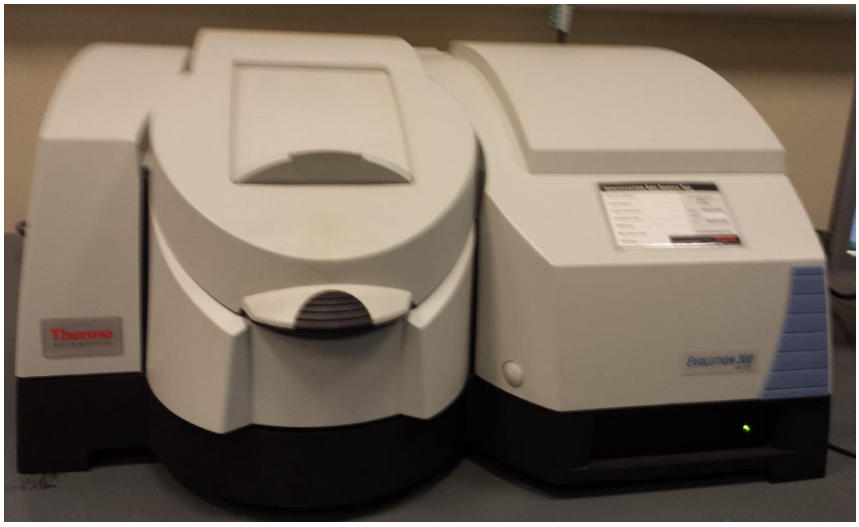

Figure 5- 5: Thermo-Scientific Evolution 300 UV-Vis double beam spectrophotometer.

5.2 Scanning Electron Microscopy

This is a technique used to investigate the nanostructures or nanoparticles present in a solution by using high beams of electron in order to reveal the morphological structure of the particles or structures. Scanning electron microscope (SEM) is a versatile and powerful tool to investigate and reveal the structure of material with high resolution at the nanoscale in a vacuum. SEM comprises of electron gun, accelerating anode, focusing and scanning magnets, secondary electron detector, backscattered electron detector and sample stage is shown in Figure 5-6 (Anon, 2018).

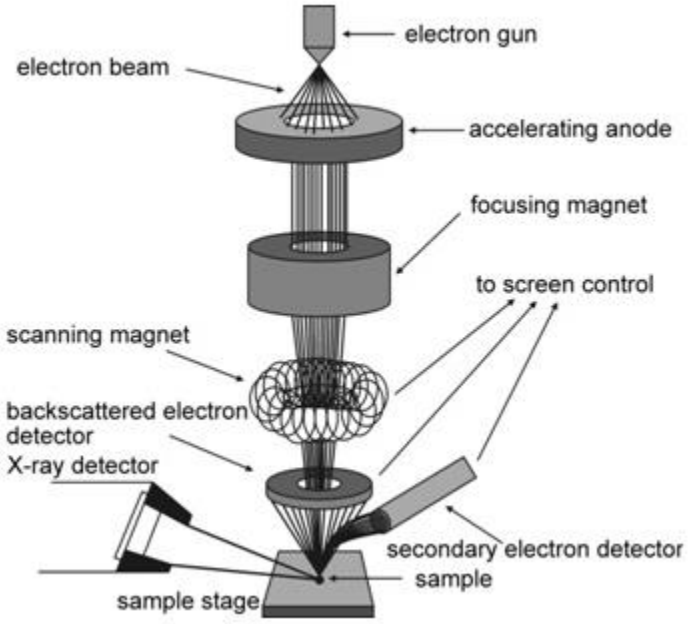

Figure 5-6: Scanning electron microscope set up (Anon, 2018).

A beam of electron is produced by thermal source (tungsten wire) or field emission by the electron gun. The electron beam is accelerated vertically through high voltage between 20 to 30 KV and pass through electromagnetic fields and lens to produce a thin beam of electron (Anon, 2018). The thin beam of electron focuses on the sample. As the beam incident on the sample, the electrons interact with the sample (scanning line by line and point by point) and scattered. There are two types of scattering (inelastic and elastic) occur during the interaction of the electron beams with the sample. Inelastic scattering occurs, when there are slight trajectory changes in which the energy lost due to the interaction of the beam electron with the sample electron. This scattering produces x-ray photon, secondary electrons and backscattered electrons and focus on the detectors place above the sample. The elastic scattering occurs as the electron trajectory changes as the kinetic energy and velocity remain constant.

The x-ray produce in the microscope as a result of interaction between the photons and the sample electrons give information about the elemental composition of the sample (energy dispersive x-ray spectrometry (EDS)), the backscattered electrons produces information about the composition of the sample and secondary electrons gives information about the surface and topography of the sample.

In this work, Carl-Zesiss EvoHD 15 and Leica S430 were used for the morphological (surface and topography), compositional and elemental of the samples under the investigation.

5.3 X-ray diffraction

This is a powerful, fast and non-destructive technique employed to characterize nanomaterial or nanoparticle in a sample by displaying the crystallographic information such as crystal size, thin film layer thickness, lattice strain, dislocation generation, roughness, orientation, dopant segregation, layer thickness fluctuations, layer tilting and distortion of material (EAG Laboratories, 2018). This technique is also referred to as x-ray crystallography and the instrument used for this technique is referred to as X-ray diffractometer. In Figure 5-7, diffractometer consist of three basic components; X-ray tube, sample holder and X-ray detector (Ksanalytical.com, 2018).

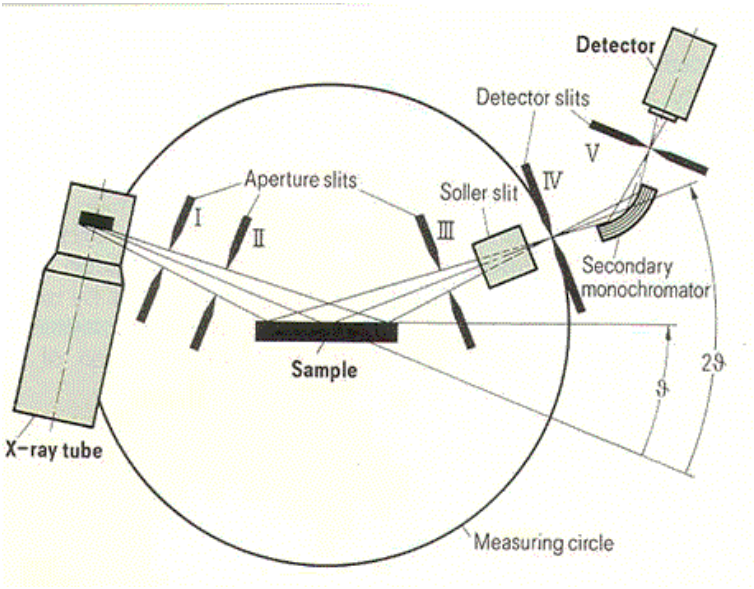

Figure 5-7: Schematic diagram of X-ray diffractometer (Ksanalytical.com, 2018).

From the x-ray tube, a highly energetic beam of x-rays of specific wavelengths at specific angle incident on the sample through aperture slits as some of the inner shell electrons of the sample is dislodged. Several beams of reflected x-rays are produced, as the wavelength of the beams of scattered x-rays was in constructive interference mode. The occurrence of interference leads to the beams of diffracted x-rays leave the surface of the sample at an equal to the angle of incident of beams of x-ray and diffraction angle which is twice that an angle is detected.

A sample with a crystal lattice planar at particular distance (d), beams of x-rays of a specific wavelength incident on the planes at angles, the path of the rays corresponding to the diffracted rays can be recorded as ABC and $(ABC)^{'}$ such that it acts as an integer multiple of wavelength. These integers lead to constructive interference due to combination of the wavelength, angle of incident and the interplanar spacing of the crystal lattice of the sample as shown in Figure 5-8.

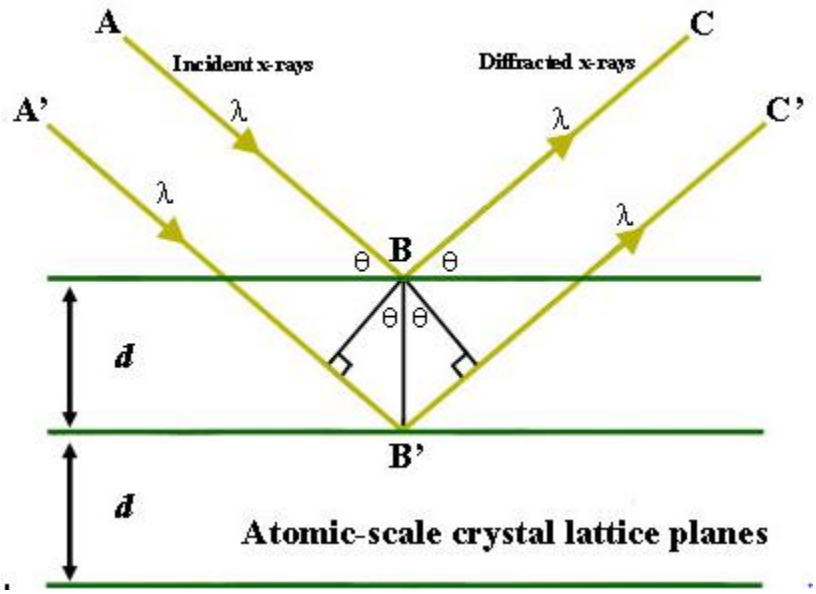

Figure 5-8: Bragg's law demonstration (Geochemical Instrumentation and Analysis, 2018).

The relationship between interplanar spacing, wavelength of the incidents rays and angle of incidence is known as Bragg's law (5.3.1):

$$n\lambda = 2d \sin\theta \ldots\ldots\ldots\ldots\ldots\ldots\ldots\ldots\ldots\ldots\ldots\ldots\ldots\ldots\ldots\ldots\ldots\ldots 5.3.1$$

Where n is an integer that depends on the number of reflected rays, λ is the wavelength of the incident rays, d is the interplanar spacing and θ is the angle of incidence. The collections of the reflected rays are used for the identification of the crystalline nature of a sample by solving Bragg's law equation (Crystalimpact.com, 2018). Also, the d-spacing (spacing lattice) can be calculated.

Furthermore, the crystal size of nanoparticle can also be calculated using debye-scherrer expression as shown in equation 5.3.2.

$$B(2\theta) = \frac{K\lambda}{L\cos\theta} \ldots\ldots\ldots\ldots\ldots\ldots\ldots\ldots\ldots\ldots\ldots\ldots 5.3.2$$

Where L is the average size of the crystalline particles, λ is the wavelength of radiation or incident ray in this study, a wavelength of copper source (0.1541 nm) were used, θ is the peak position and β is the full width half maxima (FWHM) or peak width was calculated from XRD graph using Origin 2017 software. In this study, Bruker D8 Advance diffractometer were used.

5.4 Transmission electron microscope

This is a technique of using transmission of a beam of electrons to image the inner part of a sample for high magnification. The principle of operation is similar to light microscope except high voltage transmission of electrons beam is used for the imaging. TEM is capable of operating in both imaging and diffraction mode as required by the nature of the sample (low thickness and highly transparent) (Encyclopedia Britannica, 2018). As shown in Figure 5-9, high energy electrons of about 30 KV produced by electron gun accelerated and focused on to the sample through condenser lens. The essence of anode in the instrument is to help in converging negatively charged electrons on to the sample through condenser. For nanoparticles imaging, the technique is prefer due to it higher resolution as the grain size and distribution, particle size and morphology of the sample can be determine using copper grid coated with carbon (Nanocomposix, 2018). The imaging mode of the TEM, as the electrons interact with the sample, the bright field image occurs as a shadow of the sample and this appear on the florescent screen of the instrument. The D-spacing can be measured from High-resolution transmission electron microscope (HRTEM) image of the NPs using ImageJ software in order to calculate the fringe lattice spacing.

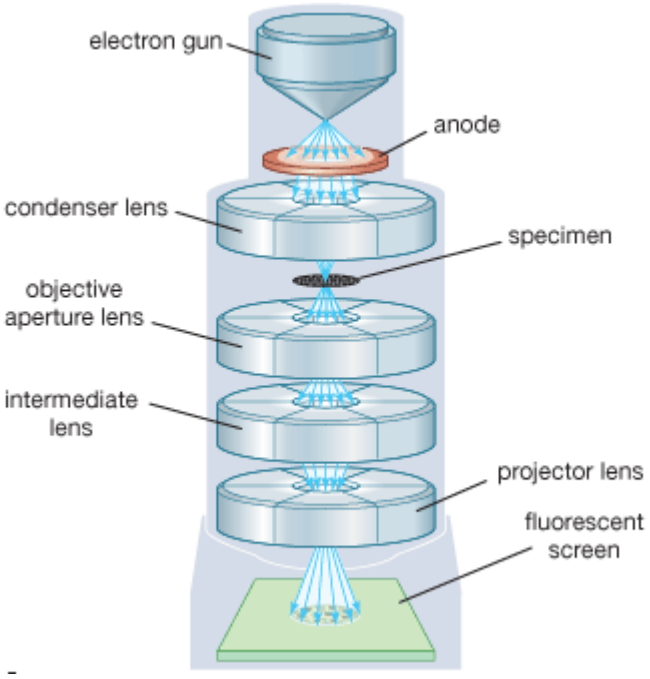

Figure 5-9: Schematic of Transmission Electron Microscope (Encyclopedia Britannica, 2018).

Selected Area Electron Diffraction (SAED)

As the electrons occur on the sample, some of the electrons travel through the sample, whereas some are scattered. The scattered electrons are of two types; elastic and inelastic. The elastic scattering electrons interact with the atoms in the sample, which makes the sample exhibit diffraction by allowing the electron to pass through the sample at a similar angle and collate using electromagnetic lenses to form a pattern of spots on the screen, each spot corresponding to a specific diffraction condition of the sample's crystal structure. When the sample is tilted, the same crystal will stay under illumination, but different diffraction conditions will be stimulated, and different diffraction spots will appear or disappear. The spots correspond to atomic spacing, providing information such as atomic arrangement, phases and orientation. The inelastic scattering electrons exhibit electron energy loss by allowing electrons to interact with the sample in which the bonding state and composition of each element in the sample is revealed. The selected area electron diffraction (SAED) pattern was achieved by directing the electron beam perpendicular to one of the nanoparticles. The crystalline nature can be identified by the SAED pattern, in the case of amprohous (diffuse rings), crystalline (bright spots), besides polynanocrystalline (small spots making up rings, each spot arising from Bragg reflection from an individual crystallite), as shown in Figure 5-10. Single spots appear only when the beam is diffracted by a single crystal and can be used to identify unknown material by indexing the patterns of the spots. The SAED of polycrystalline materials gives ring patterns analogous to those from X-ray powder diffraction and can be used to identify unknown material by indexing the ring patterns and discriminate nanocrystalline from amorphous phases. The Miller index can be measured from the SAED image of the NP, in the case of polycrystalline particles with a Debye ring measuring the diameter of each ring 2R (d-spacing) obtained using ImageJ software; if the particle is a single crystal, selected area electron diffraction will form Bragg spots, measuring the d-spacing (R) by measuring the distance between three spots using ImageJ software. In this work, a JEOL 2000FX- TEM was used to measure the diameters of the rings as seen in Figures 5-10 and 5-11:

d value calculation:

Distance between two bright spots (D) = 2 × Radius of that circle.

The distance is in reciprocal space, so we take the inverse to convert it into real space.

Thus, the formula for Interplanar spacing (d):

Interplanar spacing (d) = 2 / Distance between two bright spots

Check the ratios against the table of ratios as regards the interplannar spacing (The international Centre for Diffraction Data (ICDD) for silver, copper and gold respectively attached in Appendices A, B and C).

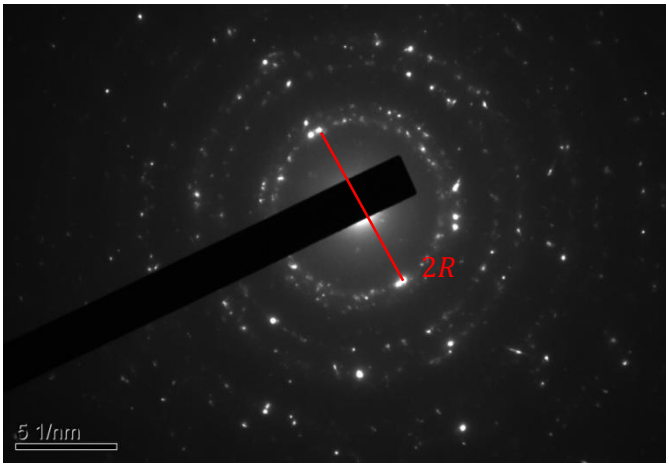

Figure 5-10: Selected area electron diffraction pattern (SAED) of AgNPs that shows the particles are polycrystalline with a Debye ring, by measuring the d-spacing which is 2.36 Å that matched the ICDD data with d-spacing 2.3592 Å, illustrating the index corresponding to (111).

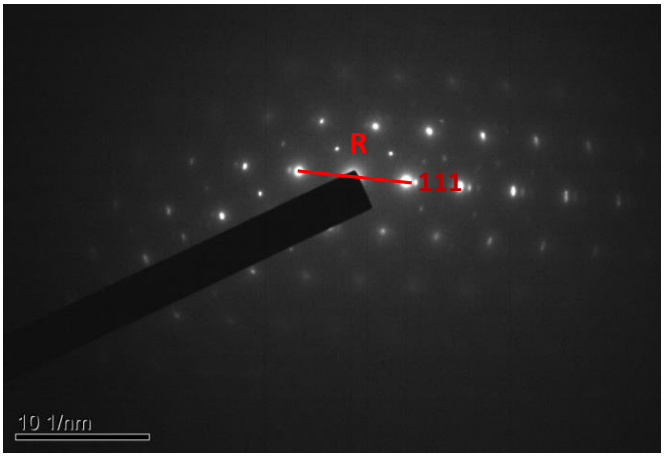

Figure 5-11: The selected area electron diffraction pattern (SAED) of the copper nanocube (CuNC) that shows the particles are a single crystal with Bragg spots, measuring the d-spacing (R) between two spots which is 2.1Å, that matched the ICDD data of copper with d-spacing 2.0871 Å, illustrating the index corresponding to (111).

5.5 Centrifugation

The rate-zonal centrifugation process is used to avoid cross-contamination of nanoparticles of different sedimentation rates through the layering of samples as a narrow zone at the top of the density gradient (Sapsford, et al. 2011). The process of rate-zonal centrifugation is elaborated in Figure 5-12. This approach ensures that the faster sedimenting particles do not become contaminated by the slower sedimenting particles as it happens during differential centrifugation. Nonetheless, the use of narrow load zone often limits the volume of a sample to 10% of what can be accommodated on the density gradient. The established gradient stabilizes the band and gives the medium, increasing viscosity and density.

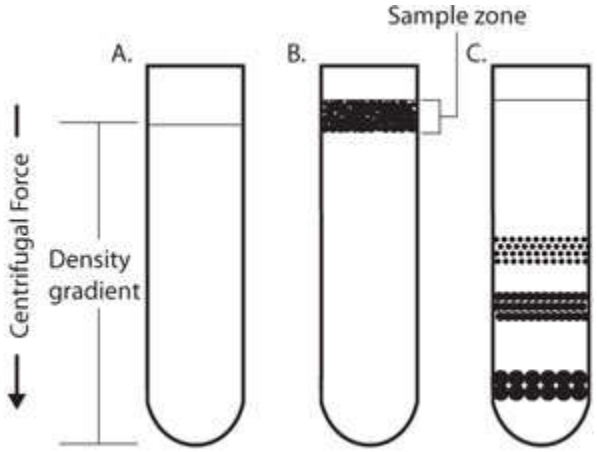

Figure 5-102: The process of rate-zonal centrifugation (Kowalczyk et al., 2011).

As shown in Figure 5-12, a nanoparticle sample is layered as a narrow zone at the top of the density gradient (B). Through centrifugal force, the particles shift at different speeds depending on their mass (C). With the rate-zonal centrifugation process, the speed at which nanoparticle material sediments mainly depends on their mass and size instead of density (Kowalczyk et al., 2011). As the particle material in a band moves down through the medium, the zones with particles of similar size form quickly sedimenting particles followed by the slower ones. Since the particle density is greater than that of the medium, all particles finally form a pellet if they are centrifuged sufficiently (Wu, et al. 2013).

The success of nanoparticle separation through centrifugation depends on the gradient medium used. The gradient medium affects the rate of sedimentation and the buoyancy density of particles. In rate-zonal separation, the function of the gradient medium is to generate a gradient of viscosity that enhances particle resolution, and at the same time ensuring the column is stable from convention currents (Schaefer, et al. 2012). An ideal density medium should contain various properties, including being sufficiently soluble, not forming solutions of high viscosity, does not tamper with the biologic activity of the sample, and be of

reasonable cost. However, no single compound satisfies this criterion. As such, different range of gradient media is used for various samples (Inagaki, et al. 2013).

In a previous research, Akbulut *et al*. (2012) have demonstrated the use of aqueous multiphase systems (MuPSs) as media for rate-zonal centrifugation. The approach separates gold nanoparticles of different sizes and shapes. The characteristic of the MuPSs gradient medium does not change during centrifugation or with time, and this stability facilitates the process of sample collection. The three-phase system of this process ensures that reaction products (large particles, nanospheres, and nanorods) are produced, where the old nanorods are enriched from 48% to 99% in a matter of 10 minutes using a benchtop centrifuge. Figure 5-13 shows this centrifugation process.

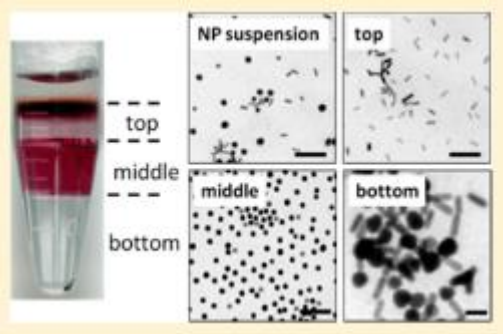

Figure 5-113: Rate-zonal centrifugation using aqueous multiphase systems (MuPSs) as media (Akbulut et al., 2012).

MuPSs offer five key advantages as a gradient medium, including stable thermodynamic phases, the sharp interface between the phases to improve particle collection after separation, independent control of viscosity at each phase; can be prepared in advance before use, and ability to be corrected if disrupted through centrifugation. As such, the ability to separate objects into different zones where every zone is separated by an interface and at equilibrium makes MuPSs particularly applicable in separating gold nanoparticles. In this work, ROTANTA 460S were used.

Chapter 6.

Synthesis of nanoparticles, characterisation, results and discussion

Synthesis of nanoparticles

I-Synthesis of silver nanoparticles

1-Materials

All chemicals for this work were purchased from Sigma-Aldrich, UK, and did not require further purification. They include silver nitride (AgNO3), sodium bromide (NaBr), polyvinylpyrrolidone (PVP) ([C6H9NO]n) and ethylene glycol (EG) (C2H6O2). All plastic equipment was cleaned using Isopropyl alcohol (I.P.A) and with D.I water, while the glassware was cleaned with acetone.

1-1 Synthesis of truncated octahedron AgNPs (AgNOct)

To synthesise AgNOct, 3ml of two EG solutions, one containing 144mM PVP and 0.11mM NaBr, the other containing 94mM AgNO3, were added dropwise via a two-channel syringe pump to 5ml of EG heated in a condenser at 160 °C. A 30µL drop of 10mM NaBr was subsequently added to the pre-heated EG. The reaction solution turned yellow in a few seconds after the addition of AgNO3 and PVP demonstrating the formation of AgNPs. After 10 minutes, the yellow colour faded in intensity due to oxidative etching and remained a light yellow colour for approximately 10 minutes before turning to brown and subsequently to grey as the NPs increased in size. The synthesised NPs were then centrifuged at 4600rpm three times and washed with de-ionised water ((DI) 18.2M Ω MilliQ) to remove any impurities and unreacted precursors. The reactions governing the formation of the particles are expressed as follows (Gupta, 2011):

$$2HOCH_2CH_2OH \rightarrow 2CH_3CHO + 2H_2O \quad (6.1.1)$$

$$2Ag^{+} + 2CH_3CHO \rightarrow CH_3CO\text{-}COCH_3 + 2Ag + 2H_{+} \quad (6.1.2)$$

These reactions usually occur in the presence of a mediating species, such as sodium bromide, sodium sulphide, sodium borohydride and hydrochloric acid. These mediators (NaBr in this case) play a role in the etching of the particle seeds, facilitating the formation of truncated octahedron. The PVP also works as a shape-control agent prompting the reduction of $AgNO_3$ onto specific crystal faces while preventing the reduction of others.

1-2 Synthesis of spherical AgNPs (AgNS)

To synthesise spherical AgNPs, an aqueous solution of $AgNO_3$ 0.001M was heated to 100°C and then 3ml of sodium citrate was added. The mixture was heated until the colour changed to yellow. To remove the contamination and unreacted precursors from the AgNSs, a combination of centrifugation and DI water washes was used three times, as before.

The particles were produced by reducing $AgNO_3$ through the following reaction (Ratyakshi *et al.*, 2009):

$$4Ag^{+} + C_6H_5O_7Na_3 + 2H_2O \rightarrow 4Ag^{0} + C_6H_5O_7H_3 + 3Na^{+} + H^{+} + O_2\uparrow \quad (6.2.1)$$

II-Synthesis of copper nanoparticles

1-Materials

All chemicals used in this study were purchased from Sigma-Aldrich, UK, and did not require further purification. They include copper sulphate ($CuSO_4$), ascorbic acid ($C_6H_8O_6$), polyvinylpyrrolidone (PVP) ($[C_6H_9NO]n$), sodium hydroxide (NaOH) and ethylene glycol (EG) ($C_2H_6O_2$).

1-1 Synthesis of spherical CuNPs (CuNS)

The CuNSs growth solution was prepared by adding 1.59g of $CuSO_4$, 1g PVP and 4.36g of Ascorbic acid all in 100ml of DI water. PVP was used as a surfactant and ascorbic acid as a reducing agent. It was then mixed and agitated with the use of a stirring magnetic bar and maintained at 80C°. CuNPs are highly unstable as they oxidise rapidly, though this can be inhibited by the use of ascorbic acid. The formation of CuNPs was confirmed once the colour of the mixture turned brick red from a blue colour. $CuSO_4$ primarily separates to Cu_2+ and SO_4- in water, and Cu_2+ ions are hydrolysed into Cu(OH2) as a precursor. Moreover, further reduction of $Cu(OH_2)$ takes place in the presence of ascorbic acid to form Cu_2O. Finally, Cu_2O is further reduced to form CuNPs. The reaction can be represented as follows (Gurav *et al.*, 2014):

$$CuSO_4 \rightarrow Cu^{2+} + SO_4^{2-} \quad (6.3.1)$$

$$2H_2O \rightarrow 2H^{+} + 2OH^{-} \quad (6.3.2)$$

$$Cu^{2+} + 2OH^{-} \rightarrow CuOH_2 \quad (6.3.3)$$

$$2Cu(OH_2) + C_6H_8O_6 \rightarrow Cu_2O + C_6H_6O_6 + 3H_2O \quad (6.3.4)$$

$$Cu_2O + C6H_8O_6 \rightarrow Cu + C_6H_6O_6 + H_2O \quad (6.3.5)$$

$$2H^{+} + SO_4^{2-} \rightarrow H_2SO_4 \quad (6.3.6)$$

1-2 Synthesis of cube CuNPs (CuNC)

5g of $CuSO_4$ and 2.5g NaOH were mixed with 50ml of ethylene glycol in a three-neck round flask equipped with a condenser and magnetic stirrer under agitation at room temperature, then boiled to reach 160 °C.

The colour of the mixture changed from blue to deep blue, to green, to yellow, to a yellowish brown and finally to red brick in 1.5 hours. The reaction can be represented as follows (Sun *et al.*, 2005):

$$HOCH_2CH_2OH \rightarrow CH_3CHO + H_2O \quad (6.4.1)$$

$$4NaOH + CuSO_4{\cdot}5H_2O \rightarrow Na_2[Cu(OH)_4] + Na_2SO_4 + 5H_2O$$

$$Na_2[Cu(OH)_4] + 2HOCH_2CH_2OH \rightarrow Na_2[Cu(OCH_2CH_2O)_2] + 4H_2O$$

$$2Na_2[Cu(OCH_2CH_2O)_2] + H_2O \rightarrow Cu_2O + CH_3COCOCH_3 + 2Na_2(OCH_2CH_2O) \quad (6.4.2)$$

$$Cu_2O + 2CH_3CHO \rightarrow 2Cu + H_2O \quad (6.4.3)$$

The synthesised nanoparticles of both shapes were centrifuged at 4600rpm three times and washed with water to remove any impurities and unreacted precursors. Freeze-drying was then used to form a powder from the copper colloid to a powder phase.

III-Synthesis of gold nanoparticles

1-Materials

Chloroauric acid (HAuCl4), Sodium citrate (C6H5O7. 3Na) and sodium bromide (NaBr) purchased from Sigma- Aldrich, U.K.)

1-1 Synthesis of spherical AuNPs (AuNS)

2.2mM sodium citrate of 150ml DI water was placed in a beaker over a hot plate for 20 minutes under continuous stirring. After boiling (100°C), 1ml drop of 25mM of HAuCl4 was added to the solution. The colour of the solution changed from yellow to light pink in a few seconds. The negatively charged citrate ions coated the seed particles and hence, were well suspended in water (McFarland *et al.*, 2004).

1-2 Synthesis of octahedron AuNPs (AuNOct)

20ml of 2.5×10^{-2} aqueous solution of HAuCl4 was placed in a conical flask fitted inside a sonicating bath at 35 KHz frequency with the power intensity of 240W/cm^2. 20ml of 2.5×10^{-2} aqueous solution of NaBr was added dropwise with the help of a burette. The mixture turned to dark yellow then to red. The suspension was subjected to ultrasonic waves for 7h (Wani *et al.*, 2013).

Table 6.1 Different shaped synthesised metal nanoparticles *in vitro* used as an antibacterial agent against *E. coli* and *E. faecium.*

Silver		Gold		Copper	
nanosphere AgNS	nanooctahedron AgNOct	nanosphere AuNS	nanooctahedron AuNOct	nanosphere CuNS	nanocube CuNC
	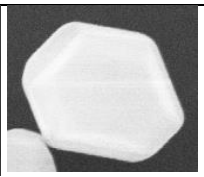		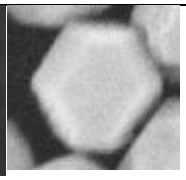		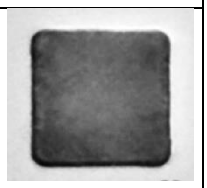

Different nanoparticle shapes were produced *in vitro*, such as copper nanoplate, gold nanowire, silver nanowire, triangle nanosilver and hexagonal plate AgNPs (Appendix D); where it has not been used for further antibacterial investigation due to time restrictions, inability to be repeated and difficulties in controlling shape and size.

IV- Results and discussion

6.1 Truncated octahedral (AgNOct) and spherical (AgNS) characterisation

The absorption spectrum of the AgNS solution in Figure 6-1b shows a sharp and intense peak at 410nm that is attributable to the surface plasmon absorption (SPR) of spherical AgNPs (Guzman *et al.*, 2012). AgNOct solution in Figure 6-1a displays an intense peak at 485nm with shoulders at 365nm and 345nm which clearly reflects anisotropic shaped NPs. The intense band at 485nm arises due to coherent dipole oscillation along the long axis of nanooctahedron, whereas the less intense transverse bands at 345 and 365 are due to dipole oscillation perpendicular to the short axis of the truncated edge of the octahedron (Acharya et al., 2018). Geometric structures were related to in-plane dipole (485nm), in-plane quadrupole plasmon resonance (365nm) and the out-of-plane dipole (345nm). The in-plane dipole plasmon band shift due to the truncated corners resulted in the red shift of SPR. The number of peaks correlates with the number of ways the electron density can be polarised (Swarnavalli *et al.*, 2011; Lee, 2010).

The shape and position of plasmon absorption of AgNPs are primarily dependent on dielectric medium, particle size and the surface adsorbed species (Pal *et al.*, 2007). Anisotropic particles such as truncated octahedrons could have two or more SPR bands depending on the shape of the particles. However, only a single SPR band is present in the absorption spectra of spherical NPs, as spherical AgNPs reduced and

stabilised by a negatively charge citrate ion and electrostatic repulsive force prevented the particle aggregation for a long time. Nevertheless, the addition of NaBr in the octahedron synthesis causes further oxidation of small particles into Ag^{+} ions as a consequence of the etching and transformation of the anisotropic shape from a spherical shape to a octahedron (Acharya *et al.*, 2018).

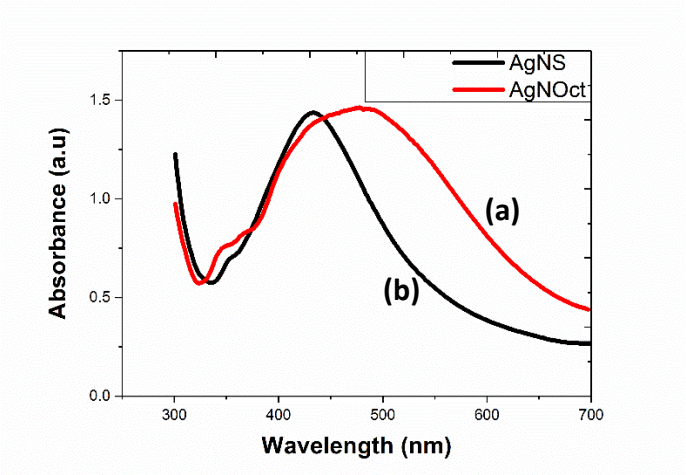

Figure 6-2: UV absorption spectra of (a) truncated octahedron (AgNOct) and (b) spherical (AgNS). AgNS shows an intense peak at 410nm, whereas AgNOct displays an intense peak at 485nm with shoulders at 345nm and 365nm.

SEM images of prepared AgNOct and AgNS are shown in Figure 6-2 (a and b respectively). The AgNOct have an average diameter of ~194nm. The size distribution is calculated from SEM images, where the polydispersity is 25% (Figure 6-3a). Figure 2b shows spherically-shaped NPs with an average diameter of ~195nm, where the polydispersity is 26% (Figure 6-3b), the lower polydispersity means that more uniform nanoparticles in size. EDX analysis of the AgNPs shows the high purity of both sets of samples. The high purity is related to the solution being centrifuged ahead of any further investigations to remove any impurities, besides unreacted precursor and solvent (Figure 6-4 a and b).

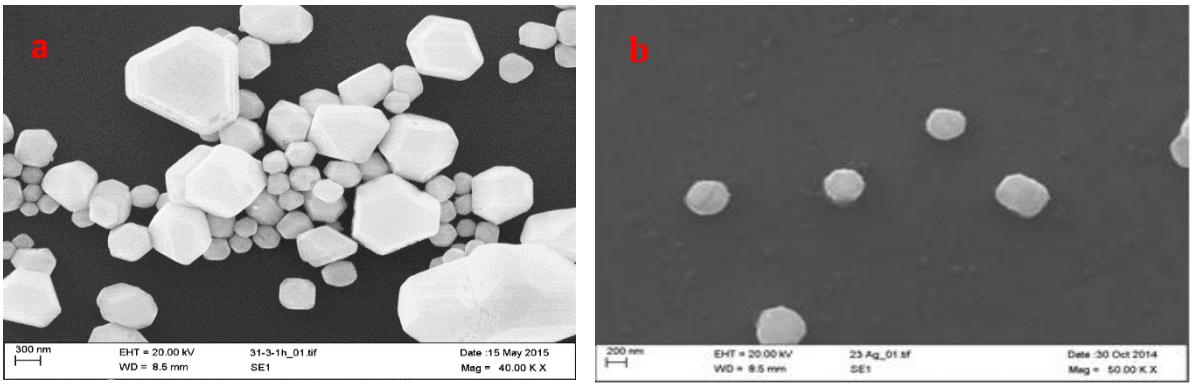

Figure 6-3: SEM images of (a) truncated octahedron shape (AgNOct) and (b) spherical shape AgNS.

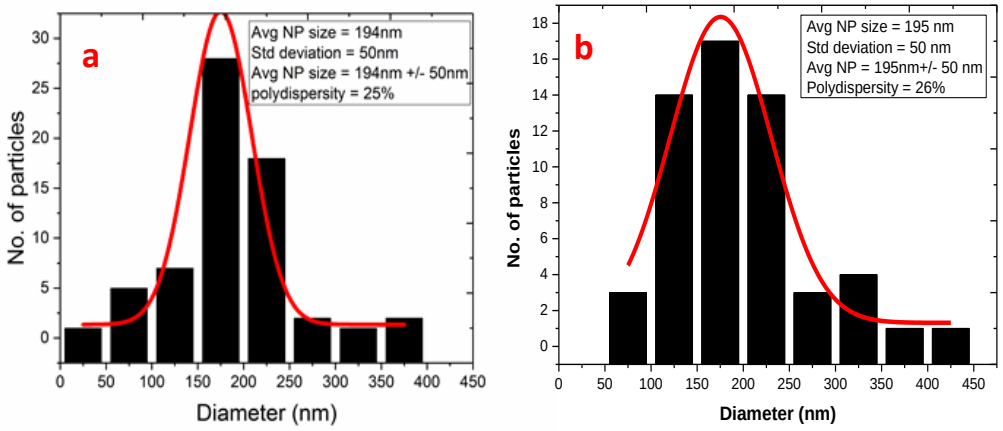

Figure 6-4: Size distribution of (a) AgNOct and (b) AgNS, shows polydispersity of 25% and 26% respectively.

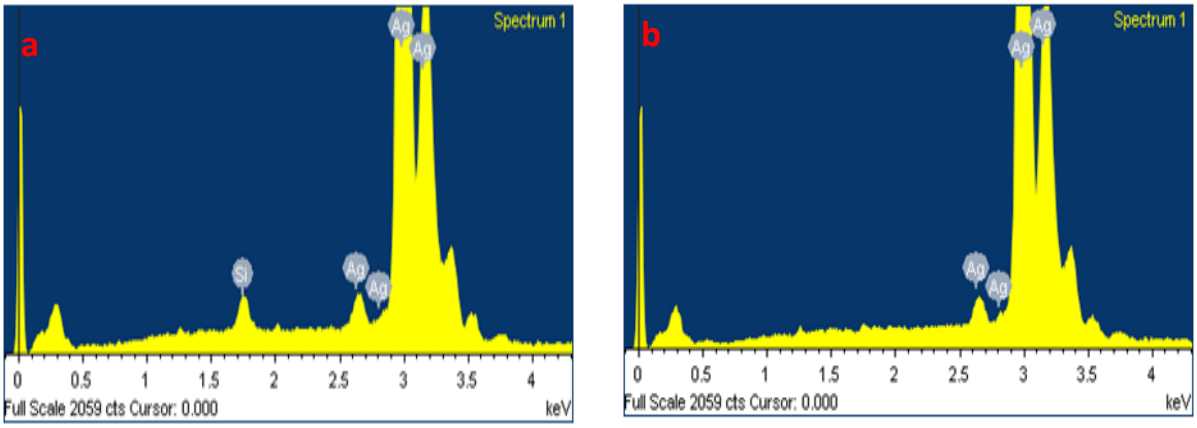

Figure 6-5: EDX of (a) AgNOct and (b) AgNS, confirming the purity of both shaped AgNPs.

XRD data shown in Figure 6-5 (a and b) confirms the formation of FCC AgNPs. Diffraction peaks at 2θ are 38, 44, 64, 77 & 81, which are attributed to (111), (200), (220), (311) and (222) lattice planes of Ag with a cubic phase (ICDD 04-0783). AgNOct is enclosed by (111) faceted plane compared with AgNS. Generally, spherical AgNPs exhibit a dominant (100) plane, while truncated octahedron AgNPs exhibit (111) a lower intensity of (100). Different crystal structures or directions may reveal different chemical and physical properties. For instance, the (111), (100) and (110) surfaces of the face centred cubic (fcc) metal have different surface atom densities, chemical reactivity and electronics structure (Zhou *et al.*, 2011; Lee *et al.*, 2007). In addition, it was argued previously that the antibacterial activity of silver is greater when high atomic density facets are present such as the {111} plane (Acharya *et al.*, 2018). It was assumed that atoms were more reactive on the facets of higher surface energy (Xia *et al.*, 2009), possibly to enhance the

antibacterial properties of AgNOct compared to AgNS (Acharya *et al.*, 2018). The presence of structural peaks in XRD patterns clearly illustrate that the AgNPs synthesised *in vitro* using the chemical method were nanocrystalline in nature. Table 6-2 illustrates the calculations obtained from XRD pattern of AgNS and AgNOct, the experimental peaks position (2θ) matches each of the peaks position values in thee ICDD which confirms the formation of FCC silver. The schematic diagram of the face-centred cubic structure (FCC) (Figure 6-6a), where the atoms are located at the eight corners of the unit cell and at the centre of each face is also termed a close packed structure. It was suggested that the truncated octahedron comprising plane (111) has higher electron density than spherical NPs, which play an essential role in antibacterial action that supports our findings with regard to (AgNOct). Figure 6-6b represents Miller indices notation of (111) plane.

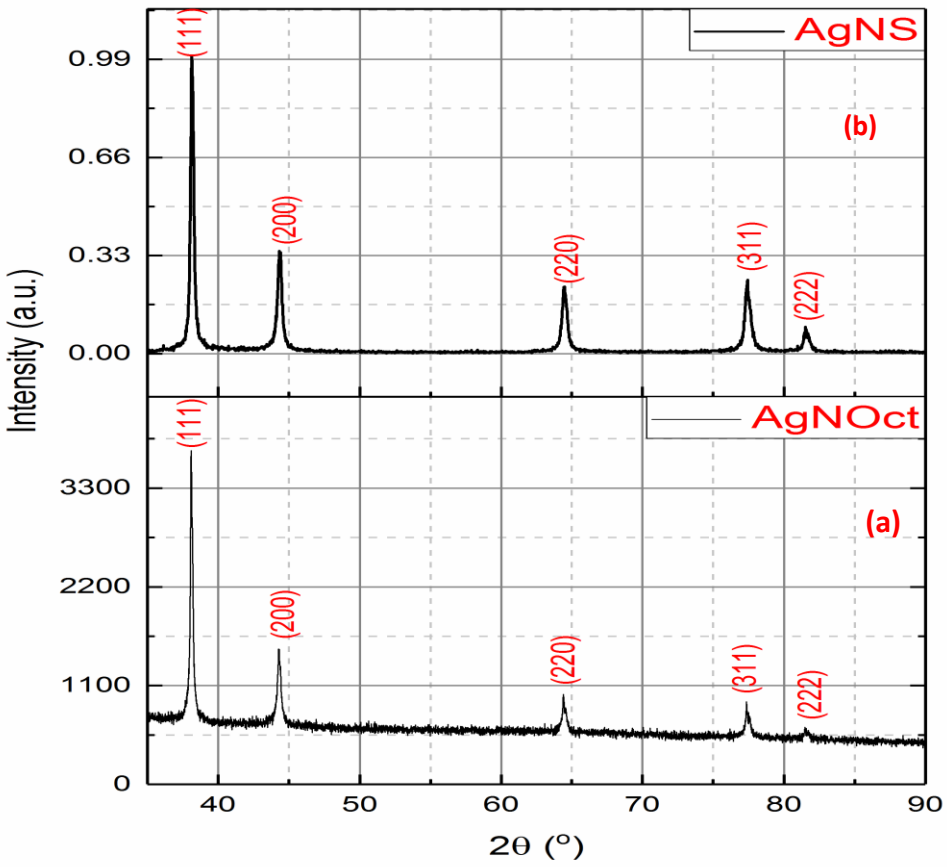

Figure 6-6: XRD pattern obtained from (a) AgNOct and (b) AgNS. Diffraction peaks at 2θ are 38, 44, 64, 77 & 81 are attributed to (111), (200), (220), (311) and (222) lattice planes of Ag with a cubic phase (ICDD card no. 04-0783), confirming both shapes are metallic FCC silver, whereas AgNOct has a higher electron density of (111) plane.

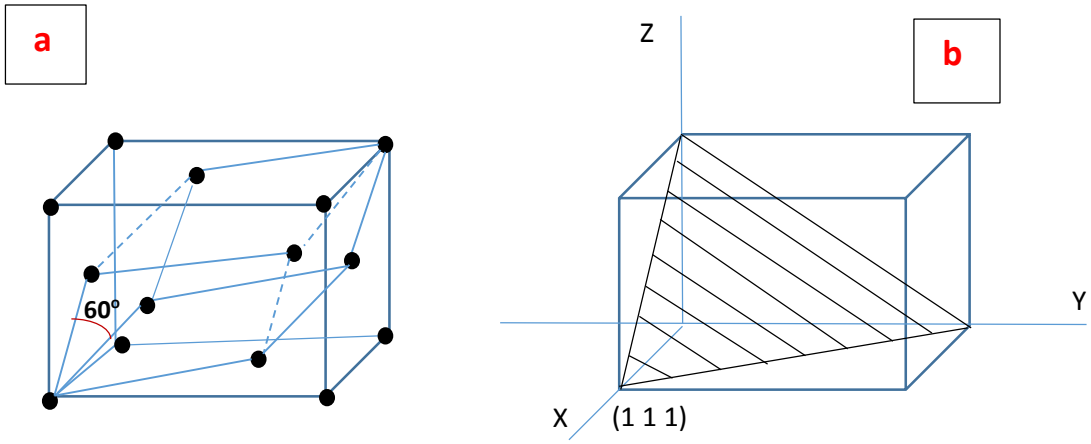

Figure 6-6*:* Face-centred cubic structure (FCC) (c) and Miller indices of (111) planes (d).

Table 6.2 Calculations obtained from the XRD pattern of AgNS and AgNOct compared with JCPDS silver values confirmed the formation of FCC silver (peak indexing from d-spacing).

2θ in degrees JCPDS silver: 04-0783	**Shape of AgNPs**	**Experimental 2θ in degrees**	**d-spacing calculating from spectra (Å)**	**hkl**	**FWHM (degree)**	**Average crystallite size**	**Experimental lattice constant a (Å)**
38.116	AgNS	38.088	2.36	111	0.21	41	4.08
	AgNOct	38.12			0.26	33	
44.277	AgNS	44.21	2.02	200	0.41	21	4.08
	AgNOct	44.28			0.35	25	
64.426	AgNS	64.48	1.44	220	0.5	19	4.08
	AgNOct	64.42			0.41	23	
77.472	AgNS	77.41	1.23	311	0.5	21	4.08
	AgNOct	77.47			0.5	23	
81.62	AgNS	81.67	1.18	222	1.43	7	4.08
	AgNOct	81.61			0.46	23	

High resolution transmission electron microscopy (HRTEM) images of AgNOct exhibit a octahedron particle as shown in Figure.6-7a; a simulation of a 3D model of truncated octahedron silver (Figure.6-7b). D-spacing was calculated from High-resolution lattice images (HRTEM) of AgNOct (Figure 6-8) that shows 2.02 Å and 2.36 Å which correspond to (200) and (111) lattice planes; either in ICDD data for silver

(2.3592 Å and 2.0431 Å) respectively (Appendix A) or calculated from the diffraction pattern using Bragg's law (Equation 5.3.1). The selected area electron diffraction pattern (SAED) of AgNOct and AgNS demonstrated that the particle is polycrystalline with a Debye ring (Figures 6-9 and 6-10). The diameter of each ring was calculated in order to measure 2R (d-spacing) and compared the calues of R (d-spacing) with XRD data or with ICDD data (see Appendix A). Table (6-3 and 6-4) illustrated the indexing plane calculated from selected area electron diffraction (SAED) that shows the same findings as the literature (Bykkam *et al.*, 2015), confirming that the particle is crystallographic for face-centred cubic (FCC) silver crystal (Theivasanthi *et al.*, 2011).

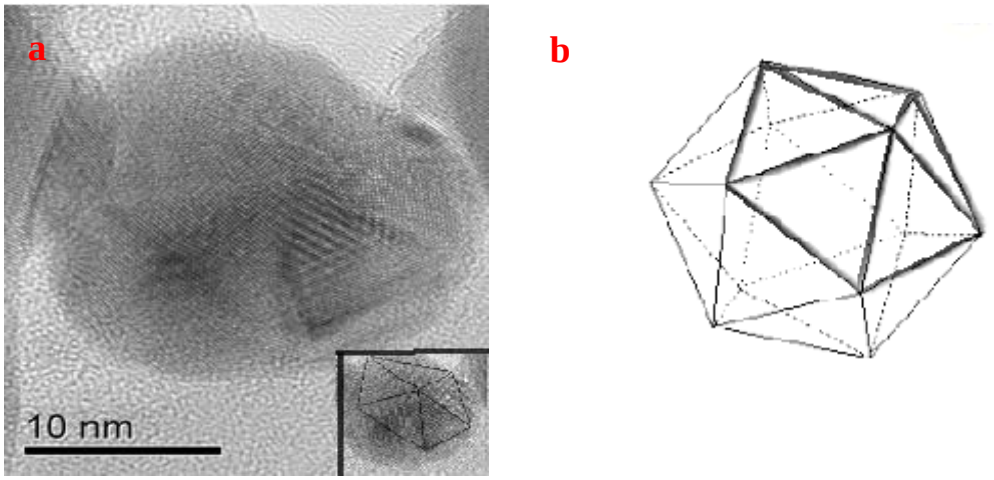

Figure 6-7: High-resolution transmission electron microscopy (HRTEM) images of truncated octahedron AgNOct (A) and (B) Simulation of a 3D model of truncated octahedron silver.

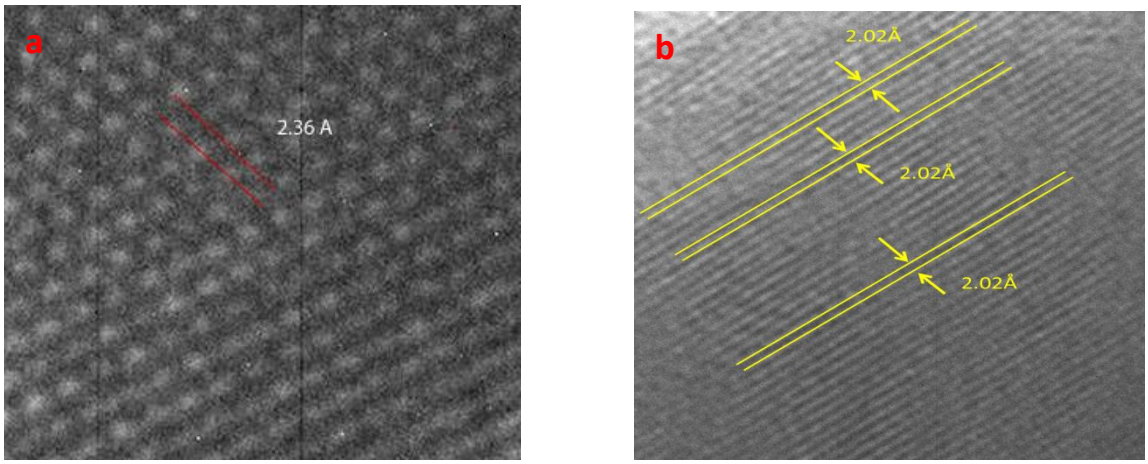

Figure 6-8: High resolution-TEM images illustrating the lattice fringe of AgNOct which confirmed the d-spacing value were indexed to: (a) lattice spacing of 2.36 Å corresponding to (111) and (b) lattice spacing of 2.02 Å corresponding to (200).

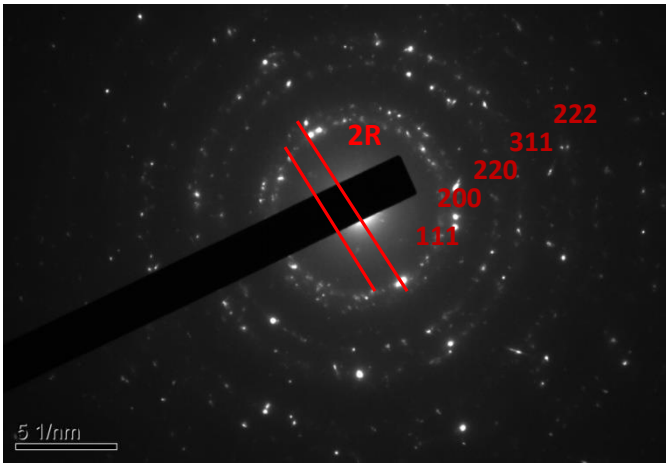

Figure 6- 9: Selected area electron diffraction pattern (SAED) of AgNOct that shows the particles are polycrystalline with a Debye ring and illustrated the index corresponding to (111), (200), (220), (311) and (222).

Table 6.3 Calculations obtained from indexing the selected area electron diffraction (SAED) of AgNOct and comparing the calues of R (d-spacing) with the XRD data or data base ICDD.

2R [1/nm]	R [1/nm]	R [nm]	Experimental R [Å] (d-spacing)	Diffraction data ICDD R [Å] (d-spacing)	h k l	Experimental 2-theta
8.41	4.209	0.236	2.36	2.3592	111	38.08
9.74	4.8715	0.202	2.02	2.0431	200	44.21
13.99	6.997	0.144	1.44	1.4447	220	64.41
16.25	8.1265	0.123	1.23	1.2320	311	77.41
10.13	5.07	0.178	1.17	1.1796	222	81.60

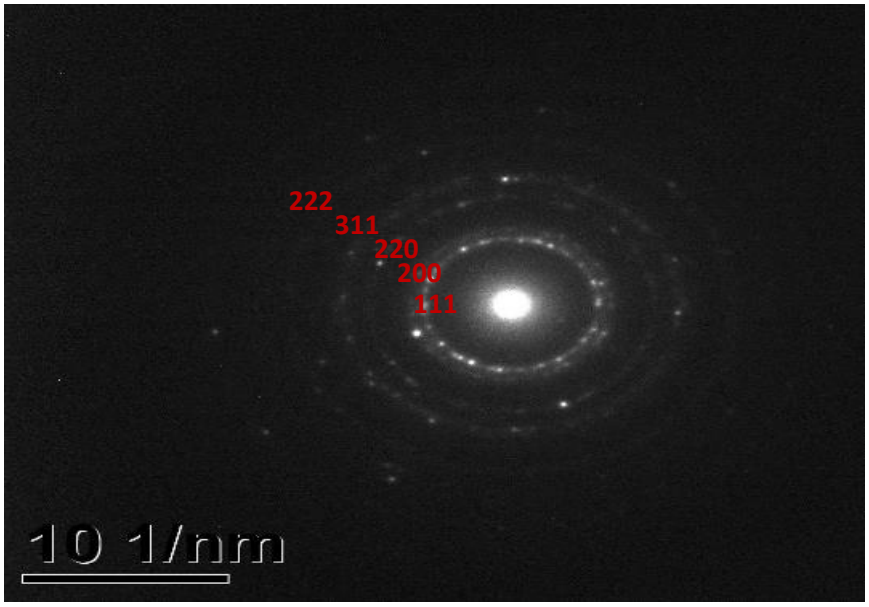

Figure 6-10: Selected area electron diffraction pattern (SAED) of AgNS that shows the particles is polycrystalline with a Debye ring and showed the index corresponding to (111), (200), (220), (311) and (222).

Table 6.4 Calculations obtained from indexing the selected area electron diffraction (SAED) of AgNS and comparing the calues of R (d-spacing) with the XRD data or data base ICDD.

2R [1/nm]	R [1/nm]	R [nm]	Experimental R [Å] (d-spacing)	Diffraction data ICDD R [Å] (d-spacing)	h k l	Experimental 2-theta
8.47	4.23	0.24	2.46	2.3592	111	38.2
9.64	4.82	0.21	2.21	2.0431	200	44.3
13.66	6.83	0.15	1.54	1.4447	220	64.4
16.61	8.31	0.12	1.23	1.2320	311	77.4
11.14	5.57	0.18	1.18	1.1796	222	81.5

6.2 Cu nanocube (CuNC) and Cu nanosphere (CuNS) characterisation

The absorption spectrum of the CuNS solution shown in Figure 6-11a shows an intense peak at 580nm, which is attributable to the surface plasmon absorption of copper nanosphere (Abdulla-Al-Mamun *et al.*, 2007). In Figure 6-11b, CuNCs illustrates three broad peaks observed at 335nm, 450nm and 785nm, respectively. The SPR agreed with the literature. It shows that the number of SPR would increase with the decrease in the symmetry of metal NPs. The absorption spectra of metal nanoparticles were mediated by surface plasmon resonances (SPRs) that shift to longer wavelengths, as the shape changed from spheres to other shapes (Wang *et al.*, 2006). CuNPs are highly unstable as they oxidise rapidly, though this can be inhibited by the use of ascorbic acid, as shown in (Appendix E), as prepared copper nanoparticles have a red brick colour and commercial copper oxide has a black colour.

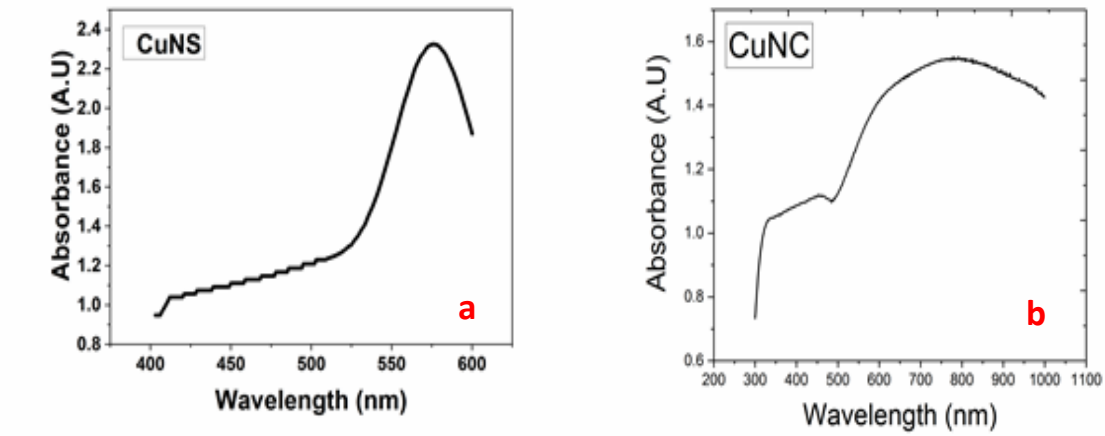

Figure 6- 71: UV spectra of (a) CuNS shows an intense peak at 580nm and (b) CuNC exhibits three broad peaks observed at 335nm, 450nm and 785nm.

SEM images of prepared CuNS and CuNC are shown in Figure 6-12 (a and b respectively). The spherically shaped nanoparticles have an average diameter of ~270nm. Figure 6-12b shows uniformly cube-shaped NPs with sides of length ~270nm. The size distribution is calculated from SEM images, where the polydispersity is 25% of spherical-shaped NPs (Figure 6-13a). Figure 6-13b explains cube-shaped NPs are a highly uniform shape where the polydispersity of 10% is low.

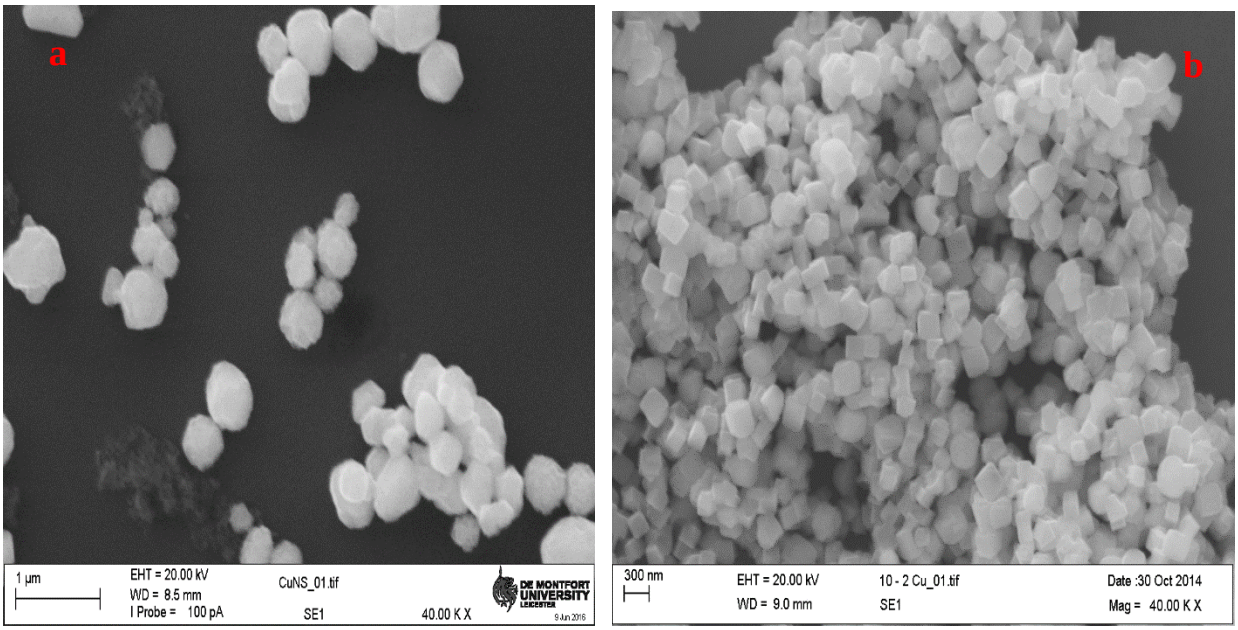

Figure 6- 82: SEM images of (a) spherical shape copper nanoparticles (CuNS) and (b) cubic shape copper nanoparticles (CuNC).

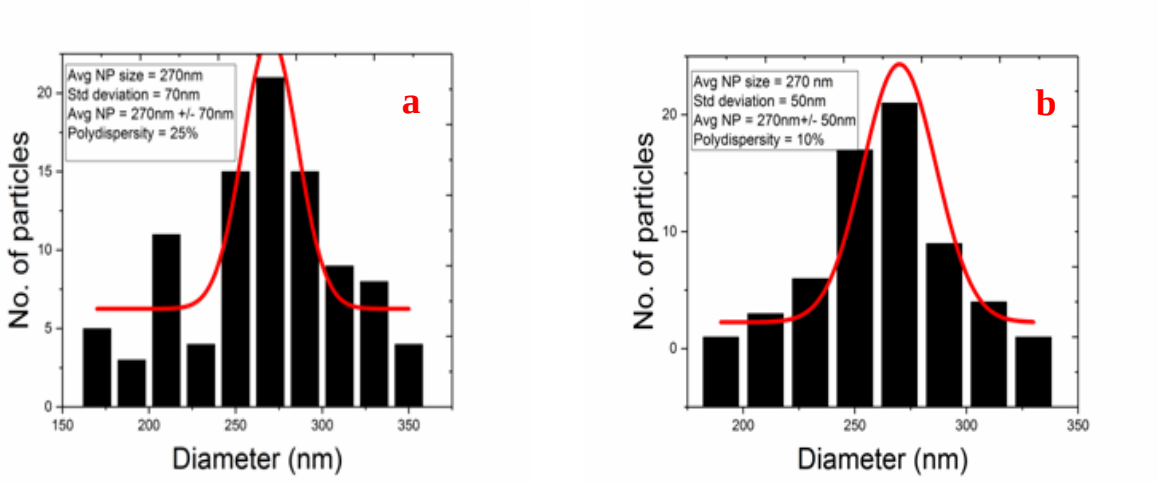

Figure 6- 93: Size distribution of (a) CuNS and (b) CuNC, shows polydispersity of 25% and 10% respectively.

EDX analysis of the CuNPs shows the presence of Cu, silicon (from the substrate) and low levels of oxygen and carbon which might be related to the surfactant used in the experiment (PVP) ([C6H9NO]n) (Figure 6-14).

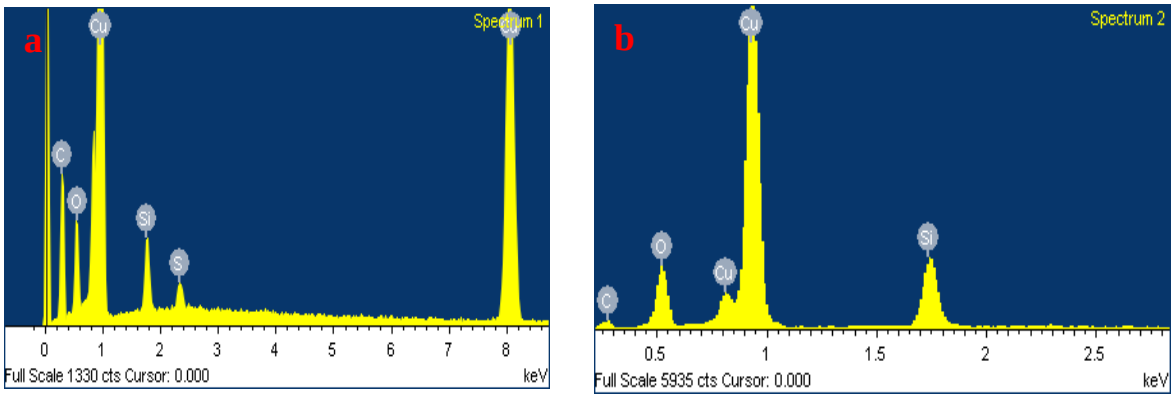

Figure 6- 104*:* EDX of (a) CuNS and (b) CuNC confirming the purity of both CuNPs shapes. Only low level oxygen and carbon which might be related to the surfactant used in the experiment (PVP) ([C6H9NO]n).

Diffraction peaks at 2θ = 43.2 and 74.4 are attributed to (111) and (220) planes of Cu with a cubic phase FCC copper (ICDD card no. 04-0836), as shown in Fig 6-15a agreed well with literature (Mowbray, 2013). The cubic structure as shown in the SEM images (Figure 6-12b) illustrates that the crystal plane enclosed by {100} on all sides suggested cubic formation due to oxidative etching during the nucleation phase of the seeds owing to a large shift in the distribution of seeds in the pathway of single crystal particles instead of twinned seeds (Mowbray, 2013). This findings agreed with the SAED pattern that confirms the particle is a single crystal with Bragg spots (see Figure 6-17). The calculation obtained from the diffraction peaks in Table 6-5 confirmed the experimental peaks position matching the ICDD Cu 04-0836 peaks position value for both shapes. However, the XRD pattern for CuNS reveals an additional peak indexed as the (220) diffraction of Cu_2O (ICDD 05-0667), as seen in Figure 6-15b that can be associated with the slow oxidation of metallic CuNPs in air to form CuO (Chen *et al.,* 2015). In addition, the intensity of (111) plane of CuNC was revealed to be much higher than the CuNS, suggesting better inhibition of the bacteria growth demonstrated from our findings in Chapter 7. Unlike AgNPs, there is a lack of studies related to the relationship between the CuNPs shape enhanced antibacterial activity with faceted structure.

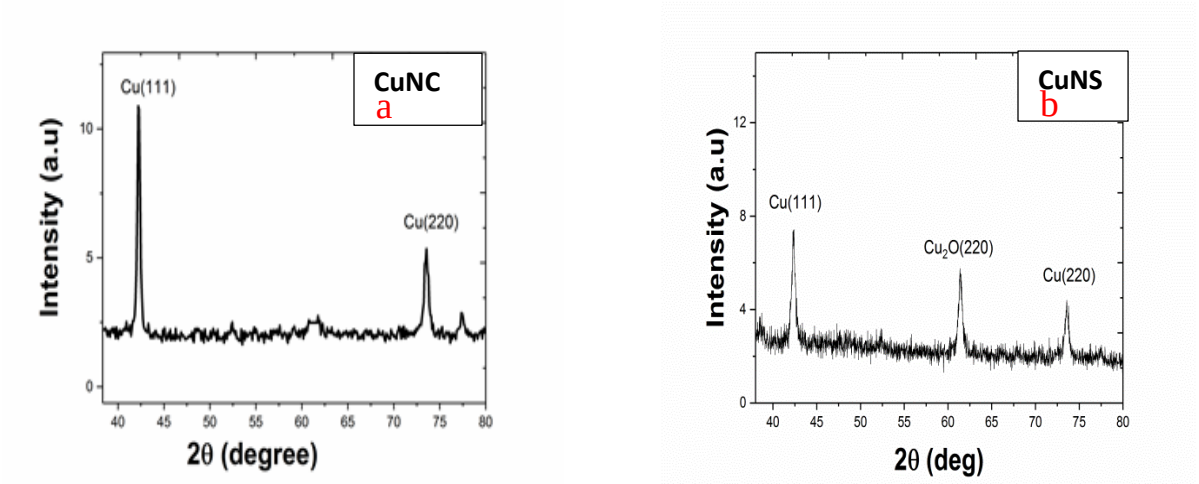

Figure 6-115: XRD pattern confirming the formation of FCC copper crystallographic (a) CuNC and (b) CuNS. Diffraction peaks at 2θ = 43.2 and 74.4 corresponding to (111) and (220) lattice planes in CuNC that agreed with cubic phase (ICDD card no. 04-0836), whereas in CuNS, the additional peak at 61 corresponds to the Cu_2O (220) plane.

Table.6-5 Calculations obtained from the XRD pattern of prepared CuNS/CuNC compared with JCPDS silver values confirmed the formation of FCC copper

2θ in degrees JCPDS copper: 04-0783	**Shape of CuNPs**	**Experimental 2θ in degrees**	**d-spacing calculating from spectra (Å)**	**hkl**	**FWHM (degree)**	**Average crystallite size**	**Experimental lattice constant a (Å)**
43.2	CuNS	42.39	2.1	Cu 111	0.80109	11	3.61
	CuNC	42.21			0.43694	20	
74.4	CuNS	73.58	1.27	Cu 220	1.38218	7	3.61
	CuNC	73.57			1.02075	10	
61.2	CuNS→Cu_2O	61.37	1.5	Cu_2O 220	1.38218	6	3.61
	CuNC	No peak					

High resolution transmission electron microscopy (HRTEM) images of CuNC shows a cube shape particle, as shown in Figure.6-16. The selected area electron diffraction pattern (SAED) of CuNC shows the particle is a single crystal with Bragg spots (Figure 6-17). The diameter between three spots was calculated as seen in Table 6-6, in order to measure R (d-spacing) and compare the calues of R (d-spacing) with XRD data or with (ICDD) that is attached to Appendix B. Spots indexing corresponding to (111) and (200) plane with d-spacing of 2.1 Å and 1.27 Å, as seen in Figure 6-17, confirmed the same results for the d-spacing

calculated using Bragg's law, as shown in Table 6-5. TEM data for CuNC shows that the particle is crystallographic for the face-centred cubic (FCC) Cu crystal ((Mowbray, 2013).

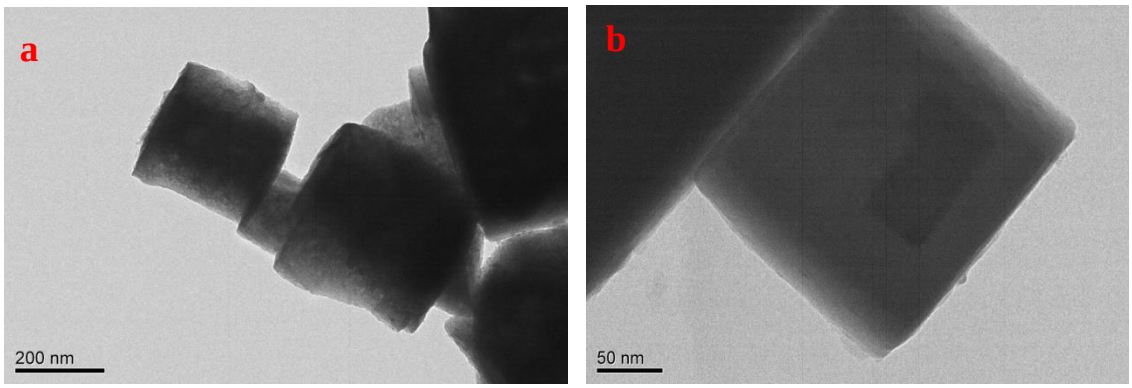

Figure 6-126: High resolution transmission electron microscopy (HRTEM) images of CuNC shows a distinct cubic shape.

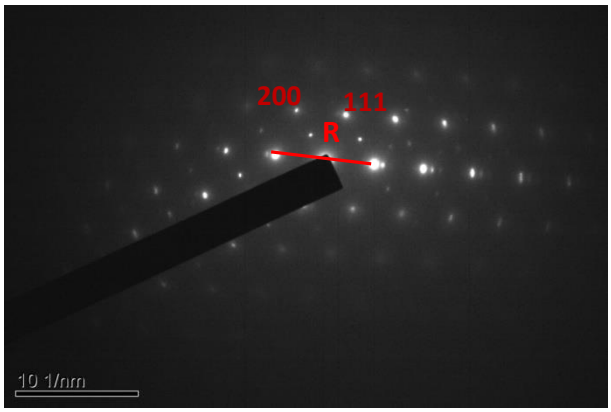

Figure 6- 137: Selected area electron diffraction pattern (SAED) of CuNC shows that the particles are a single crystal with Bragg spots. The pattern of spots corresponding to (111) and (200).

Table.6-6 Calculations obtained from indexing the selected area electron diffraction (SAED) of CuNC and comparing the calues of R (d-spacing) with XRD data or data base ICDD.

R [1/nm]	R [nm]	Experimental R [Å] (d-spacing)	Diffraction data ICDD R [Å] (d-spacing)	h k l	Experimental 2-theta
4.7913	0.20871	2.08	2.0871	111	42.21
7.8241	0.12781	1.27	1.2781	220	73.57

6.3 Truncated octahedral (AuNOct) and spherical (AuNS)

The absorption spectrum of the Au solution in Figure 6-18a shows an intense peak at 525nm and large shoulder at a lower wavelength that is attributable to the surface plasmon absorption resonance of spherical NPs (Cheng *et al.*, 2013). Figure 6-18 b shows a broad peak at 545nm that is attributable to the surface plasmon absorption of AuNOct (SPRs) that shift to longer wavelengths as the shape of the NPs changes from spherical to octahedron (Weng *et al.*, 2008).

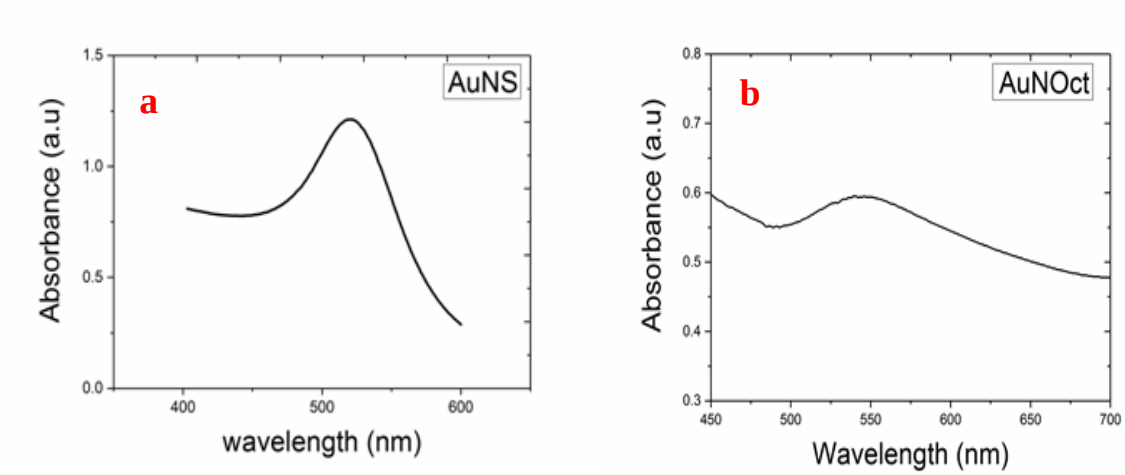

Figure 6- 148: UV absorption spectra of (a) AuNS shows an intense peak at 525nm and (b) AuNOct shows a broad peak at 545nm.

SEM images of prepared AuNSs and AuNOcts are shown in Figure 6-19 (a and b respectively). The spherically shaped nanoparticles have an average diameter of ~205nm (Figure 6-19a). The size distribution is calculated from SEM images where the polydispersity is 25% (Figure 6-20a). Figure 6-19b reveals that octahedral shaped NPs have the same average diameter of a spherical AuNS, where the polydispersity is 29% (Figure 6-20b).

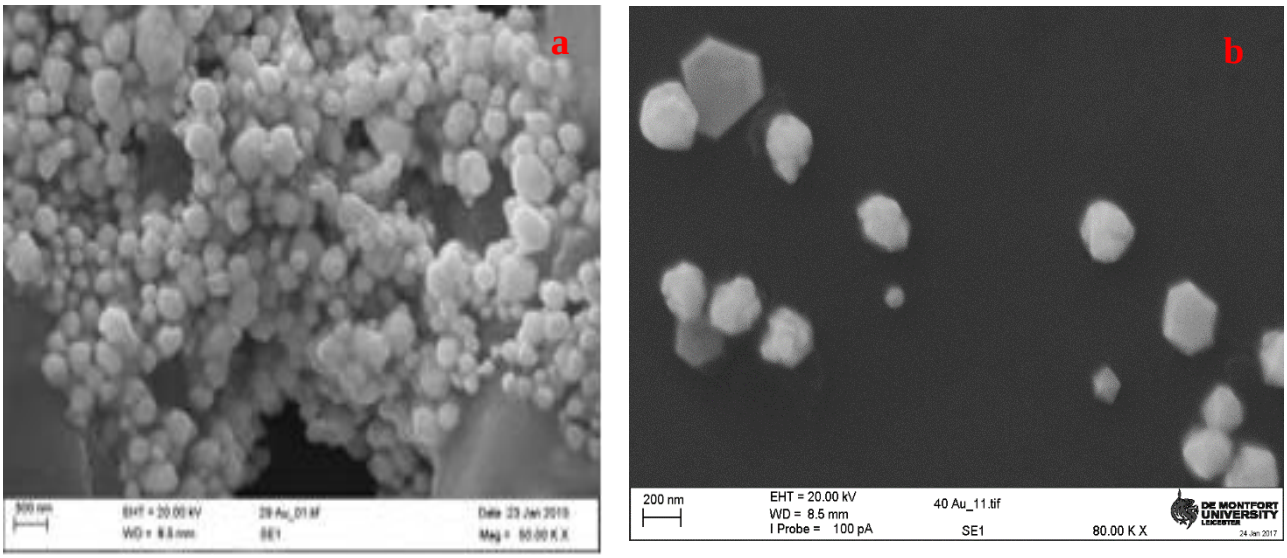

Figure 6- 159: SEM images of (a) AuNS and (b) AuNOct shows spherical and truncated octahedron shaped gold nanoparticles respectively.

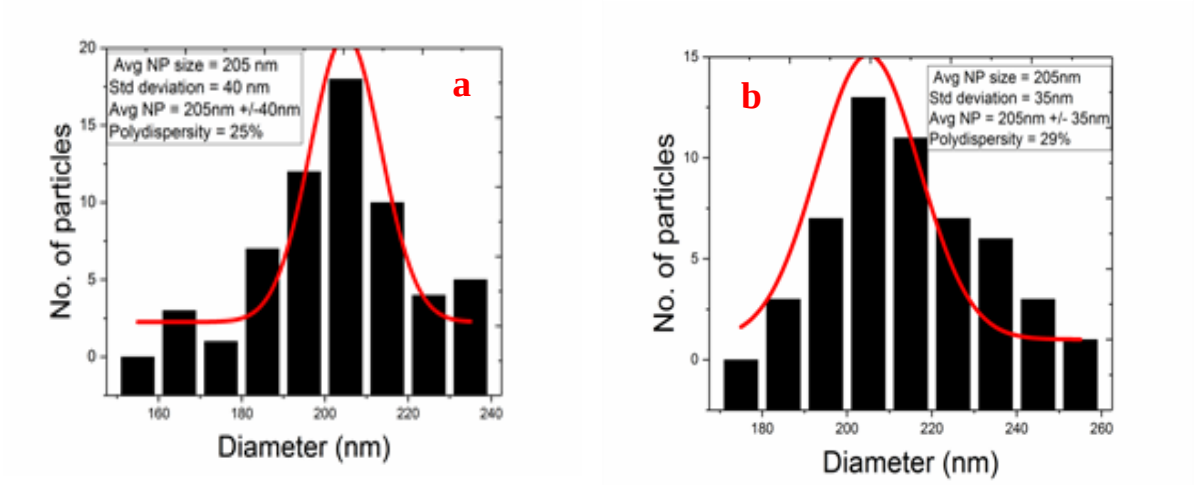

Figure 6- 20: Size distribution of (a) AuNS and (b) AuNOct illustrates polydispersity of 25% and 29% respectively.

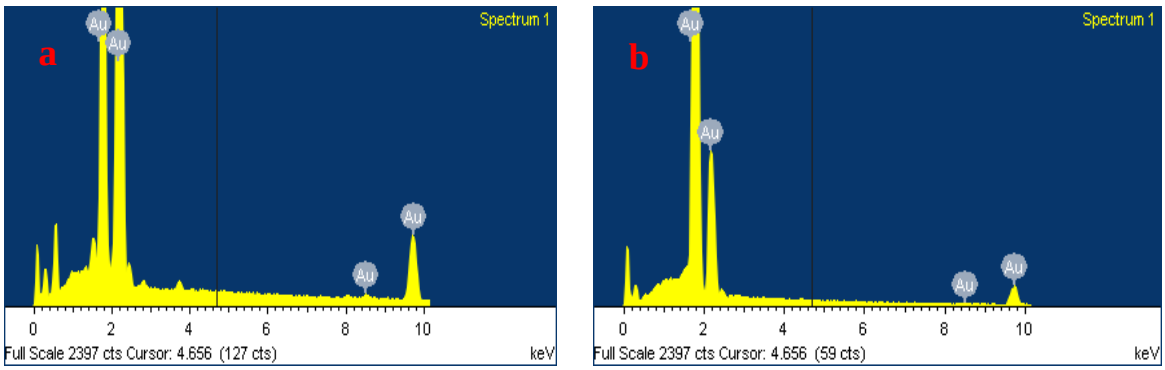

Figure 6- 161*:* EDX of (a) AuNS and (b) AuNOct.

EDX analysis of the AuNPs exhibits the high purity of both sets of samples related to removing any impurities, unreacted precursor and solvent using the centrifugation process (Figure 6-21 a and b).

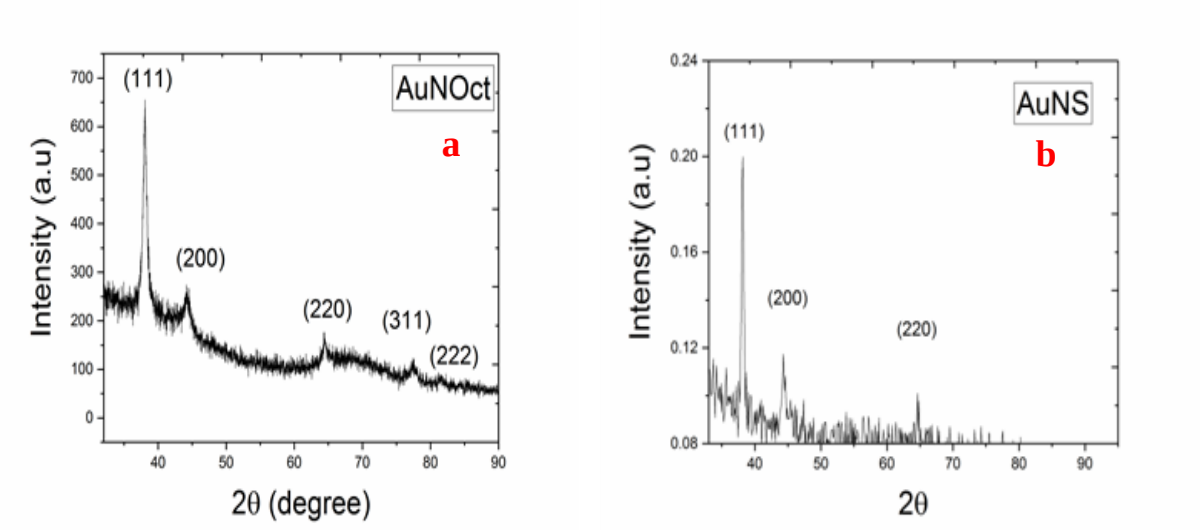

Figure 6- 172: XRD pattern confirming the formation of AuNPs: (a) AuNS and (b) AuNOct. Diffraction peaks at 2θ are 38, 44, 64, 78 & 81, which are attributed to (111), (200), (220), (311) and (222) lattice planes of Au with a cubic phase (ICDD. 04-0784) confirming both shapes were metallic FCC gold, whereas AuNOct has a higher electron density of (111) plane.

X-ray diffraction data shown in Figure 6-22 (a and b) confirms the formation of FCC AuNPs. AuNOct shows diffraction peaks at 2θ = 38, 44, 64, 78 and 81 of AuNOct are attributed to (111), (200), (220), (311) and (222) planes respectively of Au with a cubic phase (ICDD. 04-0783), as shown in table 6-7, AuNS shows only three diffraction peaks at 38, 44 and 64 corresponding to (111), (200) and (220), as seen in Figure 6-22b. AuNOct orientated by (111) plane compared to AuNS besides the position of the AuNOct peaks matching all 2θ values of the FCC (ICDD 04-0784) gold structure, while in the AuNS, two peaks are

missing. The improved AuNOct crystallinity suggesting enhanced antibacterial activity confirmed by our findings in Chapter 7.

Table.6-7 Calculations obtained from the XRD pattern of prepared AuNS/AuNOct compared with JCPDS gold values

2θ in degrees JCPDS gold: 04-0783	**Shape of AuNPs**	**Experimental 2θ in degrees**	**d-spacing calculating from spectra (Å)**	**hkl**	**FWHM (degree)**	**Average crystalline size**	**Experimental lattice constant a (Å)**
38.22	AuNS	38.139	2.36	111	0.76144	11	4.07
	AuNOct	38.003			1.1673	17	
44.43	AuNS	44.291	2.1	200	2.07035	4	4.07
	AuNOct	44.364	2.04		1.552	5	
64.64	AuNS	64.634	1.5	220	3.25735	3	4.07
	AuNOct	64.319			2.2977	4	
77.65	AuNOct	77.5563	1.231	311	1.4222	7	4.07
81.81	AuNOct	81.206	1.184	222	1.3526	8	4.07

High resolution transmission electron microscopy (HRTEM) images of AuNOct shows the lattice fringe of the particle, as illustrated in Figure 6-23. The d-spacing was measured with 2.04 Å and 2.36 Å which verified the results of the d-spacing calculated using Bragg's law, as shown in Table (6-7and 6-8). The selected area electron diffraction pattern (SAED) of AuNOct shows the particle is polycrystalline with a Debye ring (Figure 6-24) and the calues of R (d-spacing) compared with the XRD data or with (AMCSD) attached in Appendix C. Although, the SEAD pattern of AuNS shows that polycrystalline with a Debye ring has three clear rings only, as shown in Figure 6-25, the d-spacing calculated from the SAED image match the d-spacing of (AMCSD), as seen in Table 6-9. TEM data for AuNOct and AuNS confirms that the particle is crystallographic in relation to the FCC Au structure (Wani *et al.,* 2013).

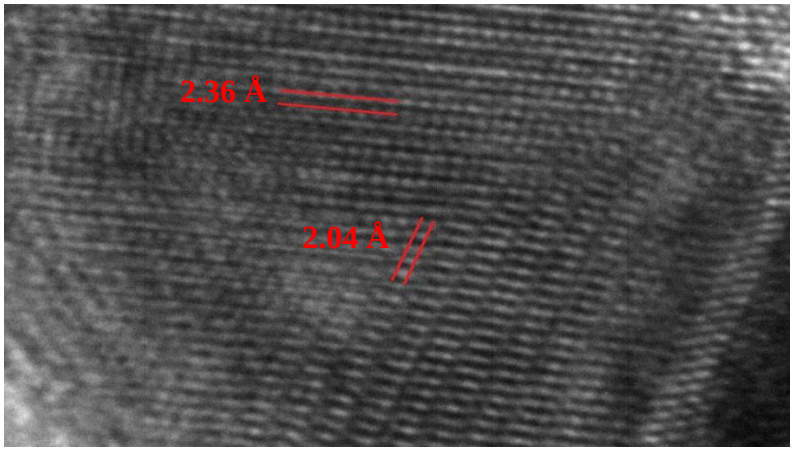

Figure 6- 183: High resolution lattice images of AuNOct that shows the d-spacing of 2.02 Å and 2.36 Å.

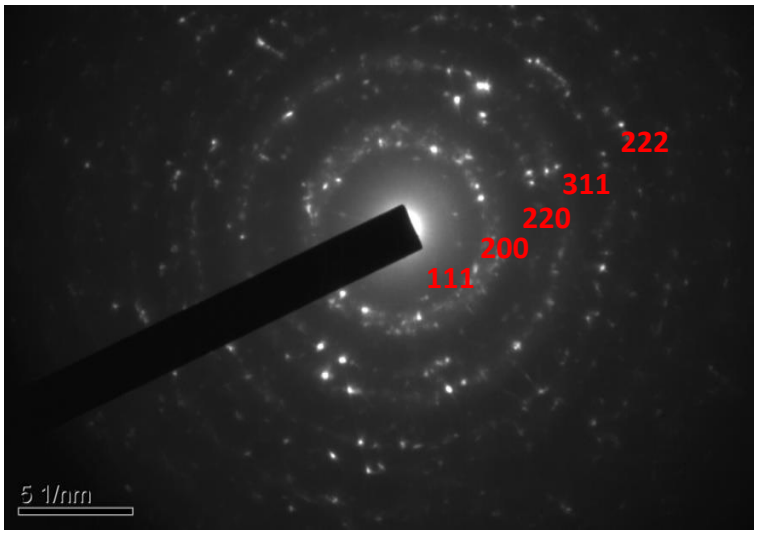

Figure 6- 194: Selected area electron diffraction pattern (SAED) of AuNOct that displays the particles are polycrystalline with Debye rings.

Table.6-8 Calculations obtained from indexing the selected area electron diffraction (SAED) of AuNOct and comparing the calues of R (d-spacing) with the XRD data or data base ICDD.

2R [1/nm]	R [1/nm]	R [nm]	Experimental R [Å] (d-spacing)	Diffraction data ICDD R [Å] (d-spacing)	h k l	Experimental 2-theta
8.494	4.2470	0.23546	2.3616	2.3619	111	38.003
9.775	4.8875	0.20	2.0460	2.0455	200	44.364
12.042	6.021	0.15	1.6608	1.4464	220	64.319
16.23	8.115	0.12	1.2322	1.2335	311	77.5563
18.446	9.223	0.11	1.0842	1.1810	222	81.206

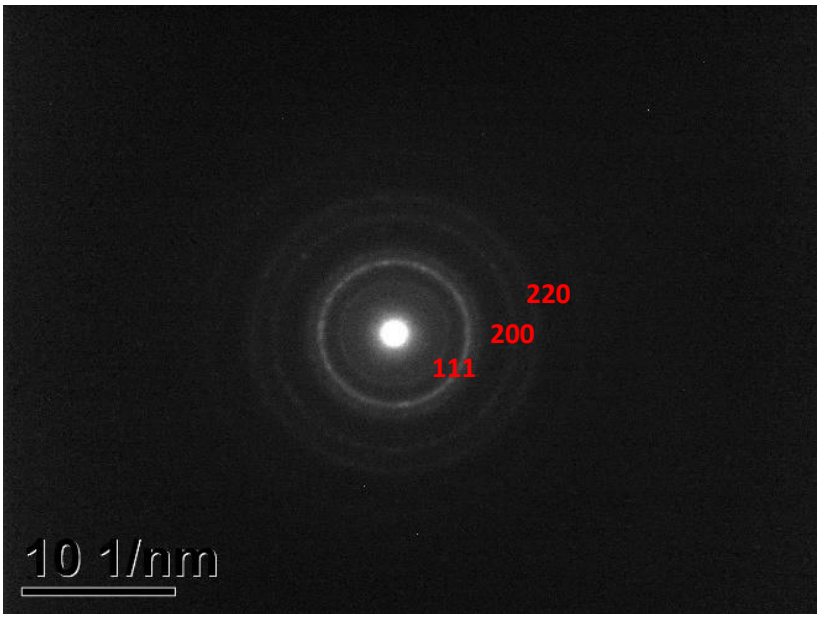

Figure 6- 205: Selected area electron diffraction pattern (SAED) of AuNS that shows the particle is polycrystalline with Debye rings.

Table.6-9 Calculations obtained from indexing the selected area electron diffraction (SAED) of AuNS and comparing the calues of R (d-spacing) with the XRD data or data base ICDD.

2R [1/nm]	R [1/nm]	R [nm]	Experimental R [Å] (d-spacing)	Diffraction data ICDD R [Å] (d-spacing)	h k l	Experimental 2-theta
7.914	3.957	0.24	2.527	2.3619	111	38.139
9.8082	4.9041	0.20391	2.1 2.04	2.0455	200	44.291
13.8704	6.9352	0.14419	1.5	2.3619	220	64.634

6.4 Summary

All nanoparticles were characterised using UV-VIS spectroscopy, SEM, EDX , XRD and TEM to confirm the presence of NPs and identify the morphology, elemental analysis, crystalline nature and lastly TEM to obtain the SAED for assignation of the crystalline nature and HRTEM for elucidation of the d-spacing of the lattice fringes. Indexing the selected area electron diffraction (SAED) of NPs and compare the calues of R (d-spacing) with XRD data or data base ICDD is evidence that all produced NPs are crystalline (single crystal or polycrystalline), which enhance the antibacterial activity of the nanoparticles unlike the amorphous properties. For example, the crystalline phase of the prepared TiO2–Ag nanoparticles calcined powder at 300 °C (CB300) had the highest antibacterial properties which inhibited bacterial growth by 90%. However, no major decrease in the number of colonies was reported in noncalcined powder (CB), because of the amorphous structure of CB. It is reasonable to say that the growth delay of *E. coli* is due to the presence of silver nanoparticles and not due to the TiO2 nanoparticles (Amin *et al.*, 2009). It was reported previously that high atomic density facets such as (111) enhance the reactivity of Ag (Acharya *et al.*, 2018; Rojas-Andrade, 2015). It was established that atoms were more reactive on the facets of higher surface energy, which may cause them to interact rapidly with oxygen-containing groups of lipopolysaccharide molecules that can result in enhanced attachment to the cell membrane of bacteria and ultimately create more rapid cell death (Acharya *et al.*, 2018).

Chapter 7.

Shape controlling synthesis of Nanoparticles

7.1 Shape controlling synthesis of Nanoparticles

Noble metal nanostructures are extensively used in a variety of applications including catalysis, electronics, biomedical research, antibacterial, surface-enhanced Raman scattering (SERS) and surface plasmon resonance (SPR). Different applications require nanostructures with specific morphologies. For instance, catalysis often demands the noble metal nanostructures to be deposited on ceramic supports with a high surface area. It has been reported that the catalytic activity and selectivity of noble metal nano structures are mostly dependent on the facets exposed on the surface (Jiang, 2011). In the recent years, metal nanoparticles have received considerable attention as they serve as building blocks for the next generation of nanodevices. Nanoparticles have unique electrical, optical and magnetic properties that primarily depend on the shape of the nanoparticles (Adams, 2003). The most common and simplest used bulk solution synthetic method for metal nanoparticles is the chemical reduction of metal precursors, using a soluble metal precursor, as well as stabilising and reducing agents. The stabilising agents cap the particles and avoid additional growth or aggregation. Reducing agents for instance, sodium borohydride (NaBr) and alcohols are most commonly used in metal nanoparticles synthesis. Organic molecules and polymers bind to the particles surface, which serve as stabiliser (Pillai, 2004).

Controlling the shape of metal NPs is important to enhance their performance in different applications, ranging from catalysis to electronics (Cao *et al.,* 2016), bio-sensing (Sannomiya *et al.,* 2009) and antibacterial activities (Acharya *et al.,* 2018). Size and shape controls in a chemical reduction method have the advantages of being a simple low cost process. The size and shape of the nanoparticles can be determined by optimising the experimental parameters, such as temperature, reaction time and molar ratio of the capping agent with the precursor (Dang *et al.,* 2011). Different crystal structures or directions may reveal different chemical and physical properties. For instance, the (111), (100) and (110) surfaces of the face centred cubic (FCC) metal have different surface atom densities, chemical reactivity and electronics structure (Zhou *et al.,* 2011; Lee *et al.,* 2007). In addition, it was argued previously that the antibacterial activity of silver is greater when high atomic density facets are present, for instance the {111} plane (Figure 7.1) represents the Miller index of (111) plane.

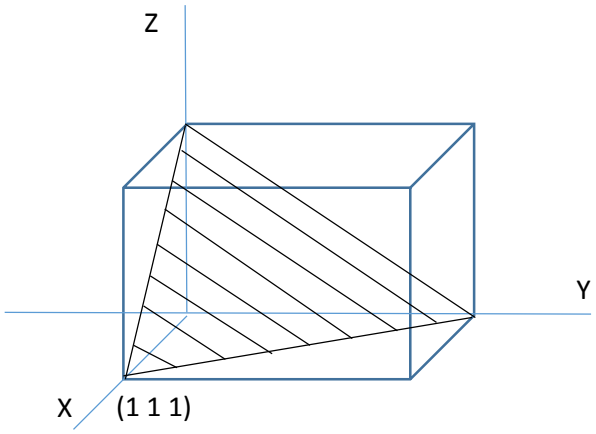

Figure 7.1: Miller indices of (111) planes.

Ag nano spheres (AgNS) were produced using $AgNO_3$ as a precursor and Sodium citrate as a weak reduction agent, as per method (II 1-2) (Ratyakshi *et al.,* 2009). The formation of spherical shape AgNPs related to citrate ion reduce the Ag ion initially as a result of capping the nanocluster by means of citrate. After the formation of the NPs no further etching afterward resulting in shape of faceted nanospheres (Figure 6-2b) (Pillai *et al.,* 2004). Ag nano octahedrons (AgNOct) were synthesised using the polyol method. The primary step in this process includes heating a polyol, for instance ethylene glycol (EG) with a precursor (AgNO3) in the presence of a polymeric capping agent such as (PVP) as per method (II 1-1). The addition of a small amount of Sodium bromide (NaBr) prior to the addition of a precursor plays a role in the etching of the particle seeds, facilitating the formation of truncated octahedron enclosed by {111} facets (Figure 6-2a). The PVP also works as a shape-control agent prompting the reduction of $AgNO_3$ onto specific crystal faces, while preventing reduction onto others (Gupta *et al.,* 2011). Additionally, it was previously reported that replacement of the catalyst (Br^-) to Cl^- or Fe^{3+} produced silver nanocubes or nanowires respectively (Wiley *et al.,* 2006).

Cu nano spheres (CuNS) were synthesised using $CuSO_4$ as a copper salt, PVP as a surfactant and ascorbic acid as a reducing agent. $CuSO_4$ primarily separates to Cu_2+ and SO_4 in water and Cu_2+ ions are hydrolysed into $Cu(OH_2)$. Further reduction of $Cu(OH_2)$ takes place in the presence of ascorbic acid to form Cu_2O. Lastly, Cu_2O is further reduced to form Cu nano sphere as per method (III 1-1)(Figure 6-11a). CuNPs are highly unstable as they oxidise rapidly, although this can be inhibited by the use of ascorbic acid (Gurav *et al.,* 2014). Cu nano cubes (CuNC) were synthesised using the polyol method. The primary step in this process includes heating a polyol such as ethylene glycol (EG) with a precursor ($CuSO_4$). The addition of a small amount of Sodium hydroxide (NaOH) prior to the addition of a precursor plays a role in the etching

of the particle seeds, facilitating the formation of a cube shape as per method (III 1-2) (Figure 6-11b). Likewise, the molar ratio (1:1) of NaOH:$CuSO_4.5H_2O$ and high temperature of 165 °C played important roles in the synthesis of copper nano cubes (Sun *et al.*, 2005).

Au nano spheres (AuNS) were created using HAuCl4 as a gold salt and Sodium citrate as a weak reduction agent, as per method (IV 1-1) (McFarland *et al.*, 2004). The formation of spherical shape AuNPs related to citrate ions reduce the Au ions firstly, while the citrate subsequently capped the nanoparticles. After the formation of the NPs, no further etching occurs afterward, resulting in nanosphere shapes (Figure 6-19a) (Kimling *et al.*, 2006; Pillai *et al.*, 2004). Au nano octahedrons (AuNOct) were synthesised using HAuCl4 as a gold salt and Sodium bromide (NaBr) as a reduction agent as per method (IV 1-2) (Wani *et al.*, 2013). AuNPs enclosed by {111} facets octahedrons (Figure 6-19b), when Br- ions present during the reaction truncated octahedron are formed (Xia *et al.*, 2009).

7.2 Shape controlling synthesis of silver nanoparticles

Silver nanoparticles have a magnitude smaller than the wavelengths of visible light that scatter and absorb light due to surface plasmon resonance; incident light occurs through oscillation of conduction electrons. The intensity and frequency of plasmon resonance strongly denote distribution of polarization charges within the nanostructure. Plasmon excitation by a silver nanostructure not only makes its colour in far-field imaging but also makes an electric field near its surface by means of magnification. In recent years, this intense near–field allowed nanoscale wavelength and localization of light for optical devices and nanolithography (Wiley, 2006). Moreover, it has been used to improve the Raman scattering from adsorbed molecules. Theoretical calculations assume that a 50nm silver sphere gives a maximum electric field enhancement factor of $\sim 10^2$ in terms of E^2, although this can be enhanced 100 fold by a sharp corner within the nanostructure, for example, a tetrahedron. Here, we produce a novel shape for first time synthesis of hexagonal prism silver nanoparticles. Synthesising nanoparticles by a solution based method has proven effective for the high-yield of nanostructures with controlled shapes and properties (Jana, 2001). Silver, copper and gold have similar features to the face centred cubic crystal structure. However, most anisotropic shapes can be grown by controlling the metal atoms assembly in solution. The development of shape controlling syntheses to produce silver nanorods, nanowire, nanoplates and triangular nanoprisms in aqueous solutions containing stabilisers (Washio, 2006). In this research, we focused on polyol synthesis where ethylene glycol (EG) serves as both reducing agent and solvent. Polymers are commonly used in the solution based synthesis of colloidal nanostructures recognised as steric capping agents or stabilisers. In particular, poly(vinyl pyrrolidone) (PVP) has gained considerable attention due to its nontoxicity, chemical stability and excellent solubility in many polar solvents (Gupta, 2011).

7.3 Experiment

7.3.1 Materials

All chemicals used in this study were purchased from Sigma-Aldrich, UK, without the need for further purification. They include silver nitride (AgNO3), sodium bromide (NaBr), polyvinylpyrrolidone (PVP) ([C6H9NO]n) and ethylene glycol (EG) (C2H6O2).

7.3.2 Synthesis of different shape AgNPs

Three different AgNPs shapes, such as truncated octahedron, hexagonal prism and nanowire were produced *in vitro* using the following method. To start the synthesis, three solutions were used, one containing 3 ml EG of 0.1M AgNO3, the other containing 3 ml EG of 144mM PVP and 0.11 mM NaBr, and the last one containing 30 ml EG of 10 mM NaBr. 5ml of EG in a three neck round bottom flask was heated on hotplate attached to a condenser at 160C**.** Then add 30ml NaBr 10mM of preheated EG and reflux for 1hour. Next add both solutions: 3ml EG of 94mM AgNO3 and 3ml EG of 144mM PVP and 0.11mM NaBr via a two channel syringe pump into 35ml EG heated. The addition of NaBr to the preheated EG before the addition of the Ag precursor is because this was found to avoid formation of spherical nanoparticles that otherwise contaminate the final product. The reaction solution turned yellow in a few seconds after the addition of AgNO3 and PVP demonstrating the formation of AgNPs. The yellow colour faded in intensity after 10 minutes because of oxidative etching and maintained a light yellow colour for approximately 1hour before turning to brown and then grey as the nanoparticles increased in size. The synthesised nanoparticles were centrifuged at 4600rpm three times and washed with DI water to remove any impurities and unreacted precursors. Truncated octahedron and hexagonal prism were synthesised using the same technique, with the only difference being the use of a condenser and hot plate respectively. To produce nanowire, increasing the concentration of PVP to 0.6M will cause elongated NPs to form a wire. The silver atoms were produced by reducing AgNO3 by way of the following reaction (Gupta, 2011).

$$2HOCH_2CH_2OH \rightarrow 2CH_3CHO + 2H_2O \quad (7.1)$$

$$2Ag^{+} + 2CH_3CHO \rightarrow CH_3CO\text{-}COCH_3 + 2Ag + 2H_{+} \quad (7.2)$$

These reactions are typically performed in the presence of a mediating species such as sodium bromide, sodium sulphide, sodium borohydride and hydrochloric acid. This mediator (NaBr) plays a role in the etching of the particle seeds, facilitating the formation of the hexagonal prism, truncated octahedron and nanowire. The PVP also works as a shape-control agent, prompting the reduction of AgNO3 onto specific crystal faces while resisting the reduction of others.

7.4 Results and discussion

The absorption spectrum of AgNPs solution was recorded, as shown in Figure 7.2. An intense peak was observed at 475nm in Figure 7.2 a and 450nm in Figure 7.2b, attributable to the surface plasmon absorption of AgNPs. Likewise, two peaks observed at 350nm and 375nm respectively in Figure 7.2a (Pal, 2007). The absorption spectra of metal nanoparticles were subjugated by surface plasmon resonances (SPRs) that shift to longer wavelengths as particle size increases. The shape and position of plasmon absorption of AgNPs are primarily dependent on dielectric medium, particle size and the surface adsorbed species. According to Mie's theory (Mie, 1976), only a single SPR band is expected in the absorption spectra of spherical nanoparticles, while anisotropic particles could increase the SPR bands to two or more SPR bands, depending on the shape of the particles. The number of SPR peaks increases as the symmetry of the nanoparticles decreases.

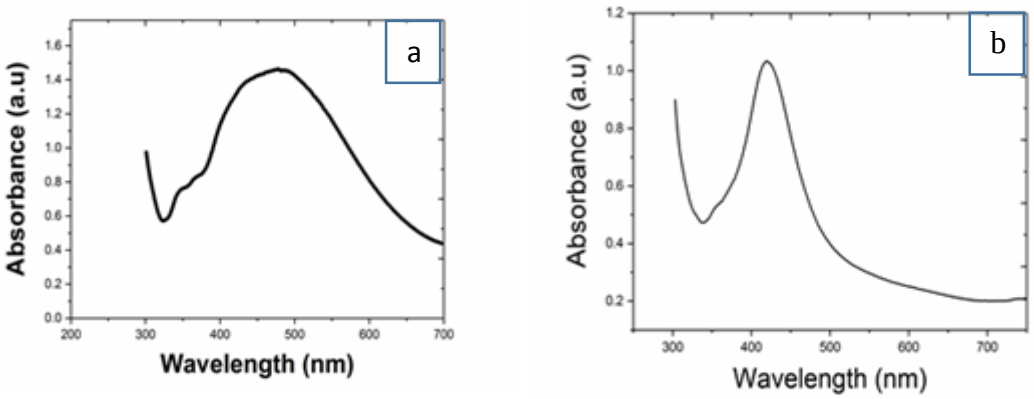

Figure 7-2: Absorption spectra of AgNPs colloidal: (a) prepared on a hot plate after 3 hours (b) prepared using a condenser after 10 minutes.

Scanning electron microscopy (SEM) images (Figures 7.3 to 7.5), revealed more significant differences between these samples in terms of particles morphology. Regarding samples prepared by a hot plate, the reaction time is 1:30 minutes and the particles are observed to be quasi spherical in shape (Figure 7.3(a)). Nevertheless, by increasing the reaction time to 3 hours, a hexagonal prism shape is formed with average size diameter ~ 519 nm (Figure 7.3(b)). However, the experiment prepared using a condenser takes only 10 minutes with a smaller nanoparticle size compared to AgNPs prepared on a hot plate with average size diameter ~194nm (Figure 7.4 (a, b)). When the reaction time is increased to 1:20 minutes, the particles are increased in size, as shown in Figure 7.4 (c, d). In each experiment conducted in air, O2 is present in the reaction solution within the entire process as well as the presence of a ligand for the metal ion. The combinations of the ligand and O2 are a result of a powerful etchant for both the nuclei and seeds. The

presence of Br^- plays a significant role in their morphology (Xia, 2009). As seen in Figure (7.3 to 7.5), AgNPs have different shapes according to the method used and the concentration of PVP, for example the particle prepared using a condenser is more likely truncated octahedron. Conversely, the AgNPs prepared by hot plate is a hexagonal prism, while it is lengthened to wire when the concentration of PVP is increased from 144mM to 0.6M, as shown in Figure 7.5 (a, b). Figure 7.6 shows the suggested growth guide for etching of nanoparticles into particular shapes.

Truncated octahedron prepared by means of a condenser was formed and the etchings started in a few minutes. Hence, the quick preparation of AgNPs lead to less uniformity (25% polydispersity). However, hexagonal prisms prepared on a hot plate were grow from seeds into spherical shapes in a few minutes and maintained as a quasi-spherical shape for 2 hours. Then after 3 hours a hexagonal prism is formed; therefore, the lengthy reaction time produces high uniformity of AgNPs (6% polydispersity) with increasing particle size, while increasing the concentration of PVP to 0.6M using a condenser will elongate the hexagonal prism to form Ag-wire with a needle like structure (pyramid hexagonal prism) in 45 minutes. Both shapes (hexagonal prism and truncated octahedron) have hexagonal facets. The hexagonal prism has (2 hexagonal and 6 square facets) and the truncated octahedron has (8 hexagonal and 4 square facets).

The reason behind the different morphologies of nanoparticles prepared by hot plate and condenser where all the parameters are kept constant such that the concentration of metal salt, capping agent and temperature, might be that the concentration of O_2 using the condenser method is less than the concentration of O_2 using the hot plate method because in the first method the vial was stoppered and sealed, whereas in the other method the vial was just covered by the beaker cover. Hence, the oxygen concentration is high compared to the condenser method that generates more etching and forms a hexagonal prism shape because the oxygen enlarged {111) rather than {100} facet in the hexagonal prism. Meanwhile, when the concentration of PVP is increased to 0.6M using the condenser method, Ag wire is formed as the increase in the concentration of PVP not only prevents aggregation but lengthens the particles and formed wire by enlarging {100} facet during the growth stage.

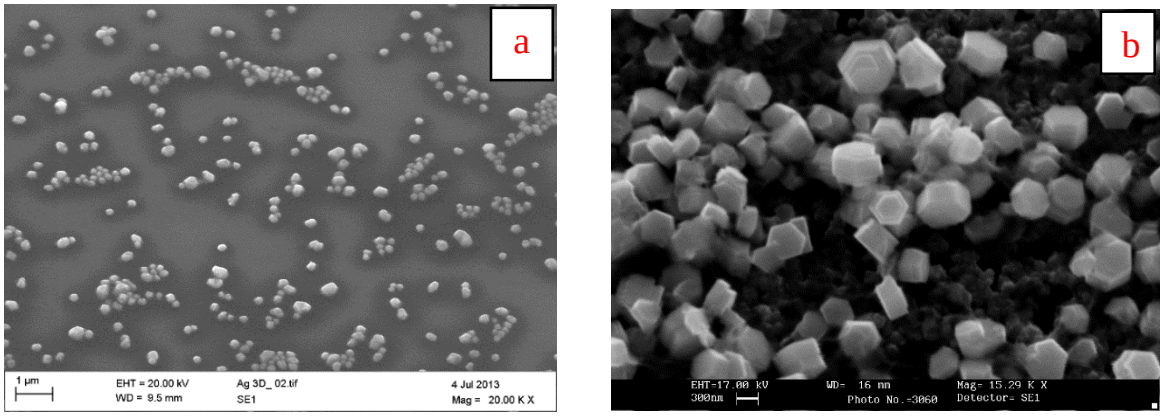

Figure 7-3: SEM images of samples prepared on a hot plate: (a) quasi-spherical AgNPs after 1:30 minutes (b) hexagonal prism AgNPs after 3 hours.

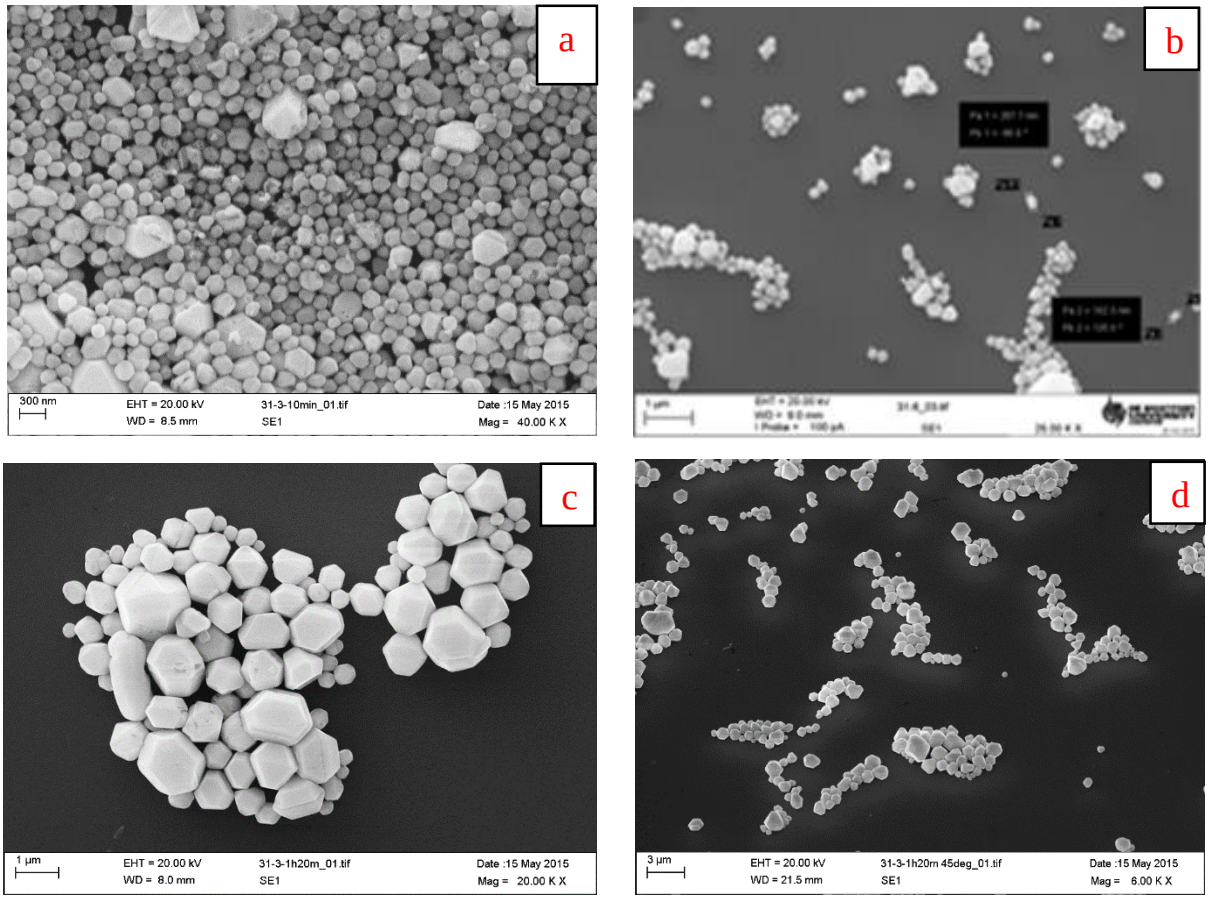

Figure 7-4: SEM images of truncated octahedron prepared using a condenser: (a, b) after 10 minutes, (c, d) after 1:20 hours.

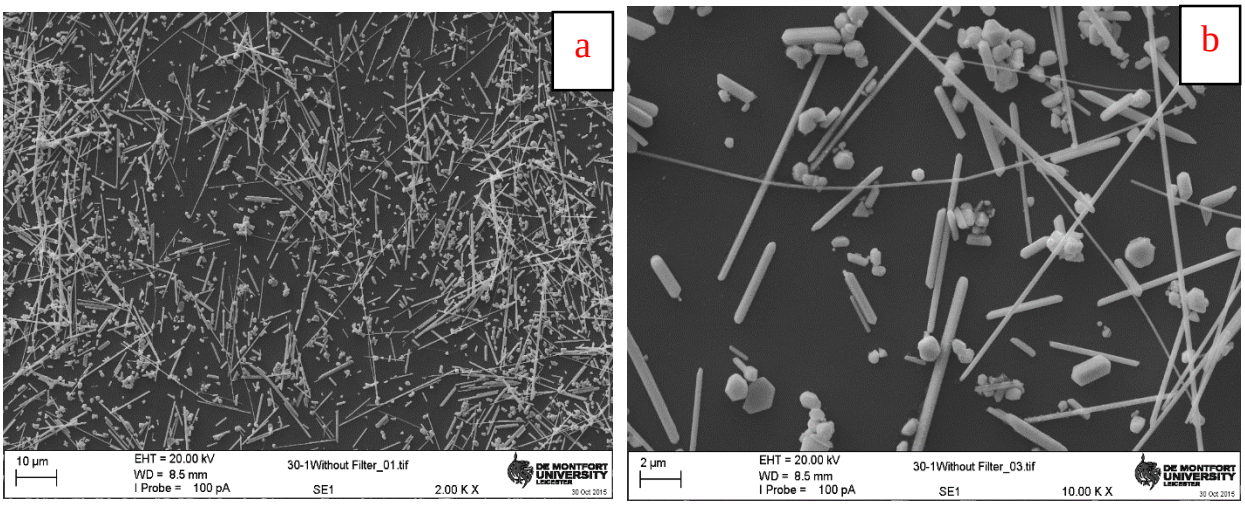

Figure 7-5: SEM images of samples prepared using a condenser: (a, b) Ag nanowires with increasing concentration of PVP to 0.6M.

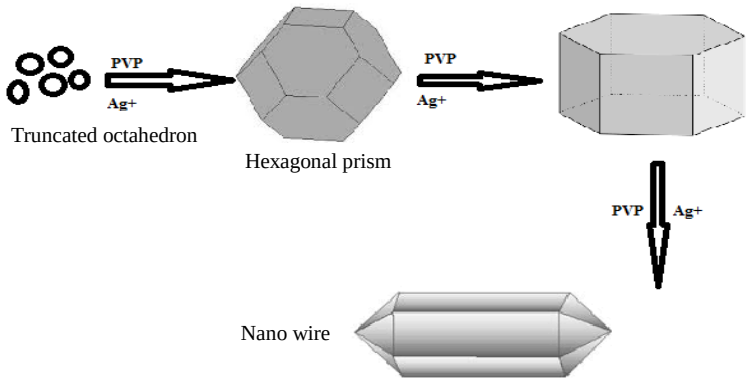

Figure 7.6: Schematic of the nucleation and growth process.

Size distribution is calculated from SEM images for prepared hexagonal AgNPs by hot plate. The reaction time was 3 hours and the average NPs size is 519nm. Where the polydispersity is 9.6% that means the particles are highly uniform (Figure 7.7 (a)). The average size is calculated from SEM images for prepared truncated octahedrons, AgNPs prepared by a condenser is 194nm where the polydispersity is 25%. This means the particles are less uniform compared with particles prepared by the hot plate (Figure 7.7 (b)). The elemental analysis shown in Figure 7.8 (a, b), using energy-dispersive spectroscopy provides the presence of silver NPs and several carbon and nitrogen atoms that are related to the stabiliser (PVP) when prepared

on the hot plate (Figure 7.8 (a)). However, the EDX for AgNPs prepared by the condenser demonstrates the purity of AgNPs.

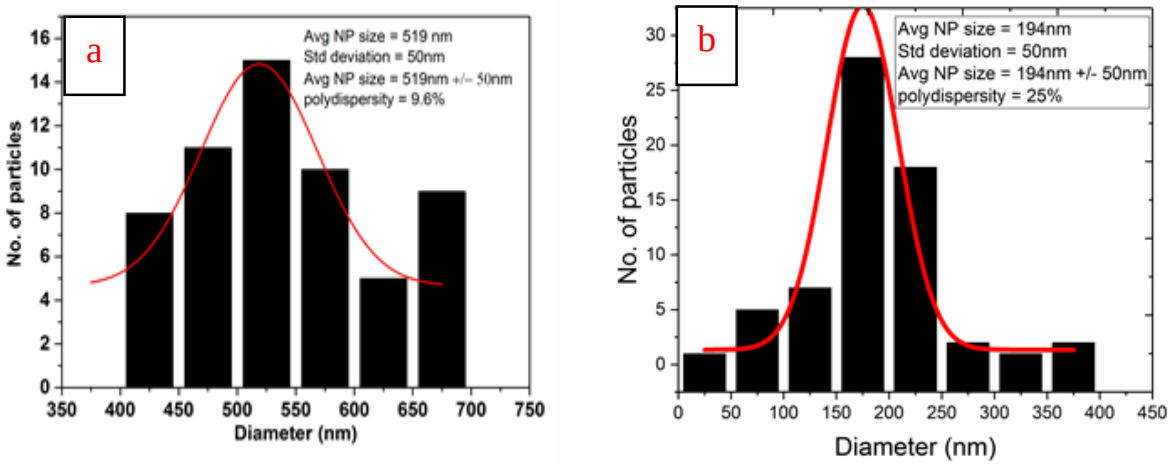

Figure 7-7: Size distribution of AgNPs (a) prepared on a hot plate after 3 hours, (b) prepared using a condenser after 10 minutes.

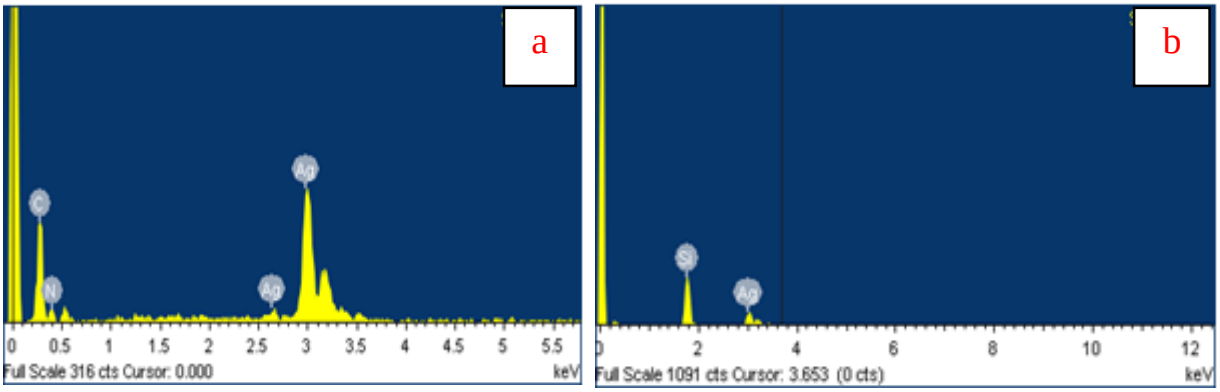

Figure 7-8: EDX for AgNPs: (a) prepared on a hot plate after 3 hours (b) prepared using a condenser after 10 minutes.

The crystal structures of AgNPs were characterised by XRD, as shown in Figure 7.9. All the reflections of the XRD pattern can be readily indexed as the face centred cubic phase of Silver (JCPDS 04-0783) and are in good agreement with 111, 200, 220, 311 and 222 lattice planes. Table 7.1 shows calculations obtained from the XRD pattern of prepared hexagonal prism AgNPs compared with ICDD silver values. The experimental 2θ values in degrees (38.08 - 44.21 – 64.41 – 77.41. 81.60) match 2θ values in ICDD silver: 04-0783. The result confirms that the samples were metallic AgNPs with hexagonal crystal structure. No diffraction peaks of silver oxide were detected in Figure 7.9, which suggests the PVP capped layer on

AgNPs prevents oxidation from forming (AgO). D-spacing was calculated from High-resolution lattice images (HRTEM) of hexagonal prism AgNPs that show 2.30 Å (Figure 7-10) which conform with (111) lattice plane (2.3592 Å) either in ICDD silver crystal structures data (Appendix A) or calculated from diffraction patterns using Bragg's law (Equation 5.3.1). XRD and HRTEM of truncated octahedron (AgNOct) were shown earlier in Chapter 6, Figures (6.5(A) and 6.8) respectively.

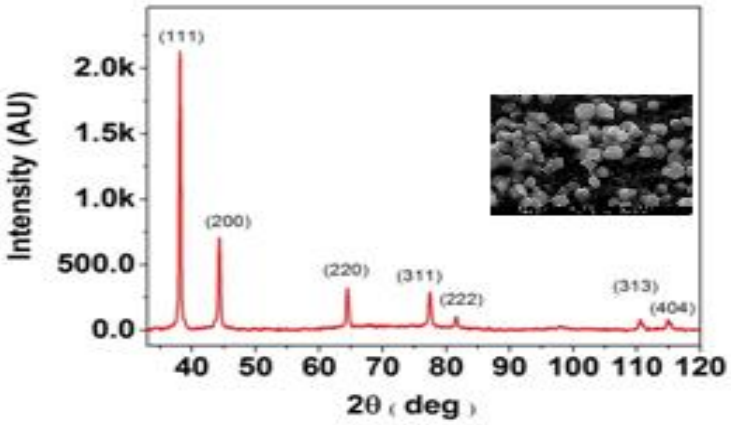

Figure 7-9: XRD pattern obtained confirming the formation of pure FCC silver from the hexagonal prism AgNPs sample.

Table.7-1 Calculations obtained from the XRD pattern of the prepared hexagonal prism (AgNPs) compared with JCPDS silver values

2θ in degrees ICDD silver: 04-0783	**Experimental 2θ in degrees**	**d-spacing calculating from spectra (Å)**	**hkl**	**Experimental lattice constant (Å)**
38.116	38.08**8**	2.36	111	4.08
44.277	44.21	2.02	200	4.08
64.426	64.41	1.44	220	4.07
77.472	77.41	1.23	311	4.08
81.62	81.60	1.18	222	4.08

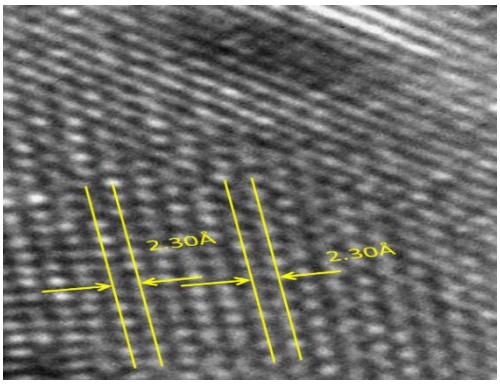

Figure 7-10: High-resolution lattice images (HRTEM) of hexagonal prism AgNPs that exhibits d-spacing of 2.30 Å.

7.5 summary

Different shape silver nanoparticles were produced *in vitro* such as truncated octahedron, hexagonal prism and nano-wire AgNPs, The size and the shape of the nanoparticles can by determined by optimising the experimental parameters for instance temperature, reaction time and molar ratio of the capping agent with the precursor (Dang *et al.*, 2011). Here, all the parameters were kept constant such as the concentration of metal salt, capping agent and temperature, whereas the difference between the experiments is the techniques used, which are the condenser and hot plate methods respectively, for producing the truncated octahedron and hexagonal prism. The reason behind the different morphology could be that the concentration of oxygen is high compared to the condenser technique that produces more etching has occurred and formed a hexagonal prism shape due to enlargement of the Oxygen {111) rather than {100} facet in the hexagonal prism. Meanwhile, when the concentration of PVP is increased to 0.6M using the condenser method Ag wire is formed because the increase in the concentration of PVP not only prevents aggregation but elongates the particles and formed wire by means of the enlarged {100} facet during the growth stage.

Different crystal structures or directions may reveal different chemical and physical properties. For instance, the (111), (100) and (110) surfaces of the face centred cubic (FCC) metal have different surface atom densities, chemical reactivity and electronic structures (Zhou *et al.*, 2011; Lee *et al*., 2007). Here, we produce a novel shape for the first time synthesis of hexagonal prism silver nanoparticles, which can been produced via the modified polyol method. Moreover, the amount of metal salt, the ratio of metal salt to stabiliser and the reaction time played a crucial role in determining the particle size and shape. The unique morphology is attributed to the presence of Br^-, whilst the oxygen concentration plays an important role in the etching process as a result of the final morphology. However, we could not produce smaller size hexagonal prism AgNPs which have an average size diameter ~ 519 nm. Truncated octahedron silver

nanoparticles (AgNOct) and silver nano sphere (AgNS) have been selected for further antibacterial activity investigation as they have a similar size diameter ~195.

Chapter 8.

Antibacterial activity studies

8.1 Introduction

The efficacy of the nanoparticles against both Gram-negative and Gram-positive bacteria will be investigated via culturing of the microorganism using nutrient broth and nutrient agar. Standard antimicrobial testing procedures will be employed, such as disc diffusion and minimum inhibitory concentration. The interaction between nanoparticles and bacterial cells will be assessed by spread plating to establish viable counts after treatment with nanoparticles. Finally, microscopy techniques will be employed (Scanning Electron Microscopy) to observe any changes in the cell membrane that might lead to bacteria death.

In this regard, this study aims to determine shape dependence NPs on the antimicrobial efficacy of (AgNS, AgNOct, CuNS, CuNC, AuNS and AuNOct) against *E.coli* and *E.faecium.*

8.2 Methodology

8.2.1 Bacterial strains and culture conditions

The antibacterial activities of the nanoparticles were investigated using *Escherichia coli* (NCTC8196) and *Enterococcus faecium* (NCTC12202) which were selected as a model for Gram-negative and Gram-positive bacteria respectively. Bacteria strains were stored in Luria Bertani broth at -80°C. The bacteria were then cultured in nutrient broth (NB) (CM0001) at 37 °C for 24 hours resulting in a final cell concentration of 8 $\log_{(10)}$ for all investigations. Cultures were stored on nutrient agar (NA) (CM0003) plates at 4 °C then the cultures were revived in NB broth and sub-cultured at regular intervals.

8.2.2 Screening of NPs for antibacterial activity

A disc diffusion method was used to determine bacterial sensitivity to metal nanoparticles. Initially, 20ml of molten nutrient agar (NA) media was poured into sterilised Petri dishes. 100µl (8 $\log_{(10)}$) of the bacteria culture was then dispensed into the plate and a sterilised spreader was used to spread the bacteria on the surface of the NA. Disc diffusion paper were impregnated with 50 µl of 100µg/ml of the nanoparticles (AgNS, AgNOct, AuNS, AuNOct, CuNS or CuNC). Discs were then placed on the NA plates, then incubated for 24 hours at 37 °C. The zone of inhibition was measured using a Vernier caliper. Measurements were taken from one edge of the clear zone to the other edge.

8.2.3 Determination of minimum inhibitory concentrations (MIC)

Minimum inhibitory concentrations (MIC) were assessed using the broth dilution method. A dilution series with 9.9 ml nutrient broth medium containing different shaped NPs (AgNS, AgNOct, AuNS, AuNOct,

CuNS or CuNC) using two-fold serial dilutions ranging from 10 µg/ml to 250µg/ml was prepared in a test tube. Each set was inoculated aseptically with 100µl (8 $\log_{(10)}$) of *E. coli* or *E. faecium* suspension and incubated for 24 hours at 37 °C. The MIC was determined by turbidity, where the minimum concentration of NPs prevents the visible growth of either *E. faecium* or *E. coli*. The MIC was defined as the lowest concentration of an antibacterial agent inhibiting the growth of a test bacterium (Giannousi, 2017).

8.2.4 Growth inhibition using a 96-well plates reader

To investigate the growth kinetic curves of bacterial cells exposed to final concentrations of either 10, 50 or 100µg of AgNS, AgNOct, CuNS or CuNC and 50, 100 or 250µg of AuNS and AuNOct, aliquots of 200µl of either *E. coli* or *E. faecium* (8 $\log_{(10)}$) in the presence of NPs were dispensed into 96-well plates. Optical densities (OD) were measured every hour (from 0 to 24 h) at 600 nm using a spectrophotometer (Spectra Max Plus 384). Optical densities for the positive control (bacteria) and negative control (metals only) were also measured.

8.2.5 Viable counts of growth inhibition

Aliquots of 100µl of overnight cultures of either *E. coli* or *E. faecium* (8 $\log_{(10)}$), were inoculated into fresh NB containing 100µg/ml of either AgNS, AgNOct or AuNS, AuNOct, CuNS or CuNC. The cultures were then incubated at 37°**C** in a shaking incubator and six samples of each metal nanoparticles were taken at 0, 2, 4, 6 and 24 hours. All the samples were serial diluted in 9.9 ml of phosphate buffered saline (PBS), then aliquots of 100µl from each dilution were spread-plated onto NA plates and incubated at 37°**C** for 24 h, and the colony-forming units (CFU) enumerated.

8.2.6 Visualisation of interaction between metal nanoparticles and bacteria using SEM

Aliquots of 100µl of overnight cultures of either *E. coli* or *E. faecium* (8 $\log_{(10)}$), were inoculated into fresh NB containing 100µg/ml of either AgNS, AgNOct or AuNS, AuNOct, CuNS or CuNC, suspensions were sonicated for 10 mins prior to usage. The cultures were then incubated at 37°C in a shaking incubator and 36 samples were taken at 0, 4 and 24 hours. Aliquots of 10 µl were deposited onto a silicon substrate the samples were then dried in sterile conditions, washed with PBS and dehydrated with 95% ethanol for 10 mins at room temperature. Samples were then mounted onto aluminium stubs and coated with 15 nm of gold in a gold coater (Quorum Q150 RS, East Sussex, UK), ready for imaging. Untreated bacteria (*E. coli* or *E. faecium*) was used as a positive control and for a comparison of morphological changes in cell membrane. The interaction between NPs and bacteria was visualised using SEM (Evo HD15 Carlzeiss, Jena, Germany).

8.2.7 Statistical analysis

All investigations were performed in triplicate on at least two separate occasions and the data were stated as mean ± standard deviation. The statistical analysis was completed using SPSS Statistics Version 22 for Windows with significance set as $p = 0.05$. Test of normality was conducted using a Kolmorgorov-Smirnov test and variance of homogeneity tested using Levines test. ANOVA (*t*-test) was carried out, if all assumptions were met one-way analysis of variance. Tukey post-hoc tests were conducted to investigate where significant differences between group means occurred. An example of ANOVA output can be found in Appendix F.

8.3 Results and discussion

8.3.1 Screening of metal NPs for antibacterial activity

Screening data as per method (8.2.2), indicates that AgNOct have greater antimicrobial efficacy against both bacteria when compared with AgNS, with zones of inhibition of 23 and 22 mm against *E. coli* and *E. faecium* respectively. This compares to inhibition zones of 21 mm against *E. coli* and 20 mm against *E. faecium* for AgNS. Figure 8-1 illustrates that CuNC are more effective on both bacteria when compared with CuNS, with zones of inhibition of 37 and 30 mm against *E. coli* and *E. faecium* respectively. This compares to inhibition zones of 35 mm against *E. coli* and 28 mm against *E. faecium* for CuNS. AuNOct have greater antimicrobial efficacy against both bacteria when compared with AuNS, with zones of inhibition of 25 and 23 mm against *E. coli* and *E. faecium* respectively. This compares to inhibition zones of 24 mm against *E. coli* and 22 mm against *E. faecium* for AuNOct.

A previous study of the zone of inhibition of CuNPs shows 15/16 mm for *S. aureus* and *E. coli* respectively (Namasivayam, 2013). Studies of zones of inhibition against *E. coli* when comparing different shape NPs showed triangle AgNPs had a zone of inhibition of 1.3 cm, while spherical AgNPs had a zone of inhibition of 0.8 cm (Van Dong, 2012). A recent study of zone of inhibition using AuNPs demonstrates inhibition zones of 31-35 mm for *E. coli* and 22-25 mm for *S. aureus* (Shamaila, 2016). Zones of inhibition data in the current study indicates that synthesised NPs inhibit the growth of *E. coli* and *E. faecium*. A greater zone of inhibition of CuNP does not necessarily indicate greater efficacy compared to AuNP or AgNP due to the solubility of the metals varying and thus having an impact on the zones of inhibitions.

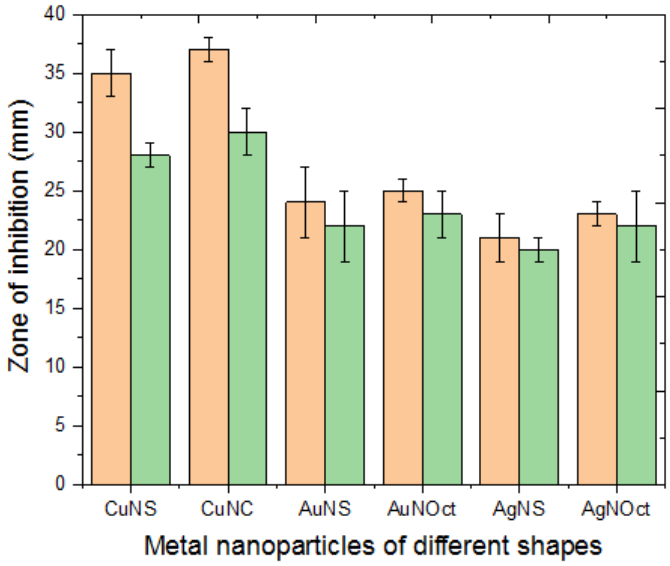

Figure 8- 1: Zone of inhibition of metal NPs with different shapes against *E. coli* and *E. faecium* (n= 6± SD).

E. coli *E. faecium*

8.3.2 Determination of minimum inhibitory concentrations (MIC) of metal NPs

The MIC of the nanoparticles inhibiting visible bacterial growth on the NB was assessed as per the method described in Section 8.2.3. *In vitro* MIC results representing the antibacterial activity of different shape NPs are shown in Table 8.1. Among these microorganisms, the MIC of AgNOct against *E. coli* was the lowest 10µg/ml, followed by the MIC of CuNC and AuNOct 15 µg/ml and 50µg/ml respectively. The MIC of AgNOct against *E. faecium* was higher than the MICs against *E. coli* 55µg/ml, followed by the MIC of CuNC and AuNOct 90 µg/ml and 100µg/ml respectively. The MICs of AuNS against *E. faecium* and *E. coli* are the highest 250µgl/ml and 230µgl/ml respectively. The results suggests that AgNOct is the greatest antimicrobial metal against *E. coli* followed by CuNC and AuNOct.

The MIC shown in this investigation were significantly lower than those previously published, demonstrating that the antibacterial effect of AgNPs against different bacterial strains can vary. For example, a study on *E. coli* by Wang (2012), revealed higher MIC (60 µg/ml) than the MIC obtained in the present study (10 µg/ml) for AgNOct. Besides, the MIC for the Gram-positive bacteria *S. aureus*, *B. subtilis* also had higher MICs (100 µg/ml) than the MICs obtained in the present research of 55 µg/ml for AgNOct against *E. faecium*.

A recent study of copper nanoparticles against *E. coli* by De Alba-Montero (2017), exhibited higher MIC (40 µg/ml) than the MIC obtained in the present study for CuNC (15 µg/ml), whereas the MIC of CuNS (125 µg/ml) is higher than the MIC of CuNPs (De Alba-Montero, 2017). However, the MIC of CuNPs for

E. faecalis was 20 µg/ml, lower than the MICs obtained in the in the present study of 90 and 130 µg/ml for CuNC and CuNS respectively.

Previous studies of gold nanoparticles against *E. coli* by Chandran *et al.* (2014), showed an MIC of 400 µg/ml which is significantly higher than the MICs obtained in the present study of 50 and 230 µg/ml for AuNOct and AuNS respectively. In addition, the MICs for the Gram-positive bacteria *S. typhi, S. enterica, B. cereus* and *S. aureus* (Chandran *et al.,* 2014), also had higher MICs (800 µg/ml) than the MICs obtained in the present research of 100 and 250 µg/ml for AuNOct and AuNS respectively.

Table 8.1 Minimum inhibitory concentration of different shaped NPs (µg/ml) against *E. coli* and *E. faecium,* (n= 6± SD)

Microorganisms	Minimum inhibitory concentration of different shape NPs (µg/ml)					
	AgNS	AgNOct	CuNS	CuNC	AuNS	AuNOct
E. coli	95±5	10±6	125±4	15±2	230±6	50±5
E. faecium	110±4	55±2	130±3	90±3	250±7	100±3

8.3.3 Determining the growth inhibition of *E. coli* and *E. faecium* in the presence of metal NPs

I- Silver nanoparticles

The efficacy of spherical and truncated octahedral AgNPs was elucidated against *E. coli* and *E. faecium* using optical density as per method 8.2.4. After a lag phase of approximately 4 hours, control cultures without AgNPs showed a sharp increase in optical density (OD). *E. coli* treated with AgNOct showed inhibited growth for all concentrations (100, 50, 10 µg) (Fig.8-2). However, growth was observed for *E. faecium* at lower concentrations (50, 10 µg), with only 100µg completely inhibiting growth (Fig.8-3). There was a significant ($p \leq 0.05$) decrease in growth for all concentrations compared to the control. The inhibitory effects observed were higher in *E. coli* compared with *E. faecium* for AgNOct. A significant ($p \leq 0.05$) decrease in absorbance was observed from 0.35au in the control to 0.08au after 24 hours treatment with 10µg AgNOct for *E. coli*. However, a decrease in absorbance was observed from 0.32au in the control to 0.18au after 24 hours treatment with 10µg AgNOct for *E. faecium*.

Inhibition of *E. coli* treated with 100µg/ml of AgNS occurred at 10 h (Fig.8-4). For *E. faecium*, inhibition occurred in the first 6h when treated with 100µg/ml of AgNS and subsequently growth began to occur (Fig.8-5). A significant ($p \leq 0.05$) decrease in absorbance was observed from 0.5au in the control to 0.18au

after 24 hours treatment with 100 µg AgNS for *E. coli*. Likewise, a significant ($p \leq 0.05$) decrease in absorbance was observed from 0.9au in the control to 0.4au after 24 hours treatment with 100µg AgNS for *E. faecium*. When viable count growth curves were generated in the presence of 100µg/ml for AgNOct and AgNS; AgNOct complete inhibited growth occurred after 4 h, suggesting a bactericidal effect, while treatment with AgNS exhibited limited growth suggesting a bacteriostatic effect. A previous study of bacterial growth kinetics reveals a similar growth curve for *E. coli* and *S. aureus* treated with different concentrations of AgNPs (Dehnavi *et al.*, 2013; Shrivastava, 2007).

The antibacterial properties of nanoparticles depend on a number of factors including the type of microorganism and the physicochemical properties of the nanoparticles (Hajipour, Fromm et al. 2012). The rate of bacterial growth can also affect the tolerance of bacteria to nanoparticles: fast-growing bacteria are more sensitive to nanoparticles than slow-growing bacteria (C. Lu, Brauer et al. 2009). This is most likely due to the expression of stress-response genes within the bacteria themselves (Ren, Hu et al. 2009).

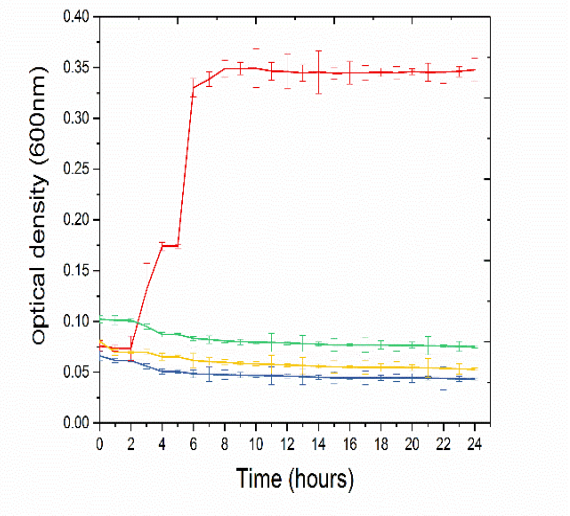

Figure 8-2: *E. coli* growth curves treated with different concentrations (µg/ml) of AgNOct (± SD, n=6), Control *E. coli* , 100µg AgNOct , 50µg AgNOct , 10 µg AgNOct

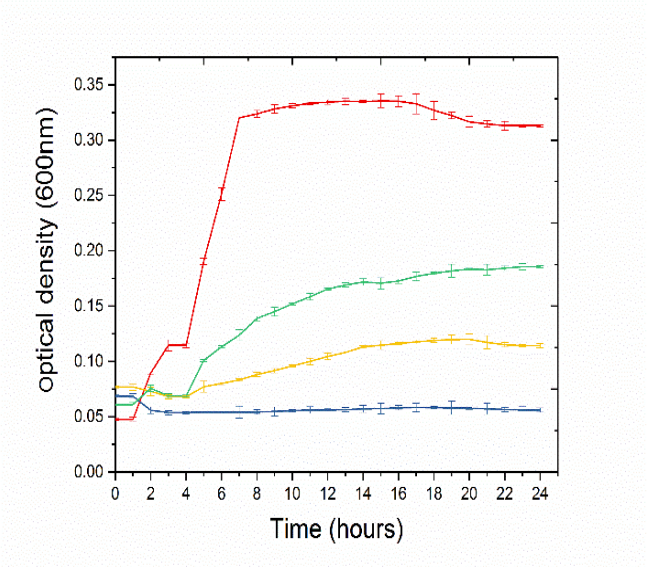

Figure 8-3: *E. faecium growth* curves treated with different concentrations (µg/ml) of AgNOct (± SD, n=6), Control *E. faecium* , 100µg AgNOct , 50µg AgNOct , 10 µg AgNOct

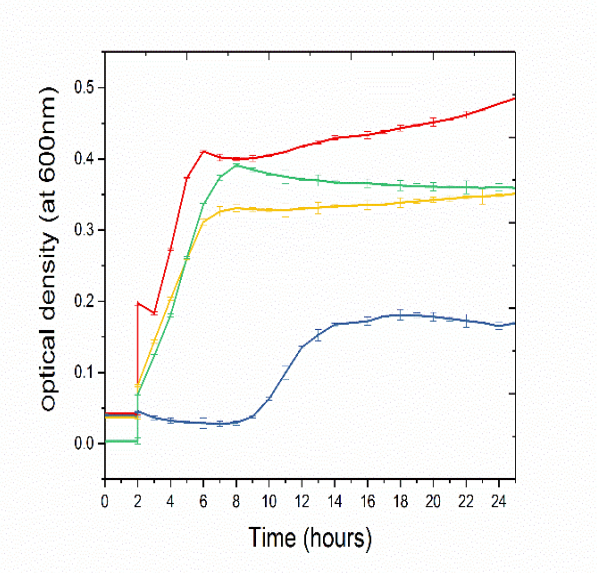

Figure 8-4: *E. coli* growth curves *treated* with different concentrations (µg/ml) of AgNS (± SD, n=6), Control *E. coli* , 100µg AgNS ,50 µg AgNS , 10 µg AgNS

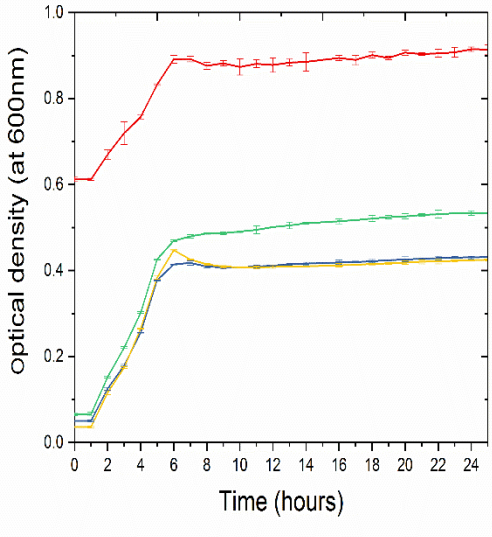

Figure 8-5: *E. faecium* growth curves treated with different concentrations (µg/ml) of AgNS (± SD, n=6), Control *E. faecium* , 100µg AgNS , 50 µg AgNS , 10 µg AgNS

II- Copper nanoparticles

The growth of *E. coli* and *E. faecium* treated with 100, 50 and 10 µg of CuNS caused growth inhibition at all concentrations, occurring at 6h and 4h respectively. The growth observed at these time points was significantly different ($p \leq 0.05$) compared to the control (Figure 8-6, 8-7). The antibacterial efficacy of CuNC against *E. coli* (Figure 8-8) was determined to be more effective than *E. faecium* and completely inhibited growth at the higher concentration of 100 µg. *E. faecium* treated with 100, 50 and 10 µg of CuNC caused only a delay in growth even at high concentrations after 6 hours growth began to take place (Figure 8-9), suggesting that CuNC was enough to result in a significant ($p \leq 0.05$) reduction in comparison to the control. Similar growth kinetics were observed for *E. coli* treated with different concentrations of CuNPs in a study by Raffi (2010).

Results from in vitro studies in animal models demonstrate size-dependent effects of Cu particles (Chen, Meng et al. 2006). For example, nanosized Cu particles have been found to be more toxic than microsized Cu particles following oral administration to rats (Chen et al. 2006). Cu ions are redox-active, meaning that the high intracellular concentration, which can result after dissolution of CuNPs inside the cell, usually results in great oxidative stress (Chen et al. 2006) . Signs of oxidative stress and genotoxicity have also been reported after cellular exposure to copper oxide nanoparticles (CuONPs) and include the generation of intercellular reactive oxygen species (ROS) and oxidative DNA lesions (Hanagata, Zhuang et al. 2011, Ahamed, Siddiqui et al. 2010). Nanoparticles of Cu and CuO have different mechanisms of toxicity following cell exposure. CuNPs target the cell membrane causing a rapid loss of its integrity, which then leads to cell death. Conversely, CuONPs appear endocytosed within cells in the first hours of interaction, which is followed by DNA damage (Midander, Cronholm et al. 2009).

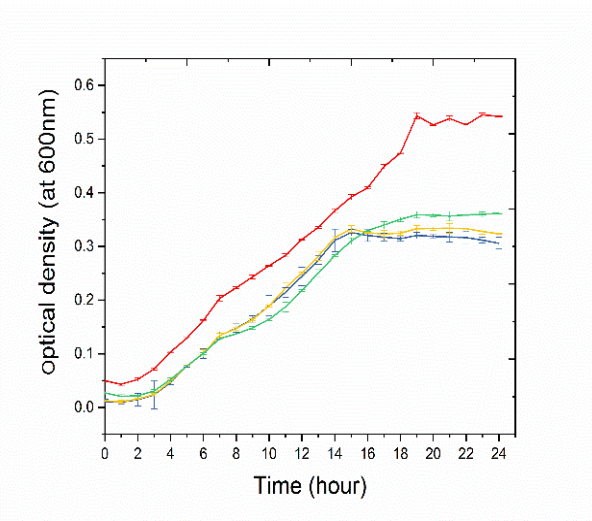

Figure 8-6: *E. coli* growth curves treated with different concentrations (µg/ml) of CuNS (± SD, n=6), Control *E. coli*, 100µg CuNS, 50µg CuNS, 10µg CuNS

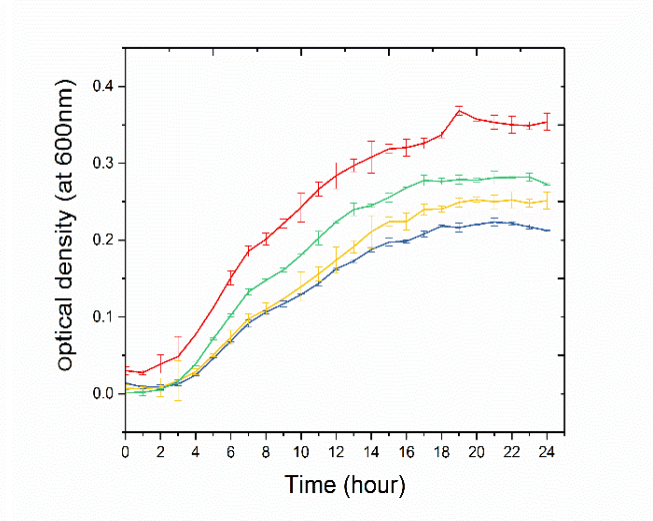

Figure 8-7: *E. faecium* growth curves treated with different concentrations (µg/ml) of CuNS (± SD, n=6), Control *E. faecium*, 100µg CuNS, 50µg CuNS, 10µg CuNS

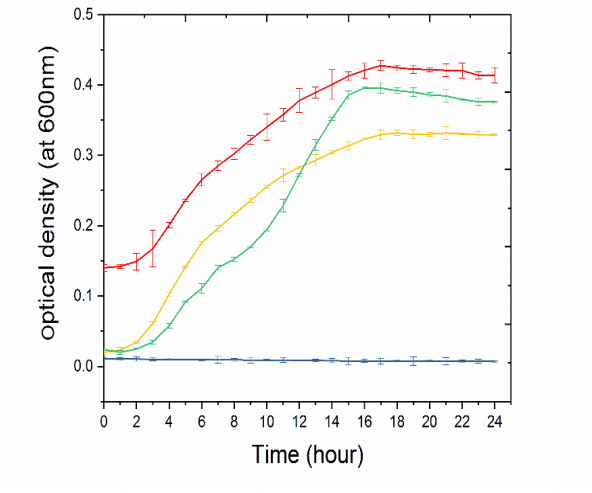

Figure 8-8: *E. coli* growth curves treated with different concentrations (µg/ml) of CuNC (± SD, n=6), Control *E. coli*, 100µg CuNC, 50µg CuNC, 10µg CuNC

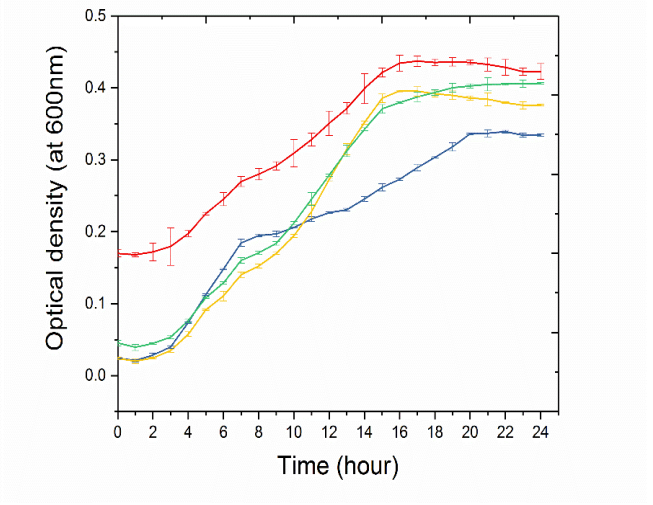

Figure 8-9: *E. faecium* growth curves treated with different concentrations (µg/ml) of CuNC (± SD, n=6), Control *E. faecium*, 100µg CuNC, 50µg CuNC, 10µg CuNC

III- gold nanoparticles

Figures 8-10 and 8-11 show the growth kinetics for *E. coli* and *E. faecium* treated with AuNS. The growth of *E. coli* and *E. faecium* treated with 250, 100, 50µg of AuNS caused only growth delay even at high concentrations but was found to be significantly different ($p \leq 0.05$) in comparison with the control medium. High concentrations of AuNOct 250/100µg were found to be more effective and completely inhibiting growth for *E. coli* (Figure 8-12). However, the lower concentration of AuNOct only shows growth delay, though statistically significant ($p \leq 0.05$) reductions were observed. *E. faecium* treated with 250, 100, 50µg of AuNOct caused a significant ($p \leq 0.05$) growth reduction in comparison with the control medium (Figure 8-13). Badwaik (2012), demonstrated similar *E. coli* and *Staphylococcus epidermidis* kinetics growth curves treated with different concentrations of AuNPs.

Gold NPs enhanced the antimicrobial activity in two steps. Firstly, they altered the membrane potential and decreased adenosine triphosphate synthase (ATP) activities, hence decreasing the metabolism process. Secondly, they prevented the subunit of the ribosome for tRNA binding, consequently disintegrating its biological mechanism. AuNPs evidenced to be low toxic to mammalian cells (Shamaila, Zafar et al. 2016). AuNPs demonstrate size dependent by enhanced the surface area to produce some electronic effects, consequently enhancing the surface reactivity of NPs. Furthermore, Bacterial proteins of the cell wall and cytoplasm were responsible for the function of the cell. AuNPs mainly interact with phosphorus- or sulfur-containing soft bases. Hence, the phosphorus-containing DNA molecules and sulfur-containing proteins are preferred sites for AuNPs to attack. AuNPs interact to thiol groups of enzymes such as nicotinamide adenine denucleotide (NADH) dehydrogenases and interrupted their respiratory chains consequently, major damage existed in the cell structures and lastly led to cell death (Cui, Zhao et al. 2012).

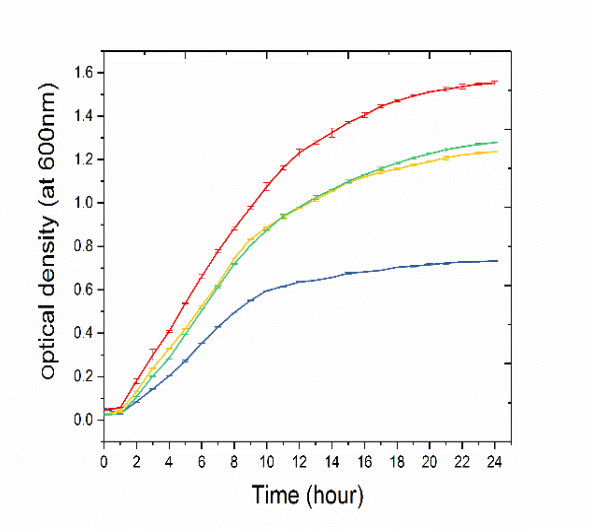

Figure 8-10: *E. coli* growth curves treated with different concentrations (µg/ml) of AuNS (± SD, n=6), Control *E. coli* , 100µg AuNS , 50µg AuNS , 10µg AuNS

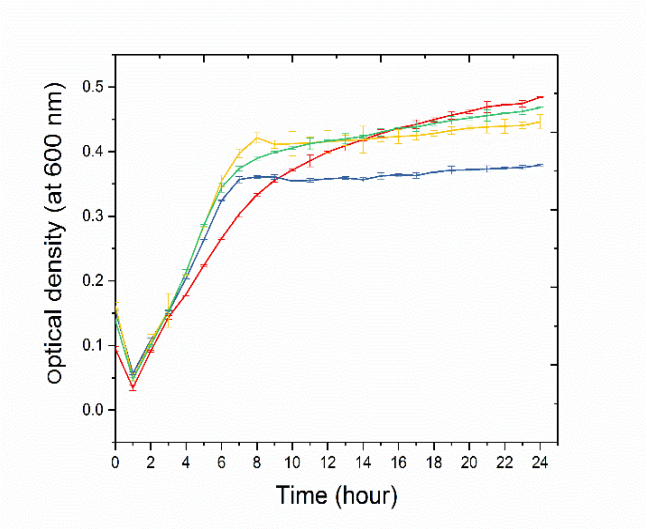

Figure 8-11: *E. faecium* growth curves treated with different concentrations (µg/ml) of AuNS (± SD, n=6), Control *E. faecium* , 100µg AuNS , 50µg AuNS , 10µg AuNS

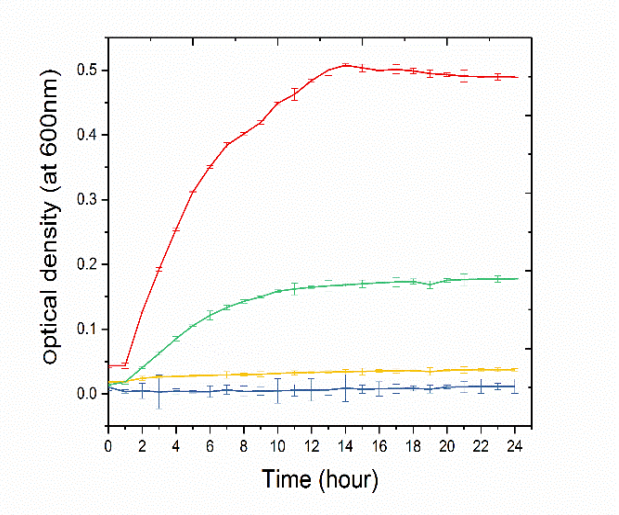

Figure 8-12: *E. coli* growth curves treated with different concentrations (µg/ml) of AuNOCT (± SD, n=6), Control *E. coli* , 100µg AuNOCT , 50µg AuNOCT , 10µg AuNOCT

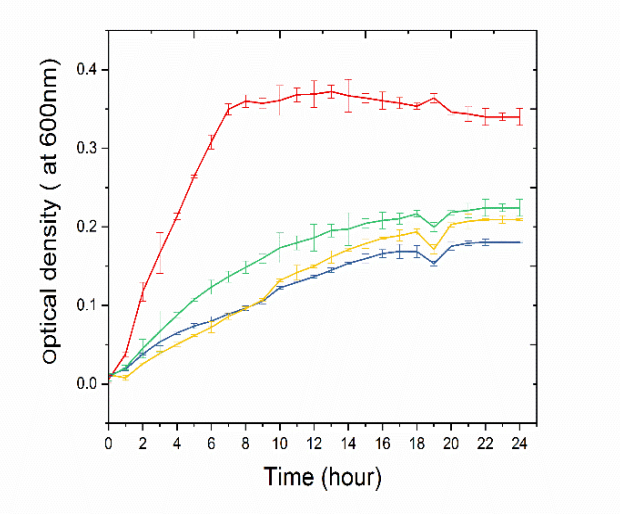

Figure 8-13: *E. faecium* growth curves treated with different concentrations (µg/ml) of AuNOCT (± SD, n=6), Control *E. faecium* , 100µg AuNOCT , 50µg AuNOCT , 10µg AuNOCT

8.3.4 Viable counts of growth inhibition for bacteria treated with NPs

Viable counts of growth inhibition for bacteria treated with NPs were enumerated as per the method in 8.2.5. The antibacterial properties of AgNS increased over 24h with a limited reduction in growth in the first 2 hours, to a significant ($p \leq 0.05$) reduction of 3.26 log(10) CFU/mL and 3.18 log(10) CFU/mL after 24 hours for *E. coli* and *E. faecium* respectively. Furthermore, the bacteria treated with AgNOct exhibits a significant ($p \leq 0.05$) reduction in growth from the first 2 hours, to a reduction of 5 log (10) CFU/mL and 8 log (10) CFU/mL for *E. faecium* and *E. coli* respectively (Table 8.2). AgNOct displays strong antibacterial activity compared with AgNS due to the geometric structure of the octahedron shape where (111) faceted is dominant, as seen in Figure 6-5 (XRD data). Generally, spherical AgNPs exhibit a dominant (100) peak, while truncated octahedron AgNPs exhibit (111) a lower intensity of (100). It was reported previously that the reactivity of Ag is enhanced by high atomic density facets such as (111) (Acharya *et al.,* 2018; Rojas-Andrade, 2015; Bao *et al.,* 2016). It was postulated that atoms were more reactive on the facets of higher surface energy, which may lead them to interact rapidly with oxygen-containing groups of lipopolysaccharide molecules that can result in enhanced attachment to the cell membrane (Xia *et al.,* 2009). The greater inhibitory effects observed in *E. coli* than in *E. faecium* might be attributed to differences in the structure and thickness of the peptidoglycan layer of their cell walls. The peptidoglycan layer of Gram-positive bacteria for instance *E. faecium* (∼20–80 nm) is thicker than that in Gram-negative bacteria such as *E. coli* (∼7–8 nm), as it includes linear polysaccharide chains cross-linked by short peptides to make a three dimensional rigid structure. This makes it more difficult for NPs to attach and penetrate (Wang, Geng *et al.,* 2012). In addition, the positively charged AgNPs are attracted electrostatically to negatively charged lipopolysaccharides and teichoic acids in Gram negative and Gram-positive bacteria respectively. This may lead to rupture and protein denaturation followed by cell death (Fayaz, Balaji *et al.,* 2010).

When viable count growth was generated in the presence of CuNC and CuNS, the use of CuNS reduced by 2.08 $\log_{(10)}$ CFU/mL and 1.98 $\log_{(10)}$ CFU/mL against *E.coli* and *E. faecium* respectively. Significant ($p \leq 0.05$) reductions of 7.92 $\log_{(10)}$ CFU/mL and 3.5 $\log_{(10)}$ CFU/mL were observed against *E. coli* and *E. faecium* respectively (Table 8.3). The antibacterial activity of CuNPs may be attributed to the NPs shape and thus to the higher surface areas and facet reactivity. It was argued previously that the reactivity of silver is greater when high atomic density facets are present, such as the {111} plane (Rojas *et al.,* 2015; Acharya *et al.,* 2018). However, in the literature, there are no links between {111} faceted CuNPs which enhanced their antibacterial activity due to a lack of studies on the effect of the shape dependent CuNPs against bacteria. In this regard, the XRD pattern for CuNCs in this work displays a higher intensity of (111) when compared with CuNSs as shown in XRD data in Figure 6-14. This could be expected as quasi spherical particles tend to exhibit lower levels of (111) facets (Wiley, Sun *et al.,* 2005). Similarly, CuNS shows an

additional peak indexed as the (220) diffraction of Cu_2O (JCPDS 05-0667) that can be associated with slow oxidation of metallic CuNPs in air to form CuO, as seen in Figure 6-14b. This could be the reason for the enhanced antibacterial activity of CuNC with no oxidation peak compared to CuNS.

A previous study shows greater inhibition of the bacteria growth by CuNPs compared to cupric oxide CuONPs. Potential reasons include the direct interaction between CuNPs and the microorganism, which cause further penetration and rupture the bacterial membrane as a consequence of cell enzyme malfunction and ultimately cell death. CuNPs show greater antibacterial activity than CuONPs, which might be associated with better electron transfer between CuNPs and the bacteria. The negatively charged bacterial cell walls and CuNPs act as good electron acceptors, both leading to the electron transfer and rupture of the bacteria membrane (Vimbela *et al.,* 2017). The toxicity of CuNPs could be related to ROS generation occurring mainly in the periplasm of *E. coli*, while Gram-positive bacteria lack a periplasm, although many are tolerant to hydrogen peroxide (Hobman and Crossman, 2015). The positive Cu^{+2} ions released from the NPs may be attracted to the negatively charged bacterial cell walls which may then be ruptured and create protein denaturation followed by cell death (Theivasanthi & Alagar, 2011). Gram-negative bacteria with a thinner peptidoglycan, is likely to occur more readily, which would help to explain the difference in the levels of inhibition here. Moreover, there is also the possibility that the active facets of differently shaped nanoparticles could be directly affecting their antibacterial behaviour.

When viable count growth was generated in the presence of AuNOct and AuNS, the use of AuNOct resulted in significant ($p \leq 0.05$) reductions of 6 $\log_{(10)}$ CFU/mL against *E. coli* and 3.10 $\log_{(10)}$ CFU/mL against *E. faecium* suggesting a bactericidal effect, whereas in the presence of AuNS reduced by ≥ 1.9 $\log_{(10)}$ CFU/mL in both organisms, a bacteriostatic effect is suggested (Table 8.4). The antibacterial activity of AuNOct may be related to their geometric structure where AuNOcts enclosed by (111) faceted shows a higher intensity of (111) when compared with AuNS, as shown in the XRD data in Figure 6-21. This could be expected as quasi spherical particles tend to exhibit lower levels of (111) facets (Zhou *et al.,* 2011; Wiley *et al.,* 2005). Although not as well studied as the antibacterial mechanism of AgNPs and there are no relationships in the literature between {111} faceted AuNPs and their enhanced antibacterial activity, AuNPs applied the antibacterial effect in two steps. First, they reformed the membrane potential by reduced adenosine triphosphate (ATP) synthase activities, consequently reducing the metabolism procedure. Secondly, they refused binding the subunit of the ribosome for tRNA, hence breaking up its biological mechanism. In addition, they evidenced being less toxic to mammalian cells (Cui, Zhao *et al.,* 2012).

The small size of AuNPs and enhanced surface area create certain electronic effects, which are helpful for improving the surface reactivity of NPs. Furthermore, the high surface area percentage directly attached with the microorganism to a huge extent and henceforth, showed improved interaction with the bacteria. These two significant factors greatly enhanced the antibacterial properties of the NPs with large surface areas. Cytoplasm and bacterial proteins of the cell wall were responsible for the function of the cell. These NPs damaged the normal functioning of these proteins causing cell death, since gold being soft acid can interact easily with phosphorus- or sulphur-containing soft bases. Hence, the phosphorus-containing DNA molecules and sulphur-containing proteins are preferred sites for AuNPs to attack. AuNPs connected to thiol groups of enzymes. For example, nicotinamide adenine dinucleotide (NADH) dehydrogenases damaged their respiratory chains. As a result, major damage occurred in the cell structures and finally led to cell death (Cui, Zhao *et al.*, 2012). Hence, the increase in the surface area could enhance the interaction of AuNOct with binding sites for the plasma membrane proteins. The antibacterial activity of AuNPs for Gram-negative bacteria is higher compared to Gram-positive because the difference in the membrane structure e.g. the peptidoglycan layer's thickness, is 50% higher in Gram-positive than in Gram-negative bacteria (Umadevi, Rani *et al.*, 2011). Therefore, higher doses of NPs are needed for Gram-positive bacteria.

Table 8.2 The $\log_{(10)}$ CFU/mL growth inhibition of *E. coli* and *E. faecium* treated with AgNOct and AgNS over 24 hours (n= 6± SD)

Time	Control counts (no NP present) for *E. coli*	*E. coli* treated with AgNS		*E. coli* treated with AgNOCT		Control counts (no NP present) for *E.faecium*	*E. faecium* treated with AgNS		*E. faecium* treated with AgNOCT	
		Viable count	Growth inhibition	Viable count	Growth inhibition		Viable count	Growth inhibition	Viable count	Growth inhibition
0 h	8±0.02	8±0.02	0 ±0.03	8±0.03	0 ±0.02	8±0.01	8±0.04	0 ±0.02	8±0.03	0 ±0.03
2 h	8±0.03	7.8±0.04	0.12 ±0.02	7.9 ±0.04	2 ±0.01	8±0.02	7.89±0.03	0.11 ±0.03	5.95±0.03	2.05 ±0.02
4 h	9±0.05	6.8±0.02	2.2 ±0.01	1±0.03	8 ±0.04	9±0.04	6.8±20.01	2.18 ±0.01	5±0.02	4 ±0.02
6 h	10±0.03	6.74±0.02	3.26 ±0.02	2±0.02	8 ±0.02	10±0.03	6.7±0.04	3.23 ±0.02	5±0.03	5 ±0.01
24 h	10±0.01	6.74±0.04	3.26 ±0.03	2±0.04	8 ±0.01	10±0.02	6.82±0.03	3.18 ±0.04	5±0.03	5 ±0.04

Table 8.3 The $\log_{(10)}$ CFU/mL growth inhibition of *E. coli* and *E. faecium* treated with CuNC and CuNS over 24 hours (n= 6± SD)

Time	Control counts (no NP present) for *E. coli*	*E. coli* treated with CuNS		*E. coli* treated with CuNC		Control counts (no NP present) for *E.faecium*	*E. faecium* treated with CuNS		*E. faecium* treated with CuNC	
		Viable count	Growth inhibition	Viable count	Growth inhibition		Viable count	Growth inhibition	Viable count	Growth inhibition
0 h	8±0.02	8±0.01	0 ± 0.04	8±0.02	0 ± 0.03	8±0.01	8±0.04	0 ± 0.01	8±0.04	0 ± 0.03
2 h	8±0.03	7.8±0.02	0.12 ± 0.03	5.65±0.03	2.35 ± 0.01	8±0.02	7.89±0.04	0.11 ± 0.04	7.89±0.03	0.11 ± 0.01
4 h	9±0.05	6.97±0.01	2.03 ± 0.01	3±0.02	6 ± 0.01	9±0.04	7.02±0.02	1.98 ± 0.03	6.68±0.03	2.32 ± 0.03
6 h	10±0.03	7.81±0.02	2.19 ± 0.02	4±0.03	6 ± 0.03	10±0.03	7.86±0.03	2.14 ± 0.01	6.68±0.04	3.32 ±0.04
24 h	10±0.01	7.92±0.03	2.08 ± 0.04	3±0.01	7 ± 0.01	10±0.02	8.02±0.02	1.98 ±0.04	6.5±0.04	3.50 ± 0.02

Table 8.4 The $\log_{(10)}$ CFU/mL growth inhibition of *E. coli* and *E. faecium* treated with AuNOct and AuNS over 24 hours (n= 6± SD)

Time	Control counts (no NP present) for *E. coli*	*E. coli* treated with AuNS		*E. coli* treated with AuNOCT		Control counts (no NP present) for *E.faecium*	*E. faecium* treated with AuNS		*E. faecium* treated with AuNOCT	
		Viable count	Growth inhibition	Viable count	Growth inhibition		Viable count	Growth inhibition	Viable count	Growth inhibition
0 h	8±0.02	8±0.01	0 ± 0.03	8±0.04	0± 0.04	8±0.01	8±0.04	0± 0.04	8±0.04	0± 0.03
2 h	8±0.03	7.95±0.02	0.05 ± 0.01	6±0.02	2± 0.03	8±0.02	7.96±0.03	0.04 ± 0.02	7.95±0.03	0.05± 0.04
4 h	9±0.05	6.9±0.02	2.10 ± 0.02	5±0.03	4 ± 0.02	9±0.04	6.83±0.04	2.17 ± 0.03	6.76±0.02	2.24 ± 0.02
6 h	10±0.03	7.82±0.02	2.18 ± 0.04	5±0.02	5± 0.03	10±0.03	7.9±0.03	2.10 ± 0.01	7.83±0.03	2.17 ± 0.01
24 h	10±0.01	8.1±0.03	1.9± 0.03	4±0.03	6± 0.04	10±0.02	8.1±0.04	1.91± 0.04	6.9±0.04	3.10± 0.03

8.3.5 Visualisation of interaction between NPs and bacteria using SEM

I- Silver nanoparticles

The interaction between bacteria and the nanoparticles was investigated by SEM as per method 8.2.6. As demonstrated in the images, *E. coli* is a rod shape and well defined texture having an average cell length of 2.7 µm and a cell width of 0.7 µm are observed (Figure.8-14, A and B) as untreated bacteria cells (control), whereas after 24 hours treatment with AgNOct, there is a total deformation and leakage of cellular material (Figure 8-14 (C)), which has been reported recently in studies of *E. coli* when treated with silver–poly(methyl methacrylate) (Ag-PMMA) nanocomposite for water treatment (Borse *et al.*, 2016). Figure 8-14 (D), shows low density cells or no growth on the sample exposed to AgNOct for 24 hours, where only AgNPs were presented, whereas *E. coli* treated with AgNS after 4 hours displays a physical interaction only between NPs and cells even after 24 hours and does not show any deformation of the cell wall (Figure 8-14 (E-F)).

The SEM image of untreated *E.faecium* looks round and double cocci (Figure 8-15 (A and B)), while 24 hours treatment with AgNS reveals unhealthy cells (Figure 8-15 (C)). *E.faecium* under SEM appeared deformed and the cell wall damaged when exposed to AgNOct after 24 hours (Figure 8-15 (D)). AgNPs cause similar cell wall disruption and have been reported previously, although in *S. aureus* rather than in *E. faecium* and the investigation performed under TEM instead of SEM microscopy (Mei *et al.*, 2013). Previous studies have shown that the antibacterial activity of AgNPs is limited in Gram-positive bacteria due to the thick peptidoglycan layer of the cell wall of (e.g. *S. aureus*), which prevented the penetration of the nanoparticles into the cytoplasm (Borse *et al.*, 2016; Mei *et al.*, 2013).

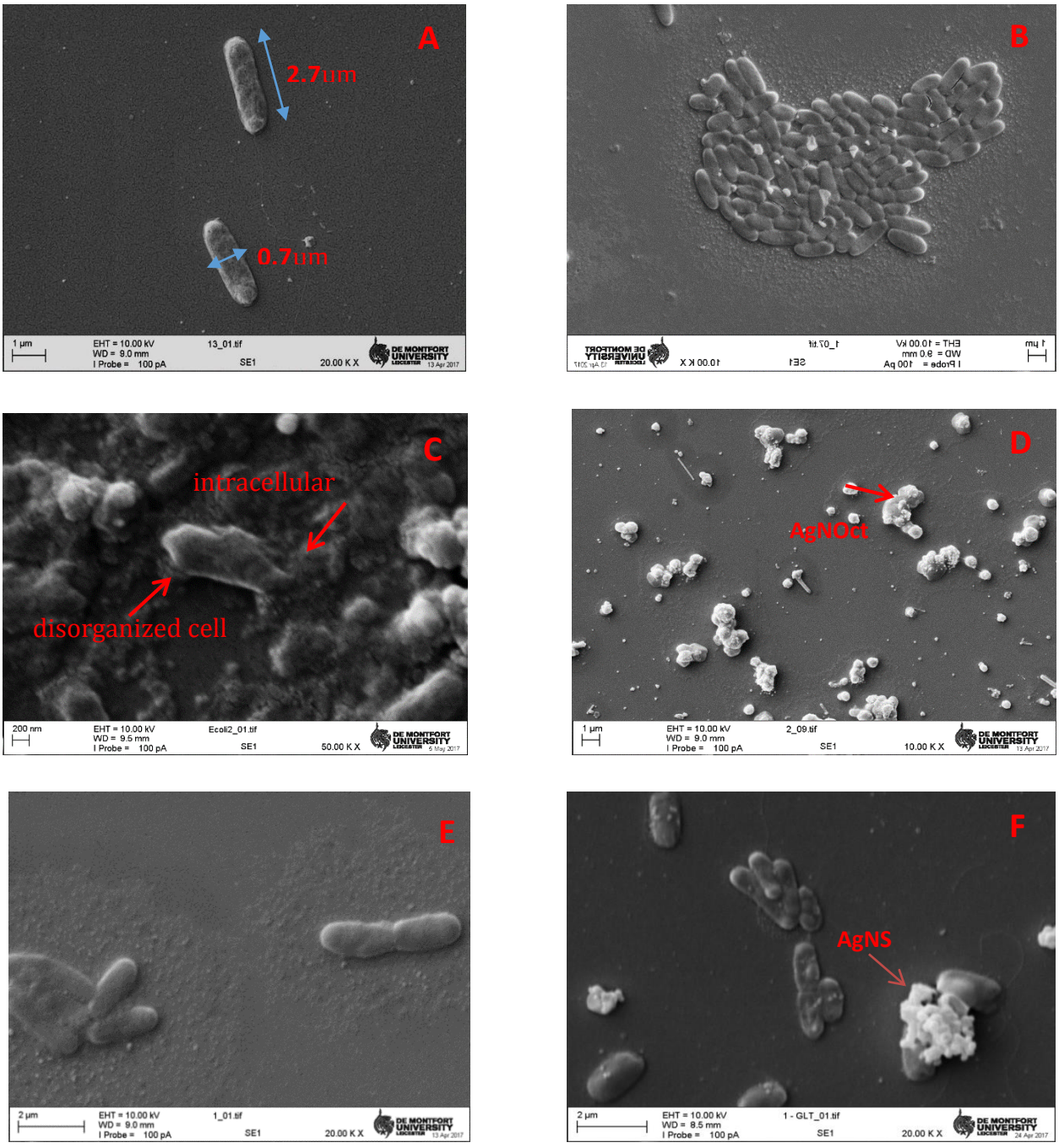

Figure 8- 14: SEM images of *E. coli*: (A) and (B) untreated cells, (C) cells exposed to AgNOct for 24hours show leakage of cellular material and total deformation of cells, (D) shows low density cells and no growth was present in the sample after 24hours, only AgNOct is shown. (E) and (F) cells exposed to AgNS for 4 and 24h respectively, show the interaction of the NPs and bacteria.

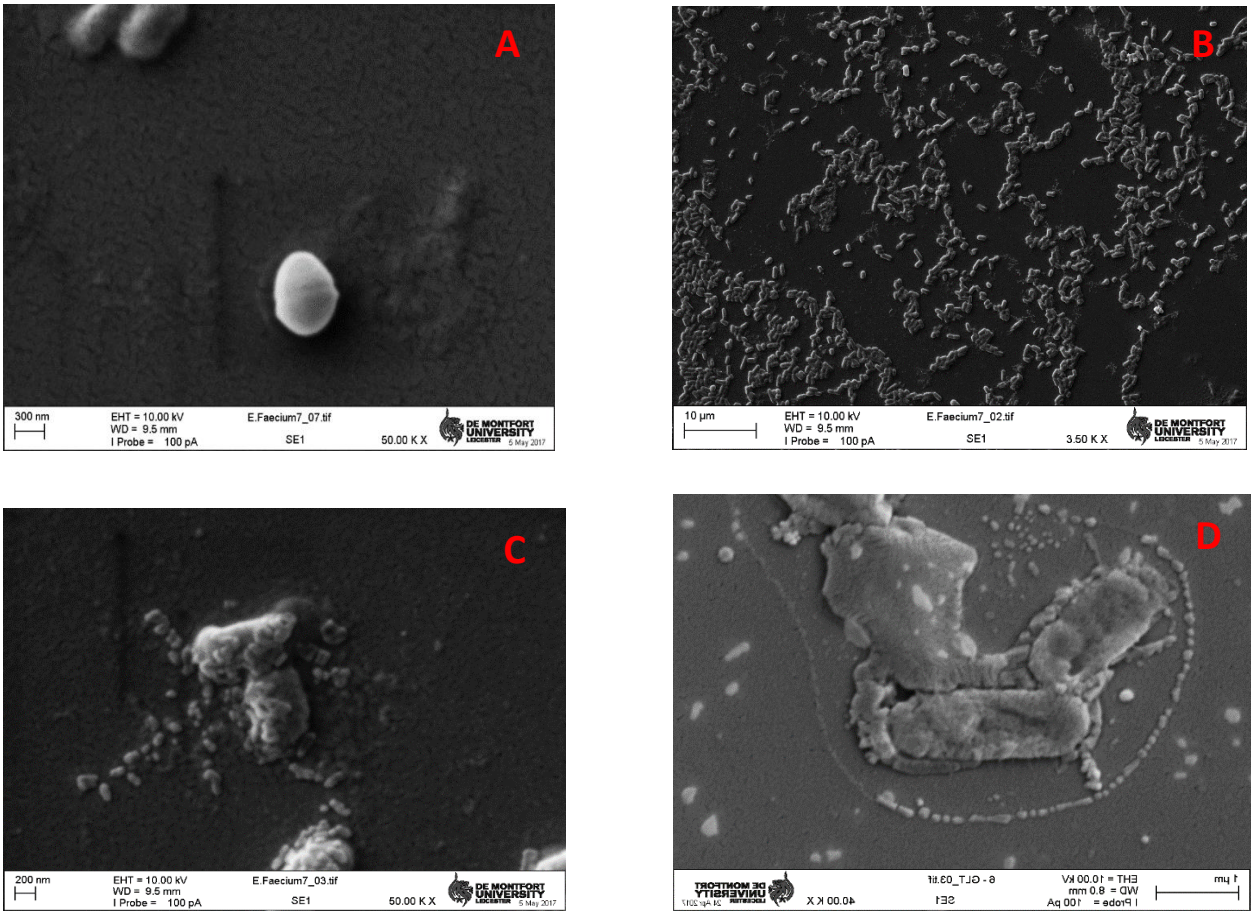

Figure 8- 15: SEM images *E. faecium*: (A) and (B) untreated cells, (C) cells exposed to AgNS for 24 hours show damaged cells. (D) cells exposed to AgNOct show cell wall damaged after 24h.

The interaction between NPs and bacteria can be explained by the following; hydrophobic interactions (Luan, 2016), electrostatic attraction (Li *et al.*, 2015), receptor–ligand (Gao, 2014) and van der Waals forces (Armentano *et al.*, 2014). NPs then penetrate inside bacterial membrane and aggregate along the metabolic pathway, deforming the shape and function of the cell wall. Subsequently, NPs interact with the intracellular material, such as enzymes, lysosomes, Deoxyribonucleic acid (DNA) and ribosomes (RNA), leading to alterations in cell membrane permeability, enzyme deactivation, protein inhibition, oxidative stress, electrolyte balance disorders and changes in gene expression (Xu, 2016; Shrivastava, 2007; Yang, 2009). Nanoparticles penetrate into cells to produce an antibacterial effect. The diffusion coefficient is ~105 cm2/s, which is the same as the oxygen diffusion coefficient. Considering the thickness of the *E. coli* cell wall with diffusion time ~107 cm2/s, the average lifetime of ROS is 105–106 s. Hence, ROS remains for a sufficient period to diffuse inside bacterial cells (Wang, 2017).

A comparison of the possible mechanisms of antibacterial action of silver ions and silver nanoparticles against Gram-positive bacteria and Gram-negative bacteria is shown in Figure 8-16 (Kędziora et al., 2018). Initially, pore formation which allowed ions leakage inside cells that will produce denaturation of structural and cytoplasmic proteins followed by inactivation of respiratory chain enzymes then to an increase in intracellular reactive oxygen species (ROS) concentration, interaction with ribosome and nucleic acids as a consequence of inhibition and may possibly cause cell death (Kędziora *et al.*, 2018).

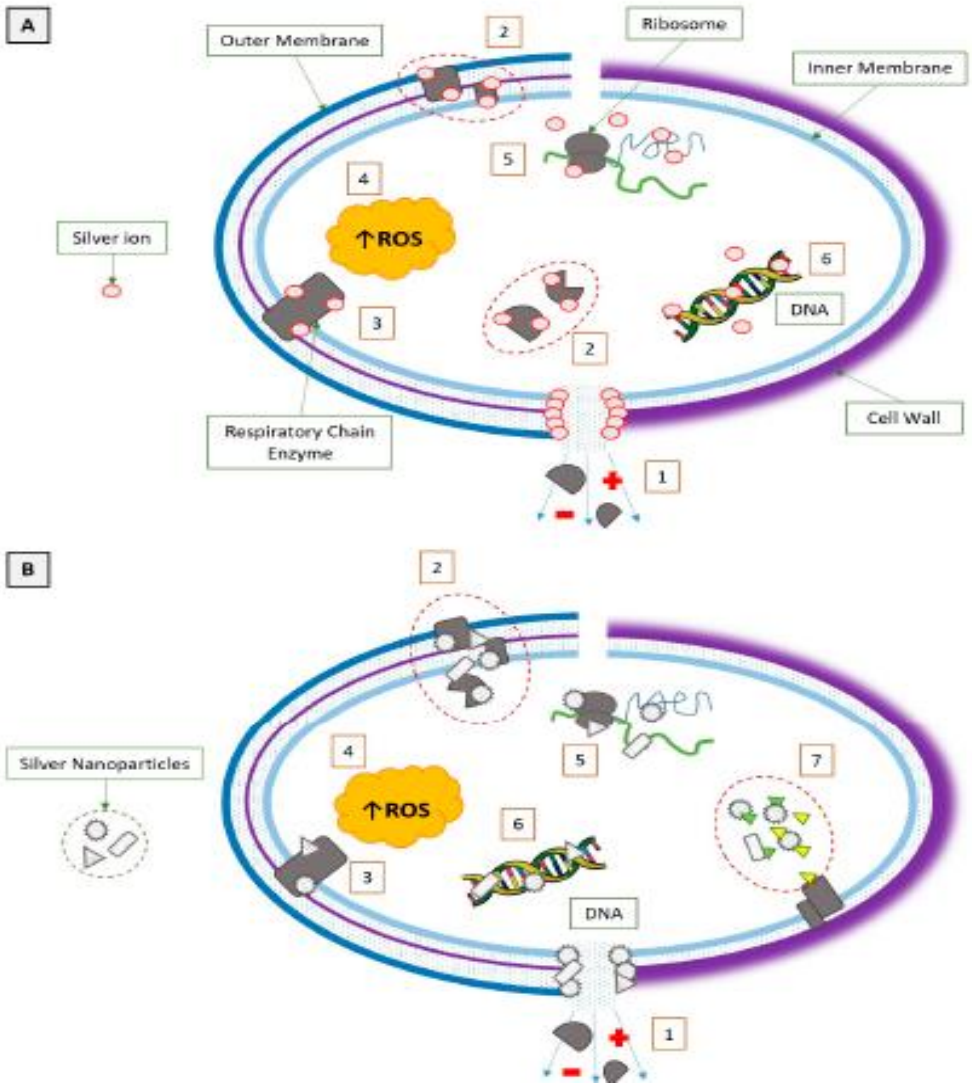

Figure 8-16: Comparison of Ag ion (A) Comparison of the silver ions (**A**) and silver nanoparticles' (**B**) mode of action for Gram-negative (**left**) and Gram-positive (**right**) bacteria. (1) Pore formation; metabolites and ions leakage (shown as plus and minus in the figure above) (2) Denaturation of structural and cytoplasmic proteins; enzymes inactivation. (3) Inactivation of respiratory chain enzymes. (4) Increase of intracellular reactive oxygen species (ROS) concentration. (5) Interaction with ribosome. (6) Interaction with nucleic acids. (7) Inhibition (Kędziora et al., 2018).

The antimicrobial efficacy of the AgNPs has been shown to be shape dependent against the organisms tested. Truncated octahedral AgNPs (AgNOct) were found to be more active on *E. coli* and *E. faecium* when compared with spherical AgNPs (AgNS). A generation of reactive oxygen species (ROS) can be produced at the cell wall affecting metabolic processes by damaging DNA reproduction followed by cell death due to oxidative stress (Vimbela *et al.,* 2017). A dominant oxidant was produced in the reaction of AgNPs with hydroxy radical (OH). This oxidizing species may lead to the bactericidal properties of AgNPs (Grumezescu, 2017). Similarly, the difference in shape resulted in differences in efficacy which may be due to the higher surface area of AgNOct compared to AgNS, and differences in active facets and surface energies. This higher reactivity may ultimately cause more rapid cell death.

II- Copper nanoparticles

The interaction between CuNPs and bacteria was investigated by SEM as per method 8.2.6. *E. coli* exposed to CuNC for 4 hours shows a physical interaction between the bacterial cell and NPs (Figure 8-17 A), whereas after 24 hours treatment with CuNC appear elongation of the cell wall, increased roughness and deformed with release of intracellular material (Figure 8-17 B).

This was previously reported in studies of copper nanoparticles when treated with *E. coli* (Díaz-Visurraga *et al.,* 2011). Low density cells or no *E. coli* growth following exposure to CuNC for 24 hours, where only NPs are present under SEM (Figure 8-17 C), whereas exposure to CuNS for 24 hours appear attached to the cell wall and partial cell wall damage (Figure 8-17 D). In contrast, untreated *E. coli* (control) was observed to be well-defined and had a healthy texture (8-17 E).

E. faecium treatment with CuNC after 24h appears to lack uniformity and was ruptured (Figure 8-18 A), as recently reported in studies of Cu2SnS3 (CTS) nanoparticles when treated with *S. aureus* (Lokhande et al., 2017). However, cells exposed to CuNS for 24 hours show partial deformation of some cells (Figure 8-18 B), in contrast to untreated *E. faecium* (control), which was observed to be well-defined and had a healthy texture (Figure 8-18 C).

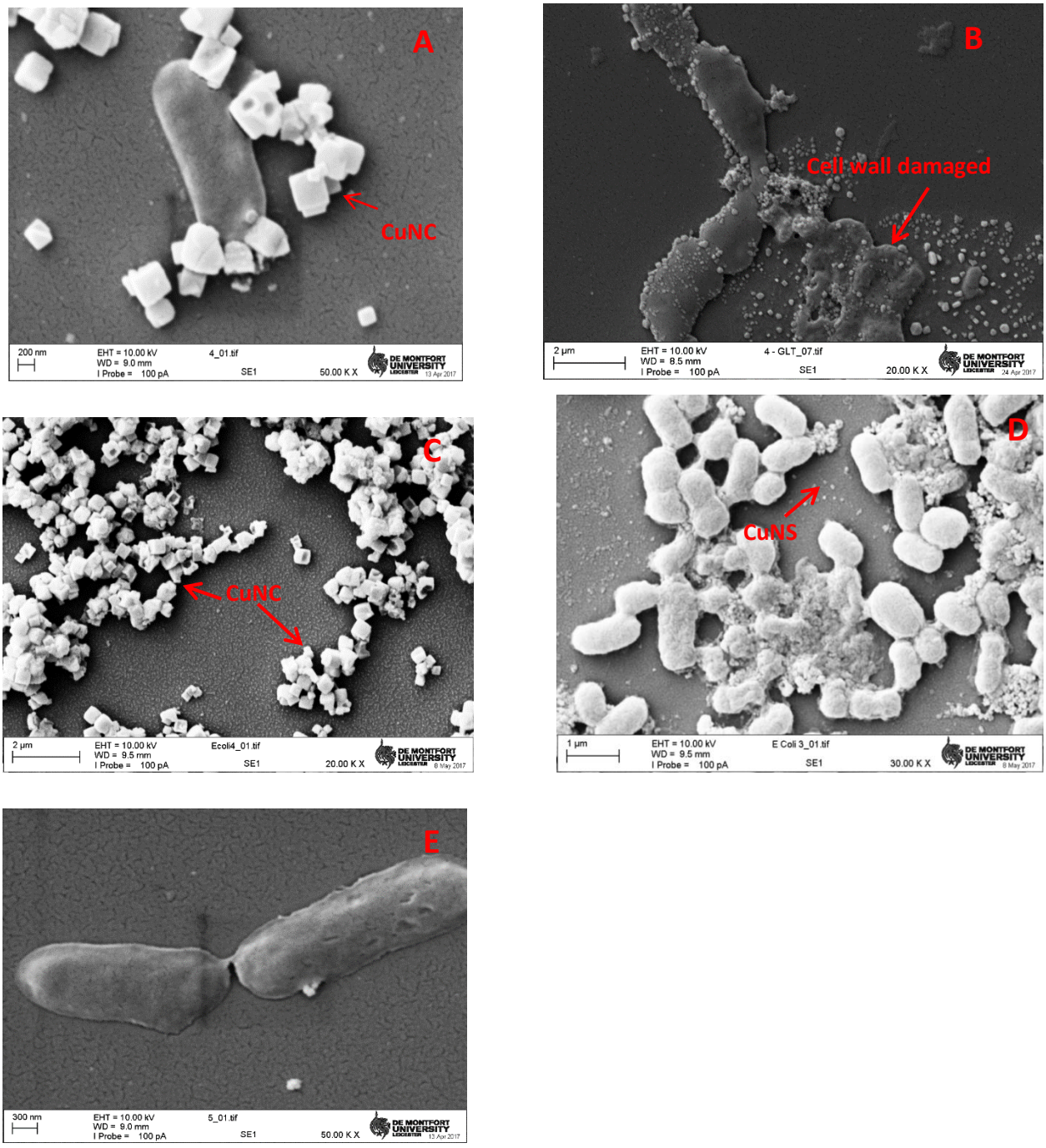

Figure 8-27: SEM images of *E. coli*: (A) treatment with CuNC after 4 hours shows NPs attached to cell wall, (B) cells exposed to CuNC for 24 hours appear rough and deformed with the release of intracellular material, (C) no bacteria growth after 24hours treatment with CuNC, while only NPs were present, (D) exposure to CuNS for 24 hours shows the interaction between NPs and bacteria cells and partial deformation of cells, (E) untreated *E. coli* (control).

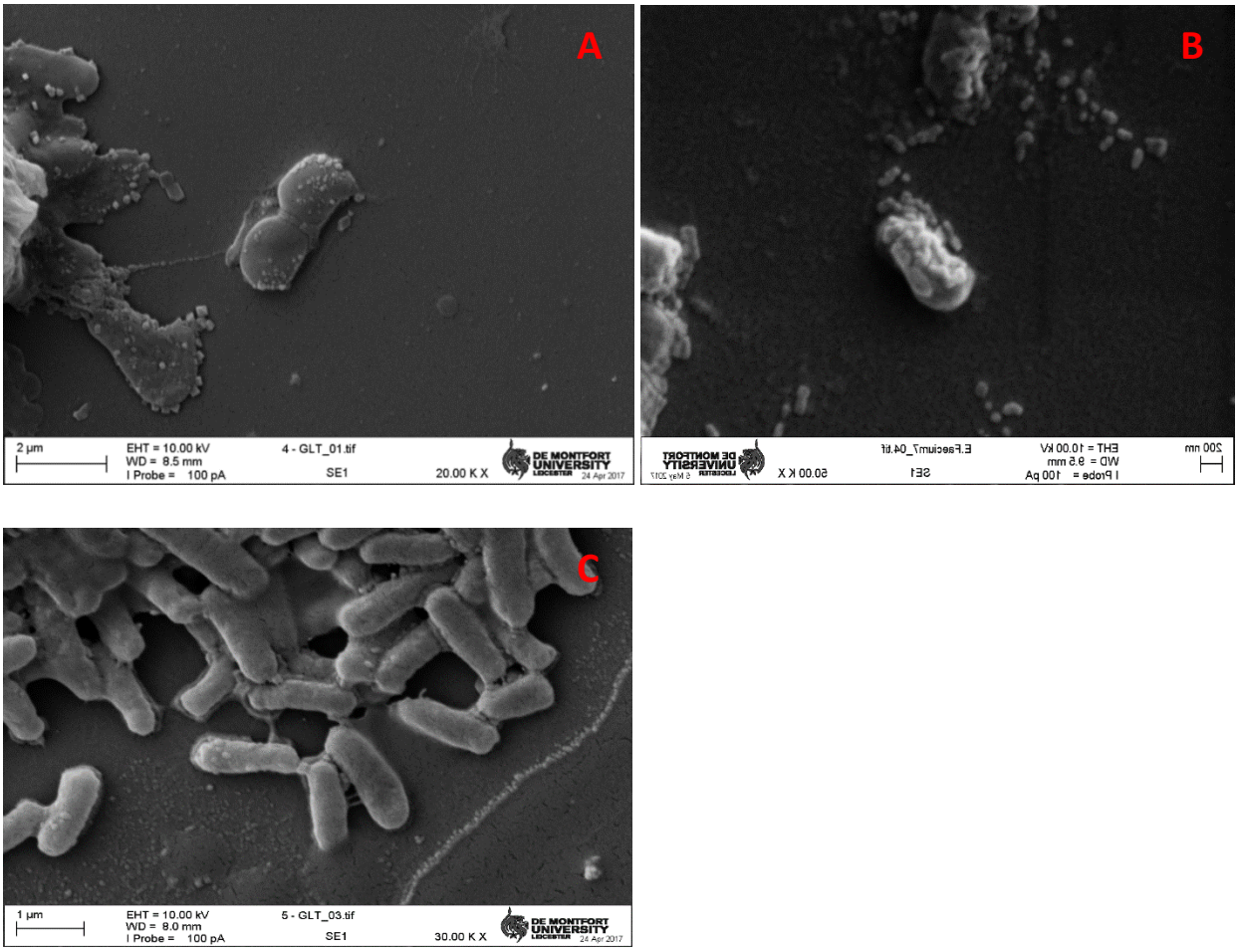

Figure 8-18: SEM images of *E. faecium*: (A) cells exposed to CuNC for 24 hours lack uniformity and were ruptured, (B) cells exposed to CuNS for 24 hours show partial deformation of some cells, (C) untreated *E. faecium* (control).

Schematic diagram of the different pathways inducing cellular toxicity by CuNPs is shown in Figure 8-19 (Chang, 2012). Three potential mechanisms based on ROS, non-homeostasis and coordination effects which explain why CuNPs exert toxic effects on bacteria. Nanoparticles can diffuse inside cells through holes present in cell membrane or pass through transporter proteins and ion channels existing on the plasma membrane. Likewise, NPs can enter cells via endocytosis (the membrane wraps around NPs and then vesicles transport into cells). Cu2+ ion generated by NPs can produce ROS through chemical reactions to inactivate DNA function and gene expression. Besides, Cu2+ ions can form chelates with biomolecules or dislodge the metal ions in specific metalloproteins, as a consequence of functional protein inactivation. Cu2+ ion generated by NPs nanoparticles can increase their local concentration and interrupt cellular metal cation homeostasis which cause cell toxicity.

Studies of the antibacterial activity of different CuNPs show that whilst both shapes were effective in inhibiting the growth of Gram-positive bacteria and Gram-negative bacteria. CuNC had the greatest effect,

which might be related to (111) facet dominant compared with CuNS. This higher reactivity may be the principal cause that ultimately led to more rapid cell death in *E. coli*, suggesting that CuNS have a bacteriostatic effect, while CuNC become bactericidal after 4 hours. The results indicate that CuNPs can be used as effective growth inhibitors in different microorganisms, making them applicable to coated medical devices food preservation and antimicrobial control systems.

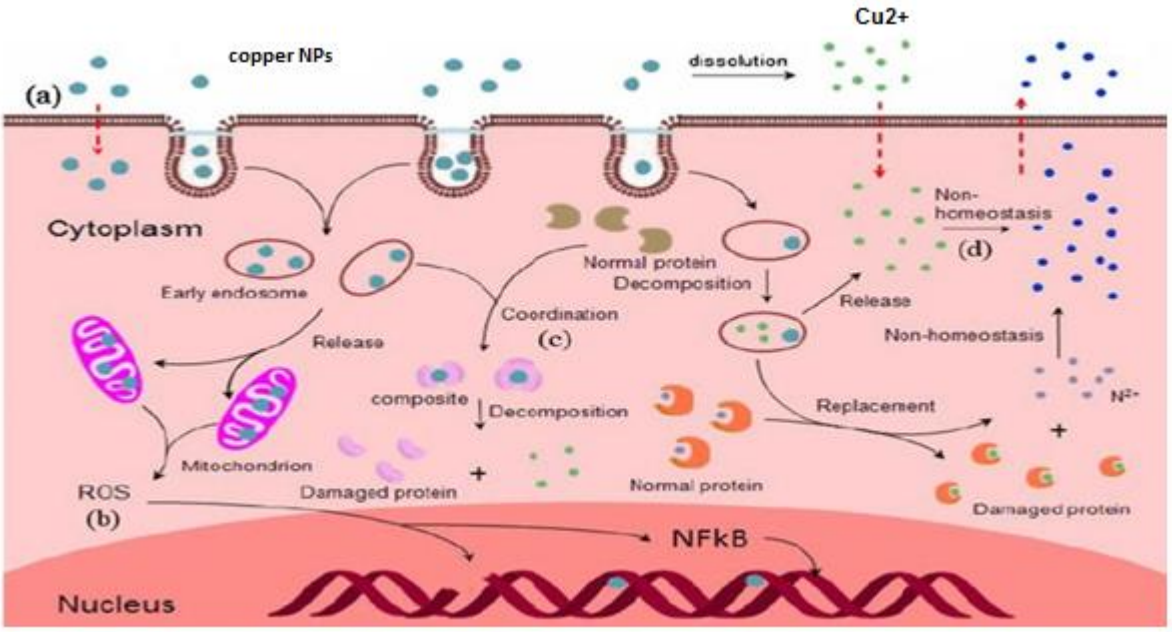

Figure 8-19: Schematic representation of the mechanism of antibacterial activity of copper nanoparticles (Chang, 2012).

III- Gold nanoparticles

The interaction between AuNPs and bacteria was investigated using SEM as per method 8.2.6. *E. coli* treated with AuNS shows a physical interaction between bacterial cell and AuNS after 24 hours (Figure 8-20 (A)). However, the cellular integrity was lost and cell wall damaged following exposure to AuNOct for 24 hours, which has been reported previously in studies of gold nanoparticles when treated with *E. coli* (Figure 8-20 (B)) (Chandran *et al.,* 2014). Conversely, untreated *E. coli* (control) appeared rod shaped and well-defined (Figure 8-20 (C)).

E. faecium treated with AuNS exhibits only interaction between AuNS and bacteria even after 24hours (Figure 8-21 (A)). Non-uniform or deformed and ruptured *E.coli* cells appear under SEM after treatment with AuNOct for 24 hours (Figure 8-21 (B)), which has been reported previously in studies of gold

nanoparticles when treated with *Bacillus cereus, S. aureus* and *Listeria monocytogenes* (Chandran *et al.*, 2014). However, untreated *E. faecium* (control) appear round and have healthy cells (Figure 8-21 (C)). Studies of the antibacterial activity of the different AuNPs indicate that whilst both shapes were effective in inhibiting the growth of Gram-positive bacteria and Gram-negative bacteria, AuNOct which had the greatest effect enhanced by (111) facet was more prevalent in the AuNOct compared with AuNS. This higher reactivity may be the principal cause that eventually led to more rapid cell death in *E. coli*, suggesting that AuNS has a bacteriostatic effect, while AuNOct become bactericidal after 4 hours. The results demonstrate that AuNPs can be used as effective growth inhibitors in different microorganisms, rendering them applicable to antimicrobial control systems, drug delivery and cancer therapy.

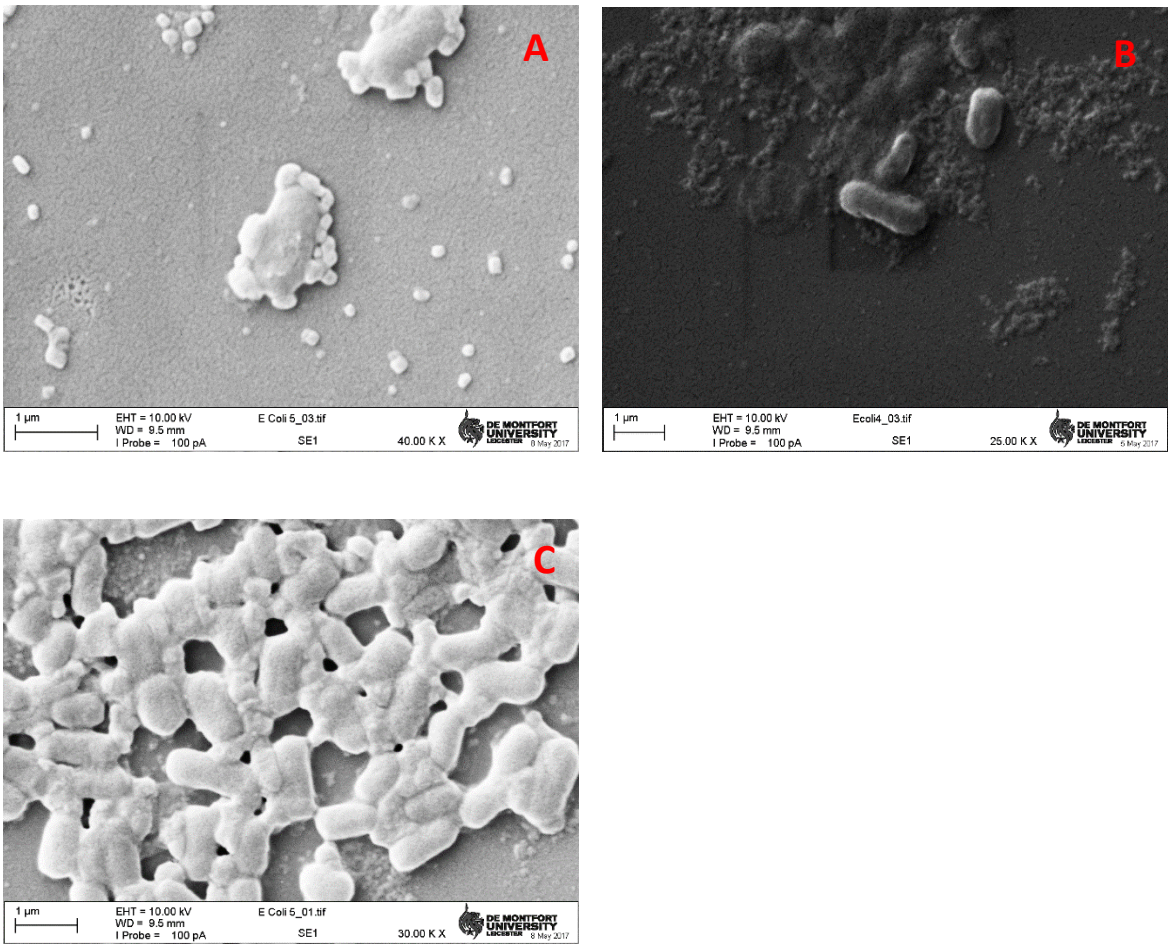

Figure 8-20: SEM images of *E. coli*: (A) treated with AuNS, (B) treated with AuNOct, (C) untreated *E. coli* (control). All after 24h.

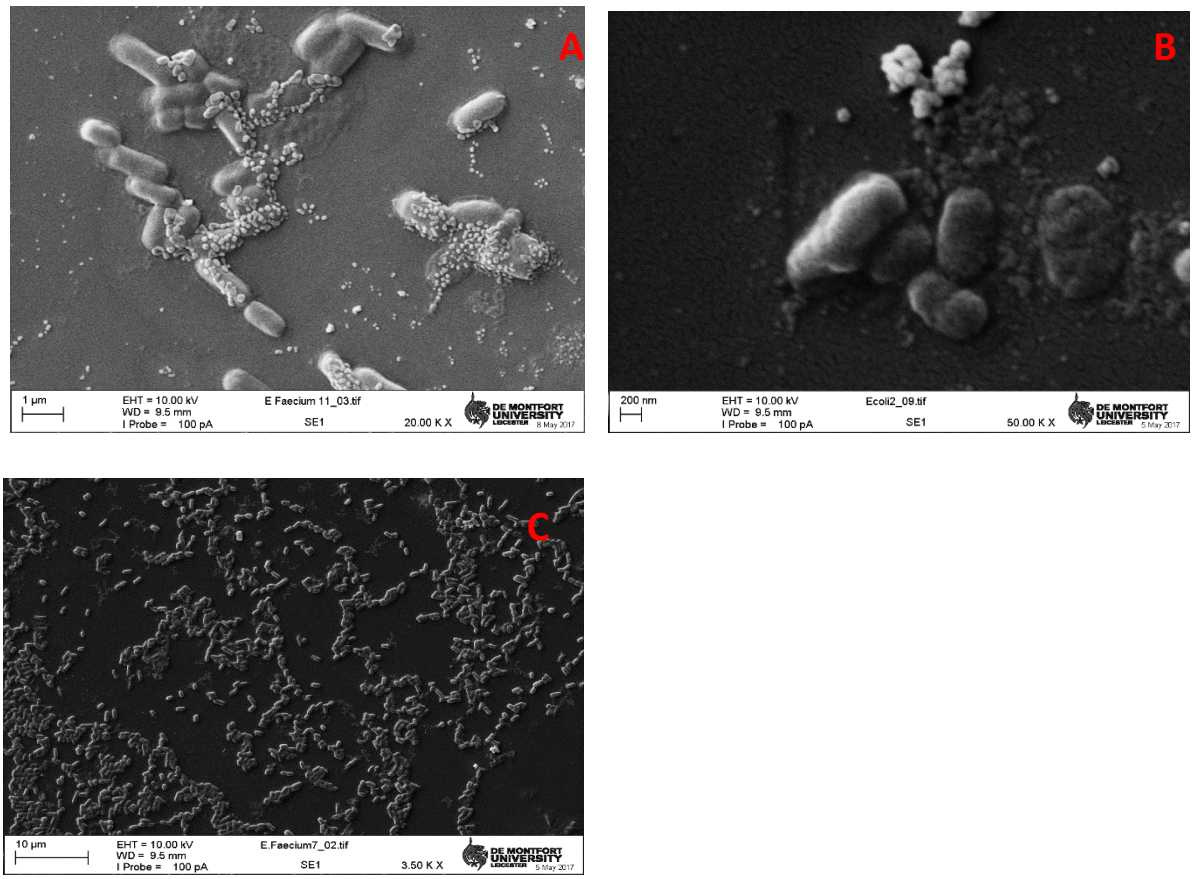

Figure 8-21: SEM images of *E. faecium*:(A) treated with AuNS, (B) treated with AuNOct, (C) untreated *E. faecium* (control). All after 24h.

8.4 Comparative studies of the efficacy of different shaped metal nanoparticles against *E. coli* and *E. faecium*

Based on the findings of the current study, it would be concluded that AgNOct, CuNC and AuNOct are the most effective shape against *E. coli* and *E. faecium* compared to the spherical shaped (AgNS, CuNS and AuNS). Among these metals, the MIC of AgNOct against *E. coli* was the lowest 10µg/ml, followed by MICs of CuNC and AuNOct 15 µg/ml and 50µg/ml respectively. The MIC of AgNOct against *E. faecium* was higher than the MIC against *E. coli* 55µg/ml, followed by MICs of CuNC and AuNOct 90 µg/ml and 100µg/ml respectively. The MICs of AuNS against *E. faecium* and *E. coli* are the highest 250µgl/ml and 230µgl/ml respectively (Table 8.1). These findings are significantly lower than 9000 µg/ml MIC concentration for a commercially manufactured AgNPs, whenever the antibacterial study had been carried out at an initial cell concentration of 10^5 CFU/ml (Acharya *et al.*, 2018; Lara *et al.*, 2011).

The results suggests that AgNOct are the most effective tested metal NPs against *E. coli* followed by CuNC and AuNOct respectively, as shown in Table 8.1 (MICs value). The viable count growth data demonstrated

that the concentrations of 10µg/ml of AgNOct resulted in a significant ($p \leq 0.05$) reduction of ≥ 8 $\log_{(10)}$ CFU/mL against *E. coli*, followed by the concentrations of 15 µg/ml and 55µg/ml of CuNC and AuNOct respectively, resulted in ≥7 and 6 $\log_{(10)}$ CFU/mL reduction against *E. coli*, as shown in Table 8-5. However, the viable count growth data demonstrated that the concentration of 55µg/ml of AgNOct resulted in a significant ($p \leq 0.05$) reduction of ≥ 5 $\log_{(10)}$ CFU/mL against *E. coli*, followed by the concentrations of 90 µg/ml and 100µg/ml of CuNC and AuNOct respectively, resulted in ≥3.50 and 3.10 $\log_{(10)}$ CFU/mL reduction against *E. faecium*, as shown in Table 8-6. The spherical shape NPs required a higher concentration, 250µg/ml of AuNS and 125µg/ml of CuNS resulting in ≥1.9 $\log_{(10)}$ CFU/mL reduction against *E. faecium*, as seen in Tables 8-7.

Table 8-5: The $\log_{(10)}$ CFU/mL growth inhibition of *E. coli* treated with AgNOct, CuNC and AuNOct over 24 h (n= 6± SD)

Time	Control growth counts (no NP metal present)	Growth inhibition of *E. coli* treated with AgNOct	Growth inhibition of *E. coli* treated with CuNC	Growth inhibition of *E. coli* treated with AuNOct
0 hours	8±0.02	0 ±0.02	0 ± 0.03	0± 0.04
2 hours	8±0.03	2 ±0.01	2.35 ± 0.01	2± 0.03
4 hours	9±0.05	8 ±0.04	6 ± 0.01	4 ± 0.02
6 hours	10±0.03	8 ±0.02	6 ± 0.03	5± 0.03
24 hours	10±0.01	8 ±0.01	7 ± 0.01	6± 0.04

Table 8.6: The $\log_{(10)}$ CFU/mL growth inhibition of *E. faecium* treated with AgNOct, CuNC and AuNOct over 24 h (n= 6± SD)

Time	Control growth counts (no NP metal present)	Growth inhibition *E. faecium* treated with AgNOct	Growth inhibition *E .faecium* treated with CuNC	Growth inhibition *E. faecium* treated with AuNOct
0 hours	8±0.01	0 ±0.03	0 ± 0.03	0± 0.03
2 hours	8±0.02	2.05 ±0.02	0.11 ± 0.01	0.05± 0.04
4 hours	9±0.04	4 ±0.02	2.32 ± 0.03	2.24 ± 0.02
6 hours	10±0.03	5 ±0.01	3.32 ±0.04	2.17 ± 0.01
24 hours	10±0.02	5 ±0.04	3.50 ± 0.02	3.10± 0.03

Table 8.7: The $\log_{(10)}$ CFU/mL growth inhibition of *E. faecium* treated with AgNS, CuNS and AuNS over 24 h (n= 6± SD)

Time	Control growth counts (no NP metal present)	Growth inhibition *E. faecium* treated with AgNS	Growth inhibition *E .faecium* treated with CuNS	Growth inhibition *E. faecium* treated with AuNS
0 hours	8±0.01	0 ±0.02	0 ± 0.01	0± 0.04
2 hours	8±0.02	0.11 ±0.03	0.11 ± 0.04	0.04 ± 0.02
4 hours	9±0.04	2.18 ±0.01	1.98 ± 0.03	2.17 ± 0.03
6 hours	10±0.03	3.23 ±0.02	2.14 ± 0.01	2.10 ± 0.01
24 hours	10±0.02	3.18 ±0.04	1.98 ±0.04	1.91± 0.05

In this study, anisotropic shapes such as the truncated octahedron or cube shape show strong antibacterial activity compared to the spherical shape. This proves the hypothesis that the efficacy of nanoparticles against bacteria depends on their shape. The reason behind that could be the geometric structure enclosed by (111) faceted contains higher atomic density (Acharya *et al.*, 2018; Bao *et al.*, 2016). The truncated face in the octahedron shape and the edge in the cube shape enabled the NPs to penetrate into the cell more rapidly and cause damage in the outer membrane (Rojas-Andrade, 2015). However, among these metals, AgNPs in the form of (AgNOct) was the most effective metal NPs against *E. coli* and *E. faecium* compared to AuNPs and CuNPs. The reason could be established by two different mechanisms of action enhanced by AgNPs. Firstly, the interaction between released Ag+ ions can bind with thiol groups (–SH) of enzymes and proteins found in the cell membrane disruption of membrane functionality by the breakdown of the Adenosine triphosphate (ATP) production pathway. AgNPs may then be deposited in the cell wall causing holes, which can easily penetrate inside bacteria and interact with intracellular components or proteins containing sulphur. Secondly, generations of reactive oxygen species (ROS) can be produced at the cell wall affecting metabolic processes by damaging DNA reproduction followed by cell death due to oxidative stress (Vimbela *et al.*, 2017). NPs generate different types of ROS by reducing oxygen molecules. For instance, hydrogen peroxide (H_2O_2), superoxide radical (O_2^-), singlet oxygen (O_2) and hydroxyl radical (OH), that display different levels of dynamics and activity. Ag produces hydroxy radical (OH) (Grumezescu, 2017) and Cu_2O generates the four types of oxidizing species (Wang *et al.*, 2017), while Au does not generate ROS due to high tolerability of this metal (Grumezescu, 2017). A previous report illustrates that (H_2O_2) and (O_2^-) produce less stress reactions, superoxide enzymes and catalase can be neutralised by endogenous antioxidants, while (O_2) and (OH) can cause acute stress reactions which lead to microbial death (Malka *et al.*, 2013). It can be concluded that a dominant oxidant was produced in the

reaction of AgNPs with hydroxy radical (OH). Thus, this oxidising species may cause the bactericidal properties of AgNPs (Grumezescu, 2017).

Chapter 9.

Conclusion

9.1 Conclusion

Bionanomaterials is an extensive field in which there is a significant potential for the development of new technologies and bioscience within all areas of healthcare arenas. Different applications for nanomaterials have been widely stated in the literature: from antimicrobials to biosensing and drug delivery. Accordingly, the objective of this study was to synthesis metal NPs of different shape for silver, gold and copper thereby optimising fabrication conditions to control the NPs size and tailor NPs shape in order to assesses their efficacy as antibacterial agents against both a Gram positive (*E. faecium*) and a Gram-negative (*E. coli*) organism

Two different shapes of each metal were obtained by chemical reduction method: spherical/octahedron silver, spherical/octahedron gold and spherical/cube Copper, where the size and shape were controlled via the precursor or reduction agent, reaction time, temperature and the molar ration between the precursor and reduction agent.

Ag nano sphere were synthesised using $AgNO_3$ as a precursor and Sodium citrate as a weak reduction agent). The formation of a spherical shape AgNPs related to citrate ion reduces the Ag ion capping the nanocluster, after the formation of the NPs no further etching afterward resulting in shape of faceted nanospheres. Ag nano octahedrons have been synthesised using polyol method, the primary step in this process includes heating a polyol such as ethylene glycol (EG) with a precursor (AgNO3) in the presence of a polymeric capping agent such as (PVP). The addition of a small amount of Sodium bromide (NaBr) prior to the addition of a precursor play a role in the etching of the particle seeds, facilitating the formation of truncated octahedron enclosed by {111} facets. The PVP also works as a shape-control agent prompting the reduction of $AgNO_3$ onto specific crystal faces while preventing reduction onto others.

Cu nano sphere have been synthesised using $CuSO_4$ as a copper salt, PVP was used as a surfactant and ascorbic acid as a reducing agent. $CuSO_4$ primarily dissociates to Cu_2+ and SO_4 in water, and Cu_2+ ions are hydrolysed into $Cu(OH_2)$. Further reduction of $Cu(OH_2)$ takes place in the presence of ascorbic acid to form Cu_2O. Lastly, Cu_2O is further reduced to form Cu nano sphere. CuNPs are highly unstable as they oxidise rapidly but this can be inhibited by the use of ascorbic acid. Cu nano cube have been synthesised using polyol method, the primary step in this process includes heating a polyol such as ethylene glycol (EG) with a precursor ($CuSO_4$). The addition of a small amount of Sodium hydroxide (NaOH) prior to the addition of a precursor play a role in the etching of the particle seeds, facilitating the formation of cube shape. Also, The molar ratio (1:1) of NaOH:$CuSO_4.5H_2O$ and high temperature 165 °C played important roles in the synthesis of copper nano cube.

Au nano sphere have been synthesised using $HAuCl_4$ as a gold salt and Sodium citrate as a weak reduction agent. The formation of a spherical shape AuNPs related to citrate ion reduce the Au ions firstly then the citrate capped the nanoparticles, after the formation of the NPs no further etching afterward resulting in shape of faceted nanospheres. Au nano octahedrons have been synthesised using $HAuCl_4$ as a gold salt and Sodium bromide (NaBr) as a reduction agent. AuNPs enclosed by {111} facets octahedrons, when Br^- ions present during reaction truncated octahedron is formed.

All nanoparticles were characterised using UV-VIS spectroscopy, SEM, EDX , XRD and TEM to confirm the presence of NPs and identify the morphology, elemental analysis, crystalline nature and lastly TEM to obtain the SAED for assignation of the crystalline nature and HRTEM for elucidation of the d-spacing of the lattice fringes. Indexing the selected area electron diffraction (SAED) of NPs and compare the calues of R (d-spacing) with XRD data or data base ICDD is evidence that all produced NPs are crystalline (single crystal or polycrystalline), which enhance the antibacterial activity of the nanoparticles unlike the amorphous properties. For example, the crystalline phase of the prepared TiO2–Ag nanoparticles calcined powder at 300 °C (CB300) had the highest antibacterial properties which inhibited bacterial growth by 90%. However, no major decrease in the number of colonies was reported in noncalcined powder (CB), because of the amorphous structure of CB. It is reasonable to say that the growth delay of *E. coli* is due to the presence of silver nanoparticles and not due to the TiO2 nanoparticles (Amin *et al.,* 2009).

MIC of AgNOct against *E. coli* was the lowest 10µg/ml, followed by MIC of CuNC and AuNOct 15 and 50µg/ml respectively. The MIC of AgNOct against *E. faecium* was higher than the MIC against *E. coli* 55µg/ml, followed by MIC of CuNC and AuNOct 90 and 100µg/ml respectively. The MICs of AuNS against *E. faecium* and *E. coli* were the highest; 250 and 230 µg/ml respectively. The results suggest that AgNOct is the most effective against *E. coli,* followed by CuNC and AuNOct respectively. Reductions in ≥ 8 $\log_{(10)}$ CFU/mL were observed for *E. coli* treatment with AgNOct. It can be concluded that the AgNOct had greatest antimicrobial activity followed by CuNC and AuNOct. However, reductions in the spherical shaped NPs (AuNS and CuNS) was the lowest inhibition, reduced by ≥ 1.9 $\log_{(10)}$ CFU/mL against *E. faecium.*

Growth inhibition was measured using optical density to investigate the growth kinetic curves of bacterial cells exposed to different concentrations of NPs. Higher concentrations of nanoparticles in solutions progressively inhibited the growth of *E. coli* and *E. faecium,* which observed that both the lag and log phase were altered by NPs. The concentration 100 µg/ml of AgNOct was found to be strongly inhibitory for *E. faecium,* whereas the lower concentration 10 µg/ml of AgNOct was found to be an effective bactericide against *E. coli*. The concentration of 100 µg/ml of AgNS was established to be strongly inhibitory for *E.*

coli, as it took 10 hours to initiate the reduction in growth, while to initiate the growth of *E. faecium* in the presence of 100 µg/ml AgNS, requires 2 hours. The present findings are in good agreement with the work of other studies (Dehnavi *et al.,* 2013; Badwaik, 2012), who stated higher inhibition kinetics against Gram-negative bacteria, such as *E. coli* as compared to Gram-positive bacteria such as *Staphylococcus epidermidis* and *S. aureus* of Ag nanoparticles.

Damage to the *E. coli* and *E. faecium* cell wall after 24h treatment with metal NPs was observed in the SEM imaging. The greater inhibitory effects observed in *E. coli* than in *E. faecium* might be attributed to differences in the structure and thickness of the peptidoglycan layer of their cell walls. The peptidoglycan layer of Gram-positive bacteria for instance *E. faecium* (∼20–80 nm) is thicker than that in Gram-negative bacteria such as *E. coli* (∼7–8 nm), as it includes linear polysaccharide chains cross-linked by short peptides to make a three dimensional rigid structure. This makes it more difficult for NPs to attach and penetrate (Wang, 2017). In addition, the positively charged AgNPs are attracted electrostatically to negatively charged lipopolysaccharides and teichoic acids in Gram negative and Gram-positive bacteria respectively; this may lead to rupture and protein denaturation followed by cell death (Acharya *et al.,* 2018).

The difference in shape resulted in differences in efficacy, which may be due to the higher surface area, and differences in active facets and surface energies. This higher reactivity may ultimately lead to more rapid cell death. It has been reported previously that the antibacterial activity of Ag is enhanced by high atomic density facets such as (111) (Acharya *et al*., 2018). It was postulated that atoms were more reactive on the facets of higher surface energy, which may cause them to interact rapidly with oxygen-containing groups of lipopolysaccharide molecules that can result in enhanced attachment to the cell membrane (Wang *et al.,* 2017). AgNPs in the form of (AgNOct) was the most effective metal NPs against *E. coli* and *E. faecium* compared to AuNPs and CuNPs, due to the generation of reactive oxygen species (ROS). Nanoparticles generate different types of ROS by reduction oxygen molecules, for instance hydrogen peroxide (H_2O_2), superoxide radical (O_2^-), singlet oxygen (O_2) and hydroxyl radical (OH), that display different levels of dynamics and activity. Ag produce hydroxy radical (OH) (Grumezescu, 2017) and Cu_2O produces four types of oxidizing species (Wang *et al.,* 2017), while Au does not generate ROS due to the high tolerability of this metal (Grumezescu, 2017). A previous report illustrated that (H_2O_2) and (O_2^-) cause less stress reactions and superoxide enzymes and catalase can be neutralised by endogenous antioxidants, while (O_2) and (OH) can cause acute stress reactions which bring about microbial death (Malka *et al.,* 2013). The results from this study suggests that AgNOct could be a potential alternative antibacterial agent against *E.coli and E. faecium*. In this domain, these findings can accelerate the use of AgNOct, CuNC and AuNOct in biological applications in the future as antimicrobial agents. Based on the above findings, it can

be concluded that the toxicity of the metal NPs against *E. coli* and *E. faecium* depends on the shape of NPs enclosed by (111) faceted and the concentrations to penetrate into the cell membrane. The actual mechanism behind the bactericidal effect of metal NPs is not well known and requires further investigation.

9.2 Future work

The next step in the progression of this research will be to further investigation the mechanisms of action of metal NPs, such as gene expression and DNA fragmentation to obtain the toxicity mechanism of NPs. Flow cytometry is a technique used to detect and measure the chemical and physical characteristics of a population of cells or particles. Cells are typically labelled with fluorescent dye (propidium iodide) and then excited by laser to emit light at varying wavelengths to distinguish dead/live cells. Flow cytometry can be used in the diagnosis of health disorders and is employed in biomarker detection, protein engineering, cell sorting and cell counting (Railean-Plugaru, 2016). The advantage of flow cytometry is the ability to examine data from tens of thousands of cells faster, and to calculate it using computer software.

In the current research, *Escherichia coli* (NCTC8196) and *Enterococcus faecium* (NCTC12202) were selected as a model for Gram-negative bacteria and Gram-positive bacteria respectively. In order to consider a AgNOct, CuNC and AuNOct as a commercial product in the healthcare arena or use it as a combination of NPs and antibiotics, the versatility of the suspension should be assessed by testing its efficacy against other human pathogens-including *E. coli* (*O157:H7*), *S. aureus*, *B. subtilis* and *K. pneumonia*, which are the major cause of infections in children and adults.

The fragment crystallizable receptor (FC receptor) result can be joined with BIOTEM data, which is an extremely important method in defining NPs internalization via bacteria cells (Acharya *et al.*, 2018). Visualisation of the interaction between NPs and bacteria using TEM will give us more information as regards the antibacterial mechanism of NPs and agglomerates around the bacteria, followed by internalization inside cytoplasm. Finally, damaging the cell membrane and leakage of cellular material lead to cell death (Espana-Sanchez, 2018). Future research emerging from this project would include further investigation using the high angle annular dark field (HAADF) technique, can be joined with scanning transmission electron microscopy (STEM) in order to generate images related to the elemental mapping of NPs inside bacteria. The electrons generated were scattered at high angles, creating an image with high contrast associated with the differences in atomic number between organic/inorganic phases (Espana-Sanchez, 2018). Increasing numbers of NPs agglomerate inside bacteria cells associated with increasing Phosphorous (P) and Sulphur (S) elements, which suggest possible phospholipid and protein damage

created by the interaction of NPs with the particular adsorption sites regularly distributed on the lipopolysaccharide outer cell of Gram-negative (Espana-Sanchez, 2018).

Further research to investigate the relationship between the NPs shape and their antibacterial properties, such as dissolved oxygen and light irradiation that might have an effect on the catalytic production of ROS along with different facets is required (Hong *et al.,* 2016). Detecting the ROS can be examined by measuring the fluorescent intensity using a different type of fluorescent probe such as 2-[6-(4-amino)phenoxy-3Hxanthen-3-on-9-yl]benzoic acid (APF), hydroethidine-dihydroethidium (DHE) and 2′7-dichlorodihydrofluorescein (DCFH) dedicated to the quantification of integrated amounts of oxidising species (Zhao and Riediker, 2014; Misawa, 2011). Recent research that measured ROS on metal oxide NPs and their bacteria toxicity, the antibacterial activity was attributed to the long-lived O_2 radicals on the NPs with the following order of $TiO_2 > ZnO > V_2O_5 > Fe_2O_3 > CeO_2 > Al_2O_3$ (Wang and Zhao, 2017). Further research to quantify ROS photogenerated on metal NPs and their bacteria toxicity is required, seeing as only a few studies were published based on a comparison of the generation of ROS on metal NPs. The actual mechanism of ROS is not well known as there are conflicting statements concerning the generation of ROS induced by NPs. For instance, recent research stated that AuNPs have a lower toxicity on bacteria than other NPs because they do not generate ROS due to the high tolerability of AuNPs (Grumezescu, 2017; Cui and Wang, 2012). However, previous research reported that AuNPs generate hydroxyl radical (OH) and superoxide anion ($O2^{-}$) (Misawa, 2011). Specifically, questions as regards whether NPs might be a possible source of ROS generation should be answered based on a uniform methodology using a specific DCFH fluorescent probe involving a specific NP shape, rather than different random shapes tested (Zhao and Riediker, 2014).

Future research as a result of this project would include further investigation into mechanisms of the action of metal oxide NPs, for example titanium dioxide (TiO_2) and zinc oxide (ZnO) nanoparticles due to their antibacterial applications including water disinfection (Li *et al.,* 2008) and coated textile fabric respectively (Perelshtein *et al.,* 2016).

References:

Abdulla-Al-Mamun, M., Kusumoto, Y., & Muruganandham, M. (2009). Simple new synthesis of copper nanoparticles in water/acetonitrile mixed solvent and their characterization. Materials letters, 63(23), 2007-2009.

Abbaschian, R. and Reed-Hill, R.E., 2008. Physical metallurgy principles. Cengage Learning.

Acharya, D., Singha, K.M., Pandey, P., Mohanta, B., Rajkumari, J. and Singha, L.P., 2018. Shape dependent physical mutilation and lethal effects of silver nanoparticles on bacteria. Scientific reports, 8(1), p.201.

Adams, D.M., Brus, L., Chidsey, C.E., Creager, S., Creutz, C., Kagan, C.R., Kamat, P.V., Lieberman, M., Lindsay, S., Marcus, R.A. and Metzger, R.M., 2003. Charge transfer on the nanoscale: current status. *The Journal of Physical Chemistry B*, *107*(28), pp.6668-6697.

Ahmad A, Mukherjee P, Senapati S, Mandal D, Khan MI, et al. (2003) Extracellular biosynthesis of silver nanoparticles using the fungus Fusarium oxysporum. Colloids Surf B Biointerfaces 28: 313-318.

Ahamed, M., Siddiqui, M.A., Akhtar, M.J., Ahmad, I., Pant, A.B. and Alhadlaq, H.A., 2010. Genotoxic potential of copper oxide nanoparticles in human lung epithelial cells. Biochemical and biophysical research communications, 396(2), pp.578-583.

Ahmed, T., Imdad, S., and Ashraf, S. 2012. Effect of size and surface ligands of silver (Ag) nanoparticles on waterborne bacteria. International Journal of Theoretical and Applied Nanotechnology, 1(1), pp.111-116.

Akbulut, O., Mace, C., Martinez, R., Kumar, A., Nie, Z., Patton, M. and Whitesides, G. (2012). Separation of Nanoparticles in Aqueous Multiphase Systems through Centrifugation. Nano Letters, 12(8), pp.4060-4064.

Alexander, L., & Klug, H. P. (1950). Determination of Crystallite Size with the X-Ray Spectrometer. Journal of Applied Physics, 21(2), 137-142.

Allaker, R.P., 2010. The use of nanoparticles to control oral biofilm formation. Journal of dental research, 89(11), pp.1175-1186.

Andrews, J. M., 2011. Determination of Minimum Inhibitory Concentrations. Journal of Antimicrobial Chemotherapy. 48, 1 Pp. 5-16. Available at http://jac.oxfordjournals.org/content/48/suppl_1/5.abstract. Accessed on 03/06/2013

Amin, S. A., Pazouki, M., & Hosseinnia, A. (2009). Synthesis of TiO 2–Ag nanocomposite with sol–gel method and investigation of its antibacterial activity against E. coli. Powder Technology, 196(3), 241-245.

Anon, (2018). [online] Available at: http://www.technoorg.hu/news-and-events/articles/high-resolution-scanning-electron-microscopy-1/ [Accessed 19 Feb. 2018].

Armentano, I., Arciola, C.R., Fortunati, E., Ferrari, D., Mattioli, S., Amoroso, C.F., Rizzo, J., Kenny, J.M., Imbriani, M. and Visai, L., 2014. The interaction of bacteria with engineered nanostructured polymeric materials: a review. *The Scientific World Journal*, *2014*.

Askeland, D.R. and Phulé, P.P., 2006. The science and engineering of materials (p. 198). Toronto: Thomson.

Atanasova, K., 2010. Interactions between porcine respiratory coronavirus and bacterial cell wall toxins in the lungs of pigs (Doctoral dissertation, Ghent University).

Badwaik, V.D., Vangala, L.M., Pender, D.S., Willis, C.B., Aguilar, Z.P., Gonzalez, M.S., Paripelly, R. and Dakshinamurthy, R., 2012. Size-dependent antimicrobial properties of sugar-encapsulated gold nanoparticles synthesized by a green method. *Nanoscale research letters*, *7*(1), p.623.

Bai, P., & Tian, G. (2013). Statistical kinetics of phase-transforming nanoparticles in LiFePO< sub> 4</sub> porous electrodes. Electrochimica Acta, 89, 644-651.

Bajpai, A.K. and Gupta, R., 2011. Magnetically mediated release of ciprofloxacin from polyvinyl alcohol based superparamagnetic nanocomposites. Journal of Materials Science: Materials in Medicine, 22(2), pp.357-369.

Baker, M. and Cohen, H., 2004. An Explanation of Miller Indices.

Balaji, S., Raghunandan, D., Basavaraja, S., Mahesh, B., Manjunath, S. Y., & Venkataraman, A. (2009). Biosynthesis of stable polyshaped gold nanoparticles from microwave-exposed aqueous extracellular anti-malignant guava (Psidium guajava) leaf extract. Nanobiotechnology, 5(1-4), 34-41.

Belle, D. 2014. Gold NPs kill MDR bacteria http://nanotechweb.org/cws/article/tech/58690,

Bao, S., Wang, Z., Gong, X., Zeng, C., Wu, Q., Tian, B. and Zhang, J., 2016. AgBr tetradecahedrons with co-exposed {100} and {111} facets: simple fabrication and enhancing spatial charge separation using facet heterojunctions. Journal of Materials Chemistry A, 4(47), pp.18570-18577.

Beyth, N., Houri-Haddad, Y., Domb, A., Khan, W. and Hazan, R., 2015. Alternative antimicrobial approach: nano-antimicrobial materials. Evidence-based complementary and alternative medicine, 2015.

Binupriya AR, Sathishkumar M, Yun SI (2010) Myco-crystallization of silver ions to nanosized particles by live and dead cell filtrates of Aspergillus oryzae var. viridis and its bactericidal activity toward Staphylococcus aureus KCCM 12256. Ind Eng Chem Res 49: 852-858.

Birla SS, Tiwari VV, Gade AK, Ingle AP, Yadav AP, et al. (2009) Fabrication of silver nanoparticles by Phoma glomerata and its combined effect against Escherichia coli, Pseudomonas aeruginosa and Staphylococcus aureus. Lett Appl Microbiol 48: 173-179.

Borges, A., Ferreira, C., Saavedra, M.J. and Simoes, M., 2013. Antibacterial activity and mode of action of ferulic and gallic acids against pathogenic bacteria. Microbial Drug Resistance, 19(4), pp.256-265.

Borse, S., Temgire, M., Khan, A. and Joshi, S., 2016. Photochemically assisted one-pot synthesis of PMMA embedded silver nanoparticles: antibacterial efficacy and water treatment. *RSC Advances*, *6*(61), pp.56674-56683.

Brandon, D. and Kaplan, W.D., 2013. Microstructural characterization of materials. John Wiley & Sons.

Brown, M.R., ALLISON, D.G. and GILBERT, P., 1988. Resistance of bacterial biofilms to antibiotics a growth-rate related effect?.

Burns, F., Fleck, L., Andaloro, B., Davis, E., Rohrbeck, J., Tice, G., et al. 2011. DuPont qualicon BAX system real-time PCR assay for Escherichia coli O157:H7. Journal of AOAC International, 94(4), pp.1117-1124.

Bykkam, S., Ahmadipour, M., Narisngam, S., Kalagadda, V.R. and Chidurala, S.C., 2015. Extensive studies on X-ray diffraction of green synthesized silver nanoparticles. Advances in Nanoparticles, 4(01), pp.1-10.

Callaway, T.R., Edrington, T.S., Loneragan, G.H., Carr, M.A. and Nisbet, D.J., 2013. Shiga toxin-producing Escherichia coli (STEC) ecology in cattle and management based options for reducing fecal shedding. Agric. Food Anal. Bacteriol, 3, pp.39-69.

Callister, W.D. and Rethwisch, D.G., 2011. Materials science and engineering (Vol. 5). NY: John Wiley & Sons.

Cao, S., Tao, F.F., Tang, Y., Li, Y. and Yu, J., 2016. Size-and shape-dependent catalytic performances of oxidation and reduction reactions on nanocatalysts. Chemical Society Reviews, 45(17), pp.4747-4765.

Carbone, M., Donia, D.T., Sabbatella, G. and Antiochia, R., 2016. Silver nanoparticles in polymeric matrices for fresh food packaging. Journal of King Saud University-Science, 28(4), pp.273-279.

Catauro, M., Raucci, M.G., De Gaetano, F. and Marotta, A., 2004. Antibacterial and bioactive silver-containing Na 2 O• CaO• 2SiO 2 glass prepared by sol–gel method. Journal of Materials Science: Materials in Medicine, 15(7), pp.831-837.

Chandra, S. and Kumar, A., 2016. Recyclable copper nanoparticles: Efficient catalyst for selective cyclization of Schiff bases. Journal of Saudi Chemical Society, 20(4), pp.367-372.

Chandran, K., Song, S. and Yun, S.I., 2014. Effect of size and shape controlled biogenic synthesis of gold nanoparticles and their mode of interactions against food borne bacterial pathogens. *Arabian Journal of Chemistry*.

Chang, Y.N., Zhang, M., Xia, L., Zhang, J. and Xing, G., 2012. The toxic effects and mechanisms of CuO and ZnO nanoparticles. Materials, 5(12), pp.2850-2871.

Chao, Y. and Zhang, T., 2011. Optimization of fixation methods for observation of bacterial cell morphology and surface ultrastructures by atomic force microscopy. *Applied microbiology and biotechnology*, *92*(2), p.381.

Chawla, K.K., 2012. Composite materials: science and engineering. Springer Science & Business Media.

Cheng, J., Bordes, R., Olsson, E., & Holmberg, K. (2013). One-pot synthesis of porous gold nanoparticles by preparation of Ag/Au nanoparticles followed by dealloying. Colloids and Surfaces A: Physicochemical and Engineering Aspects, 436, 823-829

Chen, J., Wiley, B.J. and Xia, Y., 2007. One-dimensional nanostructures of metals: large-scale synthesis and some potential applications. *Langmuir*, *23*(8), pp.4120-4129.

Chen, L., Zhang, Y., Zhu, P., Zhou, F., Zeng, W., Lu, D.D., Sun, R. and Wong, C., 2015. Copper salts mediated morphological transformation of Cu 2 O from cubes to hierarchical flower-like or microspheres and their supercapacitors performances. Scientific reports, 5, p.9672.

Chen, Z., Meng, H., Xing, G., Chen, C., Zhao, Y., Jia, G., Wang, T., Yuan, H., Ye, C., Zhao, F. and Chai, Z., 2006. Acute toxicological effects of copper nanoparticles in vivo. Toxicology letters, 163(2), pp.109-120.

Chien, W.C., Chang, C.O., Lo, Y.C., Li, Z.W. and Chou, C.S., 2005. On the Miller-indices determination of Si {1 0 0} convex corner undercut planes. Journal of Micromechanics and Microengineering, 15(4), p.833.

Cornell, R.M. and Schwertmann, U., 2003. The iron oxides: structure, properties, reactions, occurrences and uses. John Wiley & Sons.

Cover, N.F., Lai-Yuen, S., Parsons, A.K. and Kumar, A., 2012. Synergetic effects of doxycycline-loaded chitosan nanoparticles for improving drug delivery and efficacy. International journal of nanomedicine, 7, p.2411.

Crabtree, J.H., Burchette, R.J., Siddiqi, R.A., Huen, I.T., Hadnott, L.L. and Fishman, A., 2003. The efficacy of silver-ion implanted catheters in reducing peritoneal dialysis-related infections. Peritoneal Dialysis International, 23(4), pp.368-374.

Crystalimpact.com. (2018). Crystallite Size Estimation. [online] Available at: http://www.crystalimpact.com/match/help/idh_crystallite_size.htm [Accessed 21 Feb. 2018].

Cui, L., Wang, Z., Jiang, H., Parker, D., Wang, H., Su, X.Z. and Cui, L., 2012. Lack of association of the S769N mutation in Plasmodium falciparum SERCA (PfATP6) with resistance to artemisinins. *Antimicrobial agents and chemotherapy*, *56*(5), pp.2546-2552.

Cui, Y., Zhao, Y., Tian, Y., Zhang, W., Lü, X. and Jiang, X., 2012. The molecular mechanism of action of bactericidal gold nanoparticles on Escherichia coli. Biomaterials, 33(7), pp.2327-2333.

Cytodiagnostics.com. (2018). Introduction to Gold Nanoparticle Characterization - Cytodiagnostics. [online] Available at: http://www.cytodiagnostics.com/store/pc/Introduction-to-Gold-Nanoparticle-Characterization-d3.htm [Accessed 19 Feb. 2018].

Dakal, T.C., Kumar, A., Majumdar, R.S. and Yadav, V., 2016. Mechanistic basis of antimicrobial actions of silver nanoparticles. Frontiers in microbiology, 7.

Dameron CT, Reese RN, Mehra RK, Kortan AR, Carroll PJ, et al. (2009) Biosynthesis of cadmium sulphide quantum semiconductor crystallites. Nature 338:596-597.

Dang, T.M.D., Le, T.T.T., Fribourg-Blanc, E. and Dang, M.C., 2011. Synthesis and optical properties of copper nanoparticles prepared by a chemical reduction method. Advances in Natural Sciences: Nanoscience and Nanotechnology, 2(1), p.015009.

Daniel, I.M., Ishai, O. 1994. Engineering mechanics of composite materials (Vol. 3, pp. 256-256). New York: Oxford university press.

DeAlba-Montero, I., Guajardo-Pacheco, J., Morales-Sánchez, E., Araujo-Martínez, R., Loredo-Becerra, G.M., Martínez-Castañón, G.A., Ruiz, F. and Compeán Jasso, M.E., 2017. Antimicrobial properties of copper nanoparticles and amino acid chelated copper nanoparticles produced by using a soya extract. *Bioinorganic chemistry and applications*, *2017*.

De Faria, A.F., Martinez, D.S.T., Meira, S.M.M., de Moraes, A.C.M., Brandelli, A., Souza Filho, A.G. and Alves, O.L., 2014. Anti-adhesion and antibacterial activity of silver nanoparticles supported on graphene oxide sheets. Colloids and Surfaces B: Biointerfaces, 113, pp.115-124.

De Giglio, E., Cafagna, D., Cometa, S., Allegretta, A., Pedico, A., Giannossa, L.C., Sabbatini, L., Mattioli-Belmonte, M. and Iatta, R., 2013. An innovative, easily fabricated, silver nanoparticle-based titanium implant coating: development and analytical characterization. Analytical and bioanalytical chemistry, 405(2-3), pp.805-816.

Dehnavi, A.S., Raisi, A. and Aroujalian, A., 2013. Control size and stability of colloidal silver nanoparticles with antibacterial activity prepared by a green synthesis method. *Synthesis and Reactivity in Inorganic, Metal-Organic, and Nano-Metal Chemistry*, *43*(5), pp.543-551.

Dhand, V., Soumya, L., Bharadwaj, S., Chakra, S., Bhatt, D. and Sreedhar, B., 2016. Green synthesis of silver nanoparticles using Coffea arabica seed extract and its antibacterial activity. Materials Science and Engineering: C, 58, pp.36-43.

Dhulappanavar, G., Hungund, B., Ayachit, N., Bhakat, A., Singh, P.P. and Priya, S., 2011, November. Characterization of silver nanoparticles biosynthesized using lemon juice. In Nanoscience, Engineering and Technology (ICONSET), 2011 International Conference on (pp. 258-262). IEEE.

Díaz-Visurraga, J., Gutiérrez, C., Von Plessing, C. and García, A., 2011. Metal nanostructures as antibacterial agents. *Science and technology against microbial pathogens: Research, development and evaluation. Badajoz: Formatex*, pp.210-218.

Dror-Ehre, A., Mamane, H., Belenkova, T., Markovich, G., and Adin, A. 2009. Silver nanoparticle-E. coli colloidal interaction in water and effect on E. coli survival. Journal of Colloid and Interface Science, 339(2), pp.521-526.

Dontorou, A., Papadopoulou, C., Filioussis, G., Apostolou, I., Economou, V., Kansouzidou, A., et al. 2004. Isolation of a rare Escherichia coli O157:H7 strain from farm animals in Greece. Comparative Immunology, Microbiology & Infectious Diseases, 27(3), pp. 201-207.

Durán, N., Durán, M., de Jesus, M.B., Seabra, A.B., Fávaro, W.J. and Nakazato, G., 2016. Silver nanoparticles: a new view on mechanistic aspects on antimicrobial activity. Nanomedicine: Nanotechnology, Biology and Medicine, 12(3), pp.789-799.

EAG Laboratories. (2018). X-ray Diffraction Analysis | XRD | Phase Identification | EAG Laboratories. [online] Available at: http://www.eag.com/mc/x-ray-diffraction.html [Accessed 21 Feb. 2018].

Espana-Sanchez, B.L., Ávila-Orta, C.A., Padilla-Vaca, L.F., Barriga-Castro, E.D., Soriano-Corral, F., Gonzalez-Morones, P., Ramirez-Wong, D.G. and Luna-Barcenas, G., 2018. Early stages of antibacterial damage of metallic nanoparticles by TEM and STEM-HAADF. *Current nanoscience*, *14*(1), pp.54-61.

Encyclopedia Britannica. (2018). Transmission electron microscope | instrument. [online] Available at: https://www.britannica.com/technology/transmission-electron-microscope [Accessed 20 Feb. 2018].

Erni, R., Rossell, M.D., Kisielowski, C. and Dahmen, U., 2009. Atomic-resolution imaging with a sub-50-pm electron probe. Physical review letters, 102(9), p.096101.

Fayaz, A.M., Balaji, K., Girilal, M., Yadav, R., Kalaichelvan, P.T. and Venketesan, R., 2010. Biogenic synthesis of silver nanoparticles and their synergistic effect with antibiotics: a study against gram-positive and gram-negative bacteria. Nanomedicine: Nanotechnology, Biology and Medicine, 6(1), pp.103-109.

Feng, Q. L., Wu, J., Chen, G. Q., Cui, F. Z., Kim, T. N., and Kim, J. O. 2000. A mechanistic study of the antibacterial effect of silver ions on Escherichia coli and Staphylococcus aureus. Journal of Biomedical Materials Research, 52(4), pp.662-668.

Fisher, k. and Phillips, C. 2009. The ecology, epidemiology and virulence of Enterococcus. Microbiology , 155,pp.1749–1757.

Gade AK, Bonde P, Ingle AP, Marcato PD, Durän N, et al. (2008) Exploitation of Aspergillus niger for synthesis of silver nanoparticles. Journal of Biobased Materials and Bioenergy 2: 243-247.

Gao, W., Thamphiwatana, S., Angsantikul, P. and Zhang, L., 2014. Nanoparticle approaches against bacterial infections. *Wiley Interdisciplinary Reviews: Nanomedicine and Nanobiotechnology*, *6*(6), pp.532-547.

Ghorbani, H. R., Safekordi, A. A., Attar, H., & Sorkhabadi, S. M. (2011). Biological and non-biological methods for silver nanoparticles synthesis. Chemical and Biochemical Engineering Quarterly, 25(3), 317-326.

Giacovazzo, C. ed., 2002. Fundamentals of crystallography (Vol. 7). Oxford university press, USA.

Giannousi, K., Pantazaki, A. and Dendrinou-Samara, C., 2017. Copper-Based Nanoparticles as Antimicrobials. In *Nanostructures for Antimicrobial Therapy* (pp. 515-529). Elsevier.

Giasuddin, A.S.M., Jhuma, K.A. and Haq, A.M., 2013. Use of gold nanoparticles in diagnostics, surgery and medicine: a review. Bangladesh Journal of Medical Biochemistry, 5(2), pp.56-60.

Geochemical Instrumentation and Analysis. (2018). BraggsLaw. [online] Available at: https://serc.carleton.edu/research_education/geochemsheets/BraggsLaw.html [Accessed 21 Feb. 2018].

Mie, G., 1976. A contribution to the optics of turbid media, especially colloidal metallic suspensions. *Ann. Phys*, *25*(4), pp.377-445.

Grumezescu, A.M. ed., 2017. Antimicrobial Nanoarchitectonics: From Synthesis to Applications. William Andrew.

Gupta, A., Landis, R.F. and Rotello, V.M., 2016. Nanoparticle-based antimicrobials: surface functionality is critical. F1000Research, 5.

Gupta, B., Rouesnel, W., & Gooding, J. J. (2011). The Role of Oxygen in Synthesizing Monodisperse Silver Nanocubes. Australian Journal of Chemistry,64(11), 1488-1493.

Gurav, P., Naik, S.S., Ansari, K., Srinath, S., Kishore, K.A., Setty, Y.P. and Sonawane, S., 2014. Stable colloidal copper nanoparticles for a nanofluid: Production and application. Colloids and Surfaces A: Physicochemical and Engineering Aspects, 441, pp.589-597.

Guzman, M., Dille, J. and Godet, S., 2012. Synthesis and antibacterial activity of silver nanoparticles against gram-positive and gram-negative bacteria. Nanomedicine: Nanotechnology, Biology and Medicine, 8(1), pp.37-45.

Hafdallah, A. (2007). Etude du dopage des couches minces de ZnO élaborées par spray ultrasonique. Universite Mentouri Constantine

Hajipour, M. J., Fromm K. M., Ashkarran, A. A, Jimenez de Aberasturi D., de Larramendi I. R., Rojo T., Serpooshan V. et al. 2012. Antibacterial properties of nanoparticles. Trends in Biotechnology, 30(10), pp.499-511.

Hammond, C., 2001. Basics of crystallography and diffraction (Vol. 214). Oxford.

Hanagata, N., Zhuang, F., Connolly, S., Li, J., Ogawa, N. and Xu, M., 2011. Molecular responses of human lung epithelial cells to the toxicity of copper oxide nanoparticles inferred from whole genome expression analysis. ACS nano, 5(12), pp.9326-9338.

Hatchett, D.W. and White, H.S., 1996. Electrochemistry of sulfur adlayers on the low-index faces of silver. The Journal of Physical Chemistry, 100(23), pp.9854-9859.

Hendriksen, R. S., 2003. MIC susceptibility testing of Salmonella and Campylobacter.

Hensley, B.J. & Monson, J.R.T. (2015) Hospital-acquired infections. Surgery (Oxford), 33, pp. 528–533.

Hobman, J.L. and Crossman, L.C., 2015. Bacterial antimicrobial metal ion resistance. Journal of medical microbiology, 64(5), pp.471-497.

Hong, X., Wen, J., Xiong, X. and Hu, Y., 2016. Shape effect on the antibacterial activity of silver nanoparticles synthesized via a microwave-assisted method. Environmental Science and Pollution Research, 23(5), pp.4489-4497.

Inagaki S, Ghirlando R, Grisshammer R. Biophysical characterization of membrane proteins in nanodiscs. Methods. 2013;59:287–300.

Ingale, A. G., & Chaudhari, A. N. (2013). Biogenic synthesis of nanoparticles and potential applications: An eco-friendly approach. J. Nanomed. Nanotechol, 4(2013), 165-170.

Ingle, A.P., Duran, N. and Rai, M., 2014. Bioactivity, mechanism of action, and cytotoxicity of copper-based nanoparticles: a review. *Applied microbiology and biotechnology*, *98*(3), pp.1001-1009.

Ingle A, Rai M, Gade A, Bawaskar M (2009) Fusarium solani: A novel biological agent for the extracellular synthesis of silver nanoparticles. J Nanopart Res 11: 2079-2085.

Iravani, S., Korbekandi, H., Mirmohammadi, S.V. and Zolfaghari, B., 2014. Synthesis of silver nanoparticles: chemical, physical and biological methods. Research in pharmaceutical sciences, 9(6), p.385.

Jaeger, R.C., 2002. Lithography. Introduction to microelectronic fabrication. Upper Saddle.

Jain, S., Hirst, D.G. and O'sullivan, J.M., 2012. Gold nanoparticles as novel agents for cancer therapy. The British journal of radiology, 85(1010), pp.101-113.

Jamshidi, A.J., M., 2014. Synthesis of copper nanoparticles and its antibacterial activity against Escherichia coli. Asian journal of biological science . 7((4)), pp. 183-186.

Jana, N.R., Gearheart, L. and Murphy, C.J., 2001. Wet chemical synthesis of silver nanorods and nanowires of controllable aspect ratioElectronic supplementary information (ESI) available: UV–VIS spectra of silver nanorods. See http://www. rsc. org/suppdata/cc/b1/b100521i. *Chemical Communications*, (7), pp.617-618.

Janardhanan, R., Karuppaiah, M., Hebalkar, N. and Rao, T.N., 2009. Synthesis and surface chemistry of nano silver particles. Polyhedron, 28(12), pp.2522-2530.

Jeeva, K., Thiyagarajan, M., Elangovan, V., Geetha, N. and Venkatachalam, P., 2014. Caesalpinia coriaria leaf extracts mediated biosynthesis of metallic silver nanoparticles and their antibacterial activity against clinically isolated pathogens. Industrial Crops and Products, 52, pp.714-720.

Jiang, M., Cobley, C.M., Lim, B. and Xia, Y., 2011 Noble-Metal Nanostructures with Controlled Morphologies.

Jo, D.H., Kim, J.H., Lee, T.G. and Kim, J.H., 2015. Size, surface charge, and shape determine therapeutic effects of nanoparticles on brain and retinal diseases. *Nanomedicine: Nanotechnology, Biology and Medicine*, *11*(7), pp.1603-1611.

Jones, M.H. and Jones, S.H., 2003. Wet-chemical etching and cleaning of silicon. Fredericksburg, Va.: Virginia Semiconductor.

J. Sun, Y. Jing, Y. Jia, M. Tillard, C. Belin, Mat. Lett. 59 (29), 3933 (2005).

Jung, J.O., H.; Noh, H.; Ji, J. & Kim, S., (2006) "Metal nanoparticle generation using a small ceramic heater with a local heating area.". J Aerosol Sci, 37: p. 1662-1670.

Jung, W. K., Koo, H. C., Kim, K. W., Shin, S., Kim, S. H., and Park, Y. H. 2008. Antibacterial activity and mechanism of action of the silver ion in Staphylococcus aureus and Escherichia coli [down-pointing small open triangle]. Applied and Environmental Microbiology, 74(7), pp.2171–2178.

Kakani, S.L., 2006. Material science. New Age International.-1

Karpov, V. G., Nardone, M., & Grigorchuk, N. I. (2012). Nucleation of plasmonic resonance nanoparticles. Physical Review B, 86(7), 075463.

Ksanalytical.com. (2018). [online] Available at: http://www.ksanalytical.com/images/I-XRD-Diagram.gif [Accessed 21 Feb. 2018].

Kathiresan, K., Alikunhi, N. M., Pathmanaban, S., Nabikhan, A., & Kandasamy, S. (2009). Analysis of antimicrobial silver nanoparticles synthesized by coastal strains of Escherichia coli and Aspergillus niger. Canadian journal of microbiology, 56(12), 1050-1059.

Kelly, A. and Knowles, K.M., 2012. Crystallography and crystal defects. John Wiley & Sons.

Khanna, P.K., Gaikwad, S., Adhyapak, P.V., Singh, N. and Marimuthu, R., 2007. Synthesis and characterization of copper nanoparticles. Materials Letters, 61(25), pp.4711-4714.

Khatoon, U.T., Rao, K.V., Rao, J.R. and Aparna, Y., 2011, November. Synthesis and characterization of silver nanoparticles by chemical reduction method. In Nanoscience, Engineering and Technology (ICONSET), 2011 International Conference on (pp. 97-99). IEEE.

Khodashenas, B. and Ghorbani, H.R., 2015. Synthesis of silver nanoparticles with different shapes. Arabian Journal of Chemistry.

Kędziora, A., Speruda, M., Krzyżewska, E., Rybka, J., Łukowiak, A. and Bugla-Płoskońska, G., 2018. Similarities and differences between silver ions and silver in nanoforms as antibacterial agents. *International journal of molecular sciences*, *19*(2), p.444.

Kim, J. S., Adamcakova-Dodd, A., O'Shaughnessy, P. T., Grassian, V. H., and Thorne, P. S. (2011). Effects of copper nanoparticle exposure on host defense in a murine pulmonary infection model. Particle and Fibre Toxicology, 8(29), pp.1-14.

Kim, J.S., Kuk, E., Yu, K.N., Kim, J.H., Park, S.J., Lee, H.J., Kim, S.H., Park, Y.K., Park, Y.H., Hwang, C.Y. and Kim, Y.K., 2007. Antimicrobial effects of silver nanoparticles. Nanomedicine: Nanotechnology, Biology and Medicine, 3(1), pp.95-101.

Kimling, J., Maier, M., Okenve, B., Kotaidis, V., Ballot, H. and Plech, A., 2006. Turkevich method for gold nanoparticle synthesis revisited. The Journal of Physical Chemistry B, 110(32), pp.15700-15707.

Kleitz, F., Liu, D., Anilkumar, G.M., Park, I.S., Solovyov, L.A., Shmakov, A.N. and Ryoo, R., 2003. Large cage face-centered-cubic Fm 3 m mesoporous silica: synthesis and structure. The Journal of Physical Chemistry B, 107(51), pp.14296-14300.

Kowalczyk, B., Lagzi, I. and Grzybowski, B. (2011). Nanoseparations: Strategies for size and/or shape-selective purification of nanoparticles. Current Opinion in Colloid & Interface Science, 16(2), pp.135-148.

Kowshik M, Ashtaputre S, Kharrazi S, Vogel W, Urban J, et al. (2003) Extracellular synthesis of silver nanoparticles by a silver-tolerant yeast strain MKY3. Nanotechnology 14: 95-100.

Kucekova, Z., Humpolicek, P., Kasparkova, V., Perecko, T., Lehocký, M., Hauerlandová, I., Sáha, P. and Stejskal, J., 2014. Colloidal polyaniline dispersions: Antibacterial activity, cytotoxicity and neutrophil oxidative burst. Colloids and Surfaces B: Biointerfaces, 116, pp.411-417.

Kulkarni, N., & Muddapur, U. (2014). Biosynthesis of Metal Nanoparticles: A Review. Journal of Nanotechnology, 2014.

Langille, M. R., Zhang, J., Personick, M. L., Li, S., & Mirkin, C. A. (2012). Stepwise evolution of spherical seeds into 20-fold twinned icosahedra. Science, 337(6097), 954-957.

Lara, H.H., Garza-Treviño, E.N., Ixtepan-Turrent, L. and Singh, D.K., 2011. Silver nanoparticles are broad-spectrum bactericidal and virucidal compounds. Journal of nanobiotechnology, 9(1), p.30.

Lee, J.H., Kamada, K., Enomoto, N. and Hojo, J., 2007. Morphology-selective synthesis of polyhedral gold nanoparticles: What factors control the size and morphology of gold nanoparticles in a wet-chemical process. Journal of colloid and interface science, 316(2), pp.887-892.

Lee, S.J., Heo, D.N., Moon, J.H., Ko, W.K., Lee, J.B., Bae, M.S., Park, S.W., Kim, J.E., Lee, D.H., Kim, E.C. and Lee, C.H., 2014. Electrospun chitosan nanofibers with controlled levels of silver nanoparticles. Preparation, characterization and antibacterial activity. Carbohydrate polymers, 111, pp.530-537.

Lee, G.P., 2010. The chemical properties and photomorphic silver nanoparticles and their application as an antimicrobial agent ((Doctoral dissertation, Faculty of chemistry)

Lennon, A.M. and Ramesh, K.T., 2004. The influence of crystal structure on the dynamic behavior of materials at high temperatures. International journal of Plasticity, 20(2), pp.269-290.

Li, H., Chen, Q., Zhao, J. and Urmila, K., 2015. Enhancing the antimicrobial activity of natural extraction using the synthetic ultrasmall metal nanoparticles. *Scientific reports*, *5*, p.11033.

Li, Q., Mahendra, S., Lyon, D.Y., Brunet, L., Liga, M.V., Li, D. and Alvarez, P.J., 2008. Antimicrobial nanomaterials for water disinfection and microbial control: potential applications and implications. Water research, 42(18), pp.4591-4602.

Li, Y., Leung, P., Yao, L., Song, Q. W., and Newton, E. 2006. Antimicrobial effect of surgical masks coated with nanoparticles. Journal of Hospital Infection, 62(1), pp.58-63.

Lim, P.Y., Liu, R.S., She, P.L., Hung, C.F. and Shih, H.C., 2006. Synthesis of Ag nanospheres particles in ethylene glycol by electrochemical-assisted polyol process. Chemical Physics Letters, 420(4-6), pp.304-308.

Loirat, C., and Frémeaux-Bacchi, V. 2011. Atypical haemolytic uremic syndrome. Orphanet Journal of Rare Diseases, 6(60), pp.1-30.

Lokhande, A.C., Shelke, A., Babar, P.T., Kim, J., Lee, D.J., Kim, I.C., Lokhande, C.D. and Kim, J.H., 2017. Novel antibacterial application of photovoltaic Cu 2 SnS 3 (CTS) nanoparticles. *RSC Advances*, *7*(54), pp.33737-33744.

Luan, B., Huynh, T. and Zhou, R., 2016. Complete wetting of graphene by biological lipids. *Nanoscale*, *8*(10), pp.5750-5754.

Lu, C., Brauer, M.J. and Botstein, D., 2009. Slow growth induces heat-shock resistance in normal and respiratory-deficient yeast. Molecular biology of the cell, 20(3), pp.891-903.

Lu, Z., Rong, K., Li, J., Yang, H. and Chen, R., 2013. Size-dependent antibacterial activities of silver nanoparticles against oral anaerobic pathogenic bacteria. Journal of Materials Science: Materials in Medicine, 24(6), pp.1465-1471.

Malka, E., Perelshtein, I., Lipovsky, A., Shalom, Y., Naparstek, L., Perkas, N., Patick, T., Lubart, R., Nitzan, Banin, E. and Gedanken, A., 2013. Eradication of Multi-Drug Resistant Bacteria by a Novel Zn-doped CuO Nanocomposite. Small, 9(23), pp.4069-4076.

Macovei, L., and Zurek, L. 2006. Ecology of antibiotic resistance genes: characterization of enterococci from houseflies collected in food settings. Applied and Environmental Microbiology, 72(6): pp.4028–4035.

McFarland, A.D., Haynes, C.L., Mirkin, C.A., Van Duyne, R.P. and Godwin, H.A., 2004. Color my nanoworld. J. Chem. Educ, 81(4), p.544A.

Mesbahi, A., 2010. A review on gold nanoparticles radiosensitization effect in radiation therapy of cancer. Reports of Practical Oncology & Radiotherapy, 15(6), pp.176-180.

Mei, L., Lu, Z., Zhang, W., Wu, Z., Zhang, X., Wang, Y., Luo, Y., Li, C. and Jia, Y., 2013. Bioconjugated nanoparticles for attachment and penetration into pathogenic bacteria. *Biomaterials*, *34*(38), pp.10328-10337.

Midander, K., Cronholm, P., Karlsson, H.L., Elihn, K., Möller, L., Leygraf, C. and Wallinder, I.O., 2009. Surface Characteristics, Copper Release, and Toxicity of Nano-and Micrometer-Sized Copper and Copper (II) Oxide Particles: A Cross-Disciplinary Study. Small, 5(3), pp.389-399.

Misawa, M. and Takahashi, J., 2011. Generation of reactive oxygen species induced by gold nanoparticles under x-ray and UV Irradiations. *Nanomedicine: Nanotechnology, Biology and Medicine*, *7*(5), pp.604-614.

Mishin, Y., Mehl, M.J., Papaconstantopoulos, D.A., Voter, A.F. and Kress, J.D., 2001. Structural stability and lattice defects in copper: Ab initio, tight-binding, and embedded-atom calculations. Physical Review B, 63(22), p.224106.

Mittal A. K., Chisti Y., Banerjee U. C, (2013) Synthesis of metallic nanoparticles using plant extracts. Biotechnology Advances, vol. 31: 346–356.

Moritz, M. and Geszke-Moritz, M., 2013. The newest achievements in synthesis, immobilization and practical applications of antibacterial nanoparticles. Chemical Engineering Journal, 228, pp.596-613.

Mourato A, Gadanho M, Lino AR, Tenreiro R (2011) Biosynthesis of crystalline silver and gold nanoparticles by extremophilic yeasts. Bioinorg Chem Appl 2011: 546074.

Mowbray, R., 2013. Morphological Control of Copper and Cuprous Oxide Nanoparticles via Synthesis and Oxidation/Reduction Reactions (Doctoral dissertation, University of Colorado at Boulder).

Mühling, M., Bradford, A., Readman, J. W. and Somerfield, P. J. 2009. An investigation into the effects of silver nanoparticles on antibiotic resistance of naturally occurring bacteria in an estuarine sediment. Marine Environmental Research, 68 (5), pp.278–283.

Mukherji, S., Ruparelia, J., and Mukherji, S. 2012. Antimicrobial activity of silver and copper nanoparticles: variation in sensitivity across various strains of bacteria and fungi. Nano-Antimicrobials, pp.225-251.

Muniesa, M., Hammerl, J. A., Hertwig, S., Appel, B., and Brüssow, H. 2012. Shiga toxin-producing Escherichia coli O104:H4: a new challenge for microbiology. Applied and Environmental Microbiology, 78(12): pp.4065–4073.

Murray, B. E. 1990. The life and times of the Enterococcus. Clinical Microbiology Reviews, 3(1), pp.46-65.

Namasivayam, S., Rabel, A.M. and Abhraham, T., 2013. Antibacterial activity of chemogenic copper nanoparticles coated cotton fabrics against pyogenic bacteria isolated from post operative patients. In *Advanced Materials Research* (Vol. 622, pp. 842-846). Trans Tech Publications.

NanoComposix. (2018). nanoComposix • Characterization Techniques. [online] Available at: https://nanocomposix.com/pages/characterization-techniques#tem [Accessed 20 Feb. 2018].

Naser, S., Thompson, F. L., Hoste, B., Gevers, D., Vandemeulebroecke, K., Cleenwerck, I., thompson C. C., Vancanneyt M., and Swings J. 2005. Phylogeny and identification of Enterococci by atpA gene sequence analysis. Journal of Clinical Microbiology, 443(5): pp.2224–2230

National Health Service. 2017. Preventing healthcare associated Gram-negative bloodstream infections: an improvement resource: 2017, from [online] Available at: < https://improvement.nhs.uk/resources/preventing-gram-negative-bloodstream-infections/ > [Accessed 1 November 2017].

NDT Resource Center, 2016. Primary Metallic Crystalline Structures (BCC, FCC, HCP). Retrieved from; https://www.ndeed.org/EducationResources/CommunityCollege/Materials/Structure/metallic_structures.htm

Nithya R, Ragunathan R (2009) Synthesis of silver nanoparticles using Pleurotus sajor caju and its antimicrobial study. Digest Journal of Nanomaterials and Biostructures 4: 623-629

Oliver, I.W., Macgregor, K., Godfrey, J.D., Harris, L. and Duguid, A., 2015. Lipid increases in European eel (Anguilla anguilla) in Scotland 1986–2008: an assessment of physical parameters and the influence of organic pollutants. Environmental Science and Pollution Research, 22(10), pp.7519-7528.

Ouyang, Y., Cai, X., Shi, Q., Liu, L., Wan, D., Tan, S. and Ouyang, Y., 2013. Poly-l-lysine-modified reduced graphene oxide stabilizes the copper nanoparticles with higher water-solubility and long-term additively antibacterial activity. Colloids and surfaces B: Biointerfaces, 107, pp.107-114.

Palmer, K. L., Kos, V. N., and Gilmore, M. S. 2010. Horizontal gene transfer and the genomics of enterococcal antibiotic resistance. Current Opinion in Microbiology, 13(5), pp.632-639.

Pal, S., Tak, Y.K. and Song, J.M., 2007. Does the antibacterial activity of silver nanoparticles depend on the shape of the nanoparticle? A study of the gram-negative bacterium Escherichia coli. Applied and environmental microbiology, 73(6), pp.1712-1720.

Panigrahi, T. (2013). Synthesis and Characterization of Silver Nanoparticles using leaf extract of Azadirachta indica (Doctoral dissertation, NATIONAL INSTITUTE OF TECHNOLOGY ROURKELA).

Park, S., Chibli, H., Wong, J. and Nadeau, J.L., 2011. Antimicrobial activity and cellular toxicity of nanoparticle–polymyxin B conjugates. Nanotechnology, 22(18), p.185101.

Pranveer, S. (2014). Nanotechnology Science and Technology. 1st ed. Nova Science Publishers, Inc.: 1-63321-835-X, 978-1-63321-835-2, pp.1-4.

Parinov, I.A., Chang, S.H. and Topolov, V.Y. eds., 2015. Advanced Materials: Manufacturing, Physics, Mechanics and Applications (Vol. 175). Springer.

Pati, R., Mehta, R.K., Mohanty, S., Padhi, A., Sengupta, M., Vaseeharan, B., Goswami, C. and Sonawane, A., 2014. Topical application of zinc oxide nanoparticles reduces bacterial skin infection in mice and exhibits antibacterial activity by inducing oxidative stress response and cell membrane disintegration in macrophages. Nanomedicine: Nanotechnology, Biology and Medicine, 10(6), pp.1195-1208.

Paulkumar, K., Gnanajobitha, G., Vanaja, M., Rajeshkumar, S., Malarkodi, C., Pandian, K. and Annadurai, G., 2014. Piper nigrum leaf and stem assisted green synthesis of silver nanoparticles and evaluation of its antibacterial activity against agricultural plant pathogens. The Scientific World Journal, 2014.

Perelshtein, I., Ruderman, E., Perkas, N., Tzanov, T., Beddow, J., Joyce, E., Mason, T.J., Blanes, M., Mollá, K., Patlolla, A. and Frenkel, A.I., 2013. Chitosan and chitosan–ZnO-based complex nanoparticles: formation, characterization, and antibacterial activity. Journal of Materials Chemistry B, 1(14), pp.1968-1976.

Perelshtein, I., Perkas, N. and Gedanken, A., 2016. Ultrasonic Coating of Textiles by Antibacterial and Antibiofilm Nanoparticles. Handbook of Ultrasonics and Sonochemistry, pp.967-993.

Petersen, A., Bisgaard, M., and Christensen, H. 2010. Real-time PCR detection of Enterococcus faecalis associated with amyloid arthropathy. Letters in Applied Microbiology, 51(1), pp.61-64.

Pillai, Z.S. and Kamat, P.V., 2004. What factors control the size and shape of silver nanoparticles in the citrate ion reduction method?. *The Journal of Physical Chemistry B*, *108*(3), pp.945-951.

Pollini, M., Paladini, F., Catalano, M., Taurino, A., Licciulli, A., Maffezzoli, A. and Sannino, A., 2011. Antibacterial coatings on haemodialysis catheters by photochemical deposition of silver nanoparticles. Journal of Materials Science: Materials in Medicine, 22(9), pp.2005-2012.

Prabhu, S. and Poulose, E.K., 2012. Silver nanoparticles: mechanism of antimicrobial action, synthesis, medical applications, and toxicity effects. *International nano letters*, *2*(1), p.32.

Prasad K, Jha AK, Kulkarni AR (2007) Lactobacillus assisted synthesis of titanium nanoparticles. Nanoscale Res Lett 2: 248-250.

Prema, P. and Thangapandiyan, S., 2013. In-vitro antibacterial activity of gold nanoparticles capped with polysaccharide stabilizing agents. Int J Pharm Pharm Sci, 5(1), pp.310-314.

Public Health England. 2013. Independent investigation into Godstone Farm outbreak. Retrieved 2013, from [online] Available at: < http://www.hpa.org.uk/Topics/ InfectiousDiseases/InfectionsAZ/EscherichiaColiO157/IndependentInvestigationIntoGodstoneFarmOutbreak/ > [Accessed 14 May 2016].

Public Health England. 2017. Laboratory surveillance of Enterococcus spp. bacteraemia in England,

Wales and Northern Ireland: 2016. Retrieved 2017, from [online] Available at: < https://www.gov.uk/government/publications/enterococcus-spp-bacteraemia-voluntary-surveillance > [Accessed 1 November May 2017].

Public Health England. 2017. Laboratory surveillance of Escherichia coli bacteraemia in England, Wales and Northern Ireland: 2016. Retrieved 2017, from [online] Available at: < https://www.gov.uk/government/publications/escherichia-coli-bacteraemia-annual-trends-in-voluntary-surveillance > [Accessed 1 November May 2017].

Rad, M.J., 2014. Synthesis of Copper Nanoparticles and its Antibacterial Activity against Escherichia coli. Asian journal of biological science . 7((4)), pp. 183-186.

Raffi, M., Hussain, F., Bhatti, T. M., Akhter, J. I., Hameed, A., and Hasan, M. M. 2008. Antibacterial characterization of silver nanoparticles against E. coli ATCC-15224. Journal of Materials Science and Technology, 24(2), pp.192-196.

Ratyakshi, R.P. Chauhan . (2009). Colloidal Synthesis of Silver Nano Particles. Asian Journal of Chemistry Vol. 21, No. 10 (2009), S113-116

Rai, M., Yadav, A. and Gade, A., 2009. Silver nanoparticles as a new generation of antimicrobials. Biotechnology advances, 27(1), pp.76-83.

Railean-Plugaru, V., Pomastowski, P., Rafinska, K., Wypij, M., Kupczyk, W., Dahm, H., Jackowski, M. and Buszewski, B., 2016. Antimicrobial properties of biosynthesized silver nanoparticles studied by flow cytometry and related techniques. *Electrophoresis*, *37*(5-6), pp.752-761.

Ray, S., Mohan, R., Singh, J.K., Samantaray, M.K., Shaikh, M.M., Panda, D. and Ghosh, P., 2007. Anticancer and antimicrobial metallopharmaceutical agents based on palladium, gold, and silver N-heterocyclic carbene complexes. Journal of the American Chemical Society, 129(48), pp.15042-15053.

Raza, M., Kanwal, Z., Rauf, A., Sabri, A., Riaz, S. and Naseem, S., 2016. Size-and shape-dependent antibacterial studies of silver nanoparticles synthesized by wet chemical routes. *Nanomaterials*, *6*(4), p.74.

Ren, G., Hu, D., Cheng, E.W., Vargas-Reus, M.A., Reip, P. and Allaker, R.P., 2009. Characterisation of copper oxide nanoparticles for antimicrobial applications. International journal of antimicrobial agents, 33(6), pp.587-590.

Remita, S., Fontaine, P., Lacaze, E., Borensztein, Y., Sellame, H., Farha, R., Rochas, C. and Goldmann, M., 2007. X-ray radiolysis induced formation of silver nano-particles: A SAXS and UV–visible absorption spectroscopy study. Nuclear Instruments and Methods in Physics Research Section B: Beam Interactions with Materials and Atoms, 263(2), pp.436-440.

Ribeiro, T., Oliveira, M., Fraqueza, M.J., Lauková, A., Elias, M., Tenreiro, R., Barreto, A.S. and Semedo-Lemsaddek, T., 2011. Antibiotic resistance and virulence factors among enterococci isolated from chouriço, a traditional Portuguese dry fermented sausage. Journal of food protection, 74(3), pp.465-469.

Rigo, C., Ferroni, L., Tocco, I., Roman, M., Munivrana, I., Gardin, C., Cairns, W.R., Vindigni, V., Azzena, B., Barbante, C. and Zavan, B., 2013. Active silver nanoparticles for wound healing. International journal of molecular sciences, 14(3), pp.4817-4840.

Rice, P.M., Kingery, W.D., Bowen, H.K., Uhlmann, D.R., Onoda, G.Y., Hench, L.L., Wachtman, J.B., Cannon,

Rojas-Andrade, M., Cho, A.T., Hu, P., Lee, S.J., Deming, C.P., Sweeney, S.W., Saltikov, C. and Chen, S., 2015. Enhanced antimicrobial activity with faceted silver nanostructures. Journal of materials science, 50(7), pp.2849-2858.

Ruparelia, J. P., Chatterjee, A. K., Duttagupta, S. P. and Mukherji, S. 2008. Strain specificity in antimicrobial activity of silver and copper nanoparticles. Acta Biomaterialia , 4(3), pp.707-716.

Rutala, W.A. & Weber, D.J. (2011) Are room decontamination units needed to prevent transmission of environmental pathogens? Infection Control and Hospital Epidemiology, 32, pp. 743–747.

Sadeghi, B., Garmaroudi, F. S., Hashemi, M., Nezhad, H. R., Nasrollahi, A., Ardalan, S. and Ardalan, S. 2012. Comparison of the anti-bacterial activity on the nanosilver shapes: Nanoparticles, nanorods and nanoplates. Advanced Powder Technology, 23(1), pp.22–26.

Sanders, W.S. and Gibson, L.J., 2003. Mechanics of BCC and FCC hollow-sphere foams. Materials Science and Engineering: A, 352(1), pp.150-161.

Sannomiya, T., Hafner, C. and Vörös, J., 2009. Shape-dependent sensitivity of single plasmonic nanoparticles for biosensing. Journal of biomedical optics, 14(6), p.064027.

Sarkar, S., Jana, A. D., Samanta, S. K., & Mostafa, G. (2007). Facile synthesis of silver nano particles with highly efficient anti-microbial property. Polyhedron, 26(15), 4419-4426.

Salzemann, C., Lisiecki, I., Urban, J. and Pileni, M.P., 2004. Anisotropic copper nanocrystals synthesized in a supersaturated medium: Nanocrystal growth. Langmuir, 20(26), pp.11772-11777.

Slavin, Y.N., Asnis, J., Häfeli, U.O. and Bach, H., 2017. Metal nanoparticles: understanding the mechanisms behind antibacterial activity. Journal of nanobiotechnology, 15(1), p.65.

Sapsford KE, Tyner KM, Dair BJ, Deschamps JR, Medintz IL. Analyzing nanomaterial bioconjugates: a review of current and emerging purification and characterization techniques. Anal Chem. 2011;83:4453–4488.

Schaefer J, Schulze C, Marxer EE, Schaefer UF, Wohlleben W, Bakowsky U, et al. Atomic force microscopy and analytical ultracentrifugation for probing nanomaterial protein interactions. ACS Nano. 2012;6:4603–4614.

Shang, J. and Gao, X. (2014). Nanoparticle counting: towards accurate determination of the molar concentration. Chem. Soc. Rev., 43(21), pp.7267-7278.

Shrivastava, S., Bera, T., Roy, A., Singh, G., Ramachandrarao, P. and Dash, D., 2007. Characterization of enhanced antibacterial effects of novel silver nanoparticles. *Nanotechnology*, *18*(22), p.225103.

Schubert, U., 2012. Synthesis of inorganic materials. John Wiley & Sons.

Shackelford, J.F. and Muralidhara, M.K., 2005. Introduction to materials science for engineers.

Shamaila, S., Zafar, N., Riaz, S., Sharif, R., Nazir, J. and Naseem, S., 2016. Gold nanoparticles: an efficient antimicrobial agent against enteric bacterial human pathogen. Nanomaterials, 6(4), p.71.

Sharma, M., Singh, S. and Sharma, S., 2015. New Generation Antibiotics/Antibacterials: Deadly Arsenal for Disposal of Antibiotic Resistant Bacteria. J Microb Biochem Technol, 7, pp.374-379.

Sharma N, Pinnaka AK, Raje M, Fnu A, Bhattacharyya MS, et al. (2012) Exploitation of marine bacteria for production of gold nanoparticles. Microb Cell Fact 11: 86.

Sharma, V.K., Yngard, R.A. and Lin, Y., 2009. Silver nanoparticles: green synthesis and their antimicrobial activities. Advances in colloid and interface science, 145(1-2), pp.83-96.

Singh, C., Sharma, V., Naik, P.K., KHandelwal, V. and Singh, H., 2011. A green biogenic approach for synthesis of gold and silver nanoparticles using Zingiber officinale. Digest Journal of Nanomaterials and Biostructures, 6(2), pp.535-542.

Singh, P. and Raja, R.B., 2012. Synergistic effect of silver nanoparticles with the cephalexin antibiotic against the test strains. Bioresearch Bulletin, 4, pp.171-179.

Sirajuddeen, M., (2011). Body centred cubic (bcc) [available online at http://msheiksirajuddeen.blogspot.co.uk/2011/08/body-centred-cubic-bcc.html]. Accessed on 15/2/2018

Slawson RM, Lohmeier-Vogel EM, Lee H, Trevors JT (2004) Silver resistance in Pseudomonas stutzeri. Biometals 7: 30-40.

Sondi, I., and Salopek-Sondi, B. 2004. Silver nanoparticles as antimicrobial agent: a case study on E. coli as a model for Gram-negative bacteria. Journal of Colloid and Interface Science, 275 (1), pp.177–182.

Subhankari, I. and Nayak, P.L., 2013. Antimicrobial activity of copper nanoparticles synthesised by ginger (Zingiber officinale) extract. World Journal of Nano Science & Technology, 2(1), pp.10-13.

Sun, J., Jing, Y., Jia, Y., Tillard, M. and Belin, C., 2005. Mechanism of preparing ultrafine copper powder by polyol process. Materials Letters, 59(29-30), pp.3933-3936.

Swarnavalli, G., Joseph, V., Kannappan, V. and Roopsingh, D., 2011. A simple approach to the synthesis of hexagonal-shaped silver nanoplates. Journal of Nanomaterials, 2011, p.54.

Temelli, S., Eyigör, A., and Anar, S. 2012. Prevalence of Escherichia coli O157 in red meat and meat products determined by VIDAS ECPT and LightCycler PCR. Turkish Journal of Veterinary and Animal Sciences, 36(3), pp.305-310.

Thakkar KN, Mhatre SS, Parikh RY (2010) Biological synthesis of metallic nanoparticles. Nanomedicine 6: 257-262.

Theivasanthi, T. and Alagar, M., 2011. Studies of copper nanoparticles effects on micro-organisms. arXiv preprint arXiv:1110.1372.

Tian, N., Zhou, Z.Y., Yu, N.F., Wang, L.Y. and Sun, S.G., 2010. Direct electrodeposition of tetrahexahedral Pd nanocrystals with high-index facets and high catalytic activity for ethanol electrooxidation. Journal of the American Chemical Society, 132(22), pp.7580 7581.

Udayasoorian, C., Kumar, R.V. and Jayabalakrishnan, M., 2011. Extracellular synthesis of silver nanoparticles using leaf extract of Cassia auriculata. Dig J Nanomater Biostruct, 6(1), pp.279-283.

Ulrich, R.K. and Brown, W.D. eds., 2006. Advanced electronic packaging. Hoboken, NJ: Wiley.

Umadevi, M., Rani, T., Balakrishnan, T. and Ramanibai, R., 2011. Antimicrobial activity of silver nanoparticles prepared under an ultrasonic field. Int J Pharma Sci Nanotechnol 2011; 4 (3): 1491, 1496.

Vimbela, G.V., Ngo, S.M., Fraze, C., Yang, L. and Stout, D.A., 2017. Antibacterial properties and toxicity from metallic nanomaterials. International journal of nanomedicine, 12, p.3941.

Van Dong, P., Ha, C. H., Binh, L. T. and Kasbohm, J. 2012. Chemical synthesis and antibacterial activity of novel-shaped silver nanoparticles. International Nano Letters, 2(9), pp.1-9.

Velmurugan, P., Anbalagan, K., Manosathyadevan, M., Lee, K.J., Cho, M., Lee, S.M., Park, J.H., Oh, S.G., Bang, K.S. and Oh, B.T., 2014. Green synthesis of silver and gold nanoparticles using Zingiber officinale root extract and antibacterial activity of silver nanoparticles against food pathogens. Bioprocess and biosystems engineering, 37(10), pp.1935-1943.

Volkmer B. and Heinemann M. 2011. Condition-dependent cell volume and concentration of Escherichia coli to facilitate data conversion for systems biology modelling. PLoS ONE 6(7), p.e23126.

Wang, D., Zhao, L., Ma, H., Zhang, H. and Guo, L.H., 2017. Quantitative analysis of reactive oxygen species photogenerated on metal oxide nanoparticles and their bacteria toxicity: the role of superoxide radicals. *Environmental science & technology*, *51*(17), pp.10137-10145.

Wang, L., Hu, C. and Shao, L., 2017. The antimicrobial activity of nanoparticles: present situation and prospects for the future. International journal of nanomedicine, 12, p.1227.

Wang W. X, Geng L., Ding S., and Xu S. K. 2012. Facile synthesis of silver nanoparticles and their antimicrobial activity against several representative microbial species. Biomedical Engineering and Biotechnology (iCBEB), pp.287-290.

Wang, Y., Chen, P. and Liu, M., 2006. Synthesis of well-defined copper nanocubes by a one-pot solution process. Nanotechnology, 17(24), p.6000.

Wang, Y., Xie, S., Liu, J., Park, J., Huang, C. Z., & Xia, Y. (2013). Shape-Controlled Synthesis of Palladium Nanocrystals: A Mechanistic Understanding of the Evolution from Octahedrons to Tetrahedrons. Nano letters, 13(5), 2276-2281.

Wani, I.A. and Ahmad, T., 2013. Size and shape dependant antifungal activity of gold nanoparticles: a case study of Candida. Colloids and Surfaces B: Biointerfaces, 101, pp.162-170.

Washio, I., Xiong, Y., Yin, Y. and Xia, Y., 2006. Reduction by the end groups of poly (vinyl pyrrolidone): a new and versatile route to the kinetically controlled synthesis of Ag triangular nanoplates. *Advanced Materials*, *18*(13), pp.1745-1749.

Weng, C. H., Huang, C. C., Yeh, C. S., Lei, H. Y., & Lee, G. B. (2008). Synthesis of hexagonal gold nanoparticles using a microfluidic reaction system. Journal of Micromechanics and microengineering, 18(3), 035019.

West, A. R. (2007). Solid state chemistry and its applications. John Wiley & Sons.

Wiest, A., MacDougall, C.A. and Conner, R.D., US Secretary of Navy, 2015. Foams made of amorphous hollow spheres and methods of manufacture thereof. U.S. Patent 9,102,087.

Wiley, B.J., Xiong, Y., Li, Z.Y., Yin, Y. and Xia, Y., 2006. Right bipyramids of silver: a new shape derived from single twinned seeds. Nano letters, 6(4), pp.765-768.

Wiley, B., Sun, Y., Mayers, B. and Xia, Y., 2005. Shape-controlled synthesis of metal nanostructures: the case of silver. Chemistry-A European Journal, 11(2), pp.454-463.

William F..Smith and Hashemi, J., 2011. Foundations of materials science and engineering. McGraw-Hill.

Wilkinson, L.J., White, R.J. and Chipman, J.K., 2011. Silver and nanoparticles of silver in wound dressings: a review of efficacy and safety. Journal of wound care, 20(11), pp.543-549.

Witte, W., 2004. International dissemination of antibiotic resistant strains of bacterial pathogens. Infection, Genetics and Evolution, 4(3), pp.187-191.

World Health Organization (2002) Prevention of hospital-acquired infections: A pratical guide. Geneva: World Health Organisation

W.R. and Matthewson, M.J., 1997. Physical ceramics: principles for ceramic science and engineering.

Wua, H., Schwarzal, C. S and With, N., 2008.The Analysis of Minimum Inhibitory Concentration (MIC) Data for Anti-Microbial Agents from Complex Experiments. Journal of Applied Statistics. Available at http://people.stat.sfu.ca/~cschwarz/MySoftware/MIC/Paper/MICpaper.pdf Accessed on 03/6/2017

Wu, W., Huang, J., Wu, L., Sun, D., Lin, L., Zhou, Y., Wang, H. and Li, Q. (2013). Two-step size- and shape separation of biosynthesized gold nanoparticles. Separation and Purification Technology, 106, pp.117-122.

Xia, Y., Xia, X., Wang, Y., & Xie, S. (2013). Shape-controlled synthesis of metal nanocrystals. MRS bulletin, 38(04), 335-344.

Xia, Y., Xiong, Y., Lim, B., & Skrabalak, S. E. (2009). Shape-Controlled Synthesis of Metal Nanocrystals: Simple Chemistry Meets Complex Physics?. Angewandte Chemie International Edition, 48(1), 60-103.

Xia, X.J., Zhou, Y.H., Shi, K., Zhou, J., Foyer, C.H. and Yu, J.Q., 2015. Interplay between reactive oxygen species and hormones in the control of plant development and stress tolerance. Journal of experimental botany, 66(10), pp.2839-2856.

Xiong, L., Yu, H., Nie, C., Xiao, Y., Zeng, Q., Wang, G., Wang, B., Lv, H., Li, Q. and Chen, S., 2017. Size-controlled synthesis of Cu 2 O nanoparticles: Size effect on antibacterial activity and application as a photocatalyst for highly efficient H 2 O 2 evolution. *RSC Advances*, *7*(82), pp.51822-51830.

Xu, Y., Wei, M.T., Ou-Yang, H.D., Walker, S.G., Wang, H.Z., Gordon, C.R., Guterman, S., Zawacki, E., Applebaum, E., Brink, P.R. and Rafailovich, M., 2016. Exposure to TiO 2 nanoparticles increases Staphylococcus aureus infection of HeLa cells. *Journal of nanobiotechnology*, *14*(1), p.34.

Yang, L., Yan, W., Wang, H., Zhuang, H. and Zhang, J., 2017. Shell thickness-dependent antibacterial activity and biocompatibility of gold@ silver core–shell nanoparticles. *RSC Advances*, *7*(19), pp.11355-11361.

Yang, X., Li, J., Liang, T., Ma, C., Zhang, Y., Chen, H., Hanagata, N., Su, H. and Xu, M., 2014. Antibacterial activity of two-dimensional MoS 2 sheets. Nanoscale, 6(17), pp.10126-10133.

Yang, W., Shen, C., Ji, Q., An, H., Wang, J., Liu, Q. and Zhang, Z., 2009. Food storage material silver nanoparticles interfere with DNA replication fidelity and bind with DNA. *Nanotechnology*, *20*(8), p.085102.

Y. Xia, Y. Xiong, B. Lim and S. E. Skrabalak, "Shape Controlled synthesis of metal nanocrystals: Simple chemistry meets complex physics?" Angewandte chemie international edition, vol 48, no 1, pp. 60-103, 2009.

Zhang, Q., Liu, H., Wang, X., Shi, X. and Duan, X., 2009. Fabrication and characterization of nano silver powder prepared by spray pyrolysis. Journal of Wuhan University of Technology-Mater. Sci. Ed., 24(6), p.871.

Zhang, W., Li, Y., Niu, J. and Chen, Y., 2013. Photogeneration of reactive oxygen species on uncoated silver, gold, nickel, and silicon nanoparticles and their antibacterial effects. *Langmuir*, *29*(15), pp.4647-4651.

Zhang, Y., Peng, H., Huang, W., Zhou, Y. and Yan, D., 2008. Facile preparation and characterization of highly antimicrobial colloid Ag or Au nanoparticles. Journal of colloid and interface science, 325(2), pp.371-376.

Zhao, G. and Stevens, S.E., 1998. Multiple parameters for the comprehensive evaluation of the susceptibility of Escherichia coli to the silver ion. Biometals, 11(1), pp.27-32.

Zhao, J. and Riediker, M., 2014. Detecting the oxidative reactivity of nanoparticles: a new protocol for reducing artifacts. *Journal of Nanoparticle Research*, *16*(7), p.2493.

Zhao, X., Xia, Y., Li, Q., Ma, X., Quan, F., Geng, C. and Han, Z., 2014. Microwave-assisted synthesis of silver nanoparticles using sodium alginate and their antibacterial activity. Colloids and Surfaces A: Physicochemical and Engineering Aspects, 444, pp.180-188.

Zheng, F., Wang, S., Wen, S., Shen, M., Zhu, M. and Shi, X., 2013. Characterization and antibacterial activity of amoxicillin-loaded electrospun nano-hydroxyapatite/poly (lactic-co-glycolic acid) composite nanofibers. Biomaterials, 34(4), pp.1402-1412.

Zhou, Y., Kong, Y., Kundu, S., Cirillo, J. D. and Liang, H. 2012. Antibacterial activities of gold and silver nanoparticles against Escherichia coli and bacillus Calmette-Guérin. Journal of Nanobiotechnology, 10(19), pp.1-9.

Zhou, Z.Y., Tian, N., Li, J.T., Broadwell, I. and Sun, S.G., 2011. Nanomaterials of high surface energy with exceptional properties in catalysis and energy storage. Chemical Society Reviews, 40(7), pp.4167-4185.

Appendices

Appendix A:

Silver Crystal Structures

Suh I-K, Ohta H, Waseda Y

Journal of Materials Science 23 (1988) 757-760

High-temperature thermal expansion of six metallic elements measured

by dilatation method and X-ray diffraction

Locality: synthetic

Sample: at T = 293 K

_database_code_amcsd 0013118

CELL PARAMETERS: 4.0860 4.0860 4.0860 90.000 90.000 90.000

SPACE GROUP: Fm3m

X-RAY WAVELENGTH: 1.541838

MAX. ABS. INTENSITY / VOLUME**2: 565.0704150

2-THETA	INTENSITY	D-SPACING	H	K	L	Multiplicity
38.15	100.00	2.3592	1	1	1	8
44.34	46.77	2.0431	2	0	0	6
64.50	25.61	1.4447	2	2	0	12
77.74	27.18	1.2320	3	1	1	24
81.62	7.69	1.1796	2	2	2	8

==========

For reference, see Downs et al. (1993) American Mineralogist 78, 1104-1107.

Appendix B:

Copper Crystal Structures

Suh I-K, Ohta H, Waseda Y

Journal of Materials Science 23 (1988) 757-760

High-temperature thermal expansion of six metallic elements measured

by dilatation method and X-ray diffraction

Locality: synthetic

Sample: at T = 293 K

_database_code_amcsd 0013087

CELL PARAMETERS: 3.6130 3.6130 3.6130 90.000 90.000 90.000

SPACE GROUP: Fm3m

X-RAY WAVELENGTH: 1.541838

2-THETA	INTENSITY	D-SPACING	H	K	L	Multiplicity
42.35	100.00	2.0871	1	1	1	8
50.49	45.56	1.8075	2	0	0	6
74.20	23.28	1.2781	2	2	0	12

==========

XPOW Copyright 1993 Bob Downs, Ranjini Swaminathan and Kurt Bartelmehs

For reference, see Downs et al. (1993) American Mineralogist 78, 1104-1107.

Appendix C:

Gold Crystal Structures

Suh I-K, Ohta H, Waseda Y

Journal of Materials Science 23 (1988) 757-760

High-temperature thermal expansion of six metallic elements measured

by dilatation method and X-ray diffraction

Locality: synthetic

Sample: at T = 574 K

_database_code_amcsd 0013109

CELL PARAMETERS: 4.0910 4.0910 4.0910 90.000 90.000 90.000

SPACE GROUP: Fm3m

X-RAY WAVELENGTH: 1.541838

MAX. ABS. INTENSITY / VOLUME**2: 1764.453631

2-THETA	INTENSITY	D-SPACING	H	K	L	Multiplicity
38.10	100	2.3619	1	1	11	8
44.28	47.97	2.0455	2	0	0	6
64.42	28.46	1.4464	2	0	0	12
77.36	31.38	1.2335	3	1	1	24
81.50	8.96	1.1810	2	2	2	8

==========

For reference, see Downs et al. (1993) American Mineralogist 78, 1104-1107.

Appendix D

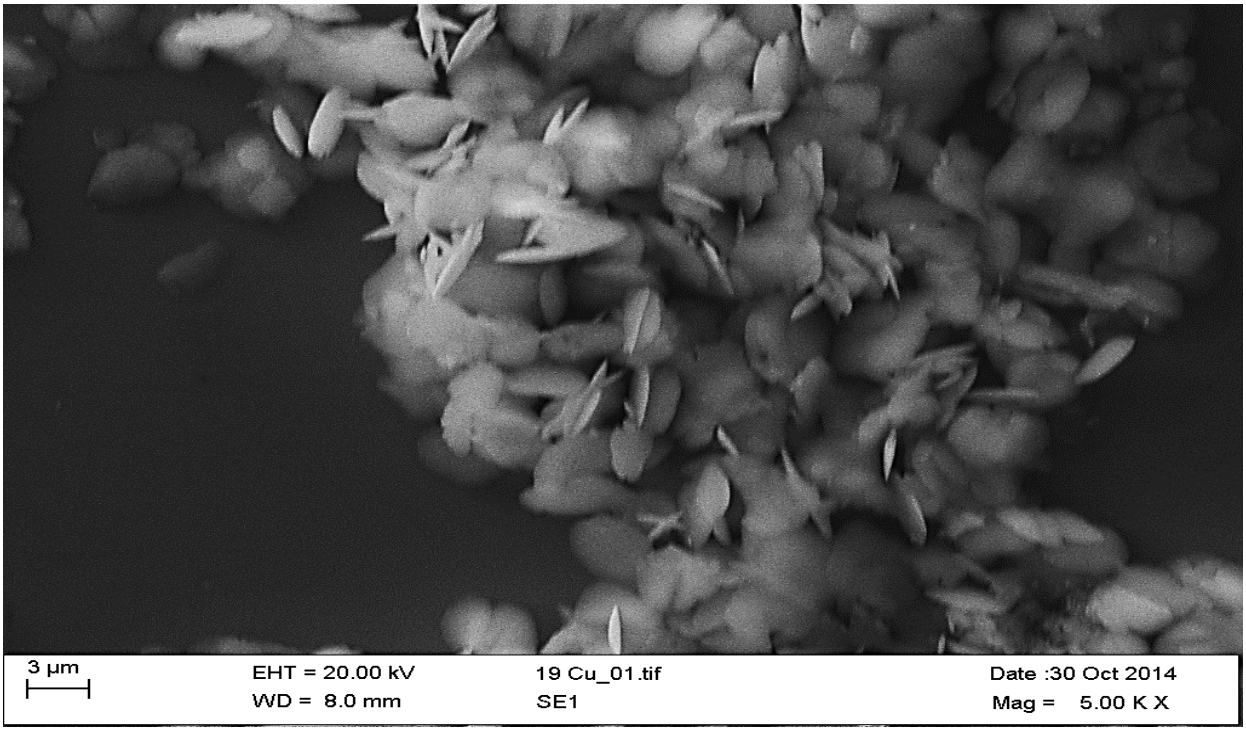

SEM image of Copper nanplate

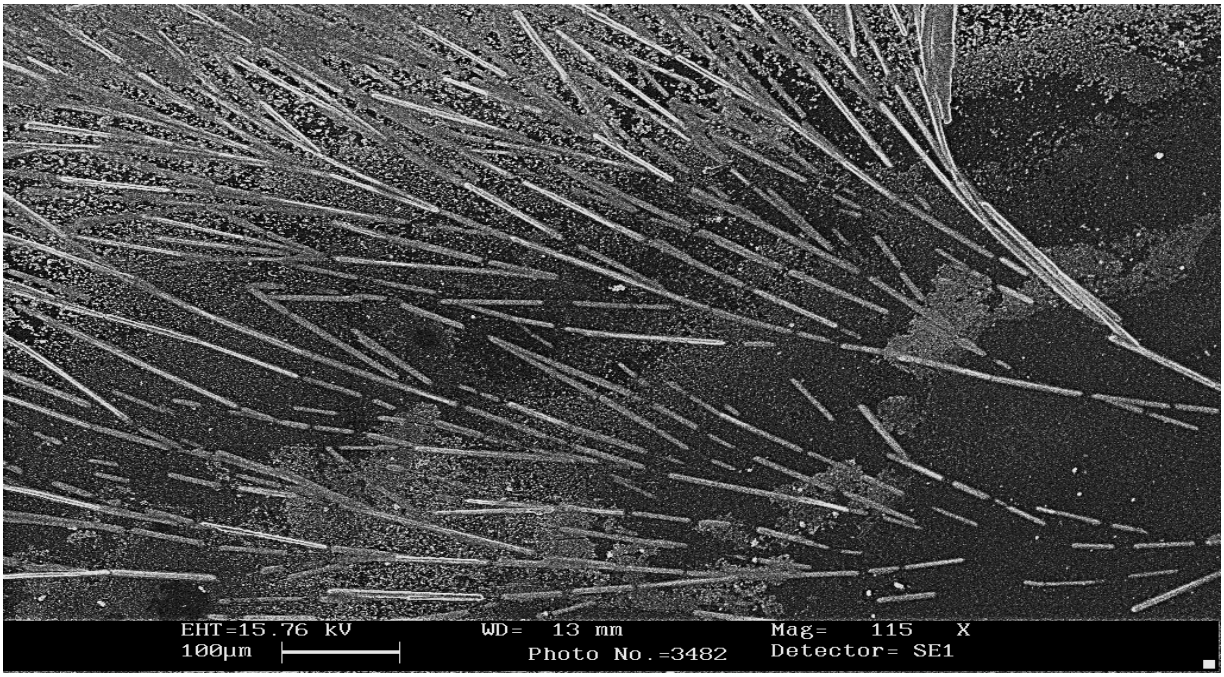

SEM image of Gold nanowire

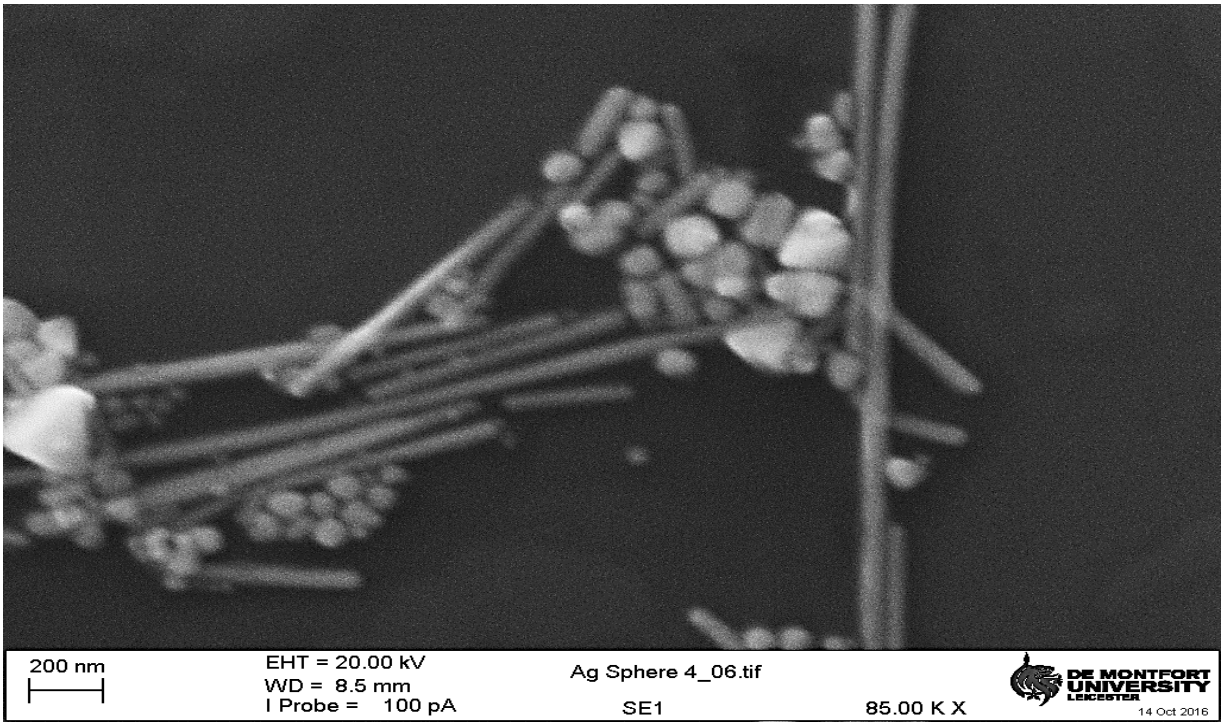

SEM image of Silver nanowire

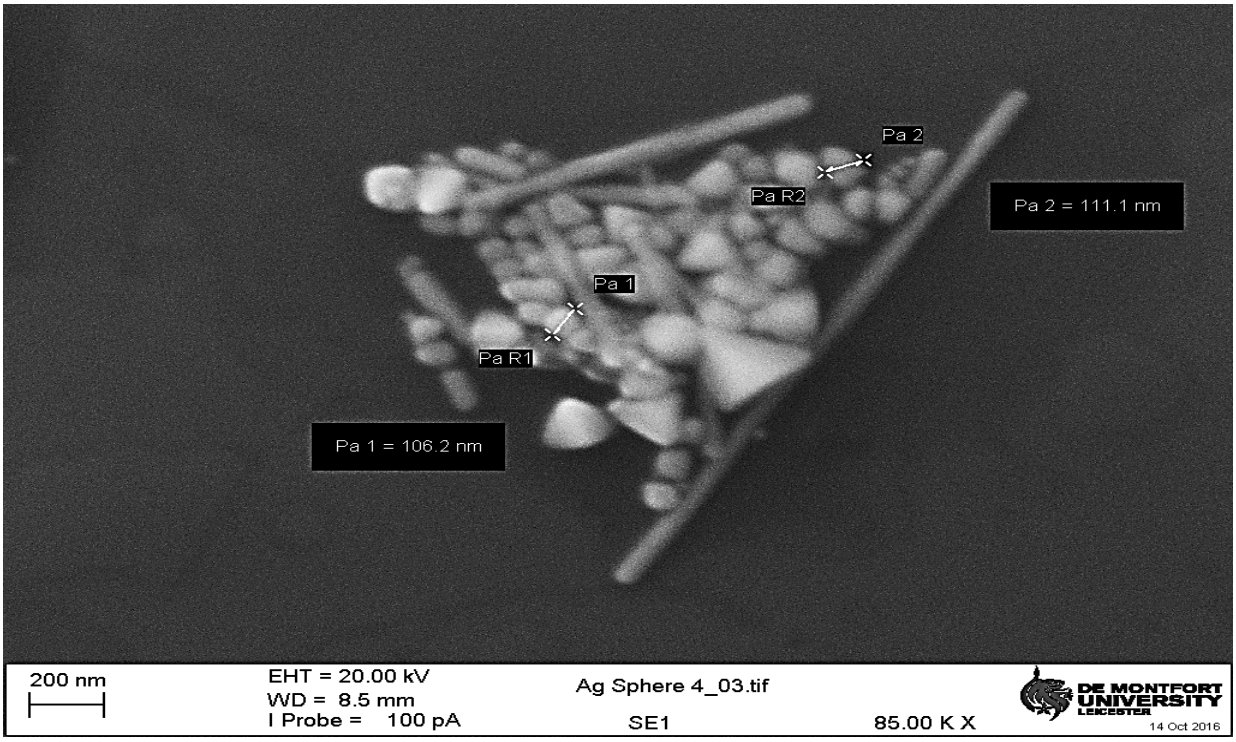

SEM image of Traingle nanosilver

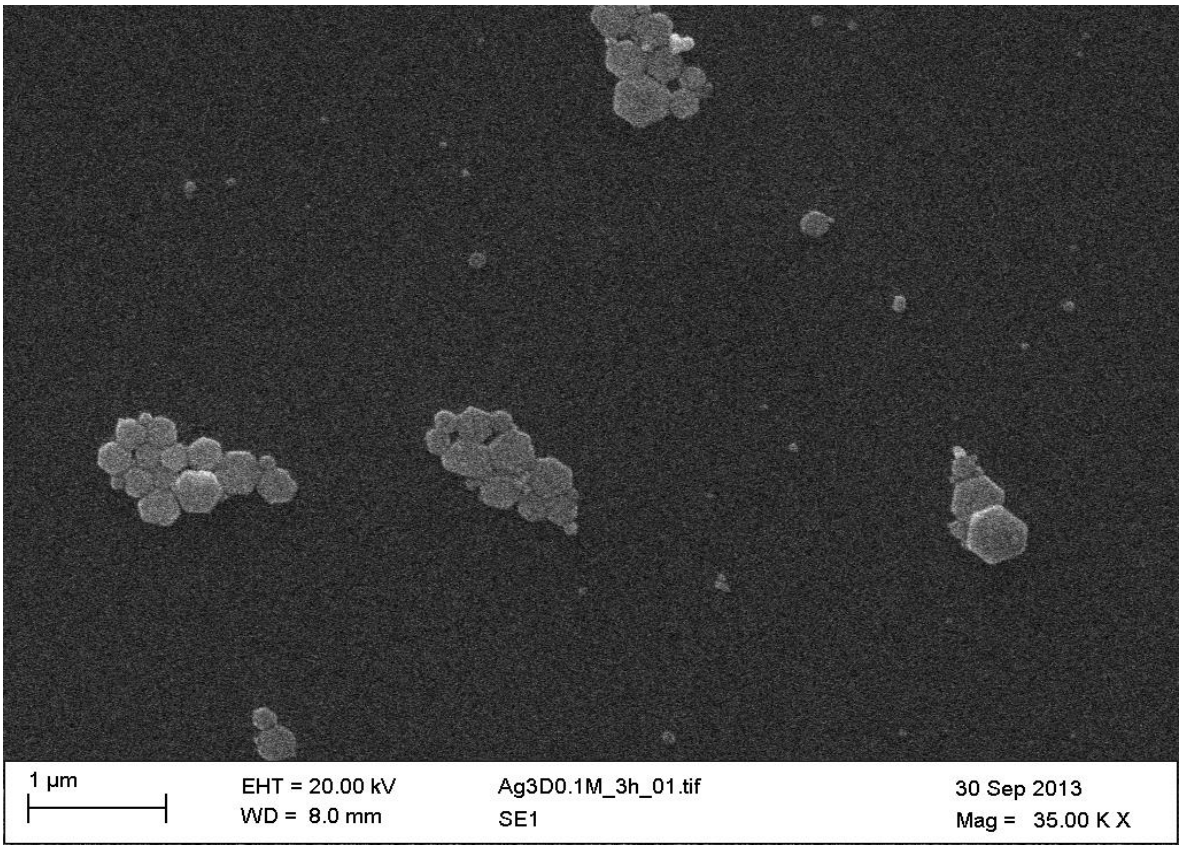

SEM image of hexagonal plate AgNPs

Appendix E

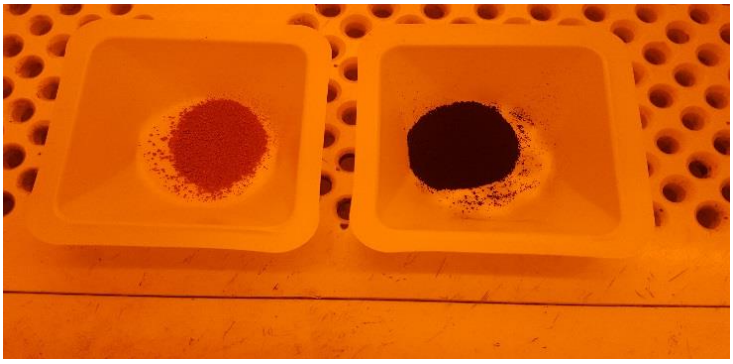

Different between copper NPs produced *in vitro* (left) and commercial copper oxide NPs

Appendix F

Explore

Case Processing Summary

Valid		Missing		Total	
N	Percent	N	Percent	N	Percent
72	100.0%	0	0.0%	72	100.0%

Descriptives

Data		Statistic	Std. Error
Mean		13.56	.04331
95% Confidence Interval for Mean	Lower Bound	13.36	
	Upper Bound	13.66	
5% Trimmed Mean		13.5512	
Median		13.3850	
Variance		.172	
Std. Deviation		.41468	
Minimum		13.00	
Maximum		14.17	
Range		1.17	
Interquartile Range		.81	
Skewness		.249	.283
Kurtosis		-1.667	.559

Tests of Normality

Kolmogorov-Smirnov[a]			Shapiro-Wilk		
Statistic	df	Sig.	Statistic	df	Sig.
.270	72	.000	.823	72	.000

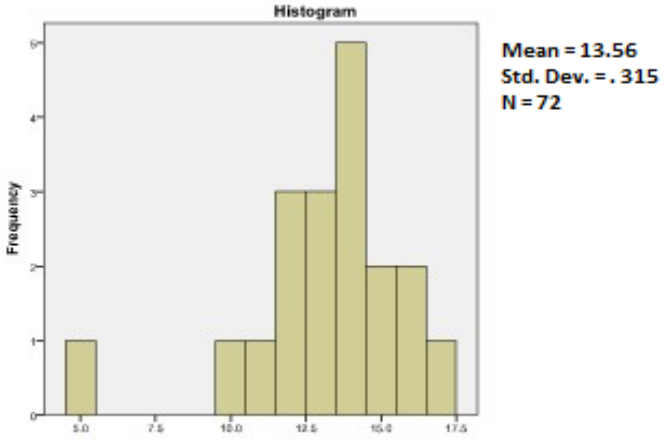
Histogram
Mean = 13.56
Std. Dev. = .315
N = 72
Frequency

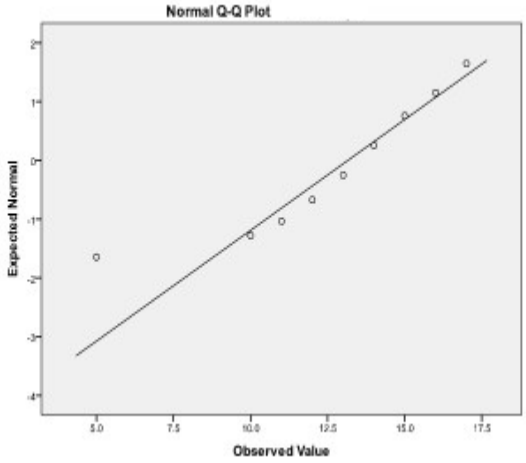
Normal Q-Q Plot
Expected Normal
Observed Value

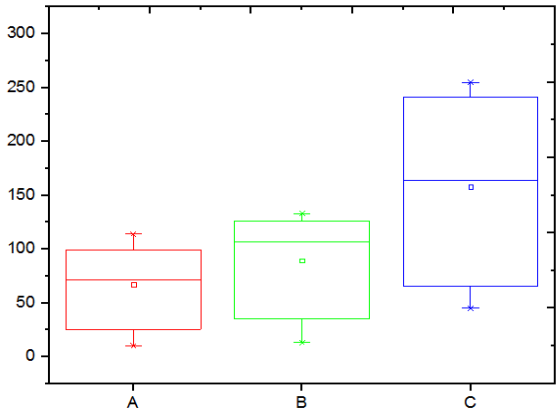
300
250
200
150
100
50
0
A
B
C